Gekoppeld experimenteel-numerieke methodologie
ter evaluatie van de rekcapaciteit van omtreklassen in pijpleidingen

Coupled Experimental-Numerical Framework
for the Assessment of Strain Capacity of Flawed Girth Welds in Pipelines

Stijn Hertelé

Promotor: prof. dr. ir. W. De Waele
Proefschrift ingediend tot het behalen van de graad van
Doctor in de Ingenieurswetenschappen

Vakgroep Mechanische Constructie en Productie
Voorzitter: prof. dr. ir. P. De Baets
Faculteit Ingenieurswetenschappen en Architectuur
Academiejaar 2011 - 2012

UNIVERSITEIT
GENT

ISBN 978-90-8578-511-8
NUR 978
Wettelijk depot: D/2012/10.500/37

Promotor

prof. dr. ir. W. De Waele

Ghent University
Faculty of Engineering
Department of Mechanical Construction and Production

Examination Committee

prof. L. Taerwe (Chair)
prof. W. De Waele
prof. R. Denys
prof. P. De Baets
prof. R. Petrov
prof. D. Vanderschueren
prof. N. O'Dowd
prof. N. Gubeljak

Research Institute

Ghent University
Department of Mechanical Construction and Production
Laboratory Soete
Technologiepark 903
B-9052 Zwijnaarde
Belgium

Tel. +32 9 331 04 74
Fax. +32 9 331 04 90
Stijn.Hertele@UGent.be

www.tribology-fatigue.ugent.be

‘The important thing is not to stop questioning. Curiosity has its own reason for existing.’

Albert Einstein

Acknowledgements

First and foremost, I would like to thank my promoter Prof. Wim De Waele for his strong support and constant availability for technical discussions, and Prof. Rudi Denys for sharing part of his invaluable decades of experience in the field of strain based design. Their guidance made working at Laboratory Soete a true privilege.

This work was made possible by the financial support of the FWO Vlaanderen (Research Foundation Flanders), grants nrs. 1.1.880.09.N.00, 1.1.880.11.N.01 and 1.5.247.08.N.00.

The technical support of some people was key to many of the obtained results. My special thanks go to:

- *Tony Lefevre for notching the medium wide plate specimens, performing most of the tensile tests examined in chapter 3 and other technical assistance,*
- *Julien De Meyer for extracting the medium wide plate specimens and welding them to end blocks,*
- *Hans Van Severen and Philip De Baere (Belgian Welding Institute) for an uncountable number of light and heavy jobs,*
- *Johan Van Den Bossche for machining small scale specimens, mounting and repairing things I broke* [1]*,*
- *Johan De Clercq for various jobs and for always being cheerful,*
- *Chris Bonne for assistance with data acquisition and filtering,*
- *Rudy Desmet for sharing experience in the field of machine design,*
- *Michel De Waele, Anja Buyse, Gert Oost and Andries Vandevyver of the Belgian Welding Insitute, for assistance and nice moments during the embedding, polishing and etching of weld macrographs,*
- *Wouter Ost for support regarding the MTS 2.5 MN test rig and data acquisition,*
- *Josiane Yde for being 'la Mama' of the laboratory,*

[1] *With a proper lever, you don't need to be strong to destroy an M125×4 thread ...*

- *my colleague and good friend Matthias Verstraete, and exceptionally strong master thesis students Karel De Keyser and Frederik Van Acker, for helping to improve the medium wide plate test procedure to its eventual stage.*

Discussions with colleagues beyond Ghent University were highly valuable to some aspects of the work performed. I would like to express my particular gratitude to

- *Prof. Noel O'Dowd, who gave me the opportunity to stay at the MSSI institute of Limerick University for effective discussions on fundamental aspects and finite element modelling of fracture mechanics.*
- *Anthony Horn, Mikhail Trull and Adam Bannister for useful general discussions on strain based assessment at Corus Swinden Technology Centre, Rotherham, UK, and for providing experimental results from the curved wide plate test 'CWP-1' reported in chapter 6.*

Further thanks go to Ralf Lichtenberger from Limess Messtechnik & Software GmbH for explaining the DIC system and always providing fast and effective support, Timothy 'Dash' Weeks from NIST for discussing optical strain measurement techniques, Gianluca De Santis from IBiTech for introducing me to the technique of nodal coordinate transformations, Gunter Coen from SCK-CEN for sharing experience with the unloading compliance measurement technique and Prof. Nele Van Caenegem for teaching me on welding metallurgy. I wish Nele good luck with her future career at Place2Stay!

Good work is impossible without a good atmosphere. I will never forget the nice moments with my 'office colleagues' Matthias Verstraete, Jeroen Van Wittenberghe, Timothy Galle and Koen Van Minnebruggen. Thanks also go to all other colleague researchers Yeczain Perez, Vanessa Rodriguez, Jan De Pauw, Wouter Ost, Felicia Jula, Gusztav Fekete, Jacob Sukumaran, Reza Hojjati Talemi, Matyas Ando, Patric Neis, Mohsen Safaei, Hanan Al Ali, Stijn Van Autrève and Simon Tavernier for nice chats, good discussions, beautiful weddings and team buildings after work. I appreciate the hospitality of Hamed Yazdani during my stay at Limerick University.

The musical company of Pink Floyd, Dire Straits, The Rolling Stones and The Doors during cycling to and from work is appreciated.

Thanks go to all my friends, whom I will not explicitly mention because of the risk of forgetting names. I promise to show my face more often after all deadlines have passed!

Finally, the highest gratitude goes to my parents Patrick and Ann, my sister Eline, and Wendy for always supporting me, and in particular to my girlfriend Sien, who unconditionally celebrated 'good' and healed 'bad' days. Thank you!

Stijn Hertelé *Ghent, 2012.*

Summary

The increasing demand for energy urges fossil fuel suppliers to exploit new oil and natural gas fields. Due to decreasing reserves, these fields have to be found in increasingly harsh environments such as seismic and arctic onshore regions and deep water offshore regions. Hostile environmental conditions can introduce longitudinal global plastic deformation into the transport pipeline, which requires a 'strain based' design approach. Such approach aims to estimate the allowable strain in the structure (rather than the allowable stress in traditional 'stress based design'). A critical point in this design is the assessment of the girth welds that connect pipe sections, given the likely presence of weld flaws that weaken the structure.

In contrast with the well developed field of stress based flaw assessment, there are no fully satisfactory methods which can account for all key influence factors on the integrity of a flawed girth weld under remote plastic straining. Available methods do not account for all key factors, are too conservative, and/or have not been successfully validated. The main cause is the large number of influences and the large sensitivity to many of these influences (compared with stress based design). As a result, experimental and numerical (finite element) approaches remain essential in the strain based assessment of a weld flaw.

This work aims to provide a better insight into the assumptions and resulting interpretation of numerical and experimental tools for the strain based flaw assessment of high strength steel pipelines. Focus goes to longitudinally tensioned girth weld surface flaws in microstructures with sufficient toughness to avoid brittle fracture. Two major failure modes are considered: (unstable) ductile tearing and plastic collapse. The main research goal is to investigate different influences of the constitutive behaviours of line pipe steel and weld metal on the strain capacity of the flawed girth weld. These influences involve weld strength mismatch, base metal heterogeneity and exact stress-strain behaviour.

The curved wide plate (CWP) test is used as investigation object. A CWP test can be described as a tensile test on an unflattened sample of a pipe containing a surface notch to simulate a girth weld flaw. It represents the structural dimensions of a full scale pipeline and can be surrounded with small

scale material tests to enable a proper evaluation of the CWP test result. Application of a pressure correction factor allows to relate the strain capacity of a CWP specimen to that of a pressurized pipeline weld joint.

Three concrete tools are elaborated within the framework of this dissertation as summarized below. The development of each tool is based on an extensive literature survey that covers its respective state of the art.

First, common practice in finite element modelling of flawed girth weldments approximates the base (line pipe) steels' constitutive behaviour by means of the standardized Ramberg-Osgood equation. This constitutive law characterizes strain hardening on the basis of one fixed strain hardening exponent and thereby introduces a dependency between uniform elongation and yield-to-tensile ratio. However, high strength line pipe steels often exhibit two distinct stages of strain hardening and, as a consequence, do not show this dependency. A new 'UGent' stress-strain model is introduced in this dissertation, specifically aiming at a better representation of high strength line pipe steels. The improvement with respect to the Ramberg-Osgood is significant. Three procedures are developed to estimate 'UGent' model parameters, allowing for different trade-offs between required input and obtained accuracy.

Second, a parametric finite element model has been developed to systematically investigate effects of constitutive properties on crack driving force and, as a result, strain capacity. This model allows to describe a wide range of geometrical pipe and weld features, different flaw locations and shapes. A framework for the incorporation of ductile tearing is introduced, using an algorithm that has been justified in literature.

Third, a literature review revealed that reported curved wide plate test results are difficult to interpret, given the absence of a standardized geometry and test protocol and limitations of instrumentation. Therefore, a medium scale (150 mm wide) variant of CWP testing has been developed for research purposes. Its geometry has been designed with attention to obtaining representative remote strain measurements. The implementation of two optimized measurement techniques allows for the quantification of surface strain distributions (optical digital image correlation) and ductile tearing (unloading compliance analysis).

These tools have allowed for the systematic investigation of different hot topics in research towards strain based flaw assessment.

First, the experimental results particularly indicate that effects of moderate line pipe steel heterogeneity on strain capacity are substantial. These effects are not accounted for in most strain based flaw assessment procedures, and are justified by means of theoretical considerations. Next, the experimental results provide the resources for a successful validation of the finite element model and the numerical ductile tearing algorithm.

The validated finite element model is then used in an extensive parametric study to investigate effects of line pipe steel constitutive behaviour and weld strength mismatch on crack driving force and strain capacity. In contrast with published literature, a weld strength definition based upon flow stress (average of yield and ultimate tensile strength) is found most appropriate to predict strain capacity. Hereby, use of the Ramberg-Osgood model can yield significantly inaccurate and unconservative predictions of strain capacity relative to the uniform elongation of the line pipe steel. As a result, the 'UGent' model for line pipe steels is advised over the Ramberg-Osgood for numerical strain based flaw assessments.

The experimental and numerical developments and results are finally combined in a top-down strategy for the strain based design of pipelines and the integrity assessment of detected girth weld flaws. This framework has been developed with attention to existing strain based design strategies and cover all significant results obtained in this dissertation.

Future research opportunities are identified in the characterization and numerical implementation of metal heterogeneity and anisotropy, further parametric studies that cover other material, geometrical and operational aspects, and a thorough quantification of the relation between strain capacity of a CWP specimen and a full scale pressurized pipeline.

Samenvatting

(Dutch summary)

De stijgende vraag naar energie dwingt grote leveranciers van fossiele brandstoffen tot het ontginnen en uitbaten van nieuwe olie- en gasvelden. Door het uitsterven van de brandstofreserves moeten nieuwe velden in steeds uitdagender (aardbevingsgevoelige, arctische, onderwater) gebieden aangesproken worden. De zware opgelegde omgevingsomstandigheden kunnen longitudinale plastische vervormingen introduceren in de transportpijpleidingen. Dergelijke vervormingen vereisen een 'rekgebaseerde' ontwerpsaanpak, waarin de toelaatbare rek geschat wordt (in tegenstelling tot traditioneel 'spanninggebaseerd' ontwerp, waar toelaatbare spanningen bepaald worden). De omtreklassen die pijpsecties verbinden zijn hierbij kritisch, gezien de waarschijnlijkheid dat deze lassen fouten bevatten die de structuur verzwakken.

In tegenstelling tot de conventionele analytische spanninggebaseerde evaluatie van lasfouten in omtreklassen, zijn er geen methodes die toelaten de invloed van alle sleutelfactoren in een rekgebaseerde evaluatie tegelijk te begroten. Beschikbare methodes verwaarlozen bepaalde sleutelfactoren, zijn te conservatief en/of zijn niet succesvol gevalideerd. Het grote aantal invloedsfactoren en de gevoeligheid aan kleine wijzingen hiervan liggen aan de basis van deze beperking. Als gevolg zijn en blijven experimentele en numerieke (eindige elementen) onderzoeksmethodes essentieel voor de rekgebaseerde evaluatie van een lasfout.

Dit werk heeft tot doel een beter inzicht te verkrijgen in de aannames en resulterende interpretatie van numerieke en experimentele middelen voor de rekgebaseerde evaluatie van lasfouten in omtreklassen van pijpleidingen. De nadruk wordt gelegd op in longitudinale trek belaste pijpleidingen met lasfouten die omgeven zijn door microstructuren met voldoende taaiheid om brosse breuk te voorkomen. Twee belangrijke faalmodes worden bekeken: (onstabiele) ductiele scheuruitbreiding en plastisch bezwijken. Het uiteindelijke hoofddoel is een studie van verschillende invloeden van het materiaalgedrag van pijpleidingstaal ('basismetaal') en lasmetaal op de rekcapaciteit van de lasverbinding. Dit materiaalgedrag heeft betrekking op sterkteverschillen tussen basis- en lasmetaal,

sterkteverschillen tussen de verschillende aan elkaar gelaste basismetalen en hun exacte spanning-rekverloop.

De gekromde brede plaat (CWP) trekproef wordt gebruikt als hoofdobject van de uitgevoerde studies. Een CWP proef is een trekproef op een niet uitgevlakte sectie van een pijpleiding, met inbegrip van een omtreklas. In deze las wordt bewust een kerf aangebracht om de aanwezigheid van een lasfout te simuleren. Een CWP proefstuk heeft afmetingen die deze van de pijpleidingomtrek benaderen en kan omringd worden door kleinschalige beproeving om een goede interpretatie van het CWP testresultaat toe te laten. De rekcapaciteit van een CWP proefstuk kan geschaald worden naar deze van een pijpleiding met inwendige druk door middel van een drukcorrectiefactor.

Drie concrete luiken zijn ontwikkeld in het eindwerk en worden hieronder samengevat. Elk luik is gefundeerd door een uitgebreide literatuurstudie die de betreffende stand van zaken in kaart brengt.

Een eerste luik betreft een specifieke aanname in de eindige elementenmodellering van omtreklassen met lasfouten. Het spanning-rekgedrag van het basismateriaal wordt typisch gemodelleerd op basis van de gestandaardiseerde Ramberg-Osgood vergelijking. Deze vergelijking beschrijft rekversteviging op basis van een machtwet met één vaste exponent. Als gevolg hiervan ontstaat er een afhankelijkheid tussen de verhouding tussen vloeigrens en treksterkte enerzijds, en de uniforme verlenging anderzijds. Hoge sterkte pijpleidingstalen tonen deze afhankelijkheid echter niet, omdat zij typisch twee afzonderlijke fases vertonen in hun rekverstevigingsgedrag. Daarom is een nieuw 'UGent' spanning-rekmodel ontwikkeld, dat toelaat het specifieke gedrag van dergelijke pijpleidingstalen beter te benaderen. De verbetering ten opzichte van het Ramberg-Osgood model is significant. Drie procedures zijn ontwikkeld om 'UGent' modelparameters te schatten op basis van experimentele data. Elke procedure is gekenmerkt door een ander evenwicht tussen vereiste informatie en verkregen nauwkeurigheid.

Een tweede luik omvat de ontwikkeling van een eindige elementenmodel voor het uitvoeren van parameterstudies. Dit model laat toe schattingen te maken van scheuraandrijvende kracht en, bijgevolg, rekcapaciteit. Een groot aantal geometrische variabelen, gerelateerd aan pijp, las en lasfout, kunnen naar wens ingesteld worden. Ductiele scheuruitbreiding wordt in rekening gebracht via een algoritme dat eerder theoretisch gerechtvaardigd werd in verscheidene bronnen.

Een derde luik betreft de ontwikkeling van een experimenteel proefstuk. Uit literatuur is gebreken dat de interpretatie van gerapporteerde CWP proefresultaten bemoeilijkt wordt door een gebrek aan standaardisering, waardoor de proefstukgeometrie en uitvoeringsdetails van de proef steeds sterk varieerden. Daarom is een middenschalige (150 mm breed) variant van de CWP proef ont-

wikkeld, in een poging geometrie en uitvoering te optimaliseren. De proefstukgeometrie verzekert een relevante en uitwisselbare meting van aangelegde rek. Digitale beeldcorrelatie begroot enerzijds de rekdistributies over het oppervlak van het proefstuk. Anderzijds wordt de hoeveelheid ductiele scheuruitbreiding opgevolgd door een meting van ontladingscompliantie. Deze twee geavanceerde meettechnieken laten een betere interpretatie van het proefresultaat toe.

De drie ontwikkelde luiken zijn vervolgens aangewend in een systematische zoektocht naar een beter begrip van factoren die een belangrijke rol spelen in een rekgebaseerde scheurevaluatie.

De experimentele resultaten tonen aan dat de invloed van een beperkte hoeveelheid sterkteheterogeniteit tussen twee gelaste pijpsecties zeer groot kan zijn. De meeste huidige analytische evaluatiemethodes laten niet toe op een expliciete manier rekening te houden met deze invloed. Deze uitspraak wordt kracht bijgezet door een theoretische denkoefening die de experimentele resultaten bevestigt. Naast deze observatie leiden de experimentele resultaten tot een validatie van het eindige elementenmodel (met inbegrip van het algoritme voor ductiele scheuruitbreiding).

Het gevalideerde eindige elementenmodel wordt vervolgens aangewend voor een uitgebreide parameterstudie die zich richt tot het constitutief gedrag van pijpleidingstaal en het sterkteverschil tussen las- en basismateriaal. In tegenstelling tot gepubliceerde literatuur wordt een begroting van dit sterkteverschil op basis van een zogenaamde vloeispanning (gemiddelde tussen vloeigrens en treksterkte) voorgesteld als de meest relevante parameter met betrekking tot rekcapaciteit. Hierbij leidt het gebruik van het Ramberg-Osgood model tot onnauwkeurige en potentieel onveilige schattingen van rekcapaciteit. Als gevolg hiervan wordt het 'UGent' model voor pijpleidingstaal geadviseerd voor numerieke evaluaties van de toelaatbaarheid van lasfouten in een rekgebaseerde context.

Tot slot worden alle numerieke en experimentele ontwikkelingen gecombineerd in systematische procedures voor het rekgebaseerd ontwerp van pijpleidingen en de rekgebaseerde evaluatie van gedetecteerde lasfouten. Deze procedures houden rekening met zowel eerder gepubliceerde ontwerpstudies als alle nieuwe resultaten uit dit werk.

Mogelijkheden tot toekomstig onderzoek hebben betrekking op de karakterisering van heterogeniteit en anisotropie van las- en basismateriaal, de implementatie hiervan in het eindige elementenmodel, verdere parameterstudies die andere invloedsfactoren benaderen, en een kwantificering van het verband tussen de rekcapaciteit van CWP proefstukken en pijpleidingen onder inwendige druk.

Contents

Symbols and acronyms

Symbols

a	flaw or notch depth	mm
a_0	initial flaw or notch depth	mm
A_0	flaw area	mm^2
c	half flaw or notch length	mm
C	sensitivity of e_{max} to OM_{FS}	-
C_d	correction factor for mismatch effects (UGent strain capacity equation)	-
C_F	safety factor (CSA pressure design equation)	-
C_J	safety factor (CSA pressure design equation)	-
C_L	safety factor (CSA pressure design equation)	-
C_m	correction factor for material variations (UGent strain capacity equation)	-
C_T	safety factor (CSA pressure design equation)	-
c_v	coefficient of variance	-
D	average pipe diameter	mm (")
D_i	inner pipe diameter	mm (")
D_o	outer pipe diameter	mm (")
D_r	relative reference strain (strain based FAD)	-
e	engineering strain	- (%)
E	Young's modulus	MPa
E'	E (plane stress) or $E/(1-\nu^2)$ (plane strain)	MPa
e_L	Lüders elongation	- (%)
E_L	slope of Lüders plateau (up-down-up model)	MPa
e_m	uniform elongation	- (%)
e_{max}	strain capacity	- (%)
$e_{max,0}$	strain capacity for zero weld flow stress overmatch	- (%)
e_o	overall strain	- (%)
e_r	remote strain	- (%)
f	void volume fraction (GTN model)	-

F	parameter in Zahoor's K_I-solution	-
$f^\star$	effective void volume fraction (GTN model)	-
f_0	initial void volume fraction (GTN model)	-
f_c	void volume fraction for coalescence (GTN model)	-
f_c	weld cap profile	mm
$f_{f,l}$	left weld fusion line profile	mm
$f_{f,r}$	right weld fusion line profile	mm
f_F	critical void volume fraction (GTN model)	-
G	linear elastic energy release rate	N/mm
G_Y	energy release rate normalization factor	N/mm
GL_i	initial LVDT gauge length	mm
h	weld misalignment	mm
h_1	tabulated factor for determination of J_{pl}	-
J	non-linear energy release rate	N/mm
J_{fp}	parameter in Boothman's J solution	-
K_1	strength coefficient (Ludwigson model)	MPa
K_2	strength coefficient (Ludwigson model)	-
K_H	strength coefficient (Hollomon model)	MPa
K_I	mode I stress intensity factor	MPa.mm$^{1/2}$
K_L	strength coefficient (Ludwik model)	MPa
K_r	relative stress intensity factor (FAD)	-
K_S	strength coefficient (Swift model)	MPa
K_V	strain hardening parameter (Voce model)	-
L	half length of prismatic CWP section	mm
l_{cap}	width of weld cap	mm
l_{HAZ}	width of heat-affected zone	mm
L_r	relative reference stress (FAD)	-
L_s	shoulder runout length of CWP specimen	mm
m	proportionality factor between J and CTOD	-
M_{FS}	weld flow stress mismatch (UGent strain capacity equation)	-
n	strain hardening exponent (Ramberg-Osgood model)	-
n_1	strain hardening exponent (Ludwigson and UGent stress-strain model)	-
n_2	strain hardening coefficient (Ludwigson model)	-
n_2	strain hardening exponent (UGent stress-strain model)	-
n_{2i}	first estimation of n_2 (UGent stress-strain model)	-
n_H	strain hardening exponent (Hollomon model)	-
n_L	strain hardening exponent (Ludwik model)	-
n_S	strain hardening exponent (Swift model)	-
OM_{FS}	weld flow stress overmatch	%
OM_{TS}	weld ultimate tensile strength overmatch	%

OM_{YS}	weld yield strength overmatch	%
p	internal pipe pressure	MPa
p	plastic strain corresponding with proof stress s_p	- (%)
P	tensile force	N
P_0	normalizing load for reference stress	N
P_c	pressure correction factor for strain capacity	-
P_L	limit load for plastic collapse	N
Q	parameter in Zahoor's K_I-solution	-
q_1	GTN model parameter	-
q_2	GTN model parameter	-
R_m	ultimate tensile strength	MPa
$R_{p0.2}$	0.2 % proof stress (measure of yield strength)	MPa
$R_{p1.0}$	1.0 % proof stress	MPa
R_s	shoulder radius of CWP specimen	mm
$R_{t0.5}$	stress at 0.5 % total strain (measure of yield strength)	MPa
s	engineering stress	MPa
s	gross longitudinal stress in FSP and CWP specimen	MPa
S_{fp}	parameter in Boothman's J solution	-
s_p	proof stress corresponding with plastic strain p	MPa
t	pipe wall thickness	mm
U_p	potential energy	J
w	strain energy density	J/mm^3
W	half width of prismatic CWP section	mm
Y	scaling factor for K_I	-
Y/T	yield-to-tensile ratio	-
z_{45°	coordinate for longitudinal sensor positioning on CWP specimen	mm
α	strain offset (Ramberg-Osgood model)	-
α'	characteristic for post necking stress-strain behaviour	-
δ	CTOD tearing resistance coefficient	
ΔGL	LVDT elongation	mm
$\Delta\vec{P}$	nodal coordinate transformation	
Δs	base metal strength heterogeneity	MPa
$\Delta\sigma_L$	stress unloading range of Lüders plateau (up-down-up model)	MPa
$\Delta\sigma_T$	FITNET temperature correction for yield strength	MPa
$\Delta\epsilon$	strain trainslation term (UGent stress-strain model)	- (%)
δt	wall thickness variation	mm
ϵ	true strain	- (%)
ϵ_0	true yield strain	- (%)

ϵ_0	strain translation term (Swift model)	- (%)
ϵ_1	first true principal strain	- (%)
ϵ_L	true Lüders elongation	- (%)
ϵ_r	true remote strain	- (%)
ϵ_{RMS}	root mean square error of model strain	- (%)
η	CTOD tearing resistance exponent	-
η	dimensionless through-thickness coordinate	-
η_{rf}	through-thickness position of boundary between root and filler weld passes	-
γ	flaw area relative to gross section area	-
ν	Poisson's coefficient	-
ϕ	angle for definition of position on crack tip	rad
ρ_i	initial flaw or notch tip radius	μm
σ	true stress	MPa
σ_0	true yield strength in several constitutive equations	MPa
$\sigma_{0.2}$	true 0.2 % proof stress (Ramberg-Osgood and UGent stress-strain model)	MPa
σ_1	transition stress (UGent stress-strain model)	MPa
σ_2	transition stress (UGent stress-strain model)	MPa
σ_c	critical stress for plastic collapse	MPa
σ_h	hydrostatic stress invariant	MPa
σ_m	true ultimate tensile strength	MPa
σ_{Mises}	Von Mises equivalent stress	MPa
$\vec{\theta}$	model parameter vector	
ζ	dimensionless longitudinal coordinate	-

Acronyms

API	American Petroleum Institute
ASTM	American Society for Testing and Materials
avg	(subscripted to symbols) average
BM	base metal (line pipe steel which is unaffected by girth weld heat input)
BP	British Petroleum
BS	British Standard
CMOD	crack mouth opening displacement
CSA	Canadian Standards Association
CTOD	crack tip opening displacement
CWP	curved wide plate
DIC	digital image correlation
DNV	Det Norske Veritas
el	(subscripted to symbols) elastic

EPFM	elastic-plastic fracture mechanics
EPRG	European Pipeline Research Group
EPRI	Electric Power Research Institute
FAD	failure assessment diagram
FBE	fusion bonded epoxy
FCAW	flux cored arc welding
FITNET	European fitness-for-service network
FS	full thickness strip
FSP	full scale (pressurized) pipe
GMAW	gas metal arc welding
GSC	gross section collapse
GTAW	gas tungsten arc welding
GTN	Gurson-Tvergaard-Needleman
HAZ	heat-affected zone (line pipe steel which is affected by girth weld heat input)
HRR	Hutchinson-Rice-Rosengren
HSLA	high strength low allow
HV	Vickers hardness
IEA	International Energy Agency
ij	(subscripted to symbols) ij-th element of a stress or strain tensor
L	longitudinal
LEFM	linear elastic fracture mechanics
LVDT	linear variable differential transducer
mat	(subscripted to symbols) critical value of material
max	(subscripted to symbols) maximum
$meas$	(subscripted to symbols) measured
min	(subscripted to symbols) minimum
MWP	medium wide plate
NDT	non-destructive testing
NSC	net section collapse
OECD	Organization for Economic Co-operation and Development
pl	(subscripted to symbols) plastic
PSL	product specification level
Q&T	quench and temper
R	resistance (in CTOD-R, J-R)
RB	round bar
ref	(subscripted to symbols) reference
RFCS	Research Fund for Coal and Steel
RO	Ramberg-Osgood
RT	room temperature
SAW	submerged arc welding
SENB	single edge notched bend
SENT	single edge notched tension

SMAW	shielded metal arc welding
SMYS	specified minimum yield strength
T	transversal
TCPL	TransCanada Pipelines Ltd.
TMCP	thermo-mechanical control process
tot	(subscripted to symbols) total
UC	unloading compliance
UG	UGent
UGent	Ghent University
UOE	U bending, O forming, Expansion
WM	weld metal
WMC	weld metal center
X-FEM	extended finite element modelling

Chapter 1

Strain based design of high strength pipelines

Part of the Trans-Alaska Pipeline System, which survived a Richter magnitude 7.9 earthquake on November 3, 2002 [1.1].

1.1 Energy and its transportation

1.1.1 Global energy demand and fossil fuel reserves

On both a macroscale and a microscale, human life involves the consumption of energy. The rising world population and the development of emerging economies lead to an increasing global energy demand. This is clearly reflected in figure 1.1, which plots the expected increase in global energy demand per fuel source for the period 2008–2035 [1.2]. In this figure, 'OECD' represents the 34 countries of the Organization for Economic Co-operation and Development, which has the mission to 'promote policies that will improve the economic and social well-being of people around the world' [1.3]. Whereas the OECD-countries aim to reduce their consumption of environmentally unfriendly fossil fuels, China is becoming an increasingly important consumer. It has been estimated that China overtook the position of world's largest energy user from the United States of America in 2009, whereas its consumption was only half that of the USA in 2000 [1.4]. As a result, the total energy demand is expected to augment with a rate similar to that of the last decades (figure 1.2, [1.5]).

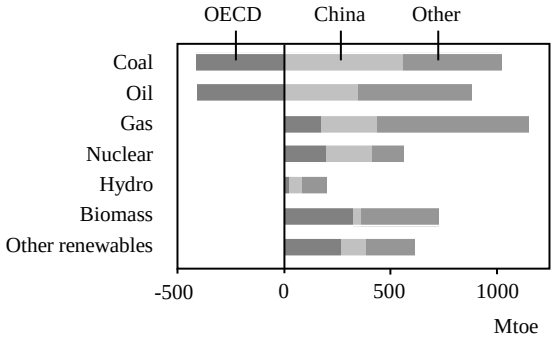

Figure 1.1: Predicted incremental primary energy demand by fuel and region, 2008–2035 (1 Mtoe = 1 million tonnes of oil equivalent = $42 \cdot 10^6$ GJ). Source: OECD/IEA [1.2].

Facing the increase in consumption of fossil fuels, which nowadays provide almost 80 % of the global energy demand [1.6], the exhaustion of earth's resources is inevitable. By means of illustration, it was estimated in 2007 that about 1,000 billion barrels of conventional oil had already been consumed, whereas the world reserves were quantified as roughly 2,000 billion barrels [1.6] (1 barrel is approximately 159 litres). As a result, the ongoing supply of fossil fuels will highly depend on the discovery and development of new fields, as illustrated in figure 1.3 for the case of oil [1.2].

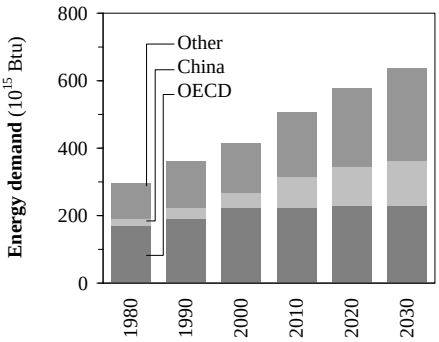

Figure 1.2: Historical and predicted evolution of energy demand (1 Btu = 1 British thermal unit = 1.055 kJ). Source: ExxonMobil [1.5].

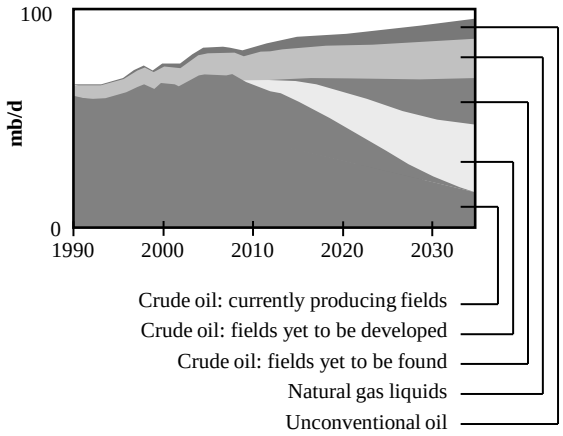

Figure 1.3: Oil supply relies on the discovery and development of new fields (1 mb/d = 1 million of barrels per day). Source: OECD/IEA [1.2].

1.1.2 Transportation of fossil fuels

Fossil fuel reserves are concentrated within a limited number of regions. For instance, about 80 % of the proven gas reserves is owned by 10 countries [1.7], of which in particular Russia, Iran and Qatar possess more than 50 % of all reserves [1.8]. Transport pipelines enable the transportation of fossil fuels from their origin to refinery plants and eventually the consumer. Pipelines have the unmistakable economical advantage over other transport options that they remain in place, i.e. energy is only required to transport the fluid or gas itself. As a result, transport pipelines have become the 'energy veins' of human society.

The history of long distance transport pipelines goes back to 1891, when a connection of nearly 200 km was established between Indiana and Chicago, USA [1.9]. Nowadays about two million kilometers of transport pipelines have been constructed over the world, most of which are located in the USA (figure 1.4 [1.10]).

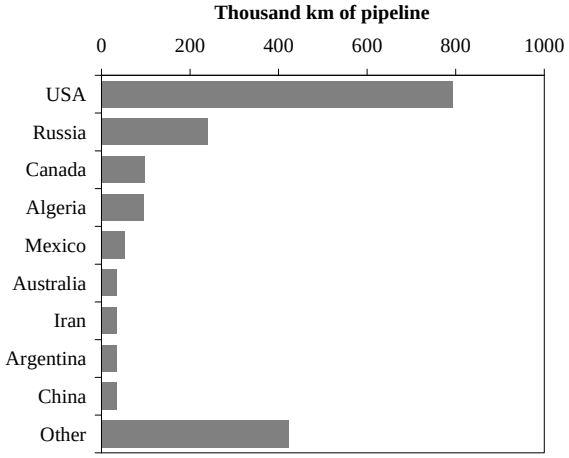

Figure 1.4: Kilometers of transport pipelines constructed (update 2005) [1.10].

As a logical consequence of both the increasing energy demand and the necessary development of new oil and gas resources, new pipelines have to be installed and operated. Table 1.1 reports on the high number of future pipeline projects (both onshore and offshore) that are in the pre-construction phase [1.11].

Table 1.1: Pipeline projects in the pre-construction phase, in descending order of total length (update September 2011) [1.11].

Region	**Nr. of projects**		**Total length**		**Average length**
		(%)	(km)	(%)	(km)
Asia	158	16.5 %	77,656	23.6 %	491
North America	282	29.4 %	76,811	23.3 %	272
Europe	163	17.0 %	47,035	14.3 %	289
Middle East	164	17.1 %	46,110	14.0 %	281
Latin America	58	6.0 %	37,526	11.4 %	647
Africa	57	5.9 %	25,504	7.7 %	447
Australasia	78	8.1 %	18,838	5.7 %	242
Total	**960**	**100 %**	**329,480**	**100 %**	**343**

1.2 Construction of a transport pipeline

Prior to putting a pipeline into operation, a sophisticated production and installation process takes place. Without having the intention to be complete – pipeline production and installation involves too many aspects to discuss within the scope of this text – this section provides a brief overview of some major steps, knowledge of which is necessary to understand the following.

Since there are some fundamental differences between the production and installation of onshore and offshore pipelines, both will be treated separately. Four aspects are discussed: pipe manufacturing, pipe coating, girth welding and pipeline installation.

1.2.1 Onshore pipelines

Pipe manufacturing

Most large diameter onshore pipelines are produced using the UOE pipe forming process, which starts from a flat plate and involves a longitudinal seam weld. The typical production range is between 16" (406 mm) up to 64" (1,626 mm) outer diameter (D_o) and, depending on material and diameter, thicknesses (t) from 6 mm up to 40 mm [1.12, 1.13]. Given its common application, further focus will be put on the UOE process.

The abbreviation 'UOE' refers to the major cold forming steps (figure 1.5 [1.14]):

- After an edge crimping stage, the plate is bent to a **U**-shape.
- The U-shape is further formed to an **O**-shape which is closed by means of SAW (submerged arc) welding, thereby creating a longitudinal seam (figure 1.6 [1.13]).
- To achieve close dimensional tolerances and – in particular – reduce pipe ovality, a plastic **E**xpansion is performed. The target expansion strain is typically situated between 0.008 and 0.014 [1.15].

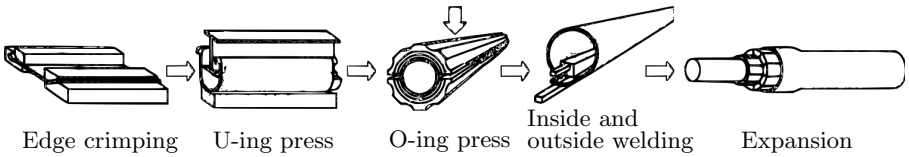

Figure 1.5: Main stages in the UOE pipe forming process [1.14].

The nominal pipe dimensions (D_o and t) are, in combination with material choice and internal pressure, mostly based upon the operational characteristics

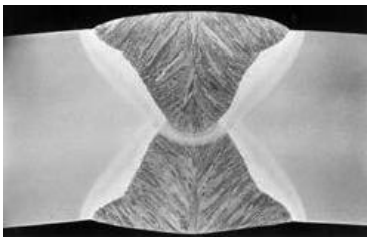

Figure 1.6: Example SAW seam weld from a UOE formed pipe [1.13].

of the pipeline and the evident requirement that the pipeline must not yield due to the applied pressure (see section 1.5.2 for more details).

Apart from the major forming and welding steps in UOE pipe production, quality control is a key aspect to obtaining a high-performance product. In particular, the following inspections are performed [1.13]:

- non-destructive examinations of the seam weld (ultrasonic and X-ray);
- an internal hydrostatic pressure test;
- a geometry check to ensure that dimensional tolerances are met.

Pipe coating

After pipe manufacturing and quality inspection, pipes are coated to prevent corrosion. As regards the outer surface coating, three different processes are applied in practice: fusion bonded epoxy, coal tar epoxy and asphalt enamel coating. Of these three, fusion bonded epoxy (FBE) coating (figure 1.7, [1.16]) is mostly applied because of its excellent adhesion characteristics, worldwide availability and better performance from a health, safety and environmental point of view [1.17]. The components of its name reveal some important characteristics of FBE coating. The coating process consists of fusion bonding between an epoxy resin and hardener component. This bonding process is triggered by temperatures between 180°C and 250°C, which has to be maintained for several minutes to allow for the complete 'curing' of the coating. To this purpose, the pipe is preheated in induction coils. An FBE coating has a minimum thickness of roughly 300 micrometers [1.17].

Girth welding

UOE produced pipes generally have a length of 12 or 18 m [1.18]. Since the aim is to obtain a long closed connection between two remote locations, many different pipes have to be circumferentially ('girth') welded together. For instance, a 350 km long pipeline – this length is close to the average length of running pipeline projects, table 1.1 – with 12 m pipes would consist of roughly 30,000

Figure 1.7: Fusion bonded epoxy (FBE) coating [1.16].

girth welds. The order of magnitude of this number and the high welding costs involved (roughly 10 to 15 % of the total project cost [1.19]) indicates that girth welding procedures not only have to be designed to provide a sufficient weld 'quality', but also to achieve high production rates under economically attractive conditions. From these considerations, manual SMAW (shielded metal arc welding) and mechanized GMAW (gas metal arc welding) have evolved into the most commonly applied girth welding techniques [1.20]. Apart from these processes, the self-shielded FCAW (flux cored arc welding) process can be applied in terrains where the transport of gas shielding involves practical issues [1.21].

The different nature of manual and mechanized welding is reflected in their bevel preparation and eventual weld profile [1.22]. Whereas the SMAW or FCAW welder practically benefits from having a wide bevel angle, mechanized GMAW welds are narrower as this requires less weld passes. This is illustrated in figure 1.8, which shows a manual and mechanized weld.

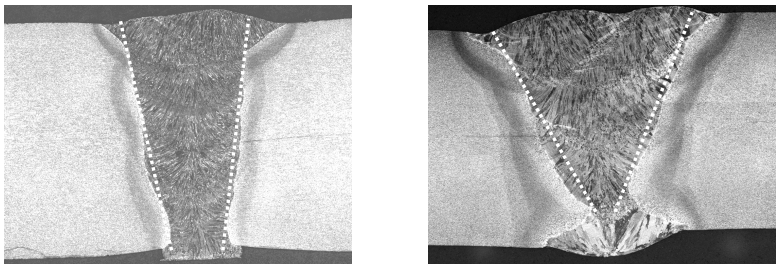

Figure 1.8: Two different weld geometries.

Pipeline installation

Onshore pipelines are mostly buried, to protect them from external damage. For cases where the interaction between the pipeline and the soil might lead to extreme loading conditions (see section 1.6), the pipeline may be installed above ground. Both possibilities are shown in figure 1.9.

(a) (b)

Figure 1.9: (a) Laying of buried pipeline (Source: Denys) [1.23]. (b) Onshore pipeline which operates above ground (Source: Guardian; Photograph: Doug Wilson/Corbis) [1.24].

1.2.2 Offshore pipelines

This section briefly tackles a selection of major differences between offshore and onshore pipelines. It should be mentioned that offshore pipe construction involves many other aspects, which are outside the scope of this dissertation.

Pipe manufacturing

For offshore pipelines, too, UOE pipe forming is commonly applied because of advantages with respect to e.g. productivity and dimensional control [1.15]. As regards the choice of pipe dimensions and steel, however, a different design strategy is to be applied. Compared to onshore pipelines which are critical towards yielding due to internal pressure, offshore pipelines may collapse from the external water pressure and may buckle during their installation. This results in a minimum required pipe thickness, an example calculation of which is given in figure 1.10, taken from [1.25].

The resistance against buckling is to a great extent influenced by the diameter-to-thickness ratio D_o/t, a larger value corresponding with a greater risk of buckling [1.26]. This is indirectly reflected in the offshore standard DNV-OS-F101 ('Submarine Pipeline Systems', 2007) [1.27], in which the design equations have the validity limit $D_o/t \leq 45$ (note that D_o/t values of 80 and above are not

uncommon for *onshore* pipelines). For thinner walled pipes, resistance against buckling has to be proven case-specifically, mostly through finite element analysis. For example, with a diameter of 1,118 mm (44") and a wall thickness 23 mm, a part of the Langeled offshore pipeline which is located in the North Sea has a maximum D_o/t ratio of 49 and buckling resistance was numerically proven in [1.28].

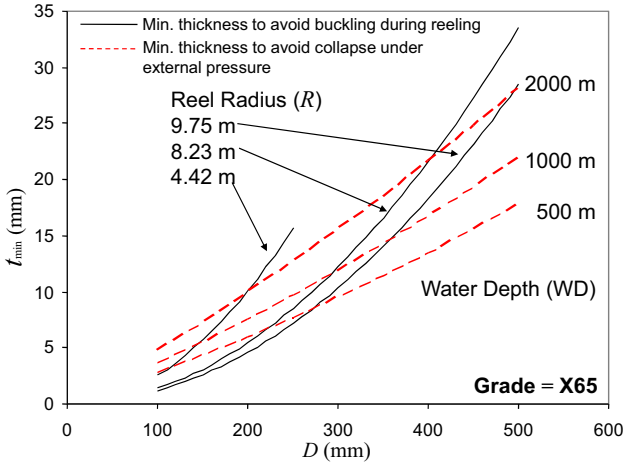

Figure 1.10: The minimum wall thickness t_{min} of offshore pipelines is often determined by buckling resistance [1.25] (D: outer diameter). Calculations have been based upon DNV-OS-F101 [1.27].

Girth welding and pipeline installation

The pipe girth welding procedure and location are closely related to the pipeline installation method. Different pipelaying methodologies exist, the most common of which are S-laying, J-laying and reeling (figure 1.11). A brief overview of (dis)advantages and limitations, based on [1.18, 1.25, 1.29, 1.30], is given in table 1.2.

Depending on the installation process, girth welding is either performed on the pipelaying vessel itself (S-lay, J-lay) or on land (reeling). In the former case, welding is generally mechanized, whereas the latter may involve manual welding.

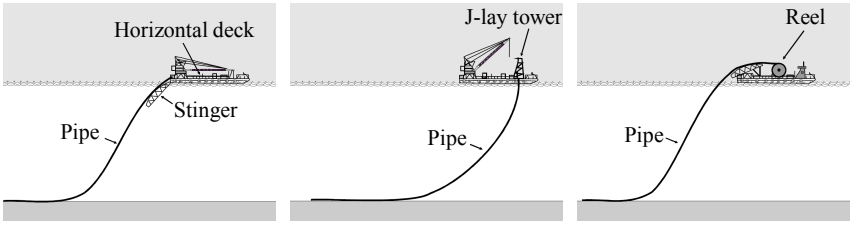

Figure 1.11: The three most common offshore pipelaying methods: (a) S-laying, (b) J-laying, (c) reeling. Taken from [1.29].

Table 1.2: Application scope of different offshore pipelaying methods [1.18, 1.25, 1.29, 1.30].

Property	**S-laying**	**J-laying**	**reeling**
Water depth	$<$ 2,000 m	up to $>$ 2,000 m	shallow & deep
Pipe diameter	$<$ 1,321 mm (52")		$<$ 458 mm (18")
Speed	$\leq$ 6.5 km/day	$\leq$ 3.2 km/day	$\leq$ 3.5 km/hour

1.3 Failure of pipelines

Pipelines can fail from a wide variety of causes that involve different possible failure mechanisms. Two fundamentally different categories can be distinguished: failure due to human interaction and failure due to environmental and/or operational factors. The former is mostly related to damage invoked during construction works, as was for instance the case for the gas pipeline explosion in Ghislenghien, Belgium on July 30, 2004 (figure 1.12 [1.31]). Whereas the avoidance of such failures is essentially based upon the effectiveness of a continuous safety policy of all involved parties, the latter is related to mechanical loading which can mostly be dealt with at the design stage. Hereby, different failure mechanisms can be distinguished by various aspects of their nature (static versus fatigue, tension versus compression, low versus high temperature, corrosion, ...).

Since the design criteria and involved calculations fundamentally differ between different failure mechanisms, covering all aspects would be too elaborate within the scope of this dissertation. Further focus is given to the failure behaviour of pipelines under static tension along the pipe axis.

Figure 1.12: The gas pipeline explosion in Ghislenghien, Belgium on July 30, 2004 caused 24 casualties [1.31].

1.4 Pipeline girth weld flaws and the weakest link of a tensioned pipeline

The processes used for pipe girth welding almost inevitably involve weld flaws, mostly occuring at or near the weld root surface [1.25]. Example flaw types observed in girth welds are hot cracking due to copper contamination when using a backing ring, lack of penetration, and lack of fusion (see e.g. figure 1.13 [1.32]). Depending on the flaw type, either the weld metal itself or the heat-affected zone (HAZ) is the more susceptible flaw location.

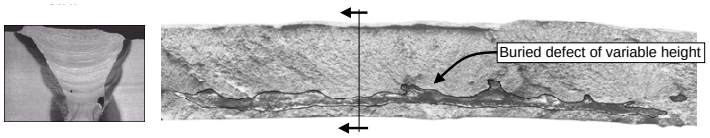

Figure 1.13: Lack of fusion defect as seen in a weld macrograph (left) and after a forced brittle fracture (right) [1.32].

Under the presence of a tensile load along the pipe axis and thus perpendicular to the girth weld, weld flaws serve as stress concentrators which may cause an unstable fracture or a leak due to through-thickness crack extension. The likeliness of failure in a girth weld is additionally promoted by the possible presence of microstructures with reduced material properties – in the weld metal and/or the HAZ – and additional stress concentrations due to geometric eccentricities like weld misalignment [1.20]. Therefore, girth welds are a potential weak link when it comes to the integrity of a pipeline under tension.

Note that, as regards the assessment of weld flaws, the focus on tension loads

can be conservatively extrapolated to girth welds under bending, by assuming that the entire cross section faces a uniform tension stress equal to the maximum bending stress (figure 1.14) [1.33–1.36].

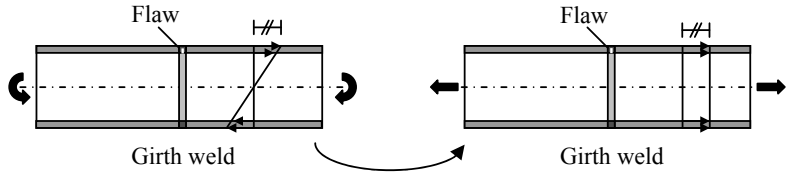

Figure 1.14: Considering the effect of weld flaws on structural integrity, pipes under bending are conservatively considered as under uniform tension.

Advances in weld design, metallurgy and welding practice have resulted in girth welds which – despite the presence of flaws – do not necessarily govern failure. Key to this is the production of welds with a sufficient toughness and a sufficient strength relative to the base (i.e. pipe) metal. Whereas the former is necessary to avoid brittle fracture, the latter – also referred to as weld strength overmatch – is required to shield the girth weld flaw from applied deformations [1.37]. As a consequence, both pipe and girth weld have to be considered in an assessment of structural integrity under longitudinal tension. In this dissertation, the presence of a sufficient toughness to avoid brittle fracture is a basic assumption and focus is given to ductile failure. Concrete guidelines for the fulfilment of this assumption are provided in section 2.6.1.

For the remainder of the dissertation, flaw height (or 'flaw depth') will be symbolized as a and flaw length as $2c$.

1.5 Increasing line pipe steel strength levels: an economically driven evolution of state-of-the-art technology

Throughout the past decades, transport pipeline practice has known a continuous tendency towards the utilization of steels with a higher strength. The characterization of pipe strength is briefly addressed in section 1.5.1. Whereas there is a clear economical explanation for the trend towards increasing strengths (section 1.5.2), the speed of evolution has been bottlenecked by the development of a state-of-the-art steelmaking practice which resulted from ever ongoing global research efforts. Today, high strength line pipe steels are unanimously

rolled using the so-called thermo-mechanical control process (TMCP). The evolution towards and characteristics of TMCP rolling are briefly addressed in section 1.5.3.

1.5.1 Pipe steel grades: a brief introduction

The strength level of pipe steel is characterized by the standard API 5L (2007) [1.38], which covers general aspects of line pipe steel such as manufacturing, chemical and mechanical properties and dimensions. Although this standard origins from the American Petroleum Institute (API), its application is worldwide. In API 5L, yield strength is reflected in the name of the steel grade. For instance, API 5L X70 is a steel with a specified minimum yield strength (SMYS) of 70 ksi (or 485 MPa). The latest update of API 5L covers grades up to API 5L X120 (SMYS = 830 MPa). Whereas this brief introduction into API 5L suffices at this point, more detail will be provided in chapter 3 (section 3.3.1).

For the remainder of this work, line pipe steel grades will be denoted without the prefix 'API 5L', e.g. grade 'API 5L X70' will be simply referred to as 'X70'.

1.5.2 Economical incentive

A key factor regarding the operation of a pipeline is the yield strength of the pipe steel. In combination with the pipe outer diameter D_o (mm) and thickness t (mm), it determines the allowable operation pressure p (MPa). Indeed, D_o, t and p determine the stress tensor in the pipe. For instance, under thin wall assumptions, the hoop stress $\sigma_{\theta\theta}$ (MPa) invoked by an internal pressure p is given by:

$$\sigma_{\theta\theta} = p\frac{D_o - 2t}{2t} \tag{1.1}$$

This relation is the basis of the pressure design in pipeline standards. For instance, CSA Z662 ('Oil & gas pipeline systems', 2007) [1.26] gives the following equation for the maximum allowable operational pressure p_{max} in a straight pipe (assuming that $D_o - 2t \approx D_o$):

$$p_{max} = \text{SMYS}\frac{2t}{D_o}C_F C_L C_J C_T \tag{1.2}$$

with C_F, C_L, C_J and C_T safety factors, respectively for design (always 0.8), location (vicinity to human activity), pipe type (e.g. UOE), and temperature.

An increase in pipe yield strength allows for higher stresses in the pipe, resulting in significant cost reductions. The major effect is that internal pressure can be increased (and hence, for a fixed mass flow of fossil fuel, diameter can be reduced) and/or pipe thickness can be reduced according to Eq. (1.2). Starting

from these effects, figure 1.15 shows that savings are achieved at many levels including manufacturing, transportation, installation and operation costs [1.39]. The potential extent of savings becomes clear by mentioning that about 40 % of the total cost of a pipeline project is somehow related to material [1.40]. In [1.41], for instance, it was calculated for a specific project that upgrading the steel from grade X70 to X100 would result in 10 % savings on the total cost. Hence, there is a huge ongoing economical incentive to pursue higher line pipe steel strengths.

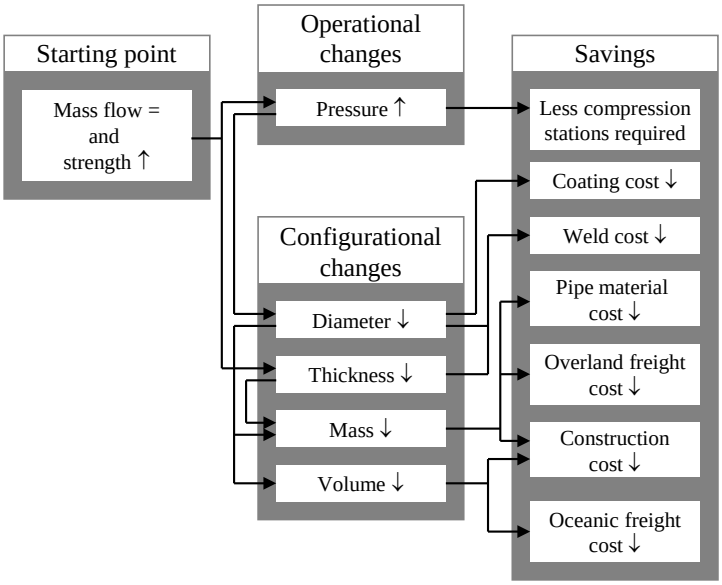

Figure 1.15: The pursue towards increasingly strong line pipe steels is economically driven [1.39].

Note that the trend towards increasing pipeline strengths is mainly driven by onshore pipeline projects. Recall that, for offshore projects, the minimum wall thickness is often not determined by the internal pressure in operation or external water pressure but rather by the required resistance against buckling (figure 1.10). In such case, there is no benefit of increasing the steel grade. In fact, higher strength steels tend to show strain hardening characteristics that increase the susceptibility to buckling [1.42]. As a consequence, the current mainstream of offshore pipelines is X52 to X70 [1.25, 1.43], whereas the use of X80 is not uncommon for recent onshore pipelines [1.44].

1.5.3 From conventional to thermo-mechanical control process rolling

If the strength consideration from section 1.5.2 were the only criterion for steel selection, it would be relatively straightforward to produce a satisfactory material with conventional rolling techniques. For instance, high strength can be readily achieved by applying a quench and temper (Q&T) rolling sequence for a steel with sufficient carbon content: such chemistry provides hardenability, which is triggered by a fast cooling rate during quenching. However, there are other – often conflicting – criteria which should be equally met, in particular:

- good weldability (for practical reasons);
- sufficient toughness, strain hardening capacity and ductility (for safety reasons).

The TMCP rolling process, developed in the 1960's [1.45], provides an answer to these demands. TMCP steels can be seen as an advanced variant of HSLA (high strength low alloy) steels, whose development in the late 1930's was based on the beneficial effects of micro-alloying. In combination with manganese (Mn) and a (very) low carbon (C) content, minor additions of alloying elements such as vanadium (V), niobium (Nb), molybdenum (Mo) and titanium (Ti) strengthen the steel through the following known mechanisms: grain refinement, solid solution and precipitation hardening. Additional strength can be achieved by increasing dislocation density and introducing a hard second phase (figure 1.16, [1.46]).

Focusing on the performance criteria next to strength, the low carbon content is a major contributor to increased weldability and toughness. The latter is also enhanced by increasing the cleanness of the produced steel. In particular, the fractions of the impurities sulphur (S) and phosphorus (P) have been reduced to extremely low values on a 'parts-per-million' (ppm) scale [1.46].

Compared to HSLA steelmaking, the TMCP process additionally relies on the effect of mechanical processing at strictly controlled and relatively low temperatures [1.47] to produce very fine grains. More concretely, the last hot rolling steps are performed below the so-called 'non-recrystallization temperature'. As a result, the severely deformed ('pancaked') austenite grains do not completely recrystallize, which provides a large number of nucleation sites for the transformation of austenite to ferrite. In particular, the micro-addition of Nb has a particularly positive effect on the non-recrystallization temperature, which is increased [1.48, 1.49]. Therefore, TMCP steels with niobium additions above 0.10 % are also referred to as HTP ('High Temperature Processed') steels. Compared to TMCP steels with low-Nb chemistries, these steels are less sensitive to process variations and, as a consequence, less variable in mechanical properties [1.46, 1.50].

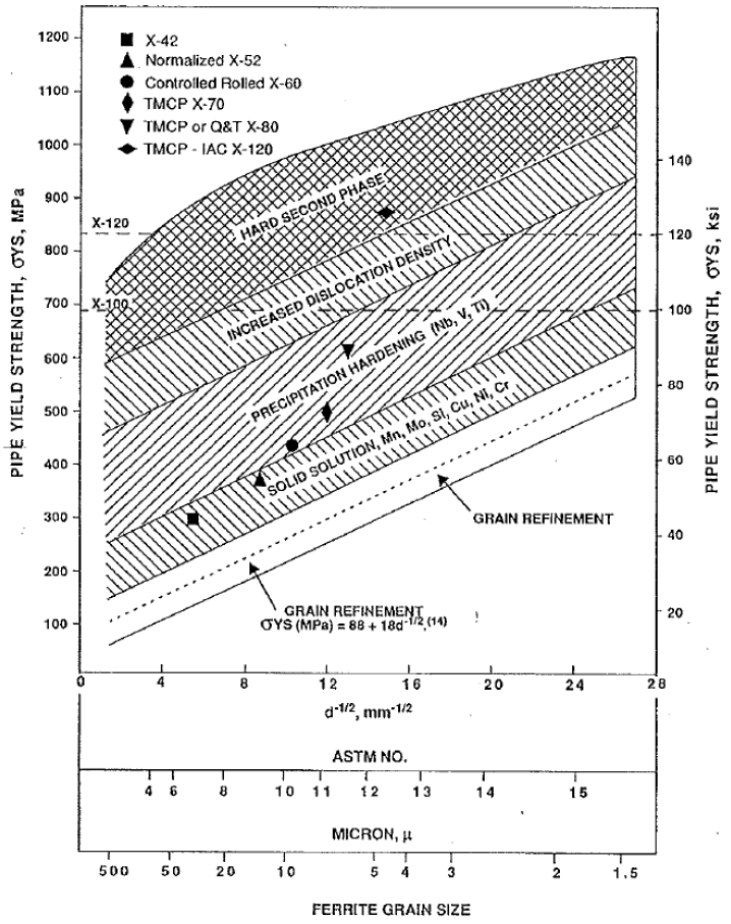

Figure 1.16: Line pipe steel yield strength as a superposition of different strengthening mechanisms [1.46].

After rolling, a cooling process can be performed to obtain an even finer microstructure. Different variants exist, such as [1.51]:

- 'accelerated cooling': moderate cooling, the formation of martensite is avoided;
- 'direct quench': very fast cooling, martensite is formed;
- 'direct quench + self tempering': very fast but short cooling, martensite at the plate surfaces is tempered by retained heat from plate core.

Considering the possible steel chemistries and thermomechanical control rolling and cooling schemes, a large variety exists between different TMCP rolling procedures – even within the same strength grade. For instance, [1.52] reports

on three fundamentally different approaches to obtain the requirements of X100 steel. The variety in production processes has historically grown from specific experience of steel producers and dynamical economical influences. The latter is mainly driven by strong fluctuations of the price of alloying elements. For instance, vanadium became extremely expensive during the late 1980's and was consequently designed out of many steels at that time [1.46].

Summarizing matters, there is no unique recipe for TMCP rolled steel and the worldwide competition to improve material properties is ongoing. This competition has contributed to the accelerated evolution of pipe steel grades from X60 (1960's) up to X120 (mid-1990's) [1.46, 1.52].

1.5.4 Challenges related to higher strength steels

Despite proven economical advantages (section 1.5.2) and numerous metallurgical research efforts (section 1.5.3), grades stronger than X80 still have to see large scale, full-potential use in pipelines [1.44, 1.46]. This seemingly contradictory observation is explained by the fact that the application of higher strength steels involves some challenges related to structural integrity, which are not yet fully solved for strength grades X100 and beyond. Of particular relevance is the following:

- As line pipe steel grade is increased, it becomes more difficult to achieve sufficiently tough welds with a desired minimum level of strength. As a result, the weld becomes more susceptible to unstable fracture and/or plastic collapse.
- Despite the application of highly advanced TMCP rolling processes, the metallurgical introduction of higher strengths in line pipe steels generally involves a reduction in ductility and strain hardening capacity (e.g. [1.53, 1.54]). As a result, the inherent buffer to sustain (un)expected plastic deformations is reduced and deformation is more readily concentrated at 'weak points' (e.g. zones of stress concentration in vicinity of flaws).

  The tendency towards both a reduced ductility and reduced strain hardening for higher strength steels is illustrated in figure 1.17, which shows four stress-strain curves ranging from grade X60 to X100.
- Whereas the heat-affected zones near welds in lower strength line pipe steels tend to be harder (and thus stronger) than the base metal [1], those near welds in higher strength base metal may be softer. This possible HAZ softening phenomenon occurs for grades X70 and above, and becomes increasingly likely and pronounced as line pipe steel grade increases. Strength reductions of roughly 20 % relative to the base metal

[1] For the remainder of this dissertation, 'base metal' refers to the line pipe steel which is unaffected by the girth weld heat input.

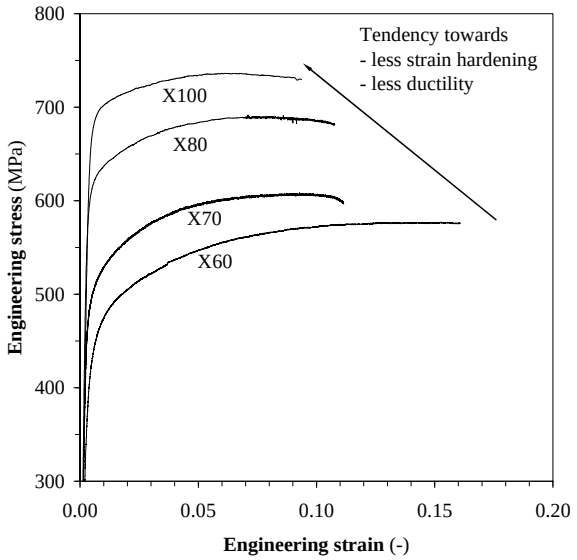

Figure 1.17: Strain hardening and ductility generally decrease as line pipe steel strength increases.

strength are not uncommon for X100 line pipe steel [1.55–1.57] (e.g. figure 1.18). HAZ softening is explained by the fact that the strength of high grade TMCP line pipe steels is to a great extent based upon grain refinement and high dislocation density, mechanisms which are both disturbed by the thermal cycle which occurs during welding [1.58].

Finite element analyses have indicated that, under certain conditions of combined internal pressure and axial tension, strain concentrations may occur in softened heat-affected zones of girth welds, which might cause failure [1.59]. Hence, the potential susceptibility of higher strength line pipe steels to HAZ softening has to be taken into account in the selection of line pipe steel and the girth weld procedure.

The last decade, the feasibility of safely operating X100 pipelines has been investigated through a series of intermediate field construction trials (table 1.3 [1.60]). Given the ongoing strong research efforts, a future application of this grade on a large scale is not unexpected.

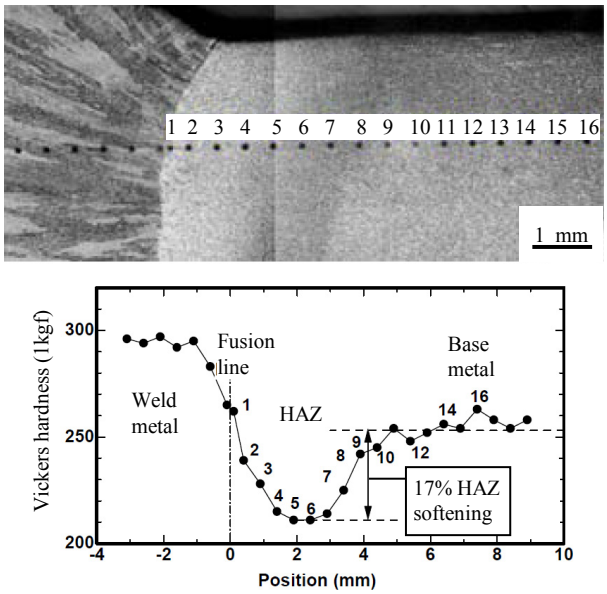

Figure 1.18: Heat-affected zone softening in an X100 line pipe steel, estimated by 1kgf Vickers hardness measurements. Taken from [1.55].

Table 1.3: Overview of X100 field construction trials [1.60].

Year	**Company** ⋆	**Project (Country)**	D_o (mm)	t (mm)	D_o/t (-)	**Length** (km)
2002	TCPL	West Path (Canada)	1,220	14.3	85	1
2004	TCPL	Godin Lake (Canada)	915	13.4	68	2
2006	TCPL	Stittsville Loop (Canada)	1,067	12.7	84	2
2006	TCPL	Stittsville Loop (Canada)	1,067	14.3	75	5
2007	TCPL	Ft. McKay (Canada)	762	9.8	78	2
2010	BP	Spadeadam (UK)	1,220	19.8	62	1

⋆ TCPL: TransCanada Pipelines Ltd.; BP: British Petroleum

1.6 Strain based design: a general context

1.6.1 Hostile environments and strain demand

Increasingly remote regions have to be explored for the development and exploitation of new oil and gas fields. Much of these regions pose severe challenges in terms of environmental conditions or accessibility. In particular, onshore pipelines may have to be located in arctic or seismic regions. For offshore pipelines, additional problems arise due to both the installation process (S-lay,

J-lay, reeling) which demands a minimum deformability and some phenomena specifically related to the submarine nature of the environment.

The abovementioned hostile environments or installation conditions can impose plastic deformations to the involved pipeline. The extent of these deformations is quantitatively expressed as a 'strain demand'. This is the global strain which occurs in the pipeline due to the imposed deformation. Table 1.4 summarizes the most common causes of plastic deformation and, for some of them, corresponding representative values for strain demand. These values have been taken from the added references and either represent maximum values (m) or values from a specific project (p).

Note that, besides the occurrence of plastic deformations, a reduction of toughness due to low temperatures is an additional issue for arctic regions. However, recalling the assumption of sufficient toughness to avoid brittle fracture (section 1.4), this issue is not further addressed in this dissertation.

Table 1.4: Overview of causes for global plastic deformation and reported strain demand values. (m): maximum value, (p): project value.

Region	**Cause**	**Strain demand (%) [Reference]**
During pipeline installation		
Offshore	Reeling	2.5 % (m) [1.25]
Offshore	S-lay, J-lay	2.0 % (m) [1.59]
During pipeline operation		
Offshore	Uneven seabed	1.0 % (p) [1.59]
Shallow offshore arctic	Ice scouring	
Onshore	Landslide	
Onshore	Mining subsidence	
Arctic permafrost	Thaw subsidence or frost heave	1.0 % (p) [1.59]
Seismic	Soil liquefaction, slope instability	3.0 % (m) [1.61]

Some causes in table 1.4 deserve a brief definition.

- Ice scouring is the deformation of the seabed or the impact of a pipe by the passage of keels of floating ice [1.59, 1.62].
- Landslides and slope instabilities represent a ground movement due to an unstable soil which collapses or shears under the action of gravity.
- Mining subsidence is a ground movement due to collapse of underlying mines.
- Frost heave represents an upward pipeline displacement, due to the growth of ice lenses around the pipeline (figure 1.19(a) [1.63]). This freezing process is triggered by a relatively 'low' temperature of the transported fluid or gas.

- Thaw subsidence represents a downward pipeline displacement, due to the melting of ice-rich soils (figure 1.19(b) [1.63]). This melting is triggered by a relatively 'high' temperature of the transported liquid or gas.
- Soil liquefaction is the loss of soil strength and stiffness under an applied stress, which mainly origins from seismic activity. This geological phenomenon is for instance highly relevant to the integrity of the recently constructed 2nd West-East gas pipeline, which crosses China and thereby is mostly situated in seismically active regions (figure 1.20 [1.64]).

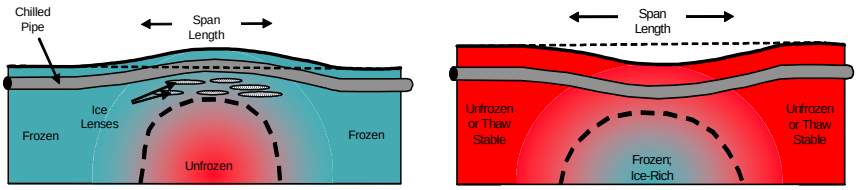

Figure 1.19: (a) Frost heave, and (b) thaw settlement [1.63].

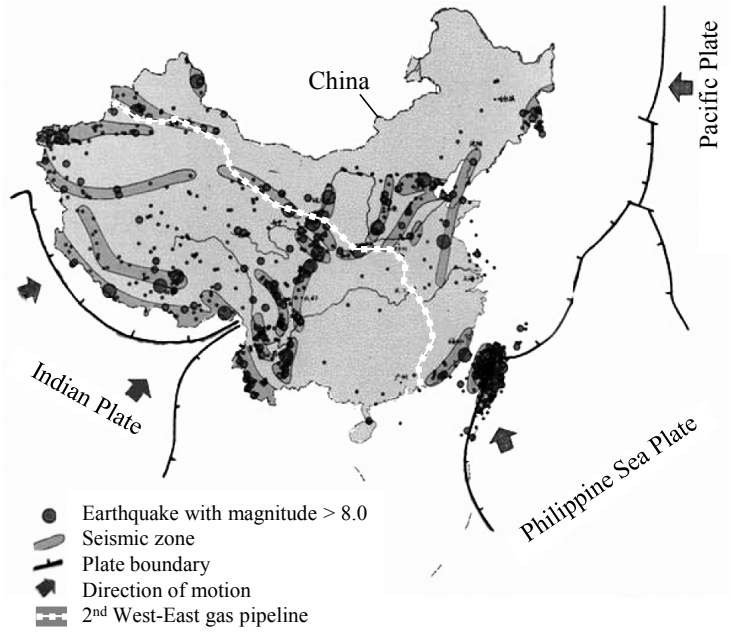

Figure 1.20: China's 2nd West-East gas pipeline crosses seismic regions with a history of severe earthquakes [1.64].

Note that the mentioned project-specific strain values need not be maximum values. For example, figure 1.21 shows a section of the 159 mm diameter Golmud-Lhasa pipeline (China, Tibet) which heaved above the ground due to permafrost effects [1.65]. From the reported description of the observed pipeline profile a maximum tensile strain of 3 % can be calculated, which is higher than the value for frost heave reported in table 1.4.

Figure 1.21: Example of frost heaving, observed in the Golmud-Lhasa pipeline [1.65].

In general, the estimation of strain demand is a highly challenging aspect in the design of pipelines facing hostile conditions [1.62], which often involves a statistical estimation of the frequency of geological phenomena with a certain severity, soil characterization and/or extensive computational models of pipe-soil interaction. Nevertheless, reported cases of imposed strains are limited to values of 4 % and below [1.66].

1.6.2 Strain capacity and strain based design

If a pipeline is not able to withstand the imposed installation or environmental tensile strains, it will leak or rupture. To ensure its integrity, a procedure must be applied to estimate the maximum allowable global strain in the pipeline. This so-called 'strain capacity' (further also denoted ϵ_{max}) evidently has to be greater than the imposed strain demand, thereby additionally respecting a certain safety margin. Strain capacity depends to a major extent on the size and position of (detected) girth weld flaws.

A strain capacity prediction procedure fits in a larger framework that aims to minimize the number of required repair welds (figure 1.22). Indeed, such repairs are undesired because they involve an additional cost and loss of time, and because the newly introduced heat input may deteriorate the mechanical properties of the surrounding material. The minimization of repair can

be performed at different stages, the third one of which is addressed in this dissertation:

- Prior to pipeline construction, installation and operation, the pipeline design (e.g. dimensions, material choice, girth weld procedure, soil modification) can be performed from a viewpoint of reducing the risk of failure (i.e. decreasing strain demand and/or increasing strain capacity for a fixed flaw size).
- The justification of weld repairs is strongly influenced by the inaccuracies of non-destructive testing. Typical flaw depth sizing errors are within the order of 1 mm [1.67] and are hence to be taken into considerable account.
- After the actual non-destructive detection of weld flaws, more accurate strain capacity prediction tools allow for an increasingly justified decision upon repair and, as a consequence, a reduction of unnecessary repair costs.

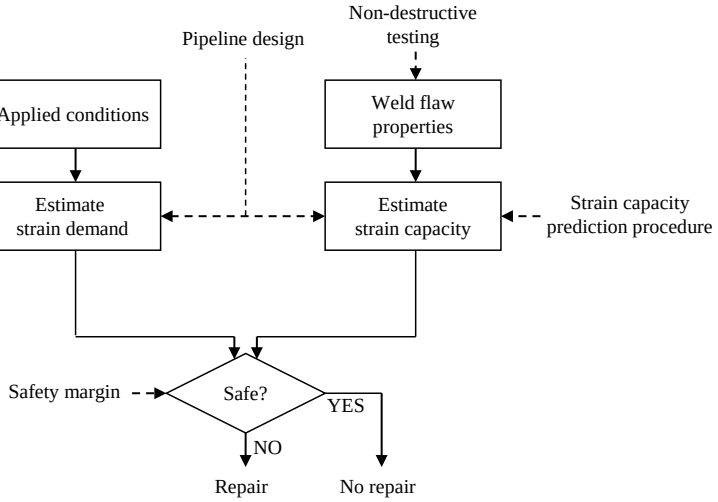

Figure 1.22: A procedure for the prediction of strain capacity plays an essential role in the framework of a strain based girth weld flaw assessment.

Traditionally, pipeline integrity calculations are based upon stresses rather than strains. For instance, the internal pressure design equation (Eq. (1.2)) aims to avoid hoop stresses above yield. Although a calculation of strain capacity through a similar 'stress based' approach (figure 1.23(a)) is physically justified, two related major objections can be made.

- After calculation of the allowable stress, a safety margin has to be applied to ensure safe operations. However, due to the non-linear post-yield

behaviour, the introduced conservativity on the level of strain capacity is much greater. This may result in an unacceptably safe design which rejects nearly all detected flaws.

- Due to the same non-linear post-yield behaviour, the conversion of an allowable stress value to an allowable strain value is highly sensitive to the exact stress-strain relation.

Given these objections, a 'strain based' approach is more appropriate for dealing with imposed plastic deformations. In such approach, strain capacity is estimated directly instead of being derived from an allowable stress (figure 1.23(b)). As a consequence, the safety margin upon strain capacity will correspond with the conservativeness, and there is no extremely sensitive conversion from stress to strain.

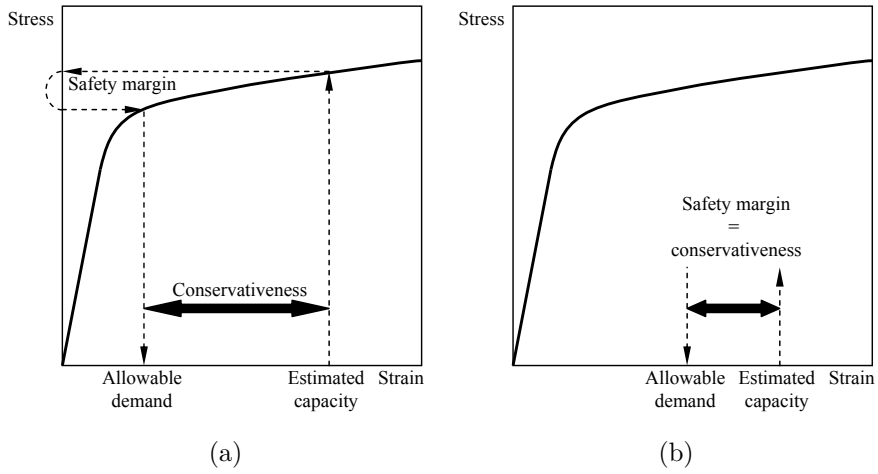

Figure 1.23: (a) Stress based design, and (b) strain based design of plastically deformed pipelines.

1.6.3 Case study: Enbridge Northern pipeline

This section illustrates some of the abovementioned aspects of strain demand and strain capacity. The following information has been taken from [1.68–1.73].

The Enbridge Northern crude oil pipeline, located in Canada and operated by Enbridge Pipelines Inc., connects the Norman Wells oil deposits (Northwest Territories) with Zama (Alberta) over a distance of 869 km (figure 1.24 [1.72]). It has been in operation since 1985 and was the first completely buried long distance pipeline in the permafrost environment of Canada. Technical data are provided in table 1.5.

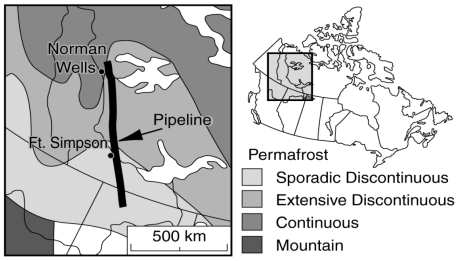

Figure 1.24: Location of the Enbridge Northern pipeline and permafrost zones [1.72].

Table 1.5: Technical specifications of the Enbridge Northern pipeline.

Characteristic	**Value**
Length	869 km
Nominal outside diameter	324 mm ($12\frac{3}{4}$")
Nominal thickness	6.35 mm ($\frac{1}{4}$")
Pipe steel grade	X52

Along its route, the Enbridge Northern pipeline encounters roughly 350 km of permafrost soils and 164 slopes which may become unstable. As a consequence, environmentally imposed plastic deformations have to be considered. At the time of construction, however, the knowledge of strain demand and capacity prediction was not as rigorous as today. Nevertheless, the design crew took two essential measures to minimize thaw and frost effects, thereby contributing to the long-time stability of the pipeline: a conscious control of the operating temperature of the pipeline, and a thermal isolation of surrounding critical slopes by the addition of wood chips.

Throughout its 25 years of operation, pipe integrity has been regularly monitored using an advanced pigging technology. Concretely, both the cross section of the pipe and the longitudinal profile of the pipe are measured. From the former measurement, six wrinkles have been detected prior to failure and repaired. From the latter measurement, strain demand has been found to take values up to 1.5 %. In the mean while, large scale tests and approximate analytical assessments have indicated a strain capacity of roughly 3 %. To date, no tensile failures have occurred.

Future challenges are caused by the effects of global warming, which will affect the soil properties. As a consequence, the stability of the entire pipeline had to be re-assessed using up-to-date information and predictions of climate change.

Summarizing the above, the example of Enbridge's Northern pipeline indicates that it is possible to safely operate a pipeline in harsh environments. An adapted design, frequent inspection and intensive (re-)assessment are key factors to obtaining this safe operation.

1.7 Summary, challenges and scope of this work

Summarizing the above, the increase in global energy demand and exhaustion of fossil fuel reserves have urged the need to design transmission pipelines from a strain based point of view, thereby accounting for imposed global plastic deformations. Of particular concern is the structural integrity of girth welds under (plastic) tension parallel to the pipe axis, as the presence of weld flaws under this condition may trigger a catastrophic failure. Hereby, particular challenges are introduced by the tendency towards the commercial implementation of increasingly strong line pipe steel on a massive scale. An essential component in the integrity assessment of a flawed girth weld is a procedure which allows for the estimation of strain capacity.

In **chapter 2** it will be shown that – despite major and ever increasing efforts during the last decades – there is no analytical procedure available for the prediction of pipeline strain capacity which is standardized, fully validated, not overly conservative or sensitive *and* covers all possible influences. All currently available procedures have limitations inherent to their assumptions or execution protocol. Therefore, the presented work addresses some closely related hot topics in strain based design:

- *How do high strength line pipe steels perform under global plastic tension, and how can this performance be characterized?*
- *What is the validity of underlying assumptions of the currently existing procedures?*
- *How should numerical and experimental results that support a strain based flaw assessment procedure be interpreted and how can their tools be optimized?*

Hereby, as mentioned in section 1.4, focus is put upon ductile failure i.e. the structure is considered to have a sufficient toughness under the operation temperature to avoid brittle fracture.

Next to the above, chapter 2 gives background on the basic concept of strain capacity. A critical literature overview is given which tackles the following questions:

- *What stress based flaw assessment techniques can be extrapolated to strain based flaw assessment techniques?*
- *What failure modes occur under global plastic tension and how are they characterized?*
- *What are the key influencing factors to strain capacity?*
- *How to determine or estimate strain capacity in a laboratory environment?*
- *What strain based procedures have been proposed so far and what are their limitations?*

Chapter 2 finally reveals concrete key issues regarding the mechanical (stress-strain) characterization of line pipe steels, and the influence of their behaviour on strain capacity. These aspects are the main topic of this dissertation, which is further structured as follows.

Chapter 3 is devoted to the experimental characterization and description of the stress-strain behaviour of (high strength) line pipe steels. Knowledge of these two aspects is important to understand the challenges related to strain capacity prediction. The following is addressed:

- *considerations for tensile testing with particular respect to specimen geometry, heterogeneity and anisotropy;*
- *the mathematical description of strain hardening behaviour.*

To investigate the possibilities and limitations of numerical modelling (upon which most analytical flaw assessment methods have been based), a finite element model of large scale girth weld tension tests has been developed. Technical aspects related to its structure are elaborated in **chapter 4**. Recommendations are provided with respect to model creation and analysis, in particular:

- *model requirements for fracture mechanics and plasticity analysis;*
- *creation and meshing of the desired geometry;*
- *the incorporation of ductile crack extension.*

Chapter 5 is dedicated to the development and optimization of an experimental girth weld fracture mechanics test for research purposes. This so-called 'medium wide plate' tension test is a smaller version of the commonly used curved wide plate tension test (see chapter 2), and quantifies effects of plas-

ticity and flaw response on strain capacity in a specimen with representative flaw dimensions. Specific attention is given to the following aspects:

- *the implementation of advanced instrumentation for the characterization of plasticity and ductile tearing;*
- *the design of specimen geometry and location of strain sensors.*

To investigate the interpretation of a curved (or medium) wide plate tension test, *experimental data* are provided and analyzed in **chapter 6**. Along with existing fracture mechanics relations, these data are then used in **chapter 7** for a critical analytical and experimental *validation of the finite element model* from chapter 4.

Eventually, **chapter 8** applies the developed numerical model in a parametric study to investigate effects of material properties on strain capacity. Attention is given to the following aspects:

- *weld strength mismatch,*
- *base metal constitutive behaviour,*
- *base metal heterogeneity.*

Conclusions and possibilities for future research are finally summarized in **chapter 9**, which is the last chapter of this dissertation. This chapter provides guidance on how to combine experimental, numerical and analytical tools for the development of a strain capacity prediction procedure.

Bibliography

[1.1] http://pubs.usgs.gov/fs/2003/fs014-03/pipeline.html. Accessed: April 1, 2009.

[1.2] http://www.worldenergyoutlook.org. Accessed: December 1, 2011.

[1.3] http://www.oecd.org/pages/0,3417,en_36734052_36734103_1_1_1_1_1,00.html. Accessed: December 1, 2011.

[1.4] *World Energy Outlook 2010 – Executive summary.* International Energy Agency, 2010. www.iea.org/Textbase/npsum/weo2010sum.pdf. Accessed: December 1, 2011.

[1.5] *The Outlook for energy: a view to 2030.* ExxonMobil, 2010. www.exxonmobil.com/Corporate/files/news_pub_eo_2010.pdf. Accessed: December 1, 2011.

[1.6] M. Asif and T. Muneer. Energy supply, its demand and security issues for developed and emerging economies. *Renewable & Sustainable Energy Reviews*, 11(7):1388–1413, 2007.

[1.7] P. Hopkins. The challenges for frontier pipeline projects. In *Proceedings of the International Conference on Application and Evaluation of High-Grade Linepipes in Hostile Environments*, pages 3–32, Pacifico Yokohama, Japan, 2002.

[1.8] L. Scheire and F. Van Den Abeele. *Wat als de olie op is?* Borgerhoff & Lamberigts, 2009. 208 pages. In Dutch. ISBN 9789089310859.

[1.9] G. Knauf. EPRG: Crack arrest and girth weld acceptance criteria for high pressure gas transmission pipelines. In *Proceedings of the International Conference on Application and Evaluation of High-Grade Linepipes in Hostile Environments*, pages 475–500, Pacifico Yokohama, Japan, 2002.

[1.10] R. Goodland, editor. *Oil and gas pipelines. Social and environmental impact assessment: state of the art.* 2005. 193 pages. Compiled for International Association of Impact Assessment (IAIA) 2005 Conference.

[1.11] SIMDEX future pipeline projects worldwide guide – update September 2011, http://www.simdex.com/future_pipeline_projects/simdex_future_pipeline_projects_worldwide_guide_statistics_web. Accessed: December 1, 2011.

[1.12] http://www.jfe-steel.co.jp/en/products/pipes/linepipe/index.html. Accessed: December 28, 2011.

[1.13] K.H. Brensing and B. Sommer. Steel tube and pipe manufacturing processes. Technical report. Source: www.smrw.de/downloads/Steel_tube_and_pipe.pdf (Salzgitter Mannesmann Röhrenwerke). Accessed: February 6, 2010.

[1.14] K. Nagai, Y. Shinohara, S. Sakamoto, E. Tsuru, H. Asahi, and T. Hara. Anisotropic strain aging behavior of high strength UOE linepipe. In *Proceedings of the 19th International Offshore and Polar Engineering Conference (ISOPE)*, pages 56–60, Osaka, Japan, 2009.

[1.15] S. Wen, S. Slater, R. Freeman, and M. Connelly. Finite element modelling of deepwater UOE linepipe manufacturing. In *Proceedings of the 30th International Conference on Ocean, Offshore and Arctic Engineering (OMAE)*, Rotterdam, The Netherlands, 2011. OMAE2011-49450.

[1.16] http://www.tzinorot.co.il/metco/templates/showpage.asp?dbid=1&lngid=1&tmid=84&fid=818. Accessed: December 2, 2011.

[1.17] J. La Fontaine, D. Smith, G. Deason, and G. Adams. Bombax pipeline project: anti-corrosion and concrete weight coating of large diameter subsea pipelines. In *Proceedings of the Offshore Technology Conference (OTC)*, Houston, Texas, USA, 2003. OTC 15274.

[1.18] S. Kyriakides and E. Corona. *Mechanics of offshore pipelines. Volume 1: Buckling and collapse*. Elsevier, 2007. 400 pages. ISBN 978-0080467320.

[1.19] G. Wilkowski, D. Rudland, D.J. Shim, F.W. Brust, and S. Babu. Advanced integration of multi-scale mechanics and welding process simulation in weld integrity assessment. Technical report, 2008. DOE Award nr. DE-FC36-04GO14040. 120 pages.

[1.20] D.P. Fairchild, M.D. Crawford, W. Cheng, M.L. Macia, N.E. Nissley, S.J. Ford, D.B. Lillig, and J. Sleigh. Girth welds for strain-based design pipelines. In *Proceedings of the 18th International Offshore and Polar Engineering Conference (ISOPE)*, pages 48–56, Vancouver, Canada, 2008.

[1.21] B.K. Narayanan, L. McFadden, M.J. Mills, and M.A. Quintana. Characterization of weld metal deposited with a self shielded flux cored electrode for pipeline girth welds and offshore structures. In *Proceedings of the 8th International Pipeline Conference (IPC)*, Calgary, Alberta, Canada, 2010. IPC2010-31406.

[1.22] Y.Y. Wang, M. Liu, and D. Rudland. Strain based design of high strength pipelines. In *Proceedings of the 17th International Offshore and Polar Engineering Conference (ISOPE)*, pages 3186–3193, Lisbon, Portugal, 2007.

[1.23] http://www.denysnv.be/projects/index/nl/3/102. Accessed: December 2, 2011. in Dutch.

[1.24] http://www.guardian.co.uk/business/2011/jan/12/alaskan-leak-oil-hits-27-month-high. Accessed: December 6, 2011.

[1.25] T. Tkaczyk. *Development of fracture mechanics based criteria for failure of reeled pipes*. PhD thesis, University of London - Imperial College of Science, Technology and Medicine - Department of Mechanical Engineering, 2010.

[1.26] *Oil & gas pipeline systems, CSA Z662*. Canadian Standards Association, Ontario, Canada, 2007.

[1.27] *Submarine Pipeline Systems, DNV-OS-F101*. Det Norske Veritas, Høvik, Norway, 2007.

[1.28] R. Bruschi, L. Vitali, E. Torselletti, D. Zenobi, A. Johannessen, and R. Holme. Langeled – Pipe capacity vs. wall thickness selection. In *Proceedings of the 17th International Offshore and Polar Engineering Conference (ISOPE)*, pages 986–994, Lisbon, Portugal, 2007.

[1.29] D. Cranswick. Brief overview of Gulf of Mexico OCS oil and gas pipelines: installation, potential impacts, and mitigation measures. Technical Report MMS 2001-067, U.S. Department of the Interior - Minerals Management Service - Gulf of Mexico OCS Region, 2001.

[1.30] A. Hilberink. *Mechanical behaviour of lined pipe*. PhD thesis, Technical University Delft, 2011.

[1.31] http://www.lesoir.be/regions/hainaut/2011-01-19/ghislenghien-l-avocat-general-denonce-la-mesinformation-815932.php. Accessed: January 21, 2011. In French.

[1.32] R. Denys and A. Lefevre. UGent guidelines for curved wide plate testing. In R. Denys, editor, *Proceedings of the 5th International Conference on Pipeline Technology*, Ostend, Belgium, 2009.

[1.33] P. Hopkins, G. Demofonti, G. Knauf, and R. Denys. An experimental appraisal of the significance of defects in pipeline girth welds. In *Proceedings of the EPRG/NG18 8th Biennial JTM on Linepipe Research*, Paris, France, 1991.

[1.34] W. Schipaanboord, R. Denys, A. Lefevre, and P. Roovers. Validation tests to support the EPRG - Tier 2 guidelines. In *Proceedings of the EPRG/NG18 8th Biennial JTM on Linepipe Research*, Paris, France, 1991.

[1.35] K.R. Jayadevan, E. Østby, and C. Thaulow. Fracture response of pipelines subjected to large plastic deformation under tension. *International Journal of Pressure Vessels and Piping*, 81(9):771–783, 2004.

[1.36] E. Østby, K.R. Jayadevan, and C. Thaulow. Fracture response of pipelines subject to large plastic deformation under bending. *International Journal of Pressure Vessels and Piping*, 82(3):201–215, 2005.

[1.37] R. Denys, W. De Waele, and A. Lefevre. Effect of pipe and weld metal post-yield characteristics on plastic straining capacity of axially loaded pipelines. In *Proceedings of the 5th International Pipeline Conference (IPC)*, Calgary, Alberta, Canada, 2004. IPC04-0768.

[1.38] *Specification for Line Pipe, API 5L, 44th edition.* American Petroleum Institute, Washington, USA, 2007.

[1.39] C.W. Petersen, K.T. Corbett, D.P. Fairchild, S. Papka, and M.L. Macia. Improving long-distance gas transmission economics: X120 development overview. In R. Denys, editor, *Proceedings of the 4th International Conference on Pipeline Technology*, volume 1, pages 3–29, Ostend, Belgium, 2004.

[1.40] A.K. Jenkins and A.G. Glover. Advances in high strength technology for natural gas transmission. In *Proceedings of the 15th International Offshore and Polar Engineering Conference (ISOPE)*, pages 24–30, Seoul, Korea, 2005.

[1.41] A. Glover and B. Rothwell. Yield strength and plasticity of high strength pipelines. In R. Denys, editor, *Proceedings of the 4th International Conference on Pipeline Technology*, volume 1, pages 65–79, Ostend, Belgium, 2004.

[1.42] W. Mohr. Local buckling as an upper limit on pipe yield strength in strain-based design. In *Proceedings of the International Conference on Application and Evaluation of High-Grade Linepipes in Hostile Environments*, pages 629–643, 2002.

[1.43] M. Hauge, H.I. Lange, and Z. Zhang. Application of X80 high strength steel for offshore pipelines. In *Proceedings of the International Conference on Application and Evaluation of High-Grade Linepipes in Hostile Environments*, pages 1033–1044, Pacifico Yokohama, Japan, 2002.

[1.44] M.A. Quintana and J. Hammond. X100 welding technology – past, present and future. In *Proceedings of the 8th International Pipeline Conference (IPC)*, Calgary, Alberta, Canada, 2010. IPC2010-31421.

[1.45] F.B. Pickering. High strength, low-alloy steels - a decade of progress. In *Proceedings of the MicroAlloying '75 Conference*, Washington, D.C., USA, 1975.

[1.46] J.M. Gray and F. Siciliano. High strength microalloyed linepipe: half a century of evolution. In *Proceedings of the 5th International Conference on Pipeline Technology*, Ostend, Belgium, 2009.

[1.47] L. Malik, R. Yee, B. Graville, and A. Dinovitzer. Optimized design parameters for welded TMCP steels. Technical Report SSC-396, Ship Structure Committee, 1997.

[1.48] M. Gräf, J Schröder, V. Schwinn, and K. Hulka. Production of large-diameter grade X70 pipes with high toughness using acicular ferrite microstructures. In *Proceedings of the International Conference on Application and Evaluation of High-Grade Linepipes in Hostile Environments*, pages 323–338, Pacifico Yokohama, Japan, 2002.

[1.49] S. Vervynckt. *Control of the non-recrystallization temperature in High Strength Low Alloy (HSLA) steels.* PhD thesis, Ghent University, 2010.

[1.50] R. Denys, S. Hertelé, and M. Verstraete. Longitudinal strain capacity of GMAW welded high niobium (HTP) grade X80 steel pipes. In *Proceedings of the International Seminar on Application of High Strength Line Pipe (HSLP)*, Xi'an, China, 2010.

[1.51] V. Schwinn, P. Fluess, and J. Bauer. Production and progress of plates for pipes with strength levels of X80 and above. In *Proceedings of the International Conference on Application and Evaluation of High-Grade Linepipes in Hostile Environments*, pages 339–353, Pacifico Yokohama, Japan, 2002.

[1.52] H.G. Hillenbrand and C. Kalwa. Production and service behavior of high-strength large-diameter pipeline. In *Proceedings of the International Conference on Application and Evaluation of High-Grade Linepipes in Hostile Environments*, pages 203–215, Pacifico Yokohama, Japan, 2002.

[1.53] A.C. Bannister, J.R. Ocejo, and F. Gutierrez-Solana. Implications of the yield stress/tensile stress ratio to the SINTAP failure assessment diagrams for homogeneous materials. *Engineering Fracture Mechanics*, 67(6):547–562, 2000.

[1.54] R. Denys, S. Hertelé, W. De Waele, and A. Lefevre. Estimate of Y/T ratio and uniform elongation capacity of pipeline steels from yield strength. In R. Denys, editor, *Proceedings of the 5th International Conference on Pipeline Technology*, Ostend, Belgium, 2009.

[1.55] M. Hamada, S. Okaguchi, H. Shitamoto, and Y. Komizo. Tensile properties and deformation behaviour at the weld position of X100 line pipe steel. In *Proceedings of the International Conference on Application and Evaluation of High-Grade Linepipes in Hostile Environments*, pages 289–305, Pacifico Yokohama, Japan, 2002.

[1.56] J. Hammond, S.A. Blackman, and M.G. Hudson. Challenges of girth welding X100 linepipe for gas pipelines. In *Proceedings of the International Conference on Application and Evaluation of High-Grade Linepipes in Hostile Environments*, pages 931–955, Pacifico Yokohama, Japan, 2002.

[1.57] R. Ishikawa, S. Endo, S. Igi, A.G. Glover, D. Horsley, M. Ohata, and M. Toyoda. Ductile fracture behaviour of girth-welded joints and strain-based design for high-strength pipeline. In R. Denys, editor, *Proceedings of the 4th International Conference on Pipeline Technology*, volume 1, pages 81–98, Ostend, Belgium, 2004.

[1.58] W. Mohr. Strain-based design: strain concentration at girth welds. Technical Report 47447GTH, Edison Welding Institute, 2007. 190 pages.

[1.59] W. Mohr. Strain-based design of pipelines. Technical Report 45892GTH, Edison Welding Institute, 2003. 68 pages.

[1.60] N.A. Millwood, J. Johnson, M. Hudson, and K. Armstrong. Construction of the X100 operational trial pipeline at Spadeadam, Cumbria, UK. In *Proceedings of the 8th International Pipeline Conference*, Calgary, Alberta, Canada, 2010. IPC2010-31469.

[1.61] T. Masuda, T. Kobayashi, K. Yoshizaki, and M. Kobayashi. Recommended practice for the design of gas transmission pipelines in areas subject to liquefaction. In *Proceedings of the International Conference on Application and Evaluation of High-Grade Linepipes in Hostile Environments*, pages 589–599, Pacifico Yokohama, Japan, 2002.

[1.62] W.C. Kan, M. Weir, M.M. Zhang, D.B. Lillig, S.T. Barbas, M.L. Macia, and N.E. Biery. Strain-based pipelines: design consideration overview. In *Proceedings of the 18th International Offshore and Polar Engineering Conference (ISOPE)*, pages 174–181, Vancouver, Canada, 2008.

[1.63] H. Arslan, J. Hamilton, L. Suvrat, K. Minnaar, B. Albrecht, M.F. Cook, and P. Wong. Strain demand estimation for pipelines in challenging arctic and seismically active regions. In *Proceedings of the 8th International Pipeline Conference (IPC)*, Calgary, Alberta, Canada, 2010. IPC2010-31505.

[1.64] H. Chen and L. Ji. The feasibility and prospect of strain-based design to pipelines in China. In *Proceedings of the 17th International Offshore and Polar Engineering Conference (ISOPE)*, pages 3049–3053, Lisbon, Portugal, 2007.

[1.65] R. He and H. Jin. Permafrost and cold-region environmental problems of the oil product pipeline from Golmud to Lhasa on the Qinghai-Tibet Plateau and their mitigation. *Cold Regions Science and Technology*, 64(3):279–288, 2010.

[1.66] D.B. Lillig. The first (2007) ISOPE strain-based design symposium - a review. In *Proceedings of the 18th International Offshore and Pipeline Conference (ISOPE)*, pages 1–12, Vancouver, Canada, 2008.

[1.67] M. Moles. Defect sizing in pipeline welds: what can we really achieve? In *Proceedings of the ASME 2004 Pressure Vessels and Piping Conference (PVP)*, San Diego, California, USA, 2004. PVP2004-2811.

[1.68] R.M. Doblanko, J.M. Oswell, and A.J. Hanna. Right-of-way and pipeline monitoring in permafrost - the Norman Wells pipeline experience. In *Proceedings of the 4th International Pipeline Conference (IPC)*, Calgary, Alberta, Canada, 2002. IPC2002-27357.

[1.69] R. Barlow, T. Farquhar, and A. Tleukulov. Northern exposure: monitoring and testing a subarctic liquids pipeline. In *Proceedings of the 5th International Pipeline Conference*, Calgary, Alberta, Canada, 2004. IPC04-0255.

[1.70] A. Dinovitzer, A. Fredj, R. Lazor, and R. Doblanko. Development and validation of a pipeline buckle and wrinkle assessment model. In *Proceedings of the 5th International Pipeline Conference (IPC)*, Calgary, Alberta, Canada, 2004. IPC04-0254.

[1.71] J. Oswell and D. Skibinsky. Thaw responses in degrading permafrost. In *Proceedings of the 6th International Pipeline Conference (IPC)*, Calgary, Alberta, Canada, 2006. IPC2006-10616.

[1.72] M.M. Burgess, J. Oswell, and S.L. Smith. Government-industry collaborative monitoring of a pipeline in permafrost - the Norman Wells pipeline experience, Canada. In *Proceedings of the 63rd Canadian Geotechnical Conference and 6th Canadian Permafrost Conference (GEO 2010)*, pages 579–586, 2010.

[1.73] I. Pederson, M. Sen, A. Bidwell, and N. Yoosef-Ghodsi. Enbridge Northern pipeline: 25 years of operations, successes and challenges. In *Proceedings of the 8th International Pipeline Conference (IPC)*, Calgary, Alberta, Canada, 2010. IPC2010-31611.

Chapter 2

Strain based flaw assessment: literature survey

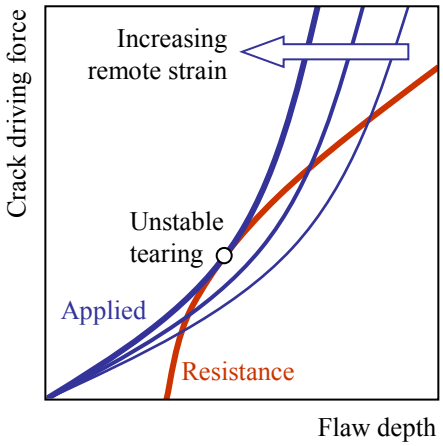

The tangency approach, which relies on crack driving force and tearing resistance, is an essential component of analytical methods to predict strain capacity.

2.1 Goal

This chapter provides a state of the art on experimental, numerical and analytical techniques to perform a strain based flaw assessment. The primary aim of the investigated methods is to estimate the strain capacity of a flawed structure with known geometrical, material, flaw and loading characteristics ('deterministic' methods). The treatment of unavoidable uncertainties for all aspects of the structural problem (e.g. flaw sizing errors, variability of material properties, ...) requires a probabilistic approach which is not further elaborated in this dissertation.

Taken as a starting point is the more widely applied field of stress based integrity. Section 2.2 provides fundamental stress based concepts involving fracture mechanics and plasticity, the understanding of which is equally essential for strain based flaw assessments. Then, the extrapolation of stress based to strain based flaw assessments is discussed in section 2.3. In this section, focus is given to introduced challenges and – consequently – additional key influence factors that arise for a strain based assessment. Next, an overview is given of experimental (section 2.4) and numerical (section 2.5) methods to estimate strain capacity. Both experimental and numerical results (or combinations) have been used to formulate analytical methods of strain capacity estimation, which are finally discussed in section 2.6. Particular attention goes to the assumptions of all methods, in order to reveal their possibilities and limitations.

2.2 Basic analytical concepts: stress based flaw assessment

Stress based flaw assessment methods involve two fundamental theories: fracture mechanics and plasticity. Both are briefly discussed in sections 2.2.1 and 2.2.2 respectively. Fracture mechanics and plasticity can be linked through the reference stress approach, which is the topic of section 2.2.3. Next, section 2.2.4 provides background on the commonly used failure assessment diagram technique. Finally, section 2.2.5 discusses how to incorporate ductile tearing into a flaw assessment.

2.2.1 Linear elastic and elastic-plastic fracture mechanics

This section provides a brief summary of fracture mechanics concepts which are important for the following. For a more elaborate background, the reader is referred to [2.1].

Fracture mechanics describes the structural response of a cracked structure, thereby focussing on unstable fracture and stable crack growth. Its foundations

originate from the early 20th century, when Griffith [2.2] performed research on the extremely brittle behaviour of glass. He found that for an infinitesimal amount of crack growth ($\mathrm{d}A_0$, if the crack surface is denoted as A_0) to occur, the release of potential energy U_p should at least be equal to the dissipated energy. This led to Irwin's definition of energy release rate G [2.3]:

$$G = -\frac{\mathrm{d}U_p}{\mathrm{d}A_0} \tag{2.1}$$

Next to the energy balance approach, cracked structures have been investigated with respect to the stress state near the crack tip. Focussing on 'mode I' loading (tension perpendicular to the crack plane) and assuming a linear elastic material, the so-called stress intensity factor K_I (MPa $\cdot$ mm$^{1/2}$) describes this stress state (symbolized by σ_{ij}) as follows [2.4]:

$$\lim_{r \to 0} \sigma_{ij} = \frac{K_I}{\sqrt{2\pi r}} f_{ij}^{(I)}(\theta) \tag{2.2}$$

where r and θ are coordinates in a polar coordinate system (with $r = 0$ at the crack tip and $\theta = 0$ the direction of the crack front), and $f_{ij}^{(I)}$ a tensor of known functions. Under linear elastic conditions, K_I is proportional to the remotely applied stress σ and generally expressed as:

$$K_I = Y\sigma\sqrt{\pi a} \tag{2.3}$$

where Y is a non-dimensional correction factor that depends on geometry and the investigated position on the crack front, and a a measure of crack size (length or depth, depending on the investigated configuration). If K_I reaches a critical value K_{mat} (the so-called fracture toughness), fracture occurs.

Energy release rate G has been theoretically linked with K_I by Irwin [2.5]:

$$G = \frac{K_I^2}{E'} \tag{2.4}$$

where E' is Young's modulus E or $E/\left(1-\nu^2\right)$ (ν is Poisson's coefficient) for plane stress or plane strain configurations, respectively.

The linear elasticity assumption restricts the validity of the abovementioned concepts to cases where remote stress does not exceed a certain fraction of the material's yield strength σ_0 (roughly 0.5 to 0.6 σ_0). Hence, the application of linear elastic fracture mechanics (LEFM) is mostly limited to brittle materials and fatigue problems. The investigation of problems which involve significant plasticity (near the crack tip or global) requires an elastic plastic fracture mechanics (EPFM) approach. To this respect, two concepts have been introduced: crack tip opening displacement CTOD (mm) and Rice's non-linear energy release rate J [2.6] (N/mm). Whereas CTOD is often defined on the basis of the so-called 90° intercept method proposed by Rice [2.6] (figure 2.1), J has a

definition similar to G for LEFM (Eq. (2.1)). However, J assumes *non*-linear elastic behaviour. Note that such behaviour is a simplification to actual elastic-plastic behaviour, as the elastic recovery upon unloading is assumed complete (i.e. there are no plastic residual strains).

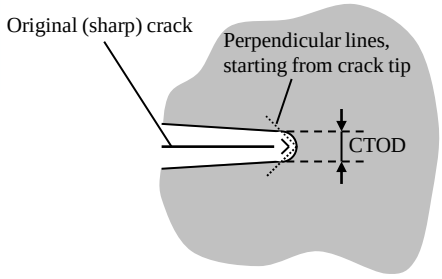

Figure 2.1: CTOD according to the 90° intercept method, proposed by Rice [2.6].

For both CTOD and J, physical relevance with regard to the stress state near the crack tip has been shown through the following:

- Similar to K_I for LEFM, J describes the crack tip stress distribution in EPFM through the so-called HRR stress field solution, deduced by Hutchinson, Rice and Rosengren [2.7, 2.8]:

$$\sigma_{ij} = \sigma_0 \left(\frac{EJ}{\alpha \sigma_0^2 I_n r} \right)^{\frac{1}{n+1}} \tilde{\sigma}_{ij}(n, \theta) \tag{2.5}$$

  where α and n describe stress-strain behaviour as defined in Eq. (2.6) ($\epsilon_0 = \sigma_0/E$), r and θ are polar coordinates as introduced for Eq. (2.3), I_n is a dimensionless factor that depends on n, and $\tilde{\sigma}_{ij}(n, \theta)$ is a tensor of dimensionless known functions.

$$\frac{\epsilon}{\epsilon_0} = \frac{\sigma}{\sigma_0} + \alpha \left(\frac{\sigma}{\sigma_0} \right)^n \tag{2.6}$$

- J and CTOD are theoretically related through the following relation [2.9–2.11]:

$$J = m \sigma_0 \text{CTOD} \tag{2.7}$$

  with m a constant that depends on the configuration and material (mostly between 1 and 2). Hence, CTOD indirectly describes the crack tip stress field through the HRR solution.

Both CTOD and J can be separated into a linear elastic and a plastic component (respectively denoted with indices '*el*' and '*pl*'). Further focus is put on

$J = J_{el} + J_{pl}$. First, given the similarity between J and G and recalling Eq. (2.4), J_{el} is related to K_I as follows:

$$J_{el} = \frac{K_I^2}{E'} \tag{2.8}$$

Second, the following general expression for J_{pl} was proposed by Kumar and Shih in the EPRI handbook (1981) [2.12]:

$$J_{pl} = \alpha \epsilon_0 \sigma_0 a h_1 \left(\frac{P}{P_0}\right)^{n+1} \tag{2.9}$$

where P_0 is a normalizing load. J_{pl} is proportional to a dimensionless factor h_1, which depends on the geometry of the structure, the crack dimensions, the strain hardening exponent n and the considered position on the crack tip front. In literature, solutions for J_{pl} are often provided on the basis of tabulated h_1-factors, which were obtained from finite element analyses.

Note that similar alternative expressions for J_{pl} have been proposed, where a in Eq. (2.9) is replaced by another dimensional characteristic and/or load represented in terms of stress. For instance, the following equation has been adopted in [2.13–2.16]:

$$J_{pl} = \alpha \epsilon_0 \sigma_0 t h_1 \left(\frac{\sigma}{\sigma_0}\right)^{n+1} \tag{2.10}$$

This relation is equally valid but requires other tabulated values for h_1 than Eq. (2.9).

2.2.2 Plastic collapse and the concept 'limit load'

Next to fracture, plastic collapse is another major failure mechanism of flawed structures. Plastic collapse corresponds with an accumulation of localized deformation which exhausts the ductility of the material (similar to localized necking in a tensile test). There are two fundamentally different collapse types (figure 2.2). First, **'net section collapse' (NSC)** involves failure in the flawed section. This failure location is typical for structures with homogeneous material properties. Second, under presence of a weld (see section 2.4.2), it is possible that failure occurs in a section remote from the flaw. This failure mode is referred to as **'gross section collapse' (GSC)** [2.17].

Net section collapse can be related to either (a small zone in vicinity of) the crack ligament or the entire flawed cross section. These approaches are referred to as **'local collapse'** and **'global collapse'**, respectively [2.18].

The actual collapse load of a structure depends on its geometry (including the properties of the flaw), load type and material behaviour. To simplify the practical development of assessment equations, materials are mostly simplified

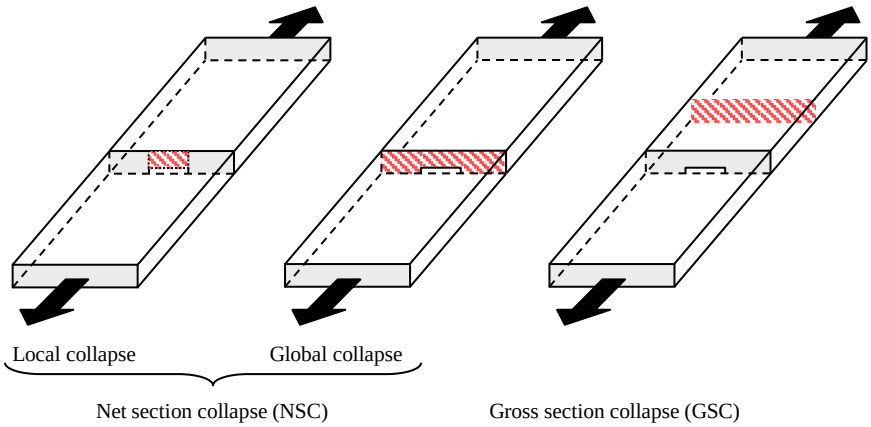

Figure 2.2: Definition of different plastic collapse types.

to an elastic – perfectly plastic constitutive law characterized by a Young's modulus E and a yield strength σ_0 (e.g. [2.19]):

$$\sigma = \min\left(E\epsilon, \sigma_0\right) \tag{2.11}$$

Hereby, strain hardening is fully neglected which – if the actual yield strength is taken for σ_0 – adds conservativeness to the calculations. Analytical limit load equations often involve an even stronger simplification, by also neglecting the linear elastic branch of the stress-strain curve. In such case, materials are assumed rigid – perfectly plastic and are fully characterized on the basis of a yield strength σ_0. Additionally, analytical assumptions have to be made regarding the stress distribution in the flawed section (e.g. figure 2.3 [2.20]).

When strain hardening is neglected, a 'limit load' P_L is referred to rather than a 'collapse load' [2.21]. Limit load equations are often translated into equations for a critical applied stress value σ_c, equal to the limit load divided by the gross section of the structure.

The limit load of a welded structure containing a weld flaw can be increased by overmatching the weld in strength, relative to the base metal [2.22]. In stress based assessments, weld strength overmatch is generally defined on the basis of the yield strengths of base and weld metal (OM_{YS}) as follows (equation given for 0.2 % proof stress $R_{p0.2}$ as a yield strength measure [1]):

$$OM_{YS} = \frac{R_{p0.2,weld} - R_{p0.2,base}}{R_{p0.2,base}} \cdot 100\% \tag{2.12}$$

[1] Yield strength is also often defined as the stress at 0.5 % total strain (chapter 3).

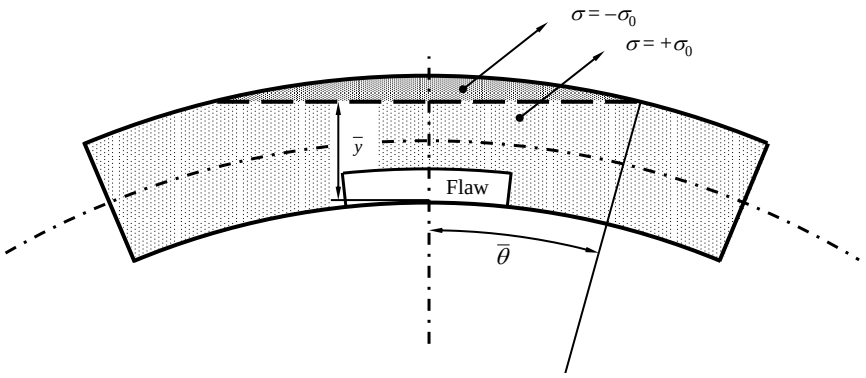

Figure 2.3: Assumed stress distribution corresponding to global net section collapse of a curved plate with surface flaw at the inner diameter surface [2.20].

2.2.3 The reference stress approach for estimation of plastic collapse and J

Eq. (2.9) has two drawbacks: it is limited to power law strain hardening materials, and it requires an h_1-factor which varies as a function of flaw size and material behaviour. In 1984, Ainsworth [2.23] overcame these issues by reformulating the equation, thereby introducing a so-called reference stress σ_{ref} which is proportional to the applied load P according to

$$\sigma_{ref} = \frac{P}{P_0}\sigma_0 \tag{2.13}$$

Ainsworth showed that a good definition of the normalizing load P_0 removes most of the material dependency of h_1 in Eq. (2.9) and allows to estimate the total J on the basis of its linear elastic component J_{el}, σ_{ref} and the reference strain ϵ_{ref} which corresponds with σ_{ref} according to the stress-strain behaviour of the material. The result was further empirically modified in [2.24] to yield the following widely used relation for J:

$$J = J_{el}\left(\frac{E\epsilon_{ref}}{\sigma_{ref}} + \frac{\sigma_{ref}^3}{2E\epsilon_{ref}\sigma_0^2}\right) \tag{2.14}$$

The accuracy of Eq. (2.14) relies on the choice for P_0. Ainsworth [2.23] found for standardized fracture mechanics test specimens that the best choice for P_0 (i.e. which eliminates the material dependency from h_1 as much as possible) is typically very close to the limit load P_L. Hence, fracture and plastic collapse can be linked by reformulating Eq. (2.13) into

$$\sigma_{ref} = \frac{P}{P_L}\sigma_0 = \frac{\sigma}{\sigma_c}\sigma_0 \tag{2.15}$$

In words, σ_{ref} equals the yield strength σ_0 when plastic collapse is achieved through the limit load equation. Recent research shows that for this definition of σ_{ref} to produce accurate J estimates, the use of a 'global collapse' limit load for P_L is mostly advised over a 'local collapse' limit load. The latter typically gives unacceptably conservative results. However, configuration specific investigations are advised as the use of a global collapse limit load may also provide slightly non-conservative J calculations [2.19, 2.25–2.27].

2.2.4 Failure assessment diagram

The failure assessment diagram (FAD) is a highly popular technique for the stress based assessment of flawed structures. It has been standardized under different but similar forms in flaw assessment standards and recommended practices such as BS 7910 (2005) [2.28], API 579 (2000) [2.29], FITNET (2008) [2.30] and R6 (1999) [2.31]. At this point, focus will be given to R6 as its FAD approach is assumed to be the most widely applied of all existing variants, and has been partially adopted by the other abovementioned standards [2.21].

The FAD is a graphical approach which combines the proximity to fracture with that to plastic collapse. In R6, the former is expressed as $K_r = K_I/K_{mat}$ on a vertical axis and the latter as $L_r = \sigma_{ref}/\sigma_0$ on a horizontal axis, (figure 2.4).

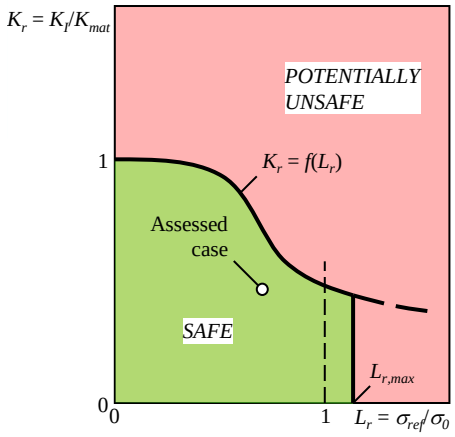

Figure 2.4: Failure assessment diagram according to R6 [2.31].

Note that, although the assessment involves plasticity, the fracture aspect is expressed in terms of K_I (or J_{el} according to Eq. (2.8)). An assessed structure (combination of material, geometry, flaw and load characteristics) represents a point on the FAD. If this point falls below a predefined line ($K_r = f(L_r)$) the

flawed structure is considered safe. On the other hand, points above the FAD line are potentially unsafe. In addition, there is a cutoff value $L_{r,max}$. If L_r exceeds this value, plastic collapse is assumed to occur. Since actual materials show strain hardening which is not incorporated in the limit load, $L_{r,max}$ can be taken larger than 1.

In R6, the reference stress approach is used for both fracture and plastic collapse. From Eqs. (2.14) and (2.15), the following expression can be derived for $f(L_r)$ (R6 Option 2):

$$f(L_r) = \left[\frac{E\epsilon_{ref}}{L_r \sigma_0} + \frac{L_r^3 \sigma_0}{2E\epsilon_{ref}} \right]^{-1/2} \tag{2.16}$$

2.2.5 The resistance curve approach for ductile tearing

The concept of fracture toughness has been based upon the conservative philosophy that, once a threshold value (J_{mat} or CTOD_{mat}) for crack driving force (J or CTOD) is reached, unstable fracture occurs. Under conditions of low stress triaxiality ('constraint') near the crack tip, however, tough materials tend to tear in a stable way prior to a possible fracture. Pipelines belong to this category of low constraint configurations [2.32]. In such case, there is no 'unique' toughness value. Alternatively, the concept of a resistance curve or 'R curve' is adopted. A resistance curve describes the required crack driving force for a certain amount of ductile tearing ($\Delta a = a - a_0$, with a_0 the initial flaw depth) to occur. The shape of an R curve depends on both material behaviour and the level of crack tip constraint. Depending on the adopted crack driving force measure, the terms J-R curve and CTOD-R curve are referred to in literature.

For advanced stress based flaw assessments, the R curve allows to estimate stable ductile tearing by determining its intersection with the crack driving force curve (crack driving force as a function of crack size, for constant loading conditions). Additionally, the onset of unstable fracture can be identified as the point where both curves touch each other tangentially. This so-called tangency approach and the R curve concept are illustrated in figure 2.5.

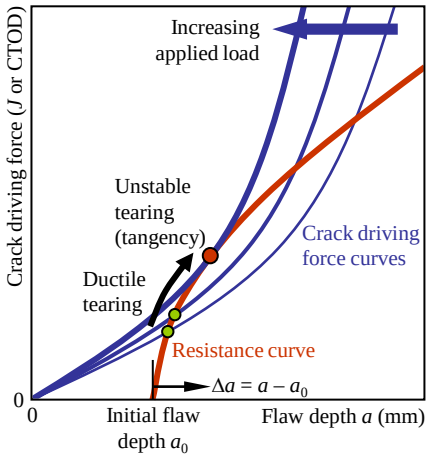

Figure 2.5: The R curve concept and tangency approach for stable and unstable ductile tearing.

2.3 From stress based to strain based flaw assessment

From section 2.2, it should be clear that stress based flaw assessment is a fairly developed field of research. Hence, the question arises to what extent existing techniques can be extrapolated into a strain based context. To answer this question, this section is divided into two parts. First, challenges additionally introduced by the strain based nature of the structural problem are discussed (section 2.3.1). Second, key factors are summarized in section 2.3.2.

2.3.1 Additional challenges

The imposition of global plastic deformations to a structure in general (and thus a pipeline in particular) requires a much greater deal of the mechanical properties that characterize a material. In particular, four additional features come into play.

First, whereas purely linear elastic behaviour is simply characterized on the basis of Young's modulus E, Poisson's coefficient ν and the yield strength which limits its applicability, plastic behaviour requires knowledge of the post-yield **strain hardening behaviour** of the involved materials (figure 2.6). This behaviour is described by a list of additional parameters such as ultimate tensile strength R_m and uniform elongation e_m. These parameters are not yet sufficient, however, as they do not describe the *shape* of the post-yield stress-strain curve which is also important [2.33].

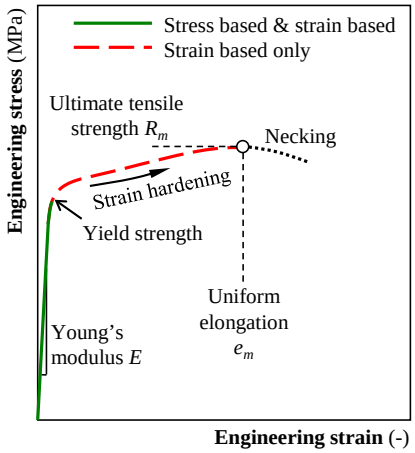

Figure 2.6: Strain based flaw assessments cover a significantly larger area of the involved materials' stress-strain curve.

A second point is that all steels behave similarly and predictably under linear elastic conditions, since E and ν are well-known and fairly constant. Hence, the only value to consider as variable for the involved materials is the yield strength. A lower bound value for this yield strength is known from the material characterization and adopted for the sake of conservativeness. Under plastic conditions, however, different steels can behave fundamentally different as their **actual post-yield characteristics** (yield strength, ultimate tensile strength, strain hardening) mostly differ. This introduces a situation of material **heterogeneity** in the structural problem, which is far more challenging to predict and describe. For instance, the presence of different material properties among different pipes will tend to concentrate plastic deformations into the weakest (i.e. least strong) pipe (figure 2.7).

Note that an effect similar to that of pipe-to-pipe heterogeneity can be caused by differences in wall thickness. If two pipes with equal material properties but slightly different thicknesses are girth welded and plastically deformed in the axial direction, the thinnest pipe will behave as a weaker structure than the thickest pipe. The presence of wall thickness variations can be pronounced. For instance, API 5L (2007) [2.34] prescribes that UOE formed pipes with an outer diameter of at least 20" (508 mm) can have a wall thickness between 92.0 % and 119.5 % of the specified nominal wall thickness.

Third, the introduction of plasticity may involve pronounced effects of material **anisotropy** (see chapter 3 for more details). Anisotropy is relevant to the strain based assessment of pipelines since the stress state of a pressurized pipe

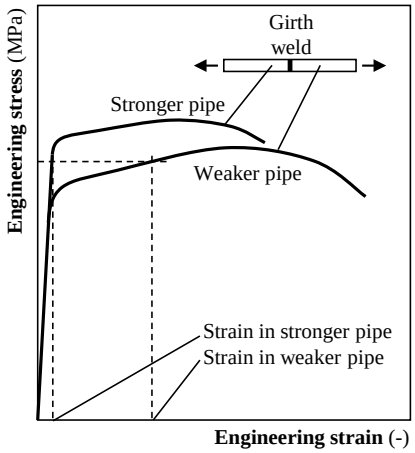

Figure 2.7: Heterogeneity between two girth welded pipes concentrates strains into the relatively 'weaker' pipe.

under (plastic) tension is biaxial. The concrete effect of anisotropy is not yet fully understood. For instance, it has been found to reduce crack driving force in [2.35] and to increase crack driving force in [2.36].

Finally, whereas the role of **ductile tearing** in stress based flaw assessments is limited to highly advanced analysis cases (i.e. cases where a minimum degree of conservativeness is desired), its incorporation is essential for strain based flaw assessments [2.37–2.39]. Indeed, considering the initiation of (stable) ductile tearing as a failure criterion rather than the onset of unstable ductile tearing may lead to overly conservative predictions of deformation capacity. On the contrary, the neglection of ductile tearing may lead to an unconservative estimation of plastic collapse [2.40]. As a result, the required characterization of the crack growth resistance behaviour (i.e. J-R or CTOD-R curve) of the involved materials (weld metal and heat-affected zone in particular) is an additional challenge. As for the analytical implementation of a ductile tearing analysis, Østby et al. argued that the tangency approach should yield conservative predictions [2.37].

2.3.2 Key factors in a strain based flaw assessment

It is evident that most key factors for a stress based flaw assessment remain essential under strain based conditions (e.g. flaw dimensions with respect to structural dimensions, for instance a/t [2.41]). A rare exception to this is the effect of welding residual stresses. Whereas these should be accounted for in stress based flaw assessments, their importance is doubted in strain based

cases. In particular, Lei [2.42] compared simulations with and without welding residual stresses and found that current stress based FAD methods from BS 7910 [2.28] and R6 [2.31] overestimate their importance in excess of yield. Moreover, the effect of residual stresses has been found to diminish as ductile tearing proceeds [2.43]. Advice on a pragmatic incorporation of welding residual stresses is further provided in section 2.6.2.1.

Next to the above influences, two factors become highly important: the post-yield strength characteristics of the involved materials and the pipe's internal pressure.

2.3.2.1 Post-yield strength characteristics

From section 2.3.1, it is clear that the post-yield stress-strain characteristics of the involved materials and their interaction majorly contribute to the strain capacity. Of particular importance are the weld strength overmatch, the uniform elongation of the base metal, the strain hardening behaviour of base and weld metal and HAZ softening.

First, the crack driving force of a flaw is reduced as the degree of **weld strength overmatch** increases, since it shields the weld from the remotely applied strain. Shown as a representative example is figure 2.8 [2.35]. Similar trends have been reported in a large number of other studies.

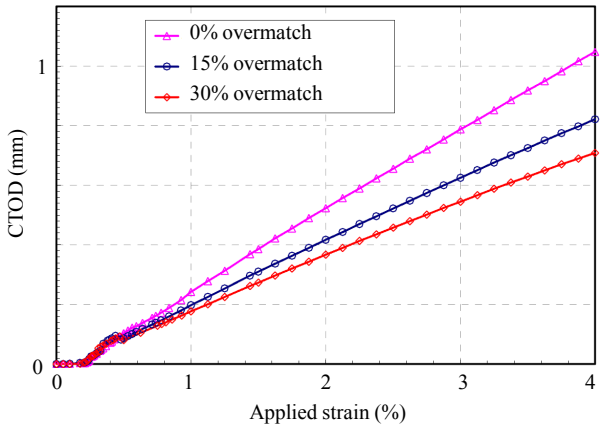

Figure 2.8: Crack driving force decreases as the degree of overmatch increases. In this figure, overmatch is defined according to Eq. (2.12). Taken from [2.35].

Notwithstanding the generally accepted importance of weld strength overmatch, there is no concensus on its definition for strain based assessments.

Extrapolated from a traditional stress based point of view, it is mostly defined on the basis of Eq. (2.12) [2.44]. Nevertheless, recent research [2.45–2.47] has indicated that a definition based upon ultimate tensile strength R_m (OM_{TS}) may be more relevant to strain capacity:

$$OM_{TS} = \frac{R_{m,weld} - R_{m,base}}{R_{m,base}} \cdot 100\% \tag{2.17}$$

Moreover, in an attempt to obtain an overmatch value that balances between OM_{YS} and OM_{TS}, it has also been proposed to base overmatch upon the average of yield and ultimate tensile strength ('flow stress' FS) in a definition similar to Eqs. (2.12) and (2.17) [2.48, 2.49]. This flow stress overmatch is denoted as OM_{FS}:

$$\begin{aligned} OM_{FS} &= \frac{FS_{weld} - FS_{base}}{FS_{base}} \cdot 100\% \\ &= \frac{(R_{p0.2,weld} + R_{m,weld}) - (R_{p0.2,base} + R_{m,base})}{R_{p0.2,base} + R_{m,base}} \cdot 100\% \end{aligned} \tag{2.18}$$

This definition was not explicitly investigated in the studies that advise OM_{TS} [2.45–2.47]. Hence, it may be that OM_{FS} is the most representative definition for strain based flaw assessment purposes.

Knowledge of the most appropriate weld strength overmatch definition is highly relevant, as the abovementioned definitions may provide fundamentally different values. For instance, a weld may be overmatching in yield strength but undermatching in ultimate tensile strength (figure 2.9) [2.50].

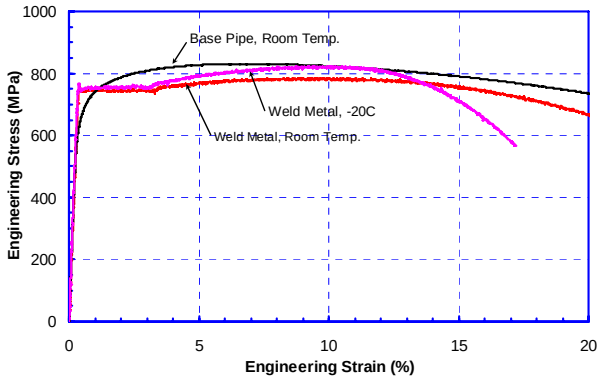

Figure 2.9: Illustration of a weld that overmatches the base metal's yield strength but undermatches its ultimate tensile strength [2.50].

A second important parameter is the **uniform elongation** e_m (figure 2.6) of the base metal. Indeed, if the weakest link of a girth weldment appears

to be one of the pipes rather than the weld (mostly in cases of high weld strength overmatch) strain capacity is delimited by necking in the pipe metal, the occurrence of which is characterized by e_m [2.51].

Third, the strain hardening behaviour of the involved materials has also received considerable attention (e.g. [2.35, 2.52]). A dimensionless parameter often reported to this respect is the **yield-to-tensile ratio** Y/T (ratio between yield and ultimate tensile strength [2]). Materials with a high Y/T-ratio have less reserve to sustain post-yield loads and, as a result, are sensitive to localized deformations. The exact influences of Y/T of both base and weld metal are challenging to separate from other, closely related aspects. For instance, OM_{YS} and OM_{TS} are related to each other through both Y/T-values as follows:

$$\frac{(Y/T)_{base}}{(Y/T)_{weld}} = \frac{OM_{TS} + 100\%}{OM_{YS} + 100\%} \tag{2.19}$$

Independent from these strength considerations, uniform elongation tends to decrease as Y/T increases (see chapter 3, section 3.6.1).

Apart from Y/T, the strain capacity of a girth weldment is also influenced by the exact **shape** of the materials' stress-strain curves. This is most easily illustrated on the basis of a heterogeneous weldment. For instance, a change in the shape of the weakest pipe's stress-strain curve in figure 2.7 could significantly change the difference between the strains at both sides of the girth weld and, as a consequence, the structural problem. For a homogeneous weldment, also, the base metal's stress-strain curve shape plays a role as it determines the load that is transferred to the girth weld given a remote strain.

Kibey et al. [2.53, 2.54] found that especially the base metals' strain hardening properties have a pronounced influence on strain capacity. In these studies, the role of weld metal stress-strain behaviour has been identified as mostly limited to ensuring sufficient weld strength overmatch levels.

Finally, **HAZ softening** has been found to localize strains if 45° shear bands can be formed across the weld cross section [2.55]. The formation of such bands is geometrically promoted as pipe wall thickness decreases and the width of the softened HAZ increases. In such cases, strain capacity reduces [2.35]. This reduction was found fairly independent of flaw size in [2.56].

2.3.2.2 Internal pressure

Recent research established that internal pressure has a significant detrimental effect on strain capacity [2.39, 2.57–2.60]. This reduction is caused by the induced hoop stress, which implies that a higher longitudinal stress is required

[2] Assuming $R_{p0.2}$ as a yield strength measure, Y/T is equal to $R_{p0.2}/R_m$.

to achieve the same degree of equivalent (Von Mises) stress in the pipe. As a consequence the required load and crack driving force increase for a fixed imposed applied deformation [2.35].

The amount of strain capacity reduction has not yet been fully quantified, due to a limited number of available data and the large number of possible influences. For instance, an important factor in the strain capacity reduction appears to be the combined effect of internal pressure and weld misalignment [2.61].

2.4 Experimental determination of deformation capacity

The large number of interacting factors that influence strain capacity (section 2.3.1) can be evaluated by means of experiments on a laboratory scale. Nevertheless, a range of possible integrity tests exists, all of which have specific advantages and limitations. This section provides a brief overview of tests related to the strain based assessment of girth weld flaws. A distinction is made between full scale testing (section 2.4.1), curved wide plate tension testing (section 2.4.2) and small scale testing (section 2.4.3).

2.4.1 Full scale pressurized pipe testing

Full scale pipe (FSP) testing aims to represent structural behaviour to a maximum degree of representativeness. Two full scale configurations are used for strain based flaw assessment, involving either four point bending or axial deformation. In both test configurations, surface notches are applied to simulate weld flaws. The notch tip is aimed to be located at either the weld metal center (WMC) or the coarse grained HAZ, both of which are most susceptible to actual weld flaws.

The advantage of the full scale pipe bend test over the full scale pipe tension test is that smaller loads are required to reach similar imposed strain levels. On the other hand, pipe tension tests have recently gained more attention as this configuration allows to simultaneously test multiple notches in a girth weld. Two notches are typically applied at opposite sides of the circumference [2.58, 2.60, 2.62]. Whereas tests with three notches per girth weld have also been reported [2.57], application of four or more notches per girth weld has been found to introduce unwanted interaction effects for results reported in [2.59].

For the specific case of full scale tension tests, typical instrumentation consists of at least the following:

- a single or double clip gauge that traverses the notch(es). Whereas a single clip gauge gives an indication of the crack mouth opening displacement

(CMOD), measurements of two clip gauges at different heights above the surface allow for the direct determination of CTOD through a triangulation of their measurements towards the crack tip [2.63];

- 'small' LVDTs or strain gauges remote from the girth weld, in order to measure the remotely applied ('remote') strain e_r. Given the possible heterogeneity between different pipes, remote strain sensors are installed at both sides of the girth weld;

- 'large' LVDTs that traverse the notched girth weld, in order to measure the global deformation of the weldment by means of an 'overall' strain e_o. This strain is compensated for the fact that the notch is traversed, by subtracting CMOD from the measured LVDT elongation ΔGL:

$$e_o = \frac{\Delta GL - \text{CMOD}}{GL_i} \tag{2.20}$$

  with GL_i the initial LVDT gauge length;

- a load cell which allows to quantify the remotely applied ('gross') stress s as tensile load divided by the unflawed initial cross section ($\pi\,(D_o - t)\,t$ for pipes).

Combining these measurements allows for the identification of different failure modes. For convenience with the remainder of the dissertation, the discussion of these failure modes is delayed to the following section (2.4.2) which deals with curved wide plate tension testing.

A significant advantage of FSP tests over other tests in general is their ability to apply an internal pressure. Drawbacks on the other hand are

- the high costs involved,

- the inability to characterize the mechanical properties in near vicinity of the girth weld by means of small scale testing (section 2.4.3), and,

- the high forces needed (especially for the tension configuration).

As a consequence of the third drawback, full scale pipe tests can only be performed at a limited number of laboratories with high load capacity test rigs such as C-FER Technologies (up to 15 MN load, figure 2.10) [2.60, 2.64, 2.65] and Stress Engineering Services (up to six million pound or roughly 26 MN load) [2.57, 2.66].

2.4.2 Curved wide plate tension testing

Given the large costs and extreme test rig specifications required for full scale testing, research laboratories have seeked for alternative large scale test methods that do not represent the full scale but provide a fair approximation.

Figure 2.10: 15 MN load frame of C-FER Technologies [2.65].

As a result, the curved wide plate tension test (further simply referred to as CWP test) was developed at Laboratory Soete, Ghent University in 1979 and has been first reported in 1986 [2.67]. Although originally intended for stress based assessments, the CWP test has evolved into a valuable tool to evaluate the strain capacity of flawed girth welds [2.68]. Ever since, Laboratory Soete undoubtedly has the largest experience in CWP testing, as several hundreds of tests have been performed there so far. This experience has led to the 'UGent [3] guidelines' for CWP testing [2.69] which provides advice for the entire test procedure.

A CWP test can be described as a tensile test on an unflattened sample of a pipe (figure 2.11(a)), containing a WMC flaw or HAZ flaw (mostly simulated by a surface notch). To apply the tensile load, the specimen is welded to two end blocks ('heads'), which requires end 'shoulders' to achieve a gradual transfer of load from the heads to the prismatic part of the specimen ('body'). Figure 2.11(b) shows an example CWP specimen.

The instrumentation for CWP testing is typically similar to that of full scale pipe tension testing. This allows for a major distinction between the following failure modes (apart from brittle fracture, which is not considered in this dissertation) [2.17]:

- local ('flaw ligament') collapse corresponding with a pop-through of the flaw, which would for an operating pipeline correspond with a leak and thus failure. A pop-through is mostly preceded by significant stable crack extension and is characterized by a sudden increase in CMOD.

[3] Abbreviation for 'Ghent University'.

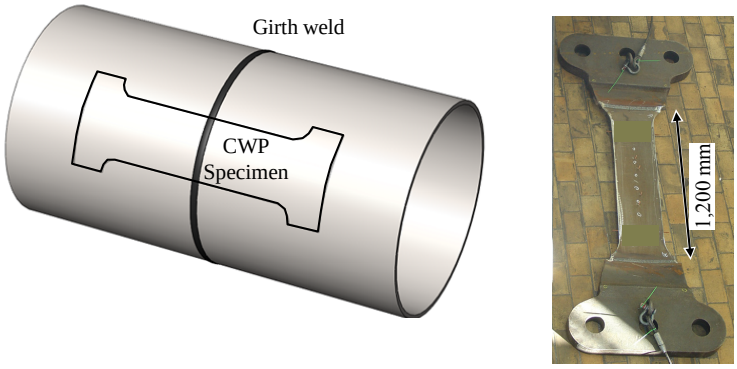

(a) (b)

Figure 2.11: (a) Sampling location of a CWP specimen, (b) Example CWP specimen (Laboratory Soete).

- global ('weld section') collapse, as deformations concentrate in the girth weld. This failure mode corresponds with a decreasing remote stress in combination with a strongly increasing CMOD.
- gross section collapse (GSC), as deformations localize in the base metal. This failure mode is identified by a decreasing remote stress in combination with a saturating CMOD.

Recall from figure 2.2 that flaw ligament collapse and weld section collapse are special cases of the broader term 'net section collapse' (NSC). The identification of failure mode from CMOD, overall strain and gross stress records is schematically summarized in figure 2.12.

The strain capacity of a CWP specimen is typically expressed as the overall strain e_o (averaged, if multiple LVDT measurements for e_o are performed) at the highest observed load (or, equivalently, gross stress) [2.38, 2.69, 2.70].

An issue related to the interpretation of CWP test results is the inability to apply an internal pressure, which has been found to strongly influence strain capacity (section 2.3.2.2). Therefore, a pressure correction factor is required to extrapolate the CWP strain capacity to pressurized pipes.

2.4.3 Small scale testing

The strain capacity of flawed girth welds is significantly influenced by aspects related to the global structure that are impossible to be properly represented in 'small' scale tests. Nevertheless, scale tests are necessary for the interpretation of large or full scale tests and/or the execution of analytical flaw assessments

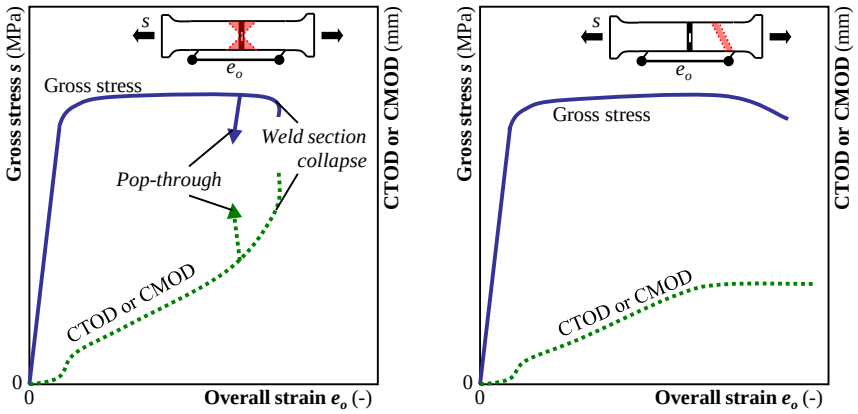

Figure 2.12: (a) Net section collapse and (b) gross section collapse.

(section 2.6). A list of the most common small scale tests is provided in table 2.1, along with their basic role. For more detailed aspects of small scale testing, the reader is referred to abundant specific literature.

2.5 Numerical determination of deformation capacity: finite element analysis

Experimental testing has the unmistakable advantage of providing information with respect to the actual investigated structural element. Nevertheless, experiments are prone to three limitations which have to be considered for the interpretation of their results.

- The results of an experiment are confined to the extent and possibilities of the applied instrumentation.
- The amount and nature of available test material limits the possibilities of performing parametric studies.
- Every experiment is prone to scatter, which may hamper its interpretation.

Finite element analysis is a complementary analysis technique with respect to experiments, as the abovementioned limitations are no longer present. Compared with experimental work, it is equally important to contribute to the better understanding of strain based weld flaw integrity.

Table 2.1: Small scale tests and their role in a strain based flaw assessment.

Test	Role
Tensile testing of base and weld metal	Qualification of materials and quantification of weld strength overmatch
Cross weld tensile testing	Qualification of weld strength relative to base metal strength
Weld macrography or micrography	Visual inspection of weld and flaw features (weld shape, microstructure, notch tip location)
Weld hardness testing	Identification of HAZ softening Estimation of ultimate tensile strength within weld [2.71]
Charpy testing	Qualitative measure of toughness
Fracture mechanics testing (SENB or SENT) ⋆	Establishment of fracture toughness or crack growth resistance curve

⋆ SENB: Single edge notched bend test, SENT: Single edge notched tension test.

Despite its specific advantages to experiments, one should bear in mind that a numerical simulation is no more than a calculation of which the result follows from a set of input assumptions (material characteristics, boundary conditions, ...). As a consequence, not all physical effects may be properly covered and the result may not be representative to reality. Therefore, an experimental validation of a finite element model is of paramount importance to the justification of its application (e.g. [2.39]).

2.6 Strain based flaw assessment procedures

The execution of large scale experiments is fairly expensive and time consuming. Therefore, attempts have been made to develop analytical procedures for the (conservative) estimation of strain capacity of pipes connected by flawed girth welds. A selection of different approaches is given below. Emphasis is put on their background and assumptions rather than their concrete form and no attempts are made to describe all particularities of each method.

Section 2.6.1 discusses the EPRG Tier 2 guidelines, which can be considered as a transition from stress based to strain based flaw assessment. Then, graphical

procedures derived from the FAD (originally intended for stress based design) are mentioned in section 2.6.2. Section 2.6.3 finally elaborates on closed-form equations specifically intended for estimating the strain capacity of flawed girth welds.

2.6.1 The EPRG Tier 2 guidelines as a boundary between stress based and strain based flaw assessment

In 1996, the European Pipeline Research Group (EPRG) published guidelines for the assessment of girth weld flaws in transmission pipelines [2.72]. The guidelines consist of multiple tiers, of which the second one has been based (and recently revised [2.73, 2.74]) upon Laboratory Soete's CWP testing database. The EPRG Tier 2 guidelines provide sufficient conditions for the achievement of remote yielding (remote strain in excess of 0.5 %) prior to girth weld failure. These sufficient conditions do not require a case-specific fracture mechanics analysis and can therefore be categorized as 'workmanship' criteria.

The EPRG Tier 2 guidelines are strain based since it is determined whether or not a strain level of 0.5 % can be achieved remote from the flawed section. The guidelines, however, do not allow for an exact estimation of strain capacity.

Of all requirements for the application of the revised Tier 2 EPRG guidelines (clearly summarized in [2.75]), relevant to this dissertation is that:

- the guidelines are restricted to linepipe steel grades X80 and below, given the additional challenges that arise for higher strength linepipe steels (see section 1.5.4) and the limited number of corresponding validation tests.

- the *actual* weld yield strength should at least evenmatch the *actual* base metal yield strength (in the pipe axis direction). Accepting line pipe steel heterogeneity (further discussed in chapter 3), this requirement has been translated to minimum specified properties by demanding that the minimum weld metal yield strength exceeds the base metal's minimum yield strength in the pipe axis direction by at least 100 MPa.

- Charpy impact energy should at least be 30 J and should be above 40 J on average. With this requirement, the EPRG guidelines provide a minimum (threshold) toughness criterion for the avoidance of brittle fracture up to yield. Recent research suggests that for plastically deformed pipelines with low weld strength overmatch, a more conservative required threshold toughness level of 60 J (minimum) / 80 J (average) is advised [2.49]. These guidelines are relevant to the basic assumption of ductile failure made for this dissertation (see section 1.4). Note that the Tier 2 EPRG guidelines, in contrast with other standards, do not require a lower limit for CTOD fracture toughness (CTOD_{mat}).

Under these – and other – requirements, the revised EPRG guidelines state that, for surface flaws with a depth a below 5 mm, base metal yielding can be reached if the flaw area does not exceed 7 % of the unflawed cross section area per 300 mm arc length. From this, simple guidance for the allowable flaw length $2c$ (per 300 mm arc length) has been derived as a function of wall thickness t [2.73] (table 2.2).

Table 2.2: EPRG guidelines for allowable flaw length to enable base metal yielding.

Flaw depth a (mm)	Allowable flaw length $2c$ (mm)
$a \leq 3$ mm	$2c \leq 7t$
3 mm $< a \leq 4$ mm	$2c \leq 5t$
4 mm $< a \leq 5$ mm	$2c \leq 3t$

Since the EPRG Tier 2 guidelines have an experimental basis, possible influences of actual material behaviour, welding residual stresses, ductile tearing and weld geometry are inherently accounted for.

2.6.2 Procedures derived from the failure assessment diagram

Although the failure assessment diagram (section 2.2.4) was originally intended for stress based flaw assessment purposes, modifications have been proposed to allow for estimations of strain capacity. Two concrete derived methods are discussed below.

2.6.2.1 DNV-RP-F108 procedure

The recommended practice DNV-RP-F108 ('Fracture control for pipeline installation methods introducing cyclic plastic strain', 2006) [2.76] provides a method for strain based flaw assessments, starting from a set of modifications to the stress based FAD level 3B from BS 7910 ('Guide on methods for assessing the acceptability of flaws in metallic structures', 2005) [2.28]. This FAD is material specific as it adopts the reference stress method (Eq. (2.16)), and incorporates ductile tearing. Further, concrete measures are provided for the incorporation of weld misalignment and residual stresses. The latter involves a correction of strain capacity based on a welding residual *strain* σ_0/E (e.g. around 0.25 % for steel with $\sigma_0 = 500$ MPa). This minor correction is supported by recent research from Tkaczyk [2.77].

DNV-RP-F108 mentions that, if internal pressure is present, the 'possible influence of the bi-axial stress state on the crack driving force must be considered

in the engineering critical assessment' [2.76]. However, explicit guidance in this respect is not given. This is probably related to its application being mostly aimed at offshore laying methods such as reeling, which do not involve internal pressure.

Further, the following remarks can be made with respect to other key factors for strain capacity:

- The application of DNV-RP-F108 requires a situation of weld strength overmatch. Nevertheless, it recommends to assume weld strength properties that match the base metal. As a result, a significant amount of conservativeness may be introduced.

- HAZ softening is not accounted for, probably since its (pronounced) occurrence is unlikely for the mainstream of offshore linepipe steels (see sections 1.5.2 and 1.5.4).

Finally it can be noted that, as explained in figure 1.23, using a stress based FAD as a starting point for a strain based flaw assessment may involve a substantial sensitivity to various input parameters. This is acknowledged in DNV-RP-F108.

2.6.2.2 Strain based failure assessment diagram

Starting from the reference stress FAD approach from R6 [2.31] (section 2.2.4) and making various simplifications, a strain based failure assessment diagram has been developed which plots the allowable $K_r = K_I/K_{mat}$ as a function of a new parameter D_r defined as $\epsilon_{ref}/\epsilon_0$ [2.78].

On the one hand, simplifications involved the assumption of a 'small' flaw, for which the reference strain (or stress) becomes approximately equal to the remote strain (or stress). As a consequence, the originally proposed strain based FAD tends to become unconservative as crack depth or length exceed certain limits, an effect which is more pronounced for low strain hardening materials [2.79] (such as higher strength line pipe steels, section 1.5.4). On the other hand, a limit $D_{r,max}$ is imposed which limits the applied strain to a level where the flow stress (as defined in section 2.3.2.1) is achieved. This limit may be overly conservative for cases where gross section collapse is reached.

Due to the generic character of the strain based FAD, explicit guidance on several aspects specifically related to girth welds (e.g. internal pressure, misalignment, anisotropy) remains vague or absent. This is a disadvantage compared to methods which have been specifically developed with a focus on the strain based assessment of pipeline girth weld flaws.

2.6.3 Strain capacity equations

Next to the methods described in section 2.6.2, closed-form strain capacity equations have been developed which do not require a graphical (i.e. FAD) approach.

2.6.3.1 CSA Z662 equation

The pipeline standard CSA Z662 (2007, Annex C) [2.80] mentions a parametric equation for strain capacity e_{max}, adopted from finite element analysis by Wang et al. [2.81]. This equation has the following structure:

$$e_{max} = f\left(\text{CTOD}_{mat}^{app}, Y/T_{base}, a/t, 2c/t\right) \tag{2.21}$$

with CTOD_{mat}^{app} the so-called 'apparent toughness'. This is a CTOD fracture toughness which represents the constraint level of the structure and which may indirectly involve effects of ductile tearing [2.82]. Validity limits are provided in table 2.3.

Table 2.3: Validity limits of the CSA strain capacity equation [2.81].

Characteristic	**Range**
Line pipe steel and weld metal properties	
Line pipe steel grade	X52 – X80
Yield-to-tensile ratio Y/T	$0.70 \leq Y/T \leq 0.95$
Uniform elongation e_m	not specified
Weld strength overmatch	at least 0 % *
Toughness	0.1 mm $\leq \text{CTOD}_{mat}^{app} \leq$ 1.0 mm
Pipe geometry properties	
Thickness t	6.35 mm $\leq t \leq$ 25.4 mm
Diameter D_o	$D_o/t \geq 32$
Weld geometry properties	
Misalignment h	not specified
Flaw geometry properties	
Flaw depth a	$a/t \leq 0.5$
Flaw length $2c$	$1 \leq 2c/t \leq 10$
Operational conditions	
Internal pressure p	not specified

* Overmatch definition (OM_{YS}, OM_{TS}, OM_{FS}) not specified.

From Eq. (2.21) and the assumptions for the numerical simulations on which it is based (reported in [2.33]), a number of unmistakable limitations can be put forward.

- The weld has been considered as having the same strength properties of the base metals, which are also assumed homogeneous. Hence, weld strength overmatch and base metal heterogeneity have not been incorporated, and the possibility of HAZ softening is neglected. Also, stress-strain behaviour has been approximated by a power law (similar to Eq. (2.6)), which does not necessarily provide a proper representation of actual material properties. Further, anisotropy has not been considered.
- The effect of internal pressure is not taken into account.
- Local geometrical effects near the weld flaw such as misalignment have not been investigated.
- Weld residual stresses have not been considered.

Since most of these limitations involve key factors addressed in section 2.3.2, a generic application of the CSA Z662 equation may be considered as highly doubtful. This is reflected in comparisons with experimental CWP data (e.g. figure 2.13 [2.81]). It can be seen that Eq. (2.21) predicts a strain capacity above 1 % for merely 4 out of 21 validations, the maximum value being lower than 1.5 %. Most likely, this follows from neglecting the beneficial effect of weld strength overmatch (figure 2.8). As a logical consequence, the strain capacity prediction of Eq. (2.21) is overly conservative for a large fraction of the depicted specimens.

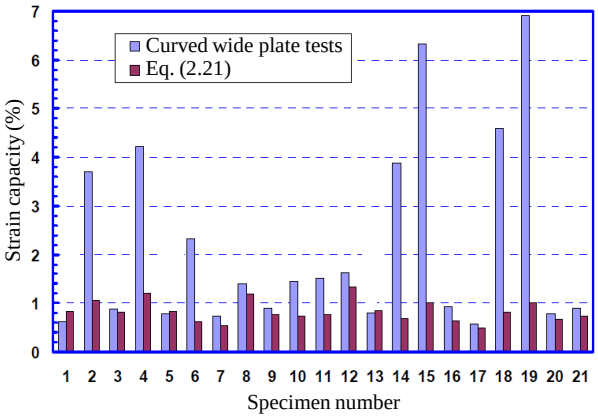

Figure 2.13: A comparison of Eq. (2.21) with CWP test results reveals significant differences with experimentally obtained strain capacities. Taken from [2.81].

Note that similar objections can be made for other attempts made to derive a strain capacity equation. For instance, an alternative equation presented

in [2.83] for welds with a yield strength overmatch of 20 % conforms with the structure of Eq. (2.21).

2.6.3.2 SINTEF procedure

During the previous decade, the Norwegian research group SINTEF developed an analytical strain based flaw assessment procedure intended for offshore pipelines. This procedure adopts the elastic plastic fracture parameter CTOD and has been fine-tuned on the basis of parametric finite element analyses. Validity limits are given in table 2.4.

Table 2.4: Validity limits of the SINTEF procedure for strain capacity prediction [2.84].

Characteristic	**Range**
Line pipe steel and weld metal properties	
Line pipe steel grade	not specified
Yield-to-tensile ratio Y/T	$0.82 \leq Y/T \leq 0.93$
Uniform elongation e_m	not specified
Weld strength overmatch	not specified
Toughness	not specified
Pipe geometry properties	
Thickness t	15 mm $\leq t \leq$ 35 mm
Diameter D_o	$20 \leq D_o/t \leq 40$
Weld geometry properties	
Misalignment h	$h \leq 0.15t$
Flaw geometry properties	
Flaw depth a	$a/t \leq 0.35$
Flaw length $2c$	$2c \leq$ 300 mm
Operational conditions	
Internal pressure p *	$\sigma_{\theta\theta}$/SMYS $\leq$ 80 %

* Related to $\sigma_{\theta\theta}$ through Eq. (1.1).

Originally assuming fixed flaw sizes [2.84], two methods to involve ductile tearing and estimate unstable crack extension (among which the tangency approach, section 2.2.5) have been reported in [2.37]. An integrated procedure has been provided in [2.85], along with experimental validations based on curved wide plate tests and full scale pressurized pipe bend tests (e.g. figure 2.14).

The SINTEF procedure can account for a wide range of effects, most notably: strain hardening (Y/T), weld yield strength mismatch (OM_{YS}), internal pressure, misalignment, wall thickness variations. In contrast, the following limitations can be noted.

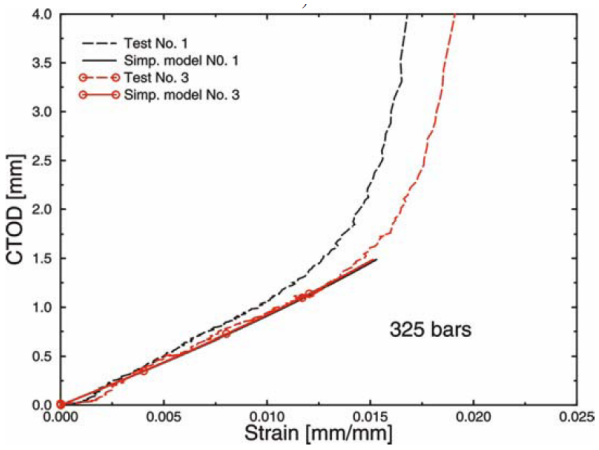

Figure 2.14: A successful validation of the SINTEF procedure, based on full scale pressurized pipe bend tests [2.85].

- Strain hardening of base and weld metals was assumed identical and isotropical, and the base metals were assumed homogeneous for the finite element simulations. Consequently, effects of pipe-to-pipe heterogeneity, anisotropy and situations where $Y/T_{base} \neq Y/T_{weld}$ have not been explicitly investigated. Also, strain hardening followed a power law relation, thereby assuming a predefined and continuously yielding stress-strain curve. The need for further work to the latter respect (i.e. the treatment of steels with a Lüders plateau) was recognized in [2.85].

- Residual stresses have not been considered. It should be noted that a pragmatic solution to this respect has been pointed out in [2.77].

2.6.3.3 ExxonMobil procedure

During the last five years, ExxonMobil has put remarkable resources in obtaining an improved understanding of girth weld integrity under plastic deformation. This has led to the development of a multi-tiered procedure for the estimation of strain capacity [2.86], based on finite element analyses discussed in [2.54].

The procedure has three levels with increasing complexity (denoted 'L1' to 'L3'). L3 corresponds with a detailed case-specific finite element analysis involving ductile tearing (by means of a constraint representative CTOD-R curve) and the tangency criterion for unstable crack extension (section 2.2.5). L3 finite element analyses performed by ExxonMobil have been successfully validated by means of full scale pressurized pipe tension tests (figure 2.15). To this respect,

actual geometry and mean material properties from small scale testing were input into the finite element models.

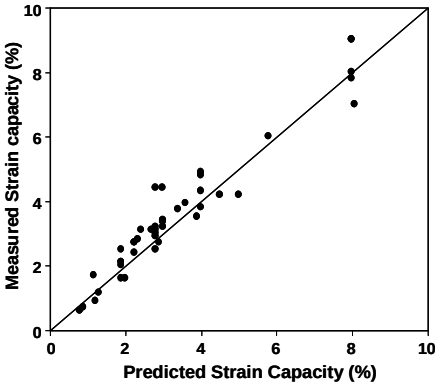

Figure 2.15: Validation of the L3 ExxonMobil procedure [2.86].

It was recognized that detailed finite element analysis is too cumbersome for routine assessments. This led to the development of L1 and L2 procedures with simplified equations (L1 requiring less input data but being more conservative), based on an extensive parametric study using the finite element model validated for L3. Prior to developing the equations, sensitivity studies were performed to identify the key influence parameters with respect to strain capacity [2.53]. As a result, a conservative L2 equation of the following structure was proposed, assuming an internal pressure equivalent which introduces a hoop stress of 80 % SMYS (see Eq. (1.1)):

$$e_{max} = f\,(\text{steel grade}, a, 2c, t, OM_{TS}, e_m, h, \text{CTOD-R curve}) \tag{2.22}$$

where h represents the possible weld misalignment. Note that weld strength overmatch is quantified on the basis of ultimate tensile strength (OM_{TS}). Table 2.5 summarizes the validity limits of the L2 equation.

From the L2 equation, a simplified L1 equation has been developed by making a set of additional conservative assumptions regarding weld misalignment, ductile tearing resistance, base metal uniform elongation.

Eq. (2.22) covers most key influence factors to strain capacity. Nevertheless, some restrictions apply for the L1 and L2 equations.

- Pipe-to-pipe heterogeneity and anisotropy have not been incorporated in the finite element analyses performed for development of the L1 and L2 equations.

Table 2.5: Validity limits of the L2 ExxonMobil procedure for strain capacity prediction [2.86].

Characteristic	Range
Line pipe steel and weld metal properties	
Line pipe steel grade	X60 – X80
Yield-to-tensile ratio Y/T	$Y/T \leq 0.90$
Uniform elongation e_m *	$0.060 \leq e_m \leq 0.120$ (X60, X70) $0.044 \leq e_m \leq 0.08$ (X80)
Weld strength overmatch	$5\% \leq OM_{TS} \leq 50$ % (X60, X70) $5\% \leq OM_{TS} \leq 20$ % (X80)
Tearing resistance	CTOD-R curve: CTOD $\geq 0.9(\Delta a)^{0.5}$
Pipe geometry properties	
Thickness t	14.3 mm $\leq t \leq$ 26.0 mm
Diameter D_o	not specified
Weld geometry properties	
Misalignment h	$h \leq 3$ mm
Flaw geometry properties	
Flaw depth a	2 mm $\leq a \leq$ 5 mm
Flaw length $2c$	20 mm $\leq 2c \leq$ 50 mm
Operational conditions	
Internal pressure p †	$\sigma_{\theta\theta}$/SMYS ≤ 80 %

* Requirement for base metal only.

† Related to $\sigma_{\theta\theta}$ through Eq. (1.1).

- A strength grade specific fixed level of HAZ softening was assumed. Moreover, equations are only provided for linepipe steel grades X60 to X80, thereby particularly excluding X100.
- The L1 and L2 equations have been developed for one specific internal pressure level (corresponding with a hoop stress of 80 % SMYS). Application of these equations for other pressure levels may be less representative. In particular, the detrimental effect of internal pressure has been observed to be most severe for hoop stress levels around 50 to 60 % SMYS rather than 80 % SMYS [2.35, 2.84].
- The L2 equation requires the selection of one of three pre-defined CTOD-R curves (of which the most conservative is adopted for the L1 equation). As a consequence, strain capacity prediction may become overly conservative in the presence of materials with a tearing resistance higher than modelled by the pre-defined CTOD-R curves.
- Case studies revealed that the L1 equation is highly restrictive due to the

severe assumption of a weld misalignment of 3 mm [2.49].

- Weld residual stresses have not been considered.

2.6.3.4 UGent equation

In 2006, Denys and Lefevre [2.87] presented a closed-form equation for the estimation of strain capacity. This equation was later modified to the following expression [2.49]:

$$e_{max} = P_c \left[\frac{Y/T_{base} + 1}{1 - Y/T_{base}} \cdot \frac{0.5 - C_m e_m M_{FS}}{C_d} \cdot \gamma + C_m e_m M_{FS} \right] \tag{2.23}$$

The expression between square brackets has been derived as a lower bound strain capacity based on 480 CWP tests performed at Laboratory Soete. Given the uniaxial character of CWP testing, a pressure correction factor P_c (< 1) has been introduced. Further, $\gamma = 2ca/2Wt$ represents the ratio of flaw area to the area of the unflawed cross section of the CWP specimen (with width $2W$), C_m is a correction factor for weld strength overmatch variability, C_d is a correction factor that takes account of a decreasing weld strength mismatch effect with increasing flaw size, and M_{FS} is a dimensionless factor directly related to weld flow stress overmatch OM_{FS}:

$$M_{FS} = \frac{FS_{weld}}{FS_{base}} = 1 + \frac{OM_{FS}}{100\%} \tag{2.24}$$

Table 2.6 summarizes the validity limits of Eq. (2.23).

Given its experimental background, Eq. (2.23) implicitly accounts for effects of weld strength overmatch, strain hardening and stress-strain curve shapes, heterogeneity, anisotropy, ductile tearing, weld residual stress, weld misalignment, and HAZ softening. As some of these effects may be change under internal pressure, a proper pressure correction factor should account for possible coupled effects. This is part of ongoing work [2.49, 2.88].

Referring back to the discussion on definition of weld strength mismatch (section 2.3.2), it can be noted that Eq. (2.23) predicts a linear relation between strain capacity and weld flow stress overmatch OM_{FS}.

Table 2.6: Validity limits of the UGent strain capacity equation [2.49].

Characteristic	Range
Line pipe steel and weld metal properties	
Line pipe steel grade	up to X80
Yield-to-tensile ratio Y/T	$Y/T \leq 0.90$
Uniform elongation e_m	not specified
Weld strength overmatch	$OM_{FS} \geq 0$ %
Charpy impact energy	$\geq$ (60 J (minimum), 80 J (average))
Pipe geometry properties	
Thickness t	$t \leq 30$ mm
Diameter D_o	not specified
Weld geometry properties	
Misalignment h	not specified
Flaw geometry properties	
Flaw depth a	$a/t \leq 0.3$
Flaw length $2c$	not specified
Operational conditions	
Internal pressure p	not specified *

* Requires knowledge of a representative pressure correction P_c.

2.7 Summary and conclusions

This chapter has shown that, whereas the field of *stress based* flaw assessment is fairly developed and has converged to a concensus upon key factors and analysis methods, some major issues regarding flaw assessment under *strain based* conditions remain unresolved. These issues are mostly related to the strength properties of all involved materials (base metals, weld metal and possibly the heat-affected zones) and the influence of internal pressure.

Given the large number of key influence factors in a strain based flaw assessment and the limited knowledge regarding the exact effects of most of them, a complete coverage of all influences is beyond the scope of this work. Therefore, this dissertation is narrowed to a manageable number of selected issues.

Focus is put on cases of a remotely applied longitudinal strain. The main aim is to provide fundamental insights into a uniaxial mechanical problem that can facilitate a better understanding of the more realistic case of biaxially loaded pipes due to combined tension – internal pressure. Additionally, emphasis is put on influences of the mechanical properties of base metal and weld strength overmatch which have so far been addressed to a limited extent.

Section 2.6 has indicated that there is no procedure yet which fully covers all discussed aspects of strain based flaw assessment. Acknowledging this absence, experimental (section 2.4) and numerical (section 2.5) studies have been and are expected to remain an essential component of the development of project specific guidelines for strain based flaw assessment. This dissertation investigates the tools that have to be used for both approaches.

- *As for the experimental investigation of girth weld integrity, attention is given to CWP testing. Indeed, CWP panels are cheaper and easier to test than full scale specimens, and the absence of internal pressure is of no concern for this work given the uniaxial nature of the considered problem.*
- *As for the numerical examination of girth weld integrity, the proper creation and analysis of representative finite element models is investigated. Particular attention goes to the validation of numerical results, aiming to answer the following question: 'To what extent can finite element modelling serve as a tool for quantitative strain capacity estimation?'.*

These aspects are discussed in the following chapters, in accordance with the structure provided in section 1.7.

Bibliography

[2.1] T.L. Anderson. *Fracture mechanics - fundamentals and applications*. CRC Press LLC, 2nd edition, 1995. 683 pages. ISBN 978-0-8493-4260-8.

[2.2] A.A. Griffith. The phenomena of rupture and flow in solids. *Philosophical Transactions, Series A*, 221:163–198, 1920.

[2.3] G.R. Irwin. Onset of fast crack propagation in high strength steel and aluminum alloys. *Sagamore Research Conference Proceedings*, 2:289–305, 1956.

[2.4] H.M. Westergaard. Bearing pressures and cracks. *Journal of Applied Mechanics*, 6:49–53, 1939.

[2.5] G. Irwin. Analysis of stresses and strains near the end of a crack traversing a plate. *Journal of Applied Mechanics*, 24(3):361–364, 1957.

[2.6] J.R. Rice. A path independent integral and the approximate analysis of strain concentration by notches and cracks. *Journal of Applied Mechanics*, 35:379–386, 1968.

[2.7] J.W. Hutchinson. Singular behaviour at the end of a tensile crack in a hardening material. *Journal of the Mechanics and Physics of Solids*, 16(1):13–31, 1968.

[2.8] J.R. Rice and G.F. Rosengren. Plane strain deformation near a crack tip in a power-law hardening material. *Journal of the Mechanics and Physics of Solids*, 16(1):1–12, 1968.

[2.9] D.S. Dugdale. Yielding of steel sheets containing slits. *Journal of the Mechanics and Physics of Solids*, 8(2):100–108, 1960.

[2.10] G.I. Barenblatt. The mathematical theory of equilibrium of cracks in brittle fracture. *Advances in Applied Mechanics*, 7:55–129, 1962.

[2.11] C.F. Shih. Relationships between the J-integral and the crack opening displacement for stationary and extending cracks. *Journal of the Mechanics and Physics of Solids*, 29(4):305–326, 1981.

[2.12] V. Kumar, M.D. German, and C.F. Shih. An engineering approach for elastic-plastic fracture analysis. Technical Report NP-1931, Electric Power Research Institute (EPRI), Schenectady, New York, USA, 1981.

[2.13] G. Yagawa, Y. Kitajima, and H. Ueda. 3-Dimensional fully plastic solutions for semielliptic surface cracks. *International Journal of Pressure Vessels and Piping*, 53(3):457–510, 1993.

[2.14] R.C. McClung, G.G. Chell, Y.-D. Lee, D.A. Russell, and G.E. Orient. Development of a practical methodology for elastic-plastic and fully plastic fatigue crack growth. Technical report, National Aeronautics and Space Administration, 1999. NASA/CR-1999-209428. 112 pages.

[2.15] Y. Lei. J-integral and limit load analysis of semi-elliptical surface cracks in plates under tension. *International Journal of Pressure Vessels and Piping*, 81(1):21–30, 2004.

[2.16] X. Wang. Fully plastic J-integral solutions for surface cracked plates under biaxial loading. *Engineering Fracture Mechanics*, 73(11):1581–1595, 2006.

[2.17] R. Denys and A. Lefevre. Failure characterisation of a girth weld with surface-breaking flaw under tensile load. In R. Denys, editor, *Proceedings of the 5th International Conference on Pipeline Technology*, Ostend, Belgium, 2009.

[2.18] A.G. Miller. Review of limit loads of structures containing defects. *International Journal of Pressure Vessels and Piping*, 32(1-4):197–327, 1988.

[2.19] Y. Lei. Use of local and global limit load solutions for plates with surface cracks under tension. *International Journal of Pressure Vessels and Piping*, 84(9):545–559, 2007.

[2.20] S. Hertelé, W. De Waele, and R. Denys. Development of an analytical reference stress equation for inner-diameter defected curved plates in tension. *International Journal of Pressure Vessels and Piping*, 88(5-7):256–261, 2011.

[2.21] U. Zerbst, R.A. Ainsworth, and K.H. Schwalbe. Basic principles of analytical flaw assessment methods. *International Journal of Pressure Vessels and Piping*, 77(14-15):855–867, 2000.

[2.22] Y.J. Kim and K.H. Schwalbe. Mismatch effect on plastic yield loads in idealised weldments I. Weld centre cracks. *Engineering Fracture Mechanics*, 68(2):163–182, 2001.

[2.23] R.A. Ainsworth. The assessment of defects in structures of strain hardening material. *Engineering Fracture Mechanics*, 19(4):633–642, 1984.

[2.24] A.G. Miller and R.A. Ainsworth. Consistency of numerical results for power-law hardening materials and the accuracy of the reference stress approximation for J. *Engineering Fracture Mechanics*, 32(2):233–247, 1989.

[2.25] Y.J. Kim and D.J. Shim. Relevance of plastic limit loads to reference stress approach for surface cracked cylinder problems. *International Journal of Pressure Vessels and Piping*, 82(9):687–699, 2005.

[2.26] M. Kamaya and H. Machida. Reference stress method for evaluation of failure assessment curve of cracked pipes in nuclear power plants. *International Journal of Pressure Vessels and Piping*, 87(1):66–73, 2010.

[2.27] Y.J. Kim. Reference stress solutions in lifing assessment of piping and plates. In *Structural Integrity and Component Life Assessment – Post Experience Course*, Imperial College, London, UK, May 12-14, 2010.

[2.28] *Guide on methods for assessing the acceptability of flaws in metallic structures, BS 7910.* British Standards Institution, London, UK, 2005.

[2.29] *Fitness for Service, API RP 579, 2nd edition.* American Petroleum Institute, Washington, USA, 2000.

[2.30] M. Koçak, S. Webster, J.J. Janosch, R.A. Ainsworth, and R. Koers, editors. *Fitness for service procedure, FITNET , MK8, vol. I: procedure.* GKSS Research Centre, ISBN 978-3-940923-00-4, 2008.

[2.31] *Assessment of the integrity of structures containing defects, R6-Revision 3.* British Energy Generation Ltd, 1999.

[2.32] N. Nourpanah and F. Taheri. Ductile crack growth and constraint in pipelines subject to combined loadings. *Engineering Fracture Mechanics*, 78(12):2010–2028, 2011.

[2.33] Y.Y. Wang, W. Cheng, M. McLamb, D. Horsley, J. Zhou, and A.G. Glover. Tensile strain limits of girth welds with surface-breaking defects - Part 1: An analytical framework. In R. Denys, editor, *Proceedings of the 4th International Conference on Pipeline Technology*, pages 235–249, Ostend, Belgium, 2004.

[2.34] *Specification for Line Pipe, API 5L, 44th edition.* American Petroleum Institute, Washington, USA, 2007.

[2.35] J.R. Gordon, N. Zettlemoyer, and W.C. Mohr. Crack driving force in pipelines subjected to large strain and biaxial stress conditions. In *Proceedings of the 17th International Offshore and Polar Engineering Conference (ISOPE)*, pages 3129–3140, Lisbon, Portugal, 2007.

[2.36] Y.Y. Wang and M. Liu. The role of anisotropy, toughness transferability, and weld misalignment in the strain based design of pipelines. In *Proceedings of the 17th International Offshore and Polar Engineering Conference (ISOPE)*, pages 3164–3171, Lisbon, Portugal, 2007.

[2.37] E. Østby, C. Thaulow, and B. Nyhus. A new approach to ductile tearing assessment of pipelines under large-scale yielding. *International Journal of Pressure Vessels and Piping*, 84(6):337–348, 2007.

[2.38] D.P. Fairchild, W. Cheng, S.J. Ford, K. Minnaar, N.E. Biery, A. Kumar, and N.E. Nissley. Recent advances in curved wide plate testing and implications for strain-based design. *International Journal of Offshore and Polar Engineering*, 18(3):161–170, 2008.

[2.39] E. Berg, E. Østby, C. Thaulow, and B. Skallerud. Ultimate fracture capacity of pressurized pipes with defects - Comparisons of large scale testing and numerical simulations. *Engineering Fracture Mechanics*, 75(8):2352–2366, 2008.

[2.40] R.M. Denys, A.A. Lefevre, P. De Baets, and J. Degrieck. Effects of stable ductile crack growth on plastic collapse defect assessments. In R.M. Denys, editor, *Proceedings of the 3rd International Conference on Pipeline Technology*, pages 169–189, Bruges, Belgium, 2000.

[2.41] K.R. Jayadevan, E. Østby, and C. Thaulow. Fracture response of pipelines subjected to large plastic deformation under tension. *International Journal of Pressure Vessels and Piping*, 81(9):771–783, 2004.

[2.42] Y. Lei. J-integral evaluation for cases involving non-proportional stressing. *Engineering Fracture Mechanics*, 72(4):577–596, 2005.

[2.43] X.B. Ren, Z.L. Zhang, and B. Nyhus. Effect of residual stresses on ductile crack growth resistance. *Engineering Fracture Mechanics*, 77(8):1325–1337, 2010.

[2.44] Y.Y. Wang, M. Liu, J. Gianetto, and B. Tyson. Considerations of linepipe and girth weld tensile properties for strain-based design of pipelines. In *Proceedings of the 8th International Pipeline Conference (IPC)*, Calgary, Alberta, Canada, 2010. IPC2010-31376.

[2.45] H. Motohashi and N. Hagiwara. Analytical study of effects of strength matching on strain capacity. In *Proceedings of the 17th International Offshore and Polar Engineering Conference (ISOPE)*, pages 3101–3106, Lisbon, Portugal, 2007.

[2.46] M.L. Macia, S. Kibey, H. Arslan, F. Bardi, S.J. Ford, W.C. Kan, M.F. Cook, and B. Newbury. Approaches to qualify strain-based designed pipelines. In *Proceedings of the 8th International Pipeline Conference (IPC)*, Calgary, Alberta, Canada, 2010. IPC2010-31662.

[2.47] S. Hertelé, W. De Waele, R. Denys, and M. Verstraete. Sensitivity of plastic response of defective pipeline girth welds to the stress-strain behavior of base and weld metal. In *Proceedings of the 30th International Conference on Ocean, Offshore and Arctic Engineering (OMAE)*, Rotterdam, The Netherlands, 2011. OMAE2011-49239.

[2.48] R. Denys, W. De Waele, A. Lefevre, and P. De Baets. An engineering approach to the prediction of the tolerable defect size for strain-based design. In *Proceedings of the 4th International Conference on Pipeline Technology*, pages 163–181, Ostend, Belgium, 2004.

[2.49] R. Denys, S. Hertelé, M. Verstraete, and W. De Waele. Strain capacity prediction for strain-based pipeline designs. In *Proceedings of the Internal Workshop on Welding of High Strength Pipeline Steels*, Araxá, Brazil, 2011. CBMM.

[2.50] D.M. Duan, Y.Y. Wang, Y. Chen, and J. Zhou. Modeling and CMOD mapping of surface-cracked wide plates. In *Proceedings of the 7th International Pipeline Conference (IPC)*, Calgary, Alberta, Canada, 2008. IPC2008-64425.

[2.51] R. Denys, S. Hertelé, W. De Waele, and A. Lefevre. Estimate of Y/T ratio and uniform elongation capacity of pipeline steels from yield strength. In R. Denys, editor, *Proceedings of the 5th International Conference on Pipeline Technology*, Ostend, Belgium, 2009.

[2.52] S. Igi and N. Suzuki. Tensile strain limits of X80 high-strain pipelines. In *Proceedings of the 17th International Offshore and Polar Engineering Conference (ISOPE)*, pages 3081–3087, Lisbon, Portugal, 2007.

[2.53] S.A. Kibey, J.A. Issa, X. Wang, and K. Minnaar. A simplified, parametric equation for prediction of tensile strain capacity of welded pipelines. In *Proceedings of the 5th International Conference on Pipeline Technology*, Ostend, Belgium, 2009.

[2.54] S. Kibey, X. Wang, K. Minnaar, M.L. Macia, D.P. Fairchild, W.C. Kan, S.J. Ford, and B. Newbury. Tensile strain capacity equations for strain-based design of welded pipelines. In *Proceedings of the 8th International Pipeline Conference (IPC)*, Calgary, Alberta, Canada, 2010. IPC2010-31661.

[2.55] W. Mohr. Strain-based design: strain concentration at girth welds. Technical Report 47447GTH, Edison Welding Institute, 2007. 190 pages.

[2.56] M. Liu, Y.Y. Wang, and D. Horsley. Significance of HAZ softening on strain concentration and crack driving force in pipeline girth welds. In *Proceedings of the 24th International Conference on Offshore Mechanics and Arctic Engineering (OMAE)*, Halkidiki, Greece, 2005. OMAE2005-67039.

[2.57] P.C. Gioielli, K. Minnaar, M.L. Macia, and W.C. Kan. Large-scale testing methodology to measure the influence of pressure on tensile strain capacity of a pipeline. In *Proceedings of the 17th International Offshore*

and Polar Engineering Conference (ISOPE), pages 3023–3027, Lisbon, Portugal, 2007.

[2.58] P.C. Gioielli, W. Cheng, K. Minnaar, and D.P. Fairchild. Characterization of the stable tearing during pipeline strain capacity tests. In *Proceedings of the 18h International Offshore and Polar Engineering Conference (ISOPE)*, pages 86–89, Vancouver, Canada, 2008.

[2.59] Y.Y. Wang, M. Stephens, and D. Horsley. Preliminary analysis of tensile strain capacity of full scale pipe test with internal pressure. In *Proceedings of the 18th International Offshore and Polar Engineering Conference (ISOPE)*, pages 40–47, Vancouver, Canada, 2008.

[2.60] M. Stephens, R. Petersen, Y.Y. Wang, R. Gordon, and D. Horsley. Large scale experimental data for improved strain-based design models. In *Proceedings of the 8th International Pipeline Conference (IPC)*, Calgary, Alberta, Canada, 2010. IPC2010-31396.

[2.61] S.A. Kibey, K. Minnaar, J.A. Issa, and P.C. Gioielli. Effect of misalignment on the tensile strain capacity of welded pipelines. In *Proceedings of the 18th International Offshore and Polar Engineering Conference (ISOPE)*, pages 90–95, Vancouver, Canada, 2008.

[2.62] S. Igi, T. Sakimoto, N. Suzuki, R. Muraoka, and T. Arakawa. Tensile strain capacity of X80 under tensile loading with internal pressure. In *Proceedings of the 8th International Pipeline Conference (IPC)*, Calgary, Alberta, Canada, 2010. IPC2010-31281.

[2.63] W. Cheng, H. Tang, P.C. Gioielli, K. Minnaar, and M.L. Macia. Test methods for characterization of strain capacity: comparison of R-curves from SENT/CWP/FS tests. In R. Denys, editor, *Proceedings of the 5th International Conference on Pipeline Technology*, Ostend, Belgium, 2009.

[2.64] W.C. Kan, M. Weir, M.M. Zhang, D.B. Lillig, S.T. Barbas, M.L. Macia, and N.E. Biery. Strain-based pipelines: design consideration overview. In *Proceedings of the 18th International Offshore and Polar Engineering Conference (ISOPE)*, pages 174–181, Vancouver, Canada, 2008.

[2.65] http://www.cfertech.com/tubular-testing-system. Accessed: January 5, 2012.

[2.66] http://www.stress.com/servicetier3.php?sid=11&pid=184. Accessed: January 5, 2012.

[2.67] B. Lian, R. Denys, and L. Van De Walle. An assessment on the effect of weld metal yield strength overmatching in pipeline girth welds. In *Proceedings of the 3rd Conference on Welding and Performance of Pipelines*, TWI, London, UK, 1986. Paper P43.

[2.68] R. Denys, A. Lefevre, and P. De Baets. A rational approach to weld and pipe material requirements for a strain based pipeline design. In *Proceedings of the International Conference on Application and Evaluation of High-Grade Linepipes in Hostile Environments*, pages 121–158, Pacifico Yokohama, Japan, 2002.

[2.69] R. Denys and A. Lefevre. UGent guidelines for curved wide plate testing. In R. Denys, editor, *Proceedings of the 5th International Conference on Pipeline Technology*, Ostend, Belgium, 2009.

[2.70] N. Yoosef-Ghodsi, D.M. Duan, Q. Chen, R. Petersen, and C. Fan. Finite element analysis of flaw growth history. In *Proceedings of the 8th International Pipeline Conference (IPC)*, Calgary, Alberta, Canada, 2010. IPC2010-31418.

[2.71] *Metallic materials – Conversion of hardness values, ISO 18265.* International Organization for Standardization, Geneva, Switzerland, 2003.

[2.72] G. Knauf and P. Hopkins. The EPRG guidelines on the assessment of defects in transmission pipeline girth welds. *3R International*, 35(10-11):620–624, 1996.

[2.73] R.M. Denys, R. Andrews, M. Zarea, and G. Knauf. Recommended revisions of the EPRG Tier 2 guidelines for the assessment of defects in transmission pipeline girth welds. In R. Denys, editor, *Proceedings of the 5th International Conference on Pipeline Technology*, Ostend, Belgium, 2009.

[2.74] R. Denys, R. Andrews, M. Zarea, and G. Knauf. EPRG Tier 2 guidelines for the assessment of defects in transmission pipeline girth welds. In *Proceedings of the 8th International Pipeline Conference (IPC)*, Calgary, Alberta, Canada, 2010. IPC2010-31640.

[2.75] R.M. Denys and W. De Waele. Comparison of API 1104-Appendix A Option 1 and EPRG-Tier 2 defect acceptance limits. In R. Denys, editor, *Proceedings of the 5th International Conference on Pipeline Technology*, Ostend, Belgium, 2009.

[2.76] *Fracture control for pipeline installation methods introducing cyclic plastic strain, DNV-RP-F108.* Det Norske Veritas, Høvik, Norway, 2006.

[2.77] T. Tkaczyk. *Development of fracture mechanics based criteria for failure of reeled pipes.* PhD thesis, University of London - Imperial College of Science, Technology and Medicine - Department of Mechanical Engineering, 2010.

[2.78] P.J. Budden. Failure assessment diagram methods for strain-based fracture. *Engineering Fracture Mechanics*, 73(5):537–552, 2006.

[2.79] P.J. Budden and M.C. Smith. Numerical validation of a strain-based failure assessment diagram approach to fracture. In *Proceedings of the ASME 2009 Pressure Vessels and Piping Division Conference (PVP)*, 2009. PVP2009-77377.

[2.80] *Oil & gas pipeline systems, CSA Z662*. Canadian Standards Association, Ontario, Canada, 2007.

[2.81] Y.Y. Wang, M. Liu, D. Horsley, and J. Zhou. A quantitative approach to tensile strain capacity of pipelines. In *Proceedings of the 6th International Pipeline Conference (IPC)*, Calgary, Alberta, Canada, 2006. IPC2006-10474.

[2.82] Y.Y. Wang, M. Liu, and D. Horsley. Apparent fracture toughness from constraint considerations and direct testing. In *Proceedings of the 17th International Offshore and Polar Engineering Conference (ISOPE)*, pages 3179–3185, Lisbon, Portugal, 2007.

[2.83] B. Liu, X.J. Liu, and H. Zhang. Tensile strain capacity of pipelines for strain-based design. In *Proceedings of the 7th International Pipeline Conference (IPC)*, Calgary, Alberta, Canada, 2008. IPC2008-64031.

[2.84] E. Østby. Fracture control - Offshore pipelines - New strain-based fracture mechanics equations including the effects of biaxial loading, mismatch and misalignment. In *Proceedings of the 24th International Conference on Offshore Mechanics and Arctic Engineering (OMAE)*, Halkidiki, Greece, 2005. OMAE2005-67518.

[2.85] E. Østby. Fracture control - Offshore pipelines JIP proposal for strain-based fracture assessment procedure. In *Proceedings of the 17th International Offshore and Polar Engineering Conference (ISOPE)*, pages 3238–3245, Lisbon, Portugal, 2007.

[2.86] D.P. Fairchild, M.L. Macia, S. Kibey, X. Wang, V.R. Krishnan, F. Bardi, H. Tang, and W. Cheng. A multi-tiered procedure for engineering critical assessment of strain-based pipelines. In *Proceedings of the 21st International Offshore and Polar Engineering Conference (ISOPE)*, pages 698–705, Maui, Hawaii, USA, 2011.

[2.87] R. Denys and A. Lefevre. Material test requirements for strain based design pipelines. In *Proceedings of the International Symposium - Microalloyed Steels for the Oil and Gas Industry*, Brazil, 2006.

[2.88] M. Verstraete, W. De Waele, R. Denys, and S. Hertelé. Pressure correction factor for strain capacity predictions based on curved wide plate testing. In *Proceedings of the 9th International Pipeline Conference (IPC)*, Calgary, Alberta, Canada, 2012. IPC2012-90592; accepted for publication.

Chapter 3

Tensile stress-strain behaviour of high strength line pipe steels

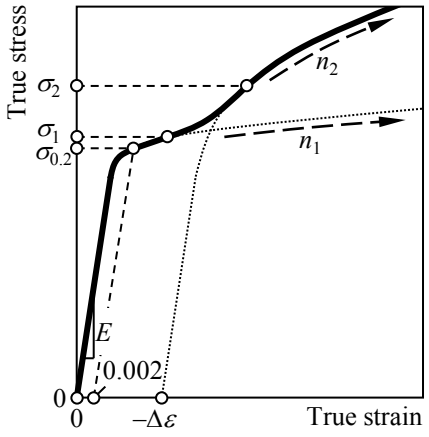

A study of 139 stress-strain curves of high strength line pipe steels led to the development of the 'UGent' stress-strain model, which is characterized by two stages of strain hardening.

3.1 Goal

Since high strength line pipe steels are produced using state-of-the art TMCP rolling processes (section 1.5.3), their post-yield performance can be expected to reveal specific characteristics. Likewise, weld metal has a particular mechanical behaviour inherent to its fundamental nature of being a cast structure. Moreover, recall that the complexity of strain based design can be largely attributed to the importance of the materials' strength properties (section 2.3.2.1). Combining these facts, it becomes clear that an accurate description, determination and – if possible – prediction of the mechanical behaviour of the materials is a key aspect in performing a sound strain based flaw assessment.

Aiming to contribute to a better understanding of the considerations above, this chapter is devoted to the stress-strain behaviour of high strength line pipe steels. First, section 3.2 reminds the reader of some basic concepts related to stress-strain behaviour. Second, section 3.3 discusses the major influences on the measured tensile behaviour of line pipe steels. Section 3.4 elaborates on different possible yielding behaviours and which of those is desired for strain based design purposes. Then, background is given on commonly applied stress-strain models, including a focus on line pipe steels (section 3.5). The common practice of line pipe steel modelling is critically compared with experimental observations for high strength line pipe steels in section 3.6. It will be shown that currently applied models are uncapable to deal with some specifically observed phenomena. To address this anomaly, section 3.7 is devoted to the development of a new ('UGent') stress-strain model for contemporary line pipe steels. To facilitate a practical application, section 3.8 elaborates on different ways to determine suited 'UGent' model parameters. In particular, a methodology to predict stress-strain behaviour from a limited set of tensile test characteristics is presented. Then, section 3.9 compares the performance of the 'UGent' model with that of the standardized Ramberg-Osgood model, in order to provide intuition on the obtained improvement. Although specifically developed for continuously yielding steels, the possibility to describe a Lüders plateau with the 'UGent' model is finally explored in section 3.10.

3.2 Basic concepts of stress-strain behaviour

To ensure a full understanding of the following, it is important to recall some basic concepts of stress-strain behaviour. Figure 3.1 provides a graphical overview. Note that some concepts have already been briefly addressed in section 2.3.1.

A stress-strain curve is typically obtained from a uniaxial tensile test. Engineering stress s (MPa) is calculated as tensile force (N) divided by the initially measured cross section (mm^2). Engineering strain e (–) follows from an ex-

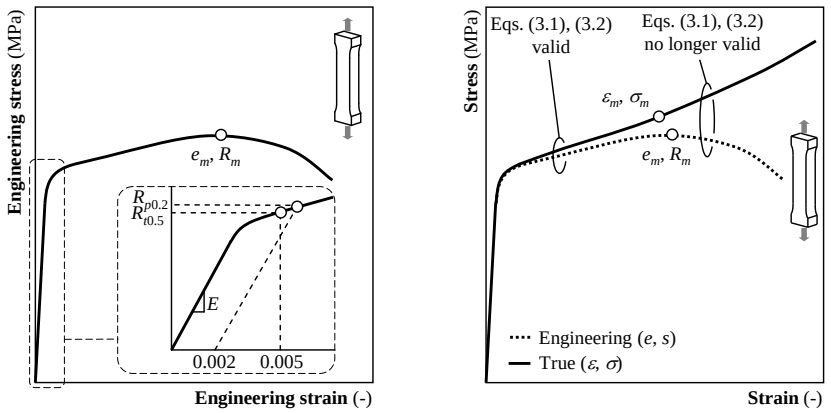

(a) (b)

Figure 3.1: (a) Graphical overview of tensile test characteristics. (b) Engineering and true stress-strain diagram.

tensometer measurement of elongation (mm), which is divided by the original extensometer gauge length (mm). For homogeneous and isotropic materials, e has a linear elastic component equal to s/E, where E is Young's modulus (MPa), and a plastic component e_{pl}. To characterize the plastic area, the following tensile test characteristics are often reported (figure 3.1(a)): yield strength (defined as the 0.2 % proof stress $R_{p0.2}$ or stress at 0.005 strain $R_{t0.5}$; MPa), ultimate tensile strength R_m (MPa), uniform elongation e_m (-) [1] and yield-to-tensile ratio $Y/T = R_{p0.2}/R_m$ or $R_{t0.5}/R_m$ (recall section 2.3.2.1).

Both engineering quantities s and e are easy to experimentally obtain, but lack physical relevance for high (plastic) deformations. Indeed, the actual ('true') stress σ (MPa) is force divided by the *actual* cross section rather than the *initial* cross section. Likewise, the actual ('true') strain ϵ (–) should be continuously updated on the basis of the *actual* extensometer gauge length rather than its *initial* value.

From the conservation of volume principle for plastic deformation it can be shown that, as long as uniform deformation takes place in the tensile test specimen, true quantities can be found from engineering quantities as follows:

$$\epsilon = \ln(1 + e) \tag{3.1}$$

$$\sigma = s(1 + e) \tag{3.2}$$

[1] Note that, in scientific literature, uniform elongation is also commonly denoted as UEl or uEL.

For true strain, also, there is a linear elastic component σ/E and a plastic component ϵ_{pl}.

When localized deformation (necking) takes place, the abovementioned is no longer valid. As a consequence, the post-necking stress-strain behaviour is hard to quantify and requires additional measurements to perform an analytical correction [3.1]. In an engineering stress-strain curve, the initiation of necking corresponds with (e_m, R_m). Using Eqs. (3.1) and (3.2), it can be shown that the onset of necking in a true stress-strain diagram (ϵ_m, σ_m) (figure 3.1(b)) has the following property (Considère's necking criterion):

$$\frac{\mathrm{d}\sigma}{\mathrm{d}\epsilon}(\epsilon_m) = \sigma_m \tag{3.3}$$

3.3 Practical considerations for measuring stress-strain behaviour of line pipe steels

This section discusses on aspects that may influence the stress-strain diagram derived from a tensile test on line pipe steel. Due to its widespread application, focus is put on UOE formed pipes (section 1.2). First, the standardized characterization of line pipe steels is briefly summarized (section 3.3.1). To evaluate its suitability for strain based purposes, a literature survey covers four factors that might affect stress-strain behaviour: the specimen orientation (section 3.3.2) and geometry (section 3.3.4), its location (section 3.3.3) and the stage of the production process at which the specimen is extracted (3.3.5). From this survey, the standardized guidelines will be critically discussed and an adapted procedure proposed in section 3.3.6.

3.3.1 Standardized characterization of line pipe steels

As already briefly addressed in section 1.5.1, the characterization of line pipe steel strength (or, more generally, stress-strain behaviour) is covered by the standard API 5L ('Specification for line pipe') (2007) [3.2]. In particular, upper and lower limits are specified for $R_{t0.5}$ and R_m as given in table 3.1.

It can be noted that similar requirements are provided in the European standard EN 10208-2 [3.3]. Table 3.1 provides equivalent steel grades according to this standard.

As for the extraction of the tensile test specimen from large diameter (outer diameter $\geq$ 219 mm or $8\frac{5}{8}$") UOE pipes (section 1.2), it is specified that

- the specimen should be oriented in the transverse direction. This specification is based on the stress based knowledge that a pipe's burst pressure is governed by the occurring hoop stresses.

Table 3.1: Upper and lower strength limits for steel grades according to API 5L (2007), product specification level 2 (PSL 2) [3.2].

API 5L grade	$R_{t0.5}$ (MPa)		R_m (MPa)		Equivalent
	min. *	max.	min.	max.	EN 10208-2 grade
X60	415	565	520	760	L415
X65	450	600	535	760	L450
X70	485	635	570	760	L485
X80	555	705	625	825	L555
X100	690	840	760	990	L690

* also denoted as SMYS, see section 1.5.1.

- the specimen should be extracted after cold expansion. This specification is based on the knowledge that cold working affects a material's strength properties.

- tensile testing should be performed at a frequency of one test per 100 pipe lengths. This specification evidently aims at large pipe production series.

Further, the performer has full freedom in choosing the specimen geometry (full thickness strip, round bar, ring expansion specimen). Hereby, a full thickness strip specimen should be flattened prior to testing, due to the pipe curvature in the transverse direction.

3.3.2 Influence of orientation of specimen sampling: anisotropy

Due to the direction-specific deformation history during plate rolling and pipe forming, longitudinal tensile properties differ by nature from transversal tensile properties [3.4]. For the specific case of high strength UOE formed pipes, it is known that longitudinal (i.e. parallel to the pipe axis) strength characteristics tend to be (significantly) lower than transveral (i.e. circumferentially oriented) strength characteristics [3.5–3.14]. This follows from the microstructure obtained by TMCP rolling [3.5, 3.15] and cold work due to UOE pipe forming (see section 3.3.5.1). A comparison based on longitudinal and transversal round bar tensile tests reveals that anisotropy is more pronounced for yield strength ($R_{p0.2}$ or $R_{t0.5}$) than for ultimate tensile strength. As regards the former, strength differences of over 100 MPa have been reported. Note that full thickness strip specimens have been excluded for comparison between longitudinal and transversal properties, given their different specimen geometry effects (see section 3.3.4).

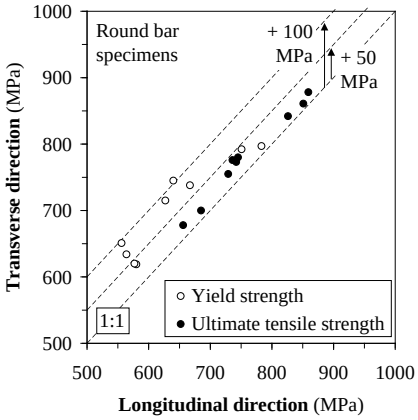

Figure 3.2: UOE formed pipes have higher strength characteristics in the transversal direction, the differences being more pronounced for yield strength than for ultimate tensile strength (results taken from [3.5, 3.7, 3.10, 3.12, 3.13]).

3.3.3 Influence of location of specimen sampling: heterogeneity

A study of the influence of specimen location can be viewed from two different angles. First, one might consider the difference in mechanical properties between two pipes that are welded together ('pipe-to-pipe heterogeneity'). Second, the variations of mechanical properties within one single pipe can be addressed ('in-pipe heterogeneity'). Both aspects are separately discussed below.

3.3.3.1 Pipe-to-pipe heterogeneity

Referring back to table 3.1, a large variety may exist between the strength characteristics of two line pipe steels that meet the same grade. For instance, the range between minimum and maximum specified yield strength values according to API 5L is 150 MPa. As a consequence, significant differences can occur between joined pipes. This is reflected in figure 3.3, which shows reported yield strength distributions of steel grades X60 to X100. The depicted data for X60 to X80 have been obtained from a study of Leis et al. [3.16] covering several thousands of kilometers pipeline in over 50 datasets of X40 to X80 steel, and represent transversal properties. The standard deviations of these distributions are fairly similar. To confirm that this observation can be extrapolated to more modern X100 steels, a distribution of yield strength properties (longitudinal) from [3.9] has been included (number of tests covered is unknown).

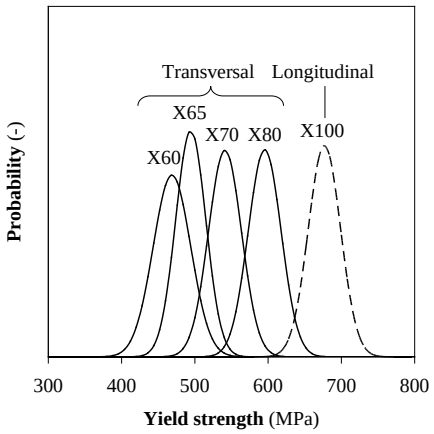

Figure 3.3: Reported yield strength distributions of X60 to X100 linepipe steel indicate a pronounced presence of heterogeneity. Data taken from [3.16] (X60 to X80) and [3.9] (X100).

As regards ultimate tensile strength, expectable manufacturing variations of between 70 and 100 MPa have been reported in [3.17].

3.3.3.2 In-pipe heterogeneity

Figure 3.3 has been based on a comparison of different pipes, originating from different suppliers and different heats. Focusing on heterogeneity within one pipe, three directions can be considered: longitudinal, circumferential (defined by an 'o-clock' position), and through-thickness. Longitudinal heterogeneity results from differences in thermal history during steel rolling, depending on the longitudinal position. Further, circumferential heterogeneity is linked with the non-axisymmetric cold forming steps during UOE pipe forming (recall figure 1.5) and through-thickness heterogeneity can be readily related to

- the steelmaking process: cooling rates are different near the surface and at mid-thickness, which produces a through-thickness grain size gradient;

- the UOE pipe forming process: depending on through-thickness position, different (compression-)tension cycles are observed (figure 3.4 [3.11]).

As a result, mechanical properties can significantly vary along all three directions [3.8, 3.18]. For instance, figure 3.5 indicates in-pipe variations of longitudinally oriented $R_{p0.2}$ and R_m of about 40 MPa and 25 MPa, respectively, for varying longitudinal and o'clock positions in an API 5L X100 line pipe steel [3.8].

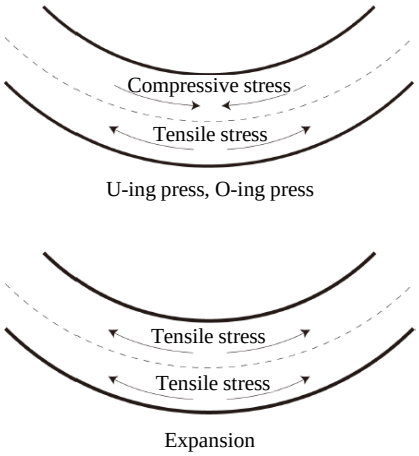

Figure 3.4: Different (compression-)tension cycles during UOE pipe forming [3.11].

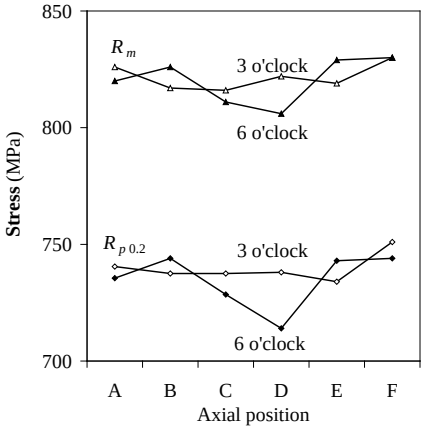

Figure 3.5: Line pipe steel stress-strain behaviour varies within a single pipe, over both the longitudinal and the circumferential (o'clock) direction [3.8].

3.3.4 Influence of test specimen geometry

Different test specimen geometries are used to characterize the tensile behaviour of line pipe steel. For longitudinal properties, a full thickness strip or round bar specimen can be extracted. For transversal properties, also possible is a ring expansion test specimen (sampling a full circumferential 'ring' of pipe material, typically between 100 and 150 mm long). Depending on the orientation of testing aimed at, different specimen types are advised.

- For longitudinal specimens on the one hand, a full thickness strip speci-

men is favourable since it provides properties that are averaged over the thickness. Such averaged properties are more representative for full scale behaviour. In contrast, a round bar specimen is mostly extracted at mid-thickness, where the strength properties generally differ from those near the pipe surface (through-thickness heterogeneity, see section 3.3.3.2).

- For transversal specimens on the other hand, full thickness strip specimens produce unrepresentatively low yield strengths. This phenomenon is caused by the Bauschinger effect [3.10, 3.19, 3.20] which inevitably occurs due to the flattening of the specimen required prior to performing the test. The underestimation of yield strength becomes more pronounced for grades higher than X70 [3.21]. Further, comparing a round bar specimen with a ring expansion specimen, the latter should be more representative since material over the full thickness (and circumference) is sampled. Their results, however, seem to deviate only slightly [3.20, 3.22, 3.23]. Since round bar tests are less expensive, they are more widely applied.

The abovelisted observations regarding full thickness strip and round bar specimens are illustrated in figure 3.6, which summarizes $R_{t0.5}$ and R_m for tensile tests on a X100 line pipe steel reported in [3.10]. Each data point represents an average of eight tests, the error bars corresponding with $\pm$ one standard deviation. Three effects are observed (also numbered in figure 3.6):

1. anisotropy (comparison between longitudinal and transversal round bar specimens),
2. Bauschinger effect due to flattening of transversal full thickness strip specimen (comparison with longitudinal full thickness strip specimen),
3. through-thickness heterogeneity (comparison between longitudinal round bar and full thickness strip specimens).

3.3.5 Stage of pipe production process during which the sample is taken

3.3.5.1 From plate to pipe: UOE pipe forming

In UOE pipe forming, the cold U bending, O forming and expansion processes add a significant buildup of plastic strain history to the material. As a consequence, comparing the two stages at which tensile test specimens can be extracted (plate or pipe), different mechanical behaviours are observed. In particular, the following trends are observed (e.g. figure 3.7, [3.20, 3.24]):

- Both yield strength and ultimate tensile strength increase due to pipe forming;

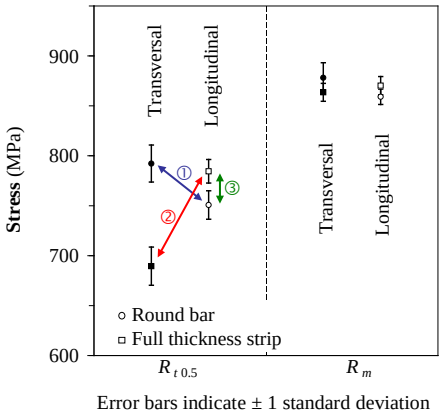

Figure 3.6: Reported yield and tensile strength values of X100 line pipe steel in different orientations and using different specimens [3.10].

- The increase in yield strength is more pronounced than the increase in ultimate tensile strength. As a consequence, Y/T is also increased;

- The observed increases are more pronounced in the transverse direction than in the longitudinal direction. This is logical since plastic strains during UOE pipe forming are transverse.

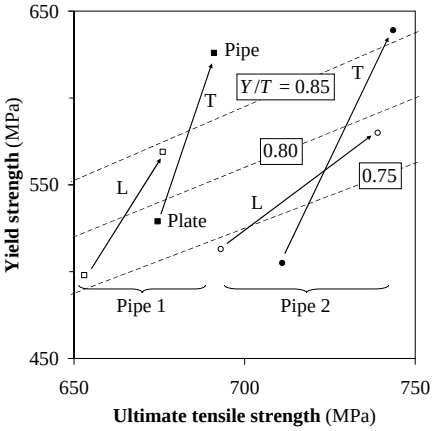

Figure 3.7: UOE pipe forming influences tensile strength characteristics (L: longitudinal direction; T: transversal direction) [3.24].

These changes and their orders of magnitude shown in figure 3.7 are confirmed in other studies. For instance, an increase in yield strength of as much as 172 MPa (transverse direction) and 73 MPa (longitudinal direction) was observed in [3.12], whereas the corresponding increase in ultimate tensile strength was 23 MPa and 13 MPa, respectively.

Given the above, it is advised to obtain properties in the as-formed condition as specified in API 5L.

3.3.5.2 Coating

After UOE pipe production, the anti-corrosive coating (section 1.2) is generally applied using the so-called Fusion Bonded Epoxy (FBE) coating process. This process involves heating the pipe up to a temperature between roughly 200°C and 250°C for several minutes [3.25]. For example, figure 3.8 shows an actual thermal profile observed during FBE coating [3.26].

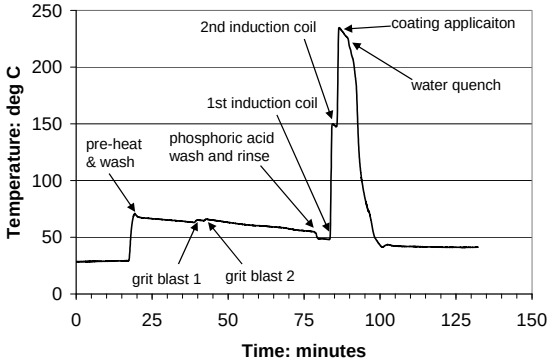

Figure 3.8: Thermal profile observed during FBE coating process [3.26].

The succession of a plastic straining history (due to UOE pipe forming) by a heat treatment (due to anti-corrosive coating) introduces a strain aging effect which changes the mechanical properties. Strain aging results from the locking of dislocations (introduced by cold forming) by carbon or nitrogen atoms [3.27]. Concrete macroscale influences are (in decreasing pronouncedness of occurrence) [3.20, 3.28–3.30]:

- changes in yield behaviour (from continuous to discontinuous with Lüders plateau, see also section 3.4);
- increase in yield strength;
- increase in Y/T and ultimate tensile strength;

- decrease in ductility.

The extent of the abovementioned changes is determined by both coating time, temperature and the strain history prior to coating [3.12, 3.27, 3.31]. To simulate a realistic coating cycle as for example shown in figure 3.8 on a laboratory scale, a heat treatment is applied during a well-defined time (often 5 minutes) after which tensile testing is performed. By means of illustration, a selection of reported results of both longitudinal and transversal tests on mostly X80 and X100 steels at various strain history levels (figure 3.9, [3.5, 3.31–3.36]) confirms the strong temperature dependency of strain aging. More importantly, its effect can be substantial as yield strength increases of 100 MPa and more have been observed.

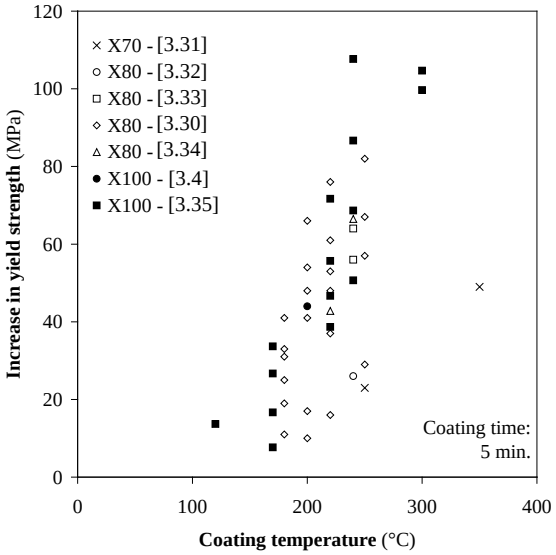

Figure 3.9: Reported yield strength changes due to thermal coating simulation.

Longitudinal stress-strain properties have a different sensitivity to strain aging than transversal properties. This has led to line pipe steel specifications which separately take both changes into account [3.8]. Studies have reported that – compared to the transverse direction – the increase in yield and ultimate tensile strength strength is either higher [3.8, 3.12, 3.27], lower [3.11, 3.34] or similar [3.37] in the longitudinal direction. More clarification to this matter is desirable.

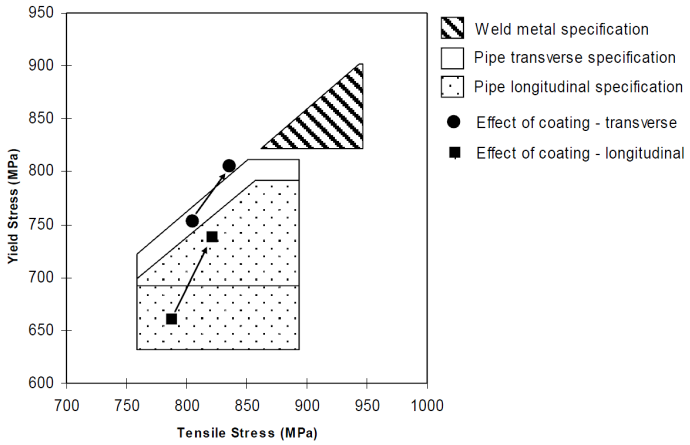

Figure 3.10: UOE line pipe steel specification with considerations of anisotropy and strain aging [3.8].

3.3.6 Summary and conclusion: choosing an appropriate tensile test procedure for strain based design

Summarizing the effects on (measured) material behaviour discussed in sections 3.3.2 to 3.3.5, the following key elements are to be taken into account.

- There are differences in yield and ultimate tensile strength (and Y/T-ratio) in the transversal and longitudinal directions. Transversal properties are important with respect to hoop stresses resulting from internal (or external) pressure. Longitudinal properties, however, are equally relevant for a strain based design since plastic deformation is imposed in the axial direction.
- Stress-strain curve shape and strength characteristics can be strongly influenced by the thermal cycle necessary for anti-corrosion coating.
- Effects of heterogeneity in a single pipe and between different pipes can be pronounced.

Therefore, the following practical suggestions are given for line pipe steel qualification in a strain based design context:

- *Tensile test specimens for investigations of longitudinal strain capacity are to be extracted in the longitudinal direction. Tensile test specimens for the quantification of resistance against yielding due to internal pressure are to be extracted in the transversal direction.*

- *Full thickness strip specimens are to be chosen for determination of longitudinal properties, since these specimens provide average properties over the full thickness of the structure which are more relevant to the structural response than localized properties. Round bar specimens are advised for determination of transversal properties since these specimens do not have to be flattened prior to testing.*
- *Tensile testing is to be performed on as-coated line pipe steel or uncoated line pipe steel which has undergone a thermal cycle to represent the coating process. In the latter case, the similarity between simulated strain aging and strain aging due to actual coating must be shown.*
- *Ample testing over the o'clock and longitudinal direction of a selection of pipes during the design phase should provide statistical distributions of not only pipe-to-pipe heterogeneity, but also in-pipe heterogeneity. This allows for the selection of worst case pipe combinations in a girth weldment, with respect to strain capacity. A further investigation in this respect is provided in chapter 8 (section 8.4).*

It can be noted that similar suggestions are already applied in practice on a company-specific level. For instance, [3.38] elaborates on a systematic tensile testing program for high grade pipe steels, developed by TransCanada Pipelines Ltd. This tensile testing program takes into account the abovementioned considerations of heterogeneity, anisotropy and thermal aging.

3.4 Continuous and discontinuous yielding behaviour

Regardless of the nature (orientation, location, production history) of a tensile test, discussed in section 3.3, two types of stress-strain curves can be distinguished depending on their initial yielding behaviour: continuous or discontinuous. On the one hand, continuous or 'round house' behaviour is characterized by a gradual onset of yielding which smoothly connects with the linear elastic stage. On the other hand, discontinuous yielding exhibits a sharp yield point, followed by a Lüders plateau (figure 3.11). In the latter case, the length of the Lüders plateau ('Lüders elongation') is denoted as e_L (engineering value) or ϵ_L (true value) (-).

Continuously and discontinuously yielding materials perform differently in a strain based context. In particular, the presence of a Lüders plateau (either in the longitudinal or the transverse direction, or both [3.39]) reduces

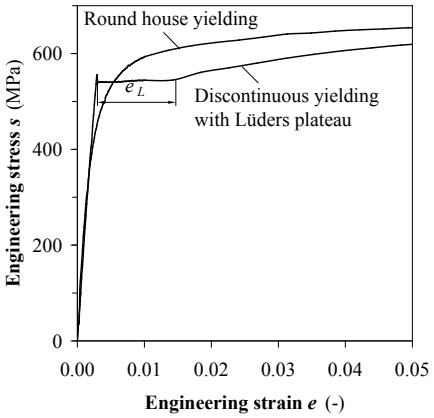

Figure 3.11: Continuous (round house) and discontinuous (Lüders plateau) strain hardening behaviour.

the buckling resistance and, as a consequence, the bending strain capacity. Therefore, strain based material procedures mostly specify that the materials should exhibit round house yielding [3.9, 3.37, 3.40–3.42]. This specification has been translated into project-specific minimum values for ratios of stresses at certain strains (e.g. figure 3.12 for the onshore Stittsville project, Ontario, Canada) [3.9, 3.37].

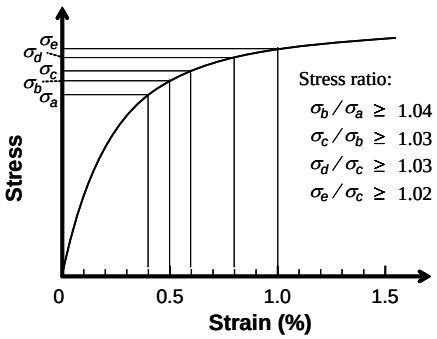

Figure 3.12: Definition of round house yielding behaviour for the onshore Stittsville project, Ontario, Canada [3.9].

3.5 Stress-strain modelling

During the design and/or analysis stage, the stress-strain behaviour of metallic materials is often modelled by means of a simple mathematical expression (also referred to as 'constitutive law'). This approach allows the post-yield behaviour to be treated by a set of parameters, thus enabling a more systematic material characterization and the execution of parametric studies through finite element modelling. Most widely used stress-strain equations have a limited number of model parameters, because of simplicity reasons. In contrast, the assumed curve shape and limited number of parameters may hamper a model's ability of accurately representing complex strain hardening curve shapes.

First, section 3.5.1 is devoted to the possibilities, limitations and analysis of existing stress-strain models. Then, the common practice for line pipe steels is elaborated in section 3.5.2.

3.5.1 Background

Table 3.2 summarizes the most frequently applied constitutive laws. Every model is briefly discussed below.

Table 3.2: An overview of commonly used existing stress-strain models (chronologically ranked)

Author (Year) [Reference]	**Model equation**
Ludwik (1909) [3.43]	$\sigma = \sigma_0 + K_L \epsilon^{n_L}$
Ramberg-Osgood (1943) [3.44]	$e = \frac{s}{E} + p\left(\frac{s}{s_p}\right)^{n_{RO}}$
Hollomon (1945) [3.45]	$\sigma = K_H \epsilon^{n_H}$
Voce (1948) [3.46]	$\sigma = \sigma_\infty - (\sigma_\infty - \sigma_0)\exp(-K_V \epsilon)$
Swift (1952) [3.47]	$\sigma = K_S (\epsilon + \epsilon_0)^{n_S}$
Ludwigson (1971) [3.48]	$\sigma = K_1 \epsilon_{pl}^{n_1} + \exp(K_2 + n_2 \epsilon_{pl})$

A first commonly used model for stress-strain behaviour was proposed as early as 1909 by Ludwik [3.43]. He suggested an empirical relationship in the form of (figure 3.13(a)):

$$\sigma = \sigma_0 + K_L \epsilon^{n_L} \tag{3.4}$$

This equations has three parameters: a yield strength σ_0, a strength coefficient K_L and a strain hardening coefficient n_L (between 0 and 1). Crussard and Jaoul [3.49] identified the possibility to determine the strain hardening parameters K_L and n_L in a double logarithmic diagram that expresses true stress differentiated with respect to true strain, versus true strain (a so-called

'differential Crussard-Jaoul analysis'). Indeed, if the experimental stress-strain curve obeys the Ludwik equation, it can in such a diagram be recognized as a straight line (figure 3.13(b)), defined by the following equation:

$$\log\left(\frac{\mathrm{d}\sigma}{\mathrm{d}\epsilon}\right) = \log\left(K_L n_L\right) + \left(n_L - 1\right)\log\left(\epsilon\right) \tag{3.5}$$

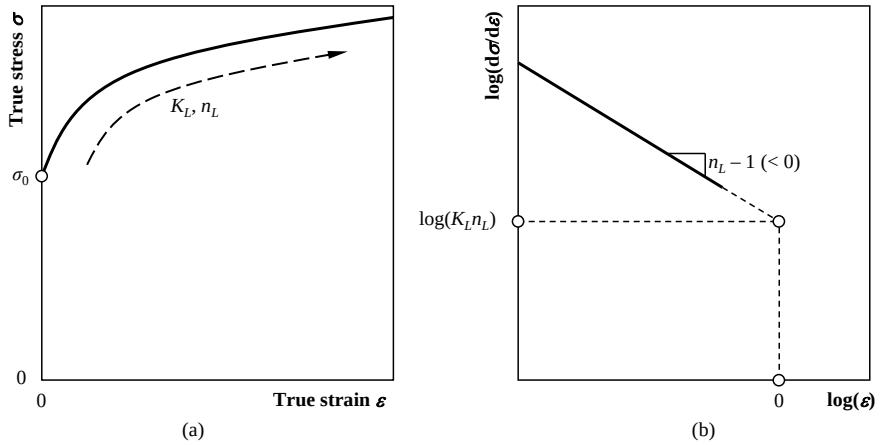

Figure 3.13: (a) Ludwik model, (b) differential Crussard-Jaoul analysis based on the Ludwik model.

In 1945, Hollomon [3.45] aimed for more simplicity by eliminating the parameter σ_0 from the Ludwik equation, yielding the following two-parameter (K_H and n_H) expression (figure 3.14(a)):

$$\sigma = K_H \epsilon^{n_H} \tag{3.6}$$

The applicability of this equation to an experimental curve can be investigated by plotting the stress-strain data in a double logarithmic diagram (figure 3.14(b)). If the Hollomon equation is respected, such diagram shows a straight line, from which K_H and n_H can be determined ('Hollomon analysis'):

$$\log\left(\sigma\right) = \log\left(K_H\right) + n_H \log\left(\epsilon\right) \tag{3.7}$$

Since the purely empirical Hollomon equation has only two parameters, it has often been reported as too simplistic to describe the full-range behaviour of some metals. Indeed, a good approximation seems mostly restricted to the area of large plastic strains [3.48, 3.50–3.54]. This was, in fact, already acknowledged by Hollomon in his original article [3.45].

Almost a decade later, Swift [3.47] proposed another power law equation, introducing a parameter ϵ_0 which can account for a possible pre-straining history

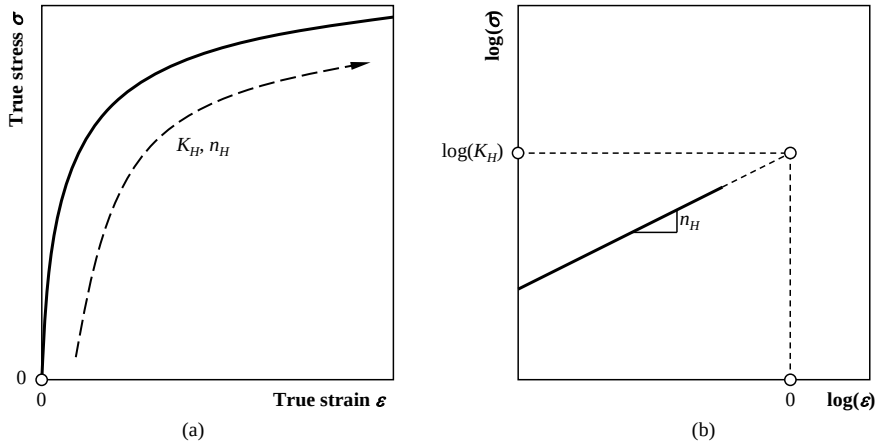

Figure 3.14: (a) Hollomon model, (b) Hollomon analysis.

(figure 3.15(a)):

$$\sigma = K_S \left(\epsilon + \epsilon_0\right)^{n_S} \tag{3.8}$$

In case the Swift equation is a good approximation, the stress-strain curve is linear in a double logarithmic plot of $\mathrm{d}\sigma/\mathrm{d}\epsilon$ against σ (figure 3.15(b)). Then, based on Eq. (3.8), the parameters K_S and n_S can be determined by fitting Eq. (3.9) to this line, which is referred to as a 'modified Crussard-Jaoul analysis' [3.55].

$$\log\left(\frac{\mathrm{d}\sigma}{\mathrm{d}\epsilon}\right) = \log\left(n_S K_S^{1/n_S}\right) + \left(1 - \frac{1}{n_S}\right)\log\left(\sigma\right) \tag{3.9}$$

A limitation of the abovementioned constitutive laws is their inability to accurately describe linear elastic behaviour. As a simple solution to this problem, true strain ϵ can be substituted by true plastic strain ϵ_{pl}, and a new model equation can be put forward by superposing this value with σ/E. An example model that puts this methodology into practice is that of Ramberg and Osgood [3.44]. This relation was originally designed in 1943 for aluminium, stainless steel and carbon steel sheet, aiming at small strains up to roughly 0.01. Short after its publication, it was modified by Hill [3.56] into the following convenient form:

$$e = \frac{s}{E} + p\left(\frac{s}{s_p}\right)^{n_{RO}} \tag{3.10}$$

In this engineering stress-strain (s-e) equation, s_p is the material's proof stress corresponding to the plastic strain p (figure 3.16). One could consider the Ramberg-Osgood model as an elastic-plastic version of the Hollomon equation, applied to engineering quantities. Note that the strain hardening exponent

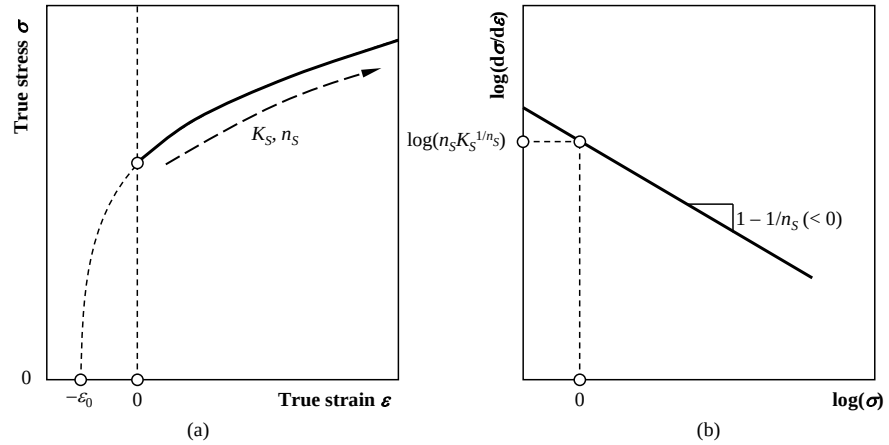

Figure 3.15: (a) Swift model, (b) modified Crussard-Jaoul analysis, based on the Swift model.

n_{RO} should be seen as the inverse of n_H in Hollomon's equation, since Eq. (3.10) expresses strain as a function of stress. Obviously, the argument of simplicity and the corresponding limitation in modelling possibilities apply here, too. Also, Eq. (3.10) fails to describe the maximum that is achieved in the engineering stress-strain curve at the ultimate tensile stress R_m.

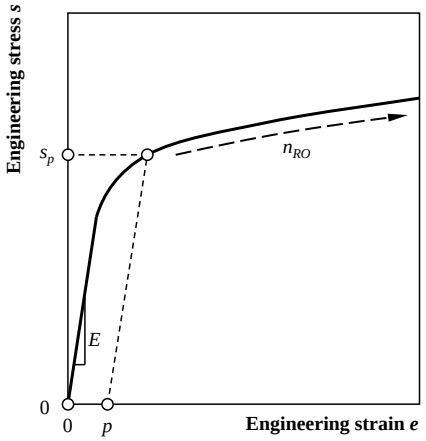

Figure 3.16: Ramberg-Osgood model according to Hill's formulation.

Although most commonly used equations (Ludwik, Hollomon, Ramberg-Osgood and Swift) are power laws, some researchers have developed stress-strain models

from a fundamentally different approach. Firstly, Voce [3.46] has proposed an exponential relation which starts at σ_0 and reaches a maximum at σ_∞ (figure 3.17(a)):

$$\sigma = \sigma_\infty - (\sigma_\infty - \sigma_0) \exp(-K_V \epsilon) \tag{3.11}$$

This equation is applicable to materials that follow a linear curve in a plot of $\mathrm{d}\sigma/\mathrm{d}\epsilon$ vs. σ, also referred to as the Kocks-Mecking work hardening model [3.57, 3.58] (figure 3.17(b)):

$$\frac{\mathrm{d}\sigma}{\mathrm{d}\epsilon} = K_V (\sigma_\infty - \sigma) \tag{3.12}$$

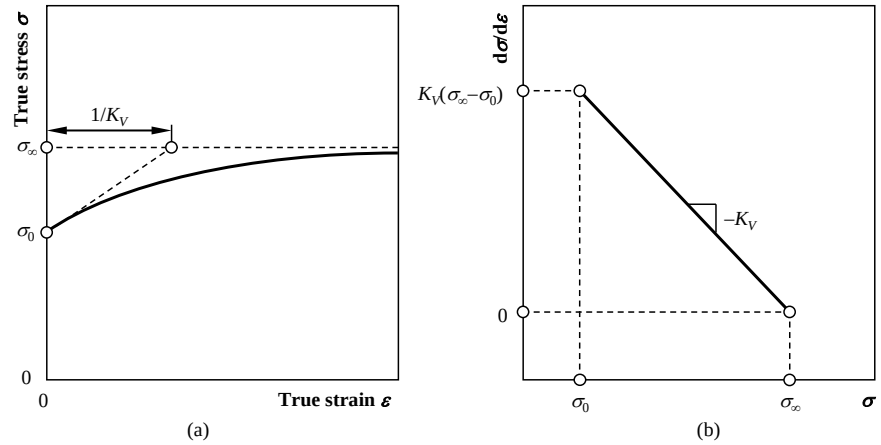

Figure 3.17: (a) Voce model, (b) Kocks-Mecking work hardening model.

Secondly, Ludwigson [3.48] found that face-centered cubic metals and alloys deviate from the Hollomon equation at low plastic strains [2]. He proposed a new relation for plastic flow behaviour, based on Eq. (3.6), including an exponential correction term ($n_2 < 0$, figure 3.18(a)):

$$\sigma = K_1 \epsilon_{pl}^{n_1} + \exp(K_2 + n_2 \epsilon_{pl}) \tag{3.13}$$

Compared to all other aforementioned models, the applicability of Ludwigson is somewhat more difficult to detect, since there is no single curve plot – logarithmic neither non-logarithmic – that shows a straight line for this equation. It merely shows a tendency towards linear behaviour for large strains in a double logarithmic stress-plastic strain diagram, as depicted in figure 3.18(b).

[2] Of these, austenitic stainless steels have deserved particular attention in literature (e.g. [3.59]). Apart from austenitic stainless steels, Ludwigson also mentioned brass, silver, copper, aluminium and nickel metals and alloys.

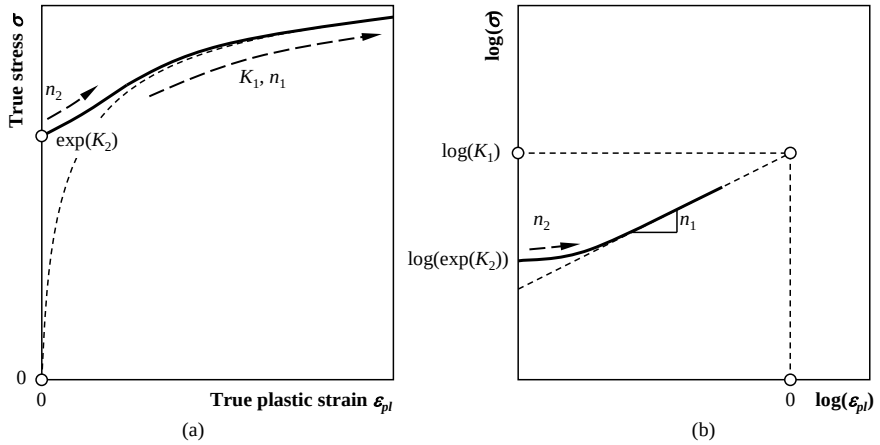

Figure 3.18: (a) Ludwigson model, (b) Ludwigson model in a double logarithmic stress-strain diagram.

Ludwigson hypothesized that his equation describes a transition from planar dislocation slip to cross slip and dislocation cell formation [3.48]. One could thus interpret its model parameters in a microstructural way [3.48, 3.60]. This explanation, however, needs more fundamental validation as it has been unsatisfactory in some cases [3.50]. Moreover, Ludwigson's original article [3.48] mentions difficulties in describing the early post-yield behaviour of aluminium and nickel with Eq. (3.13).

3.5.2 Common practice in stress-strain modelling of line pipe steels

Some pipeline-related standards such as CSA Z662 (2007) [3.61] and API 1104 (2007) [3.62] provide guidance on how to describe the constitutive behaviour of line pipe steels. Each of both standards has a particular modelling philosophy and application scope:

- CSA Z662 specifies in appendix C ('Limit states design') that different stress-strain relationships may be assumed in a structural integrity analysis, as long as the resulting predicted strength is in accordance with test results [3.61]. Particularly proposed are an elastic-perfectly plastic behaviour and the Ramberg-Osgood model.

- API 1104 (appendix A – 'Alternative acceptance standards for girth welds') contains guidance on the quantification of allowable girth weld flaw dimensions [3.62]. Two analysis options can be chosen for static loading conditions. Whereas 'Option 1' is a simplified graphical approach

that requires a minimum of input data, 'Option 2' is based on FAD principles (section 2.2.4). The fracture mechanics calculations that support the latter approach assume a Ramberg-Osgood type material behaviour.

Note that both CSA Z662 and API 1104 use the stress at 0.005 total strain $R_{t0.5}$ as a yield strength value in the following modification to Eq. (3.10):

$$e = \frac{s}{E} + \left(0.005 - \frac{R_{t0.5}}{E}\right)\left(\frac{s}{R_{t0.5}}\right)^n \tag{3.14}$$

Apart from its occurrence in standards, the Ramberg-Osgood model has also been widely applied in the finite element analysis of pipelines with flawed girth welds (e.g. for the development of the strain capacity prediction procedures of CSA Z662 [3.61] (section 2.6.3.1) and SINTEF (section 2.6.3.2)). Almost without exception, the pipe material is assumed to harden isotropically according to the Von Mises yield criterion [3.63] and homogeneously.

Further, note that the Ramberg-Osgood model has even been used to describe the constitutive behaviour of materials with a Lüders plateau (e.g. [3.64]).

Different reasons can be put forward for the high number of studies that rely on the Ramberg-Osgood model. First, with only three parameters that are easy to interpret and determine, it has the advantage of simplicity. Second, the model's popularity has been highly promoted by its incorporation into finite element analysis software (e.g. *ABAQUS*®). There, it can be readily defined in true stress - true strain terms on the basis of its model parameter values. Assuming the true 0.2 % proof stress $\sigma_{0.2}$ as a measure of yield strength, the following equation applies:

$$\epsilon = \frac{\sigma}{E} + 0.002\left(\frac{\sigma}{\sigma_{0.2}}\right)^n \tag{3.15}$$

Third, most elastic-plastic fracture mechanics concepts have been based upon a Ramberg-Osgood material behaviour (see section 2.2.1, Eq. (2.6)).

Summarizing this section, the Ramberg-Osgood model – whether applied on engineering or true quantities – represents the current mainstream in many modelling applications, including those related to strain based design.

3.6 Experimental observations

In order to evaluate the common practice in the constitutive modelling of line pipe steels (section 3.5.2), it has been evaluated on a set of 139 experimental stress-strain curves of contemporary line pipe steel grades ranging from X56 to X100. Note that the large variety between different pipe grades in

this database implies that a wide range of fundamentally different steelmaking processes is covered. All investigated stress-strain curves show a continuous yielding behaviour. Tensile test results with a Lüders plateau have been deliberately excluded because such behaviour is unfavourable in a strain based design (section 3.4). It can be noted that their treatment is briefly covered in a separate section (3.10).

Section 3.6.1 gives a detailed view on the characteristics of the investigated stress-strain curves and critically compares their behaviour with findings from literature. Then, the shape of the curves is investigated and compared with existing stress-strain models in section 3.6.2.

3.6.1 Investigated data

All investigated stress-strain curves were obtained from standard tensile tests on specimens sampled from pipes. All tests had been previously conducted for various research purposes, and were performed on the same tensile test rig. To maximize the potential variety between different curves, test specimens from both coated and uncoated pipes have been considered and different specimen geometries (flat strip, round bar) and orientations (longitudinal and transversal) are included.

The investigated ranges of common tensile test characteristics (table 3.3) confirm the statement that a collection of significantly different line pipe steels is dealt with. Note that Y/T in table 3.3 is defined as $R_{p0.2}/R_m$ and not as $R_{t0.5}/R_m$ as specified in API 5L (2007) [3.2]. This definition and the use of $R_{p0.2}$ as a yield strength value will be maintained for the description of experimental data throughout the remainder of the dissertation. The choice for $R_{p0.2}$ is motivated by combining two arguments:

- $R_{p0.2}$ has physical relevance, as it indicates the deviation from linear elastic behaviour (and, hence, the onset of plasticity). $R_{t0.5}$ on the other hand is rather an empirical measure of yielding, which is more straightforward to extract from a tensile test record than $R_{p0.2}$.
- Although $R_{p0.2}$ and $R_{t0.5}$ are fairly similar for most line pipe steels, their relation is influenced by the strength (grade) of the steel (figure 3.19). In this respect, doubts have recently been raised about the suitability of $R_{t0.5}$ to represent the physically more relevant $R_{p0.2}$ for grades X100 and above [3.10].

A visual check of the observed relations between the tabulated tensile test characteristics (figures 3.20 and 3.21) indicates a significant amount of scatter. Apart from the observed scatter, the following general trends can be identified.

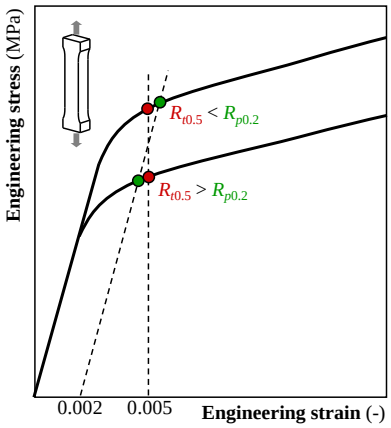

Figure 3.19: The relation between $R_{t0.5}$ and $R_{p0.2}$ depends on the strength level of the line pipe steel.

Table 3.3: Ranges of charasteristics of the 139 investigated tensile tests

Characteristic (dimension)	Minimum	Average	Maximum
API 5L grade	X56	—	X100
$R_{p0.2}$ (MPa)	393	551	743
R_m (MPa)	499	660	855
Y/T (-)	0.66	0.83	0.95
e_m (-)	0.043	0.083	0.153

- First, Y/T tends to increase as yield strength increases (figure 3.20). This observation is in accordance with literature (section 1.5.4). Different empirical upper-bound equations have been proposed for Y/T as a function of $R_{p0.2}$ or $R_{t0.5}$, notably:

  Bannister et al. (2000) [3.65] (adopted by FITNET (2008) [3.66]):

$$Y/T = \frac{1}{1 + 2\left(150/R_{p0.2}\right)^{2.5}} \tag{3.16a}$$

  API 1104 (2007) [3.62]:

$$Y/T = \frac{1}{1 + 2\left(150/R_{t0.5}\right)^{2.3}} \tag{3.16b}$$

  Denys et al. (2009) [3.67]:

$$Y/T = \frac{1}{1.01 + 3\left(250/R_{t0.5}\right)^{6}} \tag{3.16c}$$

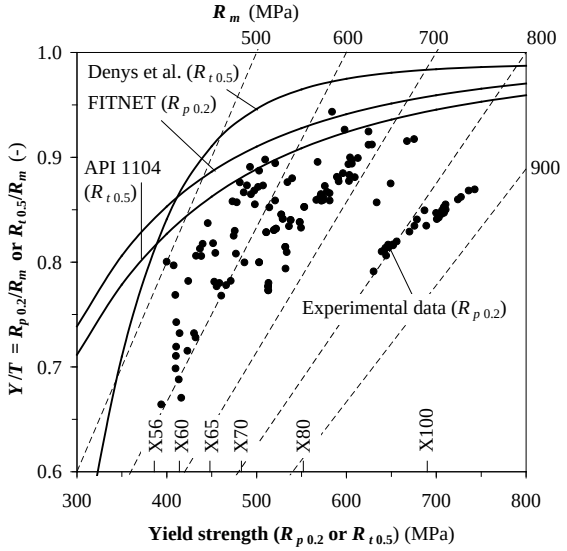

Figure 3.20: Relations between yield strength, yield-to-tensile ratio and ultimate tensile strength of the investigated steels.

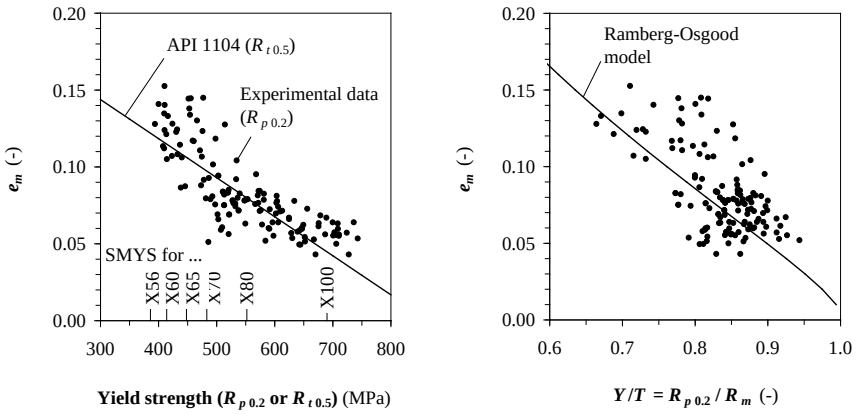

Figure 3.21: Relations between yield strength, yield-to-tensile ratio and uniform elongation of the investigated steels.

Considering the current dataset, it appears that Eq. (3.16c) provides an upper-bound Y/T-value for all datapoints. Values predicted by Eqs. (3.16a) and (3.16b), on the other hand, are slightly exceeded for some

exceptional cases.

- Uniform elongation e_m tends to decrease as yield strength increases (figure 3.21(a)), which is again confirmed in literature (section 1.5.4). An empirical equation incorporated in API 1104 [3.62] provides a fair average trend:

$$Y/T = 0.22 - 0.000254 R_{t0.5} \tag{3.17}$$

  Since Eq. (3.17) provides average values, its estimation can be either conservative or unconservative. Given the substantial amount of scatter, it can therefore be questioned whether its application is appropriate for practical designs.

- Uniform elongation e_m tends to decrease as Y/T increases (figure 3.21(b)). The general validity of this observation can be analytically proven using power law stress-strain models. For instance, assumption of the Ramberg-Osgood model (Eq. (3.15)) allows to derive the following approximate one-to-one relation between Y/T and e_m (also shown in figure 3.21(b)) (see Appendix A for a mathematical proof):

$$Y/T \approx \left[\frac{0.002}{\ln(1+e_m)}\right]^{\ln(1+e_m)} (1+e_m) \tag{3.18}$$

  Despite the predicted one-to-one relation, the amount of scatter is again unmistakable.

3.6.2 Two-stage strain hardening behaviour

Figure 3.21(b) indicates that application of the Ramberg-Osgood model may introduce errors for stress-strain curves of line pipe steels, as it is clearly incapable to capture the bulk of all observed Y/T-e_m couples. This limitation can be attributed to the observation that many line pipe steels exhibit two distinct stages of strain hardening [3.14, 3.68–3.71] (figure 3.22). Such post-yield behaviour is often referred to in literature as a 'double-n' behaviour and can be recognized as a bilinear curve in a $\log(\sigma)$ – $\log(\epsilon_{pl})$ diagram (figure 3.22(b)). In such graph, which is highly similar to a Hollomon analysis (figure 3.14(b)), the Ramberg-Osgood model behaves fully linear and therefore represents a single-stage strain hardening behaviour [3].

The observed presence of double-n strain hardening behaviour should not necessarily come as a surprise, as there are many materials that exhibit this phenomenon. To the authors' knowledge, two-stage strain hardening has been

[3] Note that, in contrast with figure 3.14(b), figure 3.22(b) depicts strain (in the vertical axis) as a function of stress (in the horizontal axis). This reflects the fact that the Ramberg-Osgood equation (Eq. (3.15)) also expresses strain as a function of stress. Hence, its strain hardening exponent represents a linear slope in the representation of figure 3.22(b) (and not figure 3.14(b)).

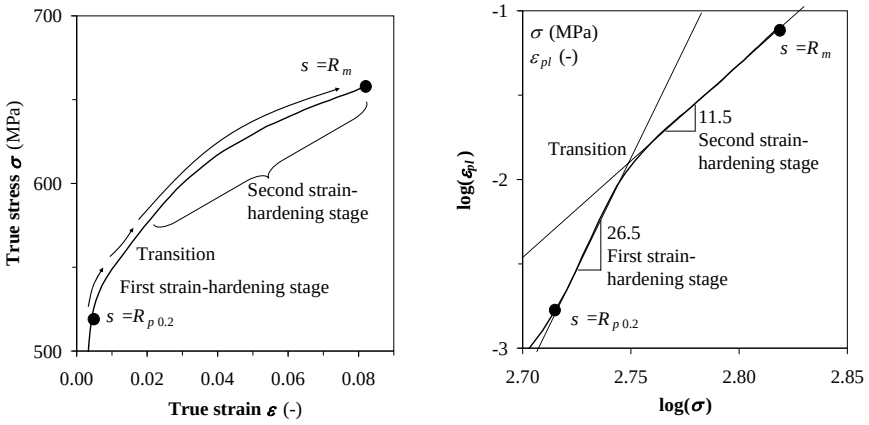

Figure 3.22: (a) Example line pipe steel (X70) stress-strain curve with two stages of strain hardening and (b) identification of double-n behaviour in a $\log(\sigma)$ - $\log(\epsilon_{pl})$ diagram.

observed in various types of steels [3.72–3.79], stainless steels [3.48, 3.51, 3.80], titanium [3.81, 3.82], copper [3.83, 3.84], nickel [3.85], and some other metals and alloys [3.60, 3.86]. Note that the possible presence of double-n behaviour is also mentioned in the ASTM standard E 646 [3.87]. Attempts have been made to explain the microstructural nature of double-n behaviour (see e.g. [3.88] for line pipe steels), but a unified theory is still lacking.

Despite the abundance of materials that have been found to harden in two stages, the efforts that have been undertaken to describe the mechanical behaviour of these metals or alloys more accurately seem fairly modest. Of all constitutive laws mentioned up to this point, only the Ludwigson equation is capable of describing strain hardening behaviour as a transition between two distinct and independent stages. However, since the exponential correction term $\exp(K_2 + n_2\epsilon_{pl})$ in Eq. (3.13) is always positive, Ludwigson's model is restricted to curves that yield at stress values greater than indicated by the power law term $K_1\epsilon_{pl}^{n_1}$ in its equation (consider small ϵ_{pl}-values in figure 3.18). Also, it was specifically developed to describe plastic flow behaviour. Ludwigson's equation is unsuited for including linear elastic deformations, as stress becomes $\exp(K_2)$ even for zero (plastic) strain. Even if a correction were to be performed (e.g. $\sigma = E\epsilon$ below, and the Ludwigson equation above a certain stress value), it would have a sharp yield point and, as a result, difficulties to describe the round house initial yielding which is desired under strain based conditions (section 3.4).

In order to deal with the lack of generous model equations for two-stage strain hardening, some material-specific relations have been proposed in literature. Most documented and explored are stainless steel alloys, which show an exceptionally pronounced 'double-n' behaviour [3.89–3.97]. Other models have additionally focused on aluminium alloys and high strength steels [3.93, 3.98]. All reported material-specific equations are piecewise combinations of – sometimes slightly modified – Ramberg-Osgood equations, possibly followed by a certain amount of linear strain hardening. Although providing excellent agreements for the specifically addressed materials, the equations in [3.89–3.98] are not generic and therefore difficult to adopt for other material categories. Indeed, they deal with some material-specific features such as a clear distinction between strain hardening behaviour before and after 0.002 (0.2 %) plastic strain (typical for stainless steels).

Summarizing this paragraph, it may be concluded that:

- *high strength line pipe steels belong to the large category of materials that exhibit two stages of strain hardening;*
- *the standardized Ramberg-Osgood model is incapable to simultaneously describe both strain hardening stages;*
- *a full-range stress-strain model for the two-stage strain hardening of these steels has not yet been developed.*

3.7 The 'UGent' stress-strain model for continuously yielding line pipe steels

Extrapolating the conclusion of section 3.6.2, there is a strong application potential for a stress-strain model that describes metals with two stages of strain hardening. This viewpoint has led to the development of the 'UGent' stress-strain model, which is the subject of the current section. Attention is given to the mathematical background (section 3.7.1) and how to interpret the model parameters (section 3.7.2). A particular focus goes to the advantages of the 'UGent' model over other models in section 3.7.3.

It must be emphasized that the development philosophy of the 'UGent' model is purely empirical. In particular, no attempts are made to link stress-strain behaviour with the material's microstructure. The 'UGent' model merely attempts to mathematically describe the macrostructural uniaxial tensile behaviour of line pipe steels. Further, in accordance with common practice (section 3.5.2), a homogeneous and isotropic material behaviour is assumed for simplicity.

3.7.1 Mathematical background

The proposed model applies to true stress and strain (σ–ϵ) values, since these quantities have more physical meaning than their engineering equivalents. Also, this allows for an accurate description up to the onset of necking. To develop its mathematical description, the following constraints were put forward (figure 3.23) [3.99]:

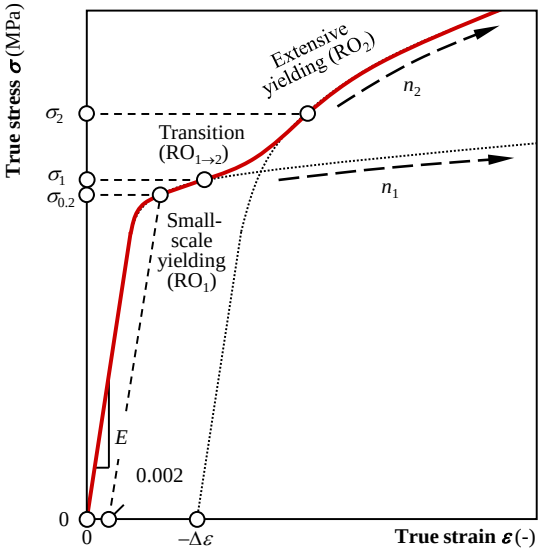

Figure 3.23: Graphical representation of the UGent model.

- In the early yielding area (small plastic strains, just after the onset of yielding), a Ramberg-Osgood equation with a first strain hardening exponent n_1 should be followed. This curve is called RO_1. Note that, by this constraint, a Lüders plateau is not explicitly included in the model. Nevertheless, an attempt has been undertaken to describe discontinuous yielding by RO_1 (see section 3.10).

- In the extensive yielding area (large plastic strains, up to the onset of necking), the curve should follow a Ramberg-Osgood equation with a second strain hardening exponent n_2, possibly translated over a certain strain value to ensure continuity. This curve is referred to as RO_2.

- Between these two yielding areas there should be a transition zone, in which the curve shape smoothly changes from RO_1 to RO_2. This curve is denoted $RO_{1\rightarrow2}$.

Strains are expressed as a function of stress in the Ramberg-Osgood equation. As a consequence, the new curve equations will also be expressed in terms of stress. Given the objective of the model to describe a 'double-n' behaviour, the introduction of two independent strain hardening exponents n_1 and n_2 should be no surprise. Additionally, two stress parameters σ_1 and σ_2 must be defined in order to delimitate each equation's application interval as follows:

$$\epsilon = \begin{cases} \mathrm{RO}_1(\sigma) & \sigma \leq \sigma_1 \\ \mathrm{RO}_{1\to 2}(\sigma) & \sigma_1 < \sigma \leq \sigma_2 \\ \mathrm{RO}_2(\sigma) & \sigma_2 < \sigma \end{cases} \tag{3.19}$$

Expressions for RO_1 and RO_2 simply follow from Eq. (3.15). To maintain an acceptable equation complexity, the commonly used 0.2 % proof stress (true value, denoted as $\sigma_{0.2}$) is used as the yield strength in *both* RO_1 and RO_2. Further, the translation strain in RO_2 is called $\Delta\epsilon$. To obtain a certain similarity with the Swift model, its sign was chosen to correspond to that of the pre-strain ϵ_0 in Eq. (3.8) (compare figure 3.23 with figure 3.15). Hence:

$$\mathrm{RO}_1(\sigma) = \frac{\sigma}{E} + 0.002\left(\frac{\sigma}{\sigma_{0.2}}\right)^{n_1} \tag{3.20}$$

$$\mathrm{RO}_2(\sigma) = \frac{\sigma}{E} + 0.002\left(\frac{\sigma}{\sigma_{0.2}}\right)^{n_2} - \Delta\epsilon \tag{3.21}$$

The gradual transition between RO_1 and RO_2 is achieved by stipulating that the slope of $\mathrm{RO}_{1\to 2}$ is a linear interpolation between that of RO_1 and RO_2:

$$\frac{\mathrm{dRO}_{1\to 2}}{\mathrm{d}\sigma} = \frac{\mathrm{dRO}_1}{\mathrm{d}\sigma} + \frac{\sigma - \sigma_1}{\sigma_2 - \sigma_1}\left(\frac{\mathrm{dRO}_2}{\mathrm{d}\sigma} - \frac{\mathrm{dRO}_1}{\mathrm{d}\sigma}\right) \tag{3.22}$$

This leads to the following expression for $\mathrm{RO}_{1\to 2}$:

$$\begin{aligned} \mathrm{RO}_{1\to 2}(\sigma) = \frac{\sigma}{E} + 0.002\left(\frac{\sigma}{\sigma_{0.2}}\right)^{n_1} + 0.002\frac{\sigma - \sigma_1}{\sigma_2 - \sigma_1}\left[\left(\frac{\sigma}{\sigma_{0.2}}\right)^{n_2}\right. \\ \left. - \left(\frac{\sigma}{\sigma_{0.2}}\right)^{n_1}\right] - \frac{0.002}{\sigma_2 - \sigma_1}\left[\frac{\sigma^{n_2+1} - \sigma_1^{n_2+1}}{(n_2+1)\,\sigma_{0.2}^{n_2}} - \frac{\sigma^{n_1+1} - \sigma_1^{n_1+1}}{(n_1+1)\,\sigma_{0.2}^{n_1}}\right] \end{aligned} \tag{3.23}$$

and for $\Delta\epsilon$ in Eq. (3.21):

$$\Delta\epsilon = \frac{0.002}{\sigma_2 - \sigma_1}\left[\frac{\sigma_2^{n_2+1} - \sigma_1^{n_2+1}}{(n_2+1)\,\sigma_{0.2}^{n_2}} - \frac{\sigma_2^{n_1+1} - \sigma_1^{n_1+1}}{(n_1+1)\,\sigma_{0.2}^{n_1}}\right] \tag{3.24}$$

As a result, Eqs. (3.19), (3.20), (3.21), (3.23) and (3.24) completely define the 'UGent' stress-strain model.

3.7.2 Interpretation of model parameters

The model contains six independent parameters (E, $\sigma_{0.2}$, n_1, n_2, σ_1 and σ_2), the interpretation of which is discussed below.

Starting at low stresses, the linear elastic area is defined by Young's elasticity modulus E. Next, just beyond the 0.2 % proof stress $\sigma_{0.2}$, early yielding is characterized by a first strain hardening exponent n_1. The higher its value, the 'sharper' the knee of the curve. Then, a transition occurs from early to extensive yielding. The extent of the transition area is determined by the two stresses σ_1 and σ_2. Finally, strains up to the onset of necking are described by the second strain hardening exponent n_2. Similar to n_1, a higher value corresponds to a flatter stress-strain curve.

3.7.3 Advantages over other existing models

In contrast with the models of Ludwik, Hollomon, Ramberg-Osgood, Voce and Swift (table 3.2), the 'UGent' model has the evident capability of representing materials with two stages of strain hardening. Further, advantages of the 'UGent' model to other existing stress-strain models that do allow for a description of 'double-n' behaviour are:

- The possibility to describe both curves with a gradually increasing work hardening behaviour ($n_1 > n_2$; curvature direction shifts upward in the transition area as in figure 3.23) and curves with a gradually decreasing work hardening behaviour ($n_1 < n_2$). As illustrated in figure 3.24, both configurations can occur for high strength line pipe steels and the possibility to represent both is therefore essential. The Ludwigson equation (Eq. (3.13)), in contrast, was specifically developed for curves that show an increasing work hardening behaviour ($n_1 > n_2$). Further, the models developed in [3.90–3.98] describe curves that do not have a clear shift in curvature direction.

- A high degree of flexibility in choosing the transition range from the first to the second yielding stage. In the 'UGent' model, this range can be deliberately chosen in terms of σ_1 and σ_2, whereas the models in [3.90–3.98] are restricted to a transition around 0.002 plastic strain.

- The 'UGent' model simultaneously describes the linear elastic stage and a smoothly initiating ('round house') yielding behaviour. As discussed in section 3.6.2, Ludwigson's equation does not contain a linear elastic stage and shows a sharp yield point.

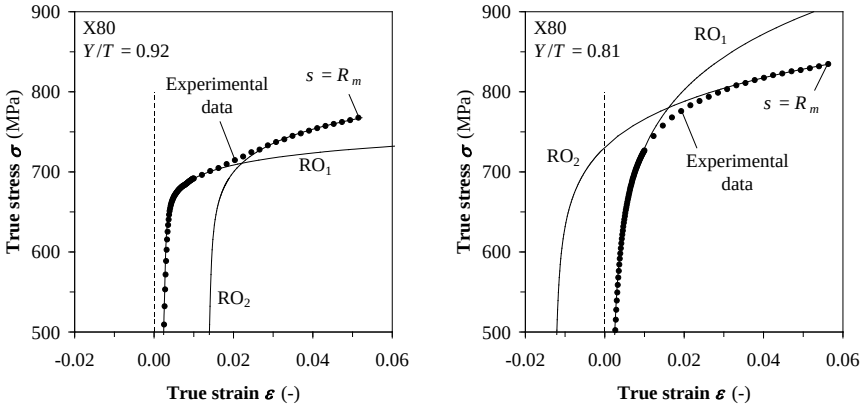

Figure 3.24: Different possible curve shapes can be observed for line pipe steels: (a) $n_1 > n_2$, (b) $n_1 < n_2$.

3.8 Determining the 'UGent' model parameters

The practical applicability of a model does not only depend on its suitability to accurately represent the subject aimed at. The availability of a procedure to determine appropriate model parameters is at least as important. This statement is highly relevant to the 'UGent' model, as the determination of six parameters may be challenging without a systematic approach.

This section discusses three fundamentally different methodologies to estimate 'UGent' model parameters: a numerical, a graphical and an analytical method. The choice of method depends on a trade-off between the accuracy of the model curve and the complexity of the analysis. In addition, the availability of information may exclude the more complex methods. An overview of these considerations is graphically summarized in table 3.4 and each method is separately discussed in sections 3.8.1 to 3.8.3. An illustrative comparison of curves obtained with different methods is given in section 3.8.4.

3.8.1 Numerical method

Optimal model representations can be numerically obtained by least-squares curve fitting. This technique aims to minimize the root mean square value of the model error, denoted ϵ_{RMS} (-), by iteratively adjusting the model parameter values through a minimization algorithm (starting from an initial guess). If this error is calculated at a discrete set of N stress-strain points (ϵ_i, σ_i), $i = 1 \ldots N$, ϵ_{RMS} is generally defined as follows:

Table 3.4: Considerations for choosing a method to determine suited 'UGent' model parameters

Method (section)	Accuracy / Complexity	Required input
Numerical (3.8.1)	↑	Full true stress-strain curve
Graphical (3.8.2)	|	Full true stress-strain curve
Analytical (3.8.3)		Limited set of engineering stress-strain characteristics

$$\epsilon_{RMS} = \sqrt{\frac{1}{N}\sum_{i=1}^{N}\left[\epsilon_i - \epsilon_{model}\left(\sigma_i, \vec{\theta}\right)\right]^2} \tag{3.25}$$

with $\epsilon_{model}\left(\sigma, \vec{\theta}\right)$ the expression that defines the stress-strain model (Eq. (3.19) for the particular case of the 'UGent' model), where $\vec{\theta}$ symbolizes the model parameters as a parameter vector. In what follows, the 'optimal' parameter set (i.e. which yields the minimal ϵ_{RMS}-value) is denoted as $\vec{\theta}^{\star}$. Note that the least-squares curve fitting method is general and can also be applied on stress-strain models other than the 'UGent' model, by simply incorporating the appropriate model definition $\epsilon_{model}\left(\sigma_i, \vec{\theta}\right)$ in Eq. (3.25).

Based on experience with curve fitting of the 'UGent' model (section 3.9.1), it has been found that three aspects influence the outcome and required computational time of the least-squares curve fitting procedure: the choice of minimization algorithm, the initial parameter guess $\vec{\theta}_0$, and the choice of data points (ϵ_i, σ_i) used in the definition of ϵ_{RMS} (Eq. (3.25)). More details on how these aspects were dealt with are provided in Appendix B and [3.100].

3.8.2 Graphical method

Although the numerical method from section 3.8.1 yields 'optimal' model parameter values $\vec{\theta}^{\star}$, it requires an iterative curve fitting protocol which may be computationally intensive and relies on a proper initial guess $\vec{\theta}_0$ to achieve the absolute minimum of ϵ_{RMS}. Consequently, this method may be too cumbersome for cases where a fast analysis is desired.

This section explains an alternative, graphical method which does not produce the optimal result but is far more intuitive to perform than the numerical

method. Similarly, the graphical method starts from an experimentally determined (true) stress-strain curve. In contrast, however, the method does not require an iterative numerical procedure. Instead, it allows to read suited model parameters (E, $\sigma_{0.2}$, n_1, n_2, σ_1, σ_2) from a well-chosen set of different graphical representations of the stress-strain curve, as discussed below. Note that similar approaches have been developed (section 3.5) for the following models:

- Ludwik model (differential Crussard-Jaoul analysis),
- Hollomon model (Hollomon analysis),
- Swift model (modified Crussard-Jaoul analysis),
- Voce model (Kocks-Mecking analysis).

First, E and $\sigma_{0.2}$ can obviously be determined as the experimentally observed Young's modulus and true yield strength. Since the difference between engineering and true values becomes academic for elastic and limited plastic deformations, one could also just equalize $\sigma_{0.2}$ to the engineering yield strength $R_{p0.2}$.

Since the plastic part of RO_1 is a Hollomon equation, n_1 can be determined by plotting $\log(\epsilon_{pl})$ against $\log(\sigma)$. If the stress-strain curve shows a two-stage strain hardening behaviour, such plot should approximately form two straight lines with a transition in between. The strain hardening exponent n_1 then corresponds to the slope of the straight line that represents the smallest values of $\log(\sigma)$ (figure 3.25(a)). This is analogous to the original Hollomon analysis in figure 3.14(b). Note that the same methodology cannot be applied for n_2, since RO_2 does not represent a Hollomon equation because of the introduction of the strain translation term $-\Delta\epsilon$.

To determine n_2, a modified Crussard-Jaoul analysis can be applied on the extensive yielding area (which was identified in the $\log(\sigma) - \log(\epsilon_{pl})$ diagram as described above). Indeed, the plastic part of RO_2 can be considered as a Swift equation (Eq. (3.8), replace ϵ_0 with $\Delta\epsilon$), again expressed in terms of stress instead of strain. If shows the following relationship in a $\log(\sigma) - \log(\mathrm{d}\sigma/\mathrm{d}\epsilon_{pl})$ diagram (figure 3.25(b)):

$$\log\left(\frac{\mathrm{d}\sigma}{\mathrm{d}\epsilon_{pl}}\right) = \log\left(\frac{\sigma_{0.2}^{n_2}}{0.002 n_2}\right) + (1 - n_2)\log(\sigma) \tag{3.26}$$

Once n_1 and n_2 have been determined, σ_1 and σ_2 can finally be tuned to serve two purposes. On the one hand, the shape and location of the transition area can be adjusted. On the other hand, a certain value of $\Delta\epsilon$ can be aimed for. A graphical method that aims for both purposes is presented in figure 3.26. It is based on a plot of strain values as a function of stress values, and consists of the following steps (also indicated in the figure):

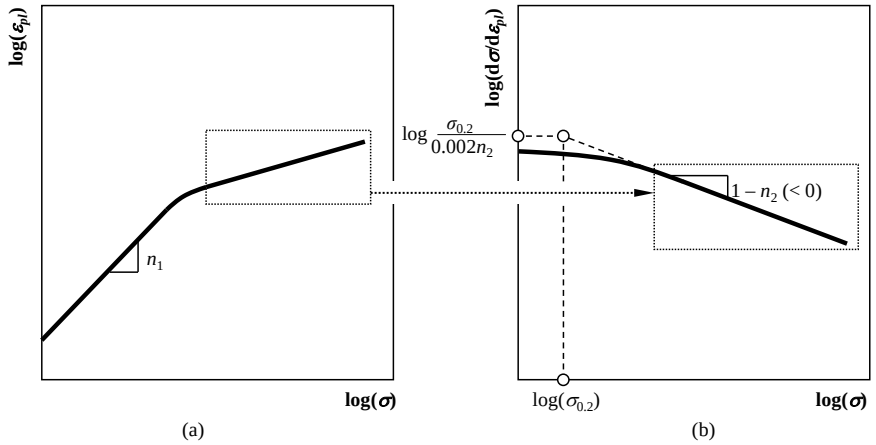

Figure 3.25: Graphical method to determine n_1 and n_2: (a) Hollomon type analysis for n_1, (b) modified Crussard-Jaoul analysis for n_2.

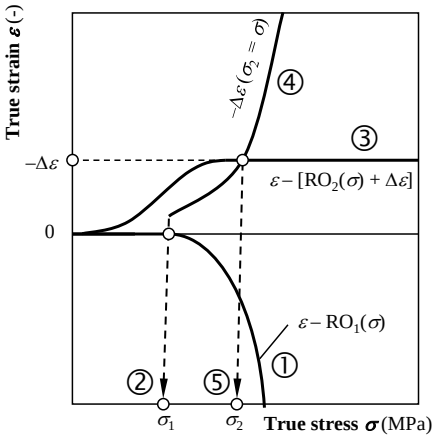

Figure 3.26: Graphical method to determine σ_1 and σ_2.

1. For all experimental datapoints, plot $\epsilon - \mathrm{RO}_1(\sigma)$ (Eq. (3.20)). This is possible, since all parameters that define RO_1 (E, $\sigma_{0.2}$, n_1) have already been determined.

2. In the early yielding area, $\epsilon - \mathrm{RO}_1(\sigma)$ is near zero. This is not the case for the transition area. Hence, σ_1 can be identified as the stress σ where $\epsilon - \mathrm{RO}_1(\sigma)$ diverges from zero.

3. For all experimental datapoints, plot $\epsilon - [\mathrm{RO}_2(\sigma) + \Delta\epsilon]$ (Eq. (3.21)). This

is possible, since all parameters that define $RO_2 + \Delta\epsilon$ (namely E, $\sigma_{0.2}$, n_2) have already been determined. If the UGent model is fully representative for the extensive yielding area, the plotted function converges to a horizontal line which corresponds with $-\Delta\epsilon$.

4. Given the determined values for n_1, n_2, $\sigma_{0.2}$ and σ_1, depict the obtained value for $-\Delta\epsilon$ as a function of σ_2 (Eq. (3.24), $\sigma_2 = \sigma$) in the same plot.

5. The value σ_2 that fits with the experimental data should provide a suited value for $-\Delta\epsilon$, which has been identified in step 3. Hence, a good value for σ_2 can be identified as the σ-value of the intersection of the horizontal line from step 3 that represents extensive yielding, and the relationship between σ_2 and $-\Delta\epsilon$ from step 4.

To assess the performance and robustness of the graphical parameter estimation method, it has been applied on the line pipe steel curve from figure 3.22. The result is shown in figure 3.27. Figure 3.27(a) shows the Hollomon-type analysis to identify n_1. Second, the modified Crussard-Jaoul analysis for n_2 is shown in figure 3.27(b). Note that, in contrast with n_1, the obtained n_2-value (15.5) does not at all agree with the slope of the corresponding linear part of figure 3.27(a) (11.5). This reflects the fact that a Hollomon-type analysis cannot be used to characterize RO_2, which is a Swift equation. Third, σ_1 and σ_2 are estimated rather arbitrarily in figure 3.27(c). Note that $\epsilon - [RO_1(\sigma) + \Delta\epsilon]$ does not converge to a horizontal line as assumed in figure 3.26, which indicates that part of the theoretical representativeness of the 'UGent' model is lost towards necking. Nevertheless, figure 3.27(d) shows that the obtained model curve provides a highly satisfactory representation of the experimental stress-strain data. Given the fairly arbitrary visual choice of some parameter values, this example indicates that the graphical method is sufficiently robust for practical use.

A more elaborate coverage of the graphical parameter determination method, including more application examples, is provided in [3.99].

3.8.3 Analytical method

Both the numerical (section 3.8.1) and the graphical (section 3.8.2) method require the entire stress-strain curve up to the point of necking as an input. Very often (literature, industrial reports, ...), however, a discrete set of commonly used tensile test characteristics is tabulated rather than providing the full curve. In such cases, application of the numerical and graphical methods becomes impossible and 'UGent' model parameters have to be estimated through an alternative procedure. To this purpose, an analytical method has been developed, which is the subject of the current section. Evidently, since this method starts from a highly limited set of input data, the calculated model parameters

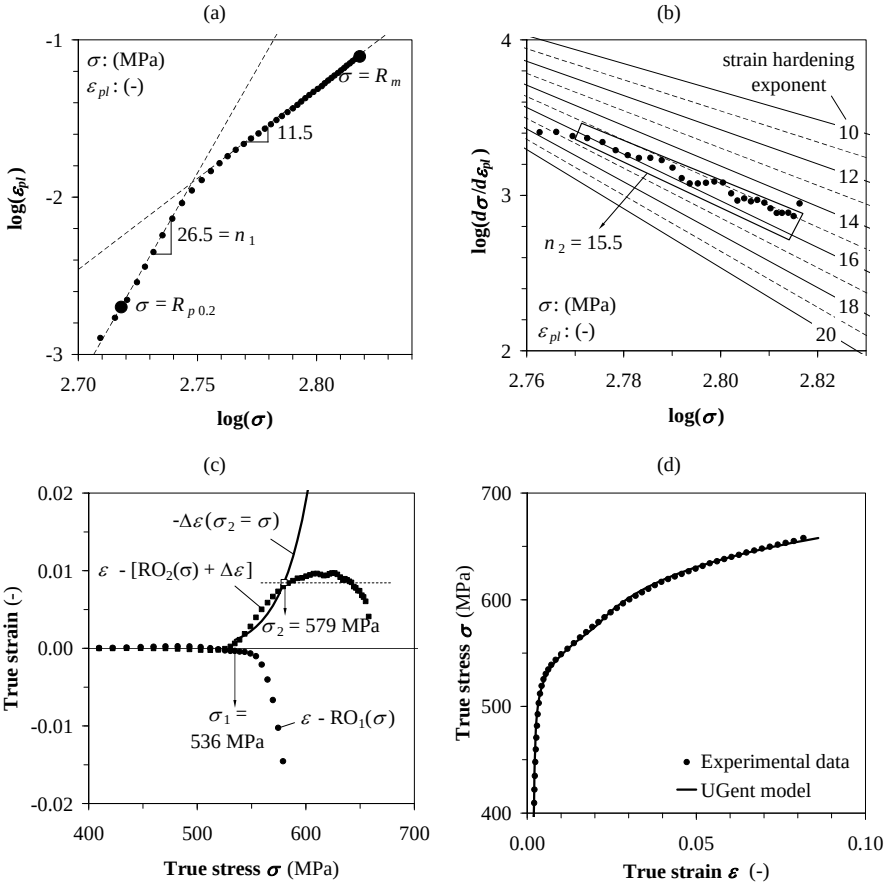

Figure 3.27: Application of the graphical method on the X70 steel from figure 3.22.

can be expected to be far from optimal. Nevertheless, it will be shown that fair approximations can be achieved.

Prior to developing the proposed methodology, four constraints were put forward:

1. All tensile test characteristics, necessary to define the model parameters, should be extracted from the experimentally determined engineering stress-strain $(s - e)$ curve rather than a curve converted into true stress and true strain $(\sigma - \epsilon)$.

2. Preferably, these tensile test characteristics should be according to common practice. In particular, Young's modulus E, yield strength $R_{p0.2}$, ultimate tensile strength R_m, yield-to-tensile ratio Y/T and uniform elon-

gation e_m deserve attention.

3. The model should provide a good description of initial yielding, arbitrarily defined in this section as the area in which ϵ_{pl} is below 0.01. This constraint was put forward because of the particular importance of initial yielding in flaw assessments [3.101].

4. The model should approach the experimental curve at the point of necking. This facilitates an accurate description of advanced plastic stress-strain behaviour, including a fair representation of R_m and e_m.

The developed procedure consists of five steps, summarized in table 3.5. Governing equations are provided in Appendix B. For a full background behind these equations, the reader is referred to [3.102, 3.103].

Table 3.5: Analytical parameter estimation method: summary of steps.

Step	Description	Result
1	Define the linear elastic area	E and $\sigma_{0.2}$
2	Define early yielding	n_1
3	First estimation of extensive yielding	Preliminary n_2-value (n_{2i})
4	Define the transition zone	σ_1 and σ_2
5	Define extensive yielding	n_2

In essence, the following is particularly worth mentioning.

- The determination of n_1 in step 2 requires a less common tensile test characteristic, namely the 1.0 % proof stress $R_{p1.0}$. Indeed, all common characteristics merely apply to the elastic stage (E), the first indication of yielding ($R_{p0.2}$) or the onset of necking (R_m, e_m). As an example, figure 3.28 shows two experimental stress-strain curves, normalized against their 0.2 % proof stress for ease of comparison. Even though the uniform elongation e_m and the relative levels of $R_{p0.2}$ and R_m (or simply Y/T) are similar, a different initial yielding behaviour is observed.

- Whereas steps 1, 2, 4 and 5 provide definitive parameter values, step 3 merely provides a preliminary value for n_2 (denoted n_{2i}). This initial guess proved to be necessary to determine σ_2 in step 4. The obtained σ_2-value is then used in step 5 to calculate a better and definitive value for n_2.

- The determination of σ_2 in step 4 has limits of validity, shown in figure 3.29. These limits of validity have been designed to represent the bulk of the 139 investigated stress-strain curves, by encapsulating their 'optimal' (n_1, n_2)-values $(n_1^\star, n_2^\star)$ determined through the numerical method (section 3.8.1).

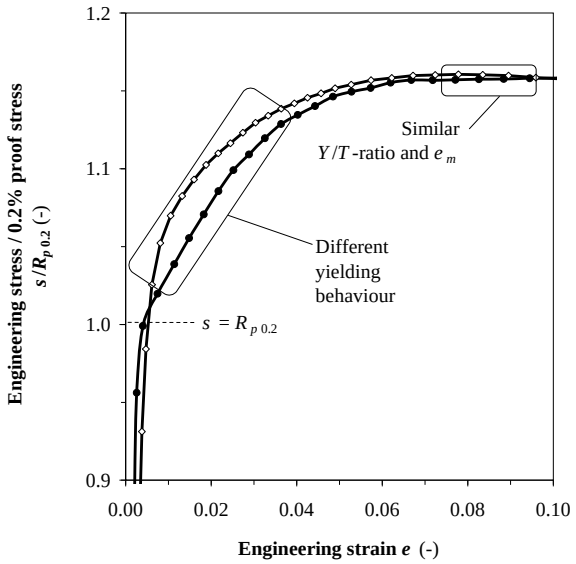

Figure 3.28: Even with equal values for Y/T and e_m, different stress-strain curve shapes can be observed.

Summarizing matters, the analytical method on the one hand provides a straightforward method to derive fair 'UGent' model representations from a limited set of characteristics. On the other hand, the less commonly reported 1.0 % proof stress $R_{p1.0}$ is required, and the proper application of the method may be limited by the validity area for step 4 (figure 3.29).

3.8.4 Illustrative comparison

By means of illustration, figure 3.30 plots stress-strain model curves obtained with the three abovementioned methods for the experimental curve earlier depicted in figure 3.22. All model curves – particularly those resulting from the numerical and graphical method which use full experimental data as an input, table 3.4 – closely approximate the experimental data. Corresponding 'UGent' model parameters are provided in table 3.6 [4]. Model parameter values resulting from different methods are generally comparable. The largest relative difference is observed for n_1, the graphical method resulting in a 13 % higher value than the numerical method.

Since the analytical method is the most approximate of all three approaches,

[4]Note that the performance of the graphical method has already been shown with this stress-strain curve in figure 3.27.

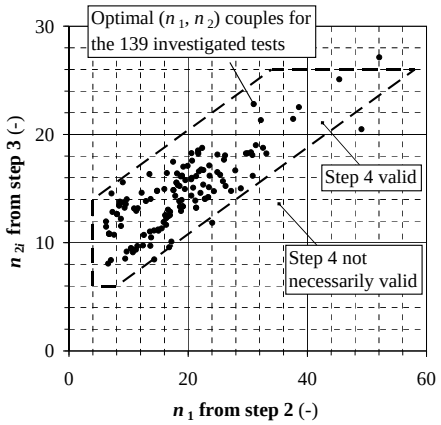

Figure 3.29: The validity area for step 4 in the analytical procedure has been based on the optimal (n_1, n_2)-couples of the 139 investigated stress-strain curves.

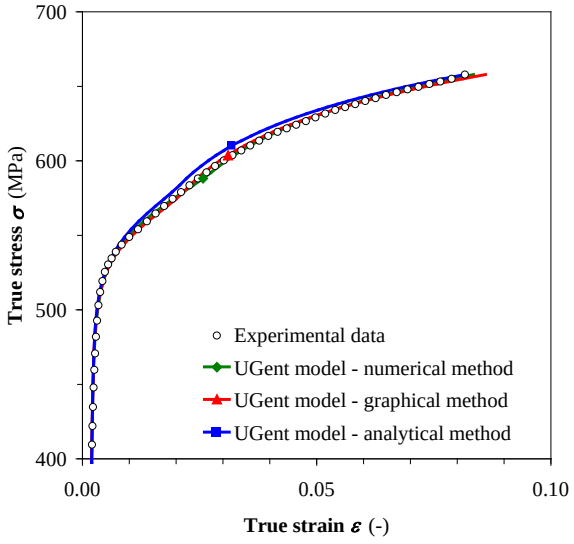

Figure 3.30: Comparison between experimental stress-strain data and 'UGent' model curves obtained from different methods.

its performance relative to the (optimal) numerical method is more elaborately compared in section 3.9.2.

Table 3.6: Graphically obtained 'UGent' model parameter values for the stress-strain curve from figure 3.22.

Method	E (MPa)	$\sigma_{0.2}$ (MPa)	n_1 (-)	n_2 (-)	σ_1 (MPa)	σ_2 (MPa)
Numerical	204,000	520	23.5	15.1	541	593
Graphical	204,000	523	26.5	15.5	536	579
Analytical	204,000	523	26.1	15.6	523	585

3.9 Comparison between the 'UGent' model and the standardized Ramberg-Osgood model

The 'UGent' model has been developed from the philosophy that the common practice of stress-strain modelling is insufficient to properly represent the full-range tensile behaviour of high strength line pipe steels. To verify and quantify this statement, its performance is compared to that of the standardized Ramberg-Osgood model. This comparison has been performed on each of the 139 investigated stress-strain curves. As regards the expression of the Ramberg-Osgood model, Eq. (3.15) is taken for the following.

First, the full potential of the 'UGent' model is explored by comparing its optimal representations with those of the Ramberg-Osgood model (section 3.9.1). To that purpose, model parameters have been obtained for both models by least-squares curve fitting as explained in section 3.8.1. Second, section 3.9.2 compares the analytical method from section 3.8.3 with both (a) the least-squares curve fitted 'UGent' models, and (b) the most commonly used analytical method to estimate Ramberg-Osgood model parameters. For the latter, $\sigma_{0.2}$ is estimated as $R_{p0.2}$, and n follows from the prerequisite that the model curve should intersect the actual stress-strain curve at the point of necking:

$$n = \frac{\ln\left(\frac{\epsilon_m - \sigma_m/E}{0.002}\right)}{\ln\left(\frac{\sigma_m}{\sigma_{0.2}}\right)} \tag{3.27}$$

Note that a similar equation is prescribed by API 1104 [3.62] for the determination of n in Eq. (3.14).

All obtained model curves have been assessed on the basis of their RMS error ϵ_{RMS} as defined in Eq. (3.25). To calculate this value, data points (ϵ_i, σ_i) have been chosen as explained in Appendix B. RMS error values for the 'UGent' model and the Ramberg-Osgood model are denoted $\epsilon_{RMS,UGent}$ and $\epsilon_{RMS,R-O}$, respectively.

3.9.1 Improvement of the 'UGent' model with respect to the Ramberg-Osgood model

Figure 3.31 compares all obtained optimal ϵ_{RMS}-values (denoted $\epsilon^{\star}_{RMS}$) from the fitted Ramberg-Osgood model and 'UGent' model for two completely different stress-strain curves. For all investigated curves, the 'UGent' model performs better. This should be of no surprise, as the Ramberg-Osgood model can be described by the 'UGent' model by setting $n_1 = n_2$. Remarkable, however, is the degree of improvement. For the complete dataset, the average $\epsilon^{\star}_{RMS}$ is roughly three times lower for the 'UGent' model (average $\epsilon^{\star}_{RMS,UGent}$ = 0.0004) than for the Ramberg-Osgood model (average $\epsilon^{\star}_{RMS,R-O} = 0.0012$). Figure 3.32(a) provides intuition on how to interpret these average values, showing an example dataset with curve fits that perform according to the average $\epsilon^{\star}_{RMS}$-values for both the 'UGent' model and the Ramberg-Osgood model.

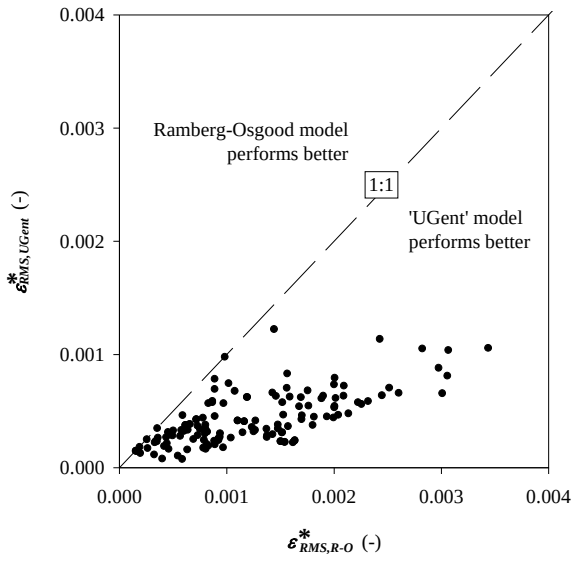

Figure 3.31: The 'UGent' model systematically performs better than the Ramberg-Osgood model.

A closer investigation reveals that the improvement obtained by the 'UGent' model is increasingly apparent for higher Y/T-ratios (figure 3.33). The average ratio $\epsilon^{\star}_{RMS,UGent}/\epsilon^{\star}_{RMS,R-O}$ evolves from 43 % ($Y/T < 0.80$) to 25 % ($Y/T > 0.90$). Apparently, the Ramberg-Osgood model tends to produce increasingly poor fits with increasing Y/T, whereas the 'UGent' model performs fairly constantly over the whole range of investigated curves. To further explore this observation, the obtained optimal values $n^{\star}$ (Ramberg-Osgood model), $n^{\star}_1$

and $n_2^\star$ ('UGent' model) are plotted against Y/T in figure 3.34. Four observations can be made:

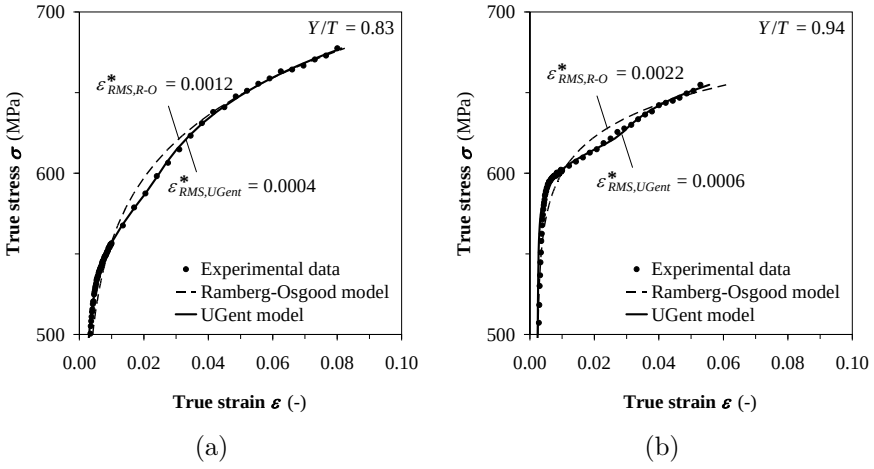

Figure 3.32: Example least-squares model curve fits (a) with near-average RMS error values, (b) for a curve with extremely pronounced double-n behaviour.

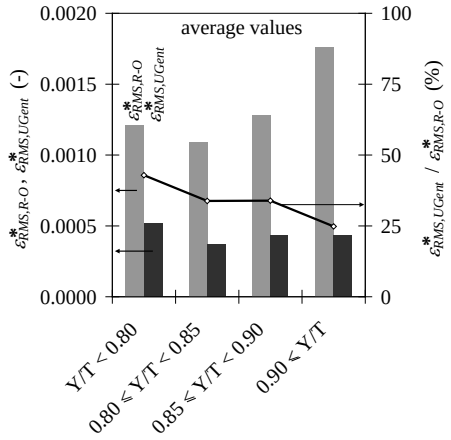

Figure 3.33: The improvement achieved by the 'UGent' model is more pronounced for higher Y/T-ratios.

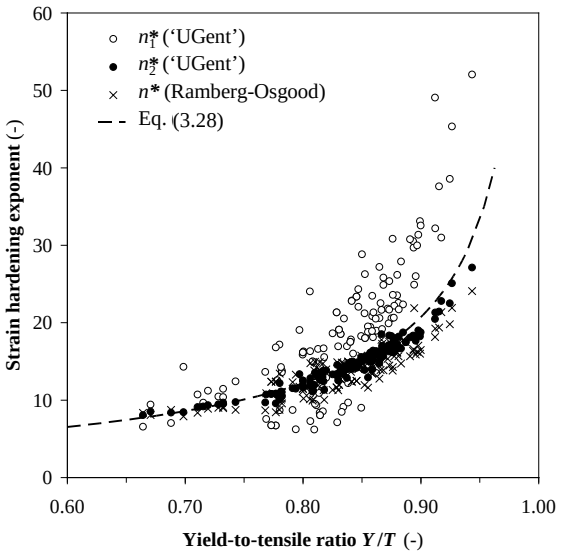

Figure 3.34: Two stage strain hardening becomes more pronounced as Y/T increases.

- For Y/T-ratios below 0.80, $n_1^\star$ and $n_2^\star$ are often similar. In these cases, strain hardening can be well described by one strain hardening exponent, as in the Ramberg-Osgood model. The potential of the 'UGent' model to provide an improvement is therefore limited.

- For Y/T-ratios above 0.80, however, there is an increasing tendency towards two-stage strain hardening behaviour as $n_1^\star$ diverges from $n_2^\star$. Eventually, the distinction between $n_1^\star$ and $n_2^\star$ becomes highly pronounced. In these cases, the 'UGent' model clearly performs better than the Ramberg-Osgood model, which explains figure 3.33. For example, a clear illustration of a curve with double-n behaviour is shown in figure 3.32(b). This curve has a very high Y/T-ratio of 0.94.

- There is a remarkable correspondence between $n_2^\star$ ('UGent' model) and $n^\star$ (Ramberg-Osgood model). This means that the curve fitted Ramberg-Osgood model mainly describes the extensive yielding area. This observation, also particularly visible in figure 3.32(b), is in accordance with findings in [3.101, 3.104].

- Apparently, n_2 ('UGent' model) and n are strongly related to Y/T. This relation is satisfactorily described by Eq. (3.28), which can be theoretically shown from the Ramberg-Osgood equation Eq. (3.15). Proof of this statement is given in Appendix A and [3.102].

$$n \quad \text{or} \quad n_2 \approx 3 + 2.5\frac{Y/T}{1.03 - Y/T} \tag{3.28}$$

Apart from providing proper post-yield curve shapes, a good model stress-strain curve should also provide an accurate representation of the experimental yield strength. Ideally, $\sigma_{0.2}$ should approximate $R_{p0.2}$. Whereas $\sigma^{\star}_{0.2}$ of the 'UGent' model is generally very close to $R_{p0.2}$ (between 96.2 % and 105.3 % of $R_{p0.2}$) for the investigated data, the Ramberg-Osgood model tends to show significantly larger variations (figure 3.35). In one case, Ramberg-Osgood's $\sigma^{\star}_{0.2}$-value was only 89.2 % of the actual yield strength, which would result in a significant and unwanted increase of conservativeness when used in a stress based design (section 2.2).

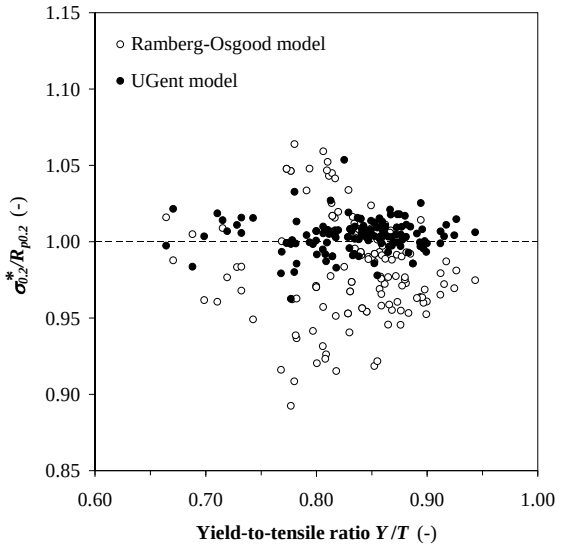

Figure 3.35: Least-squares curve fitted Ramberg-Osgood representations poorly estimate the yield strength of line pipe steels.

3.9.2 Performance of analytical model parameter estimations

3.9.2.1 'UGent' model: analytical method versus optimal model curves

Evidently, the analytical procedure starts from a limited amount of information and can therefore only strive to be approximate. To qualify its potential to

predict proper model representations, figure 3.36 compares the analytically obtained strain hardening exponents n_1 and n_2 with the numerically obtained (section 3.8.1) optimal values $n_1^\star$ and $n_2^\star$ for the 139 investigated stress-strain curves. Apparently, an excellent agreement is achieved for n_2. Scatter is more pronounced for n_1. Nevertheless, there is a clear correlation, the analytically estimated n_1 value being within 75 % and 125 % of $n_1^\star$ for 104 out of 139 investigated tests.

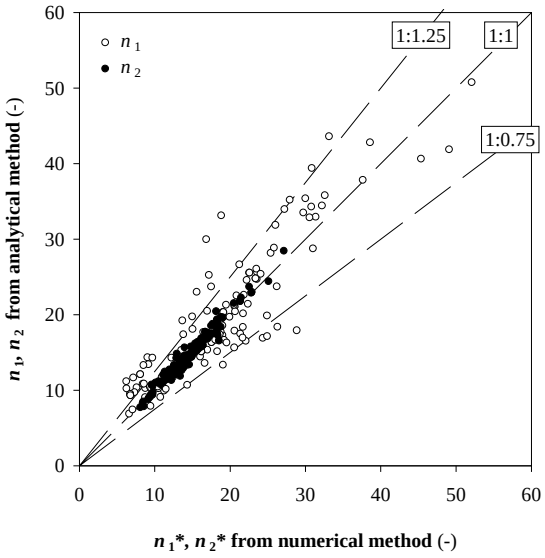

Figure 3.36: Analytically determined strain hardening exponents n_1 and n_2 give a good approximation of their optimal values. This observation is most pronounced for n_2.

The observed differences between optimal and analytically determined n_1-values result from the arbitrary choice to involve $R_{p1.0}$ in its analytical calculations. For instance, there is a scattered relation between the optimal $n_1^\star$ and $R_{p0.2}/R_{p1.0}$ (figure 3.37). Nevertheless, the use of $R_{p1.0}$ is defended by noting that – in comparison with the relation between $n_1^\star$ and Y/T (figure 3.34) – the scatter between $n_1^\star$ and $R_{p0.2}/R_{p1.0}$ is significantly smaller. Concretely, the coefficient of determination (better known as the R^2-value) of its exponential regression is 0.80, which is much closer to unity than that of an exponential regression for the Y/T – $n_1^\star$ plot (namely 0.57).

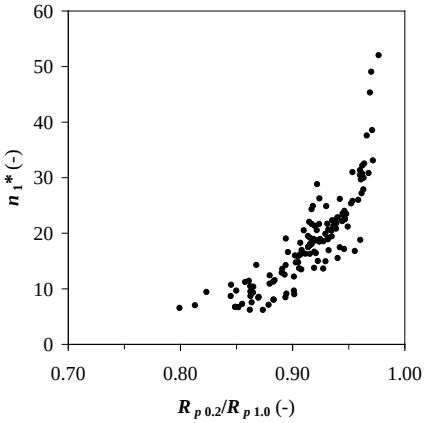

Figure 3.37: The relation between the optimal strain hardening exponent $n_1^\star$ and $R_{p0.2}/R_{p1.0}$ is scattered but stronger than that between $n_1^\star$ and Y/T (figure 3.34).

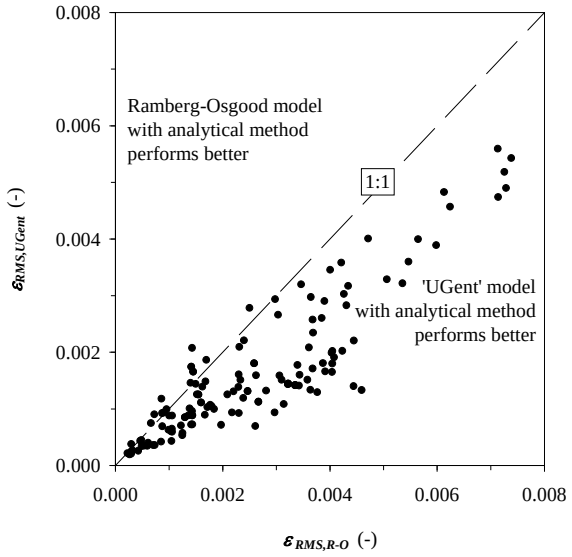

Figure 3.38: Apart from some rare exceptions, the analytically determined 'UGent' model performs better than the analytically determined Ramberg-Osgood model.

3.9.2.2 'UGent' model versus Ramberg-Osgood model: comparison of performances of analytical methods

Figure 3.38 compares the analytically obtained ϵ_{RMS}-values for the estimated Ramberg-Osgood models (Eq. (3.27)) and 'UGent' models. For 89 % of all investigated tests (124 out of 139), the 'UGent' model performs better than the Ramberg-Osgood model. On average, ϵ_{RMS} is 38 % lower for the 'UGent' model (0.0016) as compared to the Ramberg-Osgood model (0.0026). For some rare cases only, the RMS-value for the 'UGent' model was up to 145 % of that for the Ramberg-Osgood model.

To illustrate the average improvement obtained, figure 3.39(a) shows an example curve with model representations that roughly perform according to the average ϵ_{RMS}-values for both the 'UGent' model and the Ramberg-Osgood model. Whereas the average improvement seems moderate, the result was much clearer for other cases. From the visual inspection of all investigated curves, it appeared to be common for the UGent model to properly describe both the initial and the advanced yielding stage, which was not the case for the Ramberg-Osgood model. Figure 3.39(b) depicts the curve that showed the greatest improvement ($\epsilon_{RMS,UGent}$ 73 % lower than $\epsilon_{RMS,R-O}$). Similar to the numerically obtained optimal models (figure 3.33), the degree of improvement is more significant for steels with higher Y/T-ratios (figure 3.40).

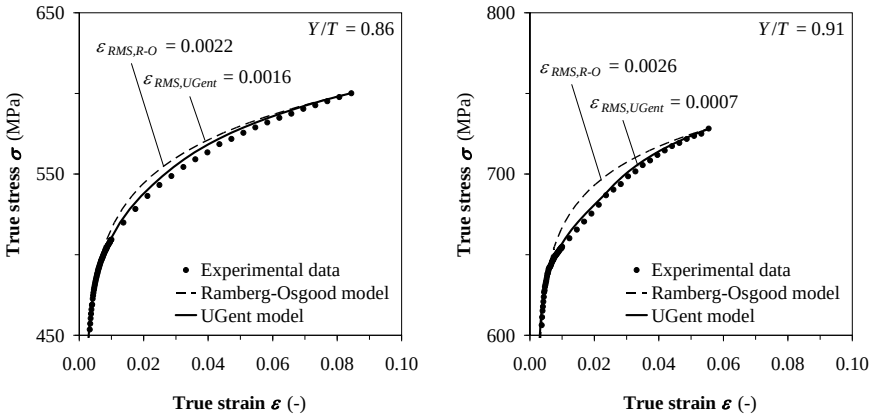

(a) (b)

Figure 3.39: Examples of analytically determined models (a) with near-average RMS error values, (b) with the best observed improvement by the 'UGent' model.

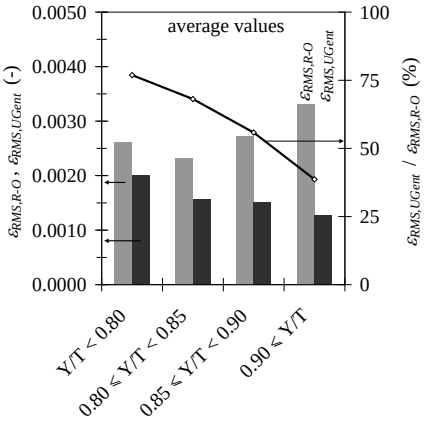

Figure 3.40: Applying the analytical methods to determine model parameters, the improvement achieved by the 'UGent' model is more pronounced for higher Y/T-ratios.

3.10 Extended use of the 'UGent' model: discontinuously yielding steels

Although developed to describe 'double-n' behaviour in continuously yielding steels, it is also possible for the 'UGent' model to represent discontinuously yielding steels whose Lüders plateau (at a stress level $\sigma_{0.2}$) is followed by power law hardening (with a strain hardening exponent n_2). This possibility may be interesting for finite element modelling applications, assuming that the 'UGent' model has been programmed into the software package.

To achieve a discontinuous yielding stage, n_1 has to be given an extremely high value (e.g. as much as 10^4). The true Lüders elongation ϵ_L can then be set by choosing σ_1 and σ_2 as follows:

$$\sigma_1 = \sigma_2 = \sigma_{0.2} \left(\frac{\epsilon_L}{0.002} \right)^{1/n_1} \tag{3.29}$$

Note that, in strict mathematical terms, Eq. (3.29) violates the prerequisite $\sigma_1 < \sigma_2$ in the definition of the 'UGent' model (Eq. (3.19)). This anomaly may be numerically solved by slightly increasing σ_2 (e.g. by as little as 10^{-8} MPa).

The exponent n_2 fully represents the strain hardening stage after completion of discontinuous yielding and remains approximately related to Y/T through Eq. (3.28).

Figure 3.41 provides proof of the 'UGent' model's ability to introduce a Lüders

plateau into the modelled stress-strain curve. n_1 is taken 10^4 after which σ_1 is obtained from Eq. (3.29), aiming at a true Lüders elongation $\epsilon_L = 0.02$. σ_2 is taken $\sigma_1 + 10^{-8}$ MPa and n_2 is chosen 15.

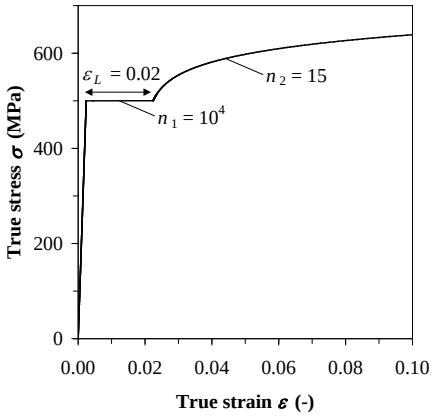

Figure 3.41: Illustrative example of a discontinuously yielding stress-strain curve, obtained with the 'UGent' model.

3.11 Summary and conclusions

Given its reported particular importance for strain based flaw assessments, this chapter has devoted particular attention to both the measurement and analysis of a line pipe steel's tensile stress-strain behaviour.

First, a literature survey for UOE formed pipes has revealed that many factors influence a pipe's stress-strain behaviour, which is observed to be anisotropic and highly heterogeneous. To this respect this chapter allows to conclude that, for strain based flaw assessment purposes, *longitudinal full thickness strip specimens* should be extracted *after anti-corrosive coating (or a simulation of its related thermal cycle)* from a *sufficient number of pipes* and at a *sufficient number of (o'clock and longitudinal) positions within each pipe*. Although the term 'sufficient' is not concretized at this point, it should be possible to characterize the distributions of (and relations between) stress-strain properties such as yield strength, ultimate tensile strength and uniform elongation. As regards yield strength, $R_{p0.2}$ is preferred over $R_{t0.5}$ given its physical relevance and the dependency of the relation between both on line pipe steel grade.

Second, an overview of commonly applied stress-strain models and graphical methods to analyze them has been provided. Particular attention has been de-

voted to the Ramberg-Osgood model, which is advised in the pipeline standards CSA Z662 [3.61] and API 1104 [3.62].

Using a database of 139 tensile tests on API 5L X56 to X100 steel, it has been shown that the Ramberg-Osgood model is highly limited to represent realistic full-range line pipe steel stress-strain behaviours. This limitation comes from the experimentally observed presence of two distinct stages of strain hardening ('double-n' behaviour), which appears to be highly common from a literature survey.

To enable a better mathematical representation of the mechanical behaviour of line pipe steels, a new 'UGent' stress-strain model has been empirically developed. In addition, three different methods – numerical, graphical and analytical – have been developed to estimate suited model parameters. The proper performance of each method has been shown from an experimental validation. The choice of method depends on a trade-off between availability of data and the degree of accuracy and effort. In particular, the analytical method merely requires a limited set of commonly reported tensile test characteristics (E, $R_{p0.2}$, R_m, e_m) and the 1.0 % proof stress $R_{p1.0}$. To promote the practical applicability of the method, the author encourages the acquisition and reporting of this proof stress.

Application of the 'optimal' numerical method on the 139 investigated tests allowed to conclude that

- the improvement of the 'UGent' model to the standardized Ramberg-Osgood model is substantial;
- this improvement is particularly pronounced for line pipe steels with increasing Y/T-ratio. In particular, double-n behaviour tends to be pronounced for steels with $Y/T > 0.80$;
- least-squares curve fitted Ramberg-Osgood equations may severely misestimate yield strength which – if adopted – has consequences for both stress based and strain based flaw assessments.

Summarizing matters, the presented chapter can be seen as a step forward towards the better characterization, understanding and description of the stress-strain behaviour of high strength line pipe steels.

Potential for future work is seen in

- the implementation of the 'UGent' model into routines of finite element software such as $ABAQUS^{®}$;
- the characterization of material heterogeneity and anisotropy;

- the investigation of the fundamental aspects of 'double-n' behaviour from a microstructural point of view.

Bibliography

[3.1] P.W. Bridgman. *Studies in large plastic flow and fracture.* McGraw-Hill, New York, 1952.

[3.2] *Specification for Line Pipe, API 5L, 44th edition.* American Petroleum Institute, Washington, USA, 2007.

[3.3] *Steel pipes for pipelines for combustible fluids - Technical delivery conditions – Part 2: Pipes of requirement class B, EN 10208-2.* European Committee for Standardization, Brussels, Belgium, 2009.

[3.4] K. Nagai, Y. Shinohara, S. Sakamoto, E. Tsuru, H. Asahi, and T. Hara. Anisotropy of the stress-strain curves for line pipe steels. In *Proceedings of the 8th International Pipeline Conference (IPC)*, Calgary, Alberta, Canada, 2010. IPC2010-31169.

[3.5] H. Hillenbrand, A. Liessem, F. Grimpe, and V. Schwinn. Manufacturing of X100 pipes for the TAP project. In *Proceedings of the 6th International Pipeline Conference (IPC)*, Calgary, Alberta, Canada, 2006. IPC2006-10257.

[3.6] Y.Y. Wang and M. Liu. The role of anisotropy, toughness transferability, and weld misalignment in the strain based design of pipelines. In *Proceedings of the 17th International Offshore and Polar Engineering Conference (ISOPE)*, pages 3164–3171, Lisbon, Portugal, 2007.

[3.7] I. Takeuchi, M. Matsumura, S. Okaguchi, H. Shitamoto, S. Fujita, and A. Yamamoto. Property of X80 grade SAW pipes for resistance to ground movement. In *Proceedings of the 7th International Pipeline Conference (IPC)*, Calgary, Alberta, Canada, 2008. IPC2008-64512.

[3.8] J. Johnson, M. Hudson, N. Takahashi, M. Nagase, and A. Yamamoto. Specification and manufacturing of pipes for the X100 operational trial. In *Proceedings of the 7th International Pipeline Conference (IPC)*, Calgary, Alberta, Canada, 2008. IPC2008-64653.

[3.9] N. Ishikawa, M. Okatsu, S. Endo, J. Kondo, J. Zhou, and D. Taylor. Mass production and installation of X100 linepipe for strain-based design application. In *Proceedings of the 7th International Pipeline Conference (IPC)*, Calgary, Alberta, Canada, 2008. IPC2008-64506.

[3.10] R. Klein, L. Collins, F. Hamad, X. Chen, and D.Q. Bai. Determination of mechanical properties of high strength pipeline. In *Proceedings of the 7th International Pipeline Conference (IPC)*, Calgary, Alberta, Canada, 2008. IPC2008-64101.

[3.11] K. Nagai, Y. Shinohara, S. Sakamoto, E. Tsuru, H. Asahi, and T. Hara. Anisotropic strain aging behavior of high strength UOE linepipe. In *Proceedings of the 19th International Offshore and Polar Engineering Conference (ISOPE)*, pages 56–60, Osaka, Japan, 2009.

[3.12] D.H. Seo, J.Y. Yoo, W.H. Song, and K.B. Kang. Development of X100 linepipe steel with high deformation capacity. In *Proceedings of the 7th International Pipeline Conference (IPC)*, Calgary, Alberta, Canada, 2008. IPC2008-64220.

[3.13] H. Shitamoto, M. Hamada, O. Okaguchi, N. Takahashi, N. Yamamoto, I. Takeuchi, and S. Fujita. Effect of thermal aging on deformability of X80 SAW pipes. In R. Denys, editor, *Proceedings of the 5th International Conference on Pipeline Technology*, Ostend, Belgium, 2009.

[3.14] Y. Bian, C. Penniston, L. Collins, and R. Mackenzie. Evaluation of UOE and spiral-welded line pipe for strain based designs. In *Proceedings of the 8th International Pipeline Conference (IPC)*, Calgary, Alberta, Canada, 2010. IPC2010-31315.

[3.15] C. Stallybrass, J. Konrad, H. Meuser, and F. Grimpe. High strength heavy plate optimized for application in remote areas and low-temperature service. In *Proceedings of the 8th International Pipeline Conference (IPC)*, Calgary, Alberta, Canada, 2010. IPC2010-31227.

[3.16] B.N. Leis and E.B. Clark. Implications and trends in SMYS built into pipelines. In *Proceedings of the 8th International Pipeline Conference (IPC)*, Calgary, Alberta, Canada, 2010. IPC2010-31523.

[3.17] M.L. Macia, S. Kibey, H. Arslan, F. Bardi, S.J. Ford, W.C. Kan, M.F. Cook, and B. Newbury. Approaches to qualify strain-based designed pipelines. In *Proceedings of the 8th International Pipeline Conference (IPC)*, Calgary, Alberta, Canada, 2010. IPC2010-31662.

[3.18] E. Tsuru, H. Asahi, N. Doi, and M. Murata. Methodology for measurement of mechanical properties to predict collapse pressure of UOE pipes. In *Proceedings of the 17th International Offshore and Polar Engineering Conference (ISOPE)*, pages 3269–3275, Lisbon, Portugal, 2007.

[3.19] P. Thibaux, D. Van Hoecke, and G. De Vos. Influence of forming and flattening on the measured tensile properties of linepipe. In *Proceedings of the 6th International Pipeline Conference (IPC)*, Calgary, Alberta, Canada, 2006. IPC2006-10116.

[3.20] A. Liessem, J. Schroder, M. Pant, G. Knauf, S. Zimmermann, C. Stallybrass, and M. Erdelen-Peppler. Investigation of the stress-strain behaviour of large-diameter X100 linepipe in view of strain-based design

requirements. In *Proceedings of the 7th International Pipeline Conference (IPC)*, Calgary, Alberta, Canada, 2008. IPC2008-64553.

[3.21] G. Knauf, G. Hohl, and F.M. Knoop. The effect of specimen type on tensile test results and its implications for linepipe testing. *3R*, 40:655–661, 2001.

[3.22] A. Glover and B. Rothwell. Yield strength and plasticity of high strength pipelines. In R. Denys, editor, *Proceedings of the 4th International Conference on Pipeline Technology*, volume 1, pages 65–79, Ostend, Belgium, 2004.

[3.23] L.K. Ji, H.Y. Chen, C.Y. Huo, H.L. Li, C.J. Zhuang, S.T. Gong, W.Z. Zhao, and H.L. Gao. Key issues in the specifaction of high strain line pipe used in strain-based designed districts of the 2nd West to East pipeline. In *Proceedings of the 7th International Pipeline Conference (IPC)*, Calgary, Alberta, Canada, 2008. IPC2008-64504.

[3.24] H. Asahi, T. Hara, E. Tsuru, and H. Morimoto. Development and commercialization of high-strength linepipe. In *Proceedings of the 5th International Conference on Pipeline Technology*, Ostend, Belgium, 2009.

[3.25] G. Shigesato, Y. Shinohara, T. Hara, M. Sugiyama, and H. Asahi. Thermal aging during coating of X80 high strength steel for line pipe. In *Proceedings of the 17th International Offshore and Polar Engineering Conference (ISOPE)*, pages 2983–2987, Lisbon, Portugal, 2007.

[3.26] R. Noecker, N. Nissley, M. Ning, N. Thirumalai, P. Wojtulewicz, and M. Hukle. Stain aging of C-Mn line pipe steels: an analytical approach to compare strain aging heat treatments. In *Proceedings of the 30th International Conference on Ocean, Offshore and Arctic Engineering (OMAE)*, Rotterdam, The Netherlands, 2011. OMAE2011-49917.

[3.27] Y. Li, W. Zhang, S. Gong, L. Ji, C. Huo, and Y. Feng. Study on tensile property and strain ageing behaviour of X100 linepipe. In *Proceedings of the 8th International Pipeline Conference (IPC)*, Calgary, Alberta, Canada, 2010. IPC2010-31180.

[3.28] A. Liessem, M.K. Graef, G. Knauf, and U. Marewski. Influence of the thermal treatment on mechanical properties of UOE linepipe. In R. Denys, editor, *Proceedings of the 4th International Conference on Pipeline Technology*, pages 1265–1281, Ostend, Belgium, 2004.

[3.29] M.W. Hukle, D.S. Hoyt, J.B. LeBleu, J.P. Dwyer, and A.M. Horn. Qualification of welding procedures for ExxonMobil high strain pipelines. In *Proceedings of the 25th International Conference on Offshore Mechanics and Arctic Engineering (OMAE)*, Hamburg, Germany, 2006. OMAE2006-92503.

[3.30] D.M. Duan, J. Zhou, B. Rothwell, D. Horsley, and N. Pussegoda. Strain aging effects in high strength line pipe materials. In *Proceedings of the 7th International Pipeline Conference (IPC)*, Calgary, Alberta, Canada, 2008. IPC2008-64427.

[3.31] H.Y. Chen, L.K. Ji, Y. Feng, and W. Xie. Strain aging effects on mechanical properties of X80 high strength line pipe. In *Proceedings of the 5th International Conference on Pipeline Technology*, Ostend, Belgium, 2009.

[3.32] A. Liessem, G. Knauf, and S. Zimmermann. Strain based design - what the contribution of a pipe manufacturer can be. In *Proceedings of the 17th International Offshore and Polar Engineering Conference (ISOPE)*, pages 3156–3163, Lisbon, Portugal, 2007.

[3.33] Y. Shinohara, T. Hara, E. Tsuru, H. Asahi, Y. Terada, N. Doi, N. Ayukawa, and M. Murata. Development of a high strength steel line pipe for strain-based design applications. In *Proceedings of the 17th International Offshore and Polar Engineering Conference (ISOPE)*, pages 2949–2954, Lisbon, Portugal, 2007.

[3.34] E. Tsuru, K. Yoshida, S. Shirakami, and T. Kuwabara. Numerical simulation of buckling resistance for UOE line pipes with orthogonal anisotropic hardening behavior. In *Proceedings of the 18th International Offshore and Polar Engineering Conference (ISOPE)*, pages 104–110, Vancouver, Canada, 2008.

[3.35] T. Hara, Y. Shinohara, Y. Terada, H. Asahi, and N. Doi. Development of high-deformable high-strength line pipe suitable for strain-based design. In *Proceedings of the 5th International Conference on Pipeline Technology*, Ostend, Belgium, 2009.

[3.36] T. Hara, Y. Terada, Y. Shinohara, A. Hitoshi, and N. Doi. Metallurgical design and development of high deformable X100 line pipe steels suitable for strain-based design. In *Proceedings of the 7th International Pipeline Conference (IPC)*, Calgary, Alberta, Canada, 2008. IPC2008-64234.

[3.37] A. Liessem, R. Rueter, M. Pant, and V. Schwinn. Production and development update of X100 for strain-based design application. In *Proceedings of the 5th International Conference on Pipeline Technology*, Ostend, Belgium, 2009.

[3.38] D.M. Duan, J. Zhou, B. Rothwell, D. Taylor, and K. Widenmaier. A systematic material evaluation program for high grade line pipe materials. In *Proceedings of the 7th International Pipeline Conference*, Calgary, Alberta, Canada, 2008. IPC2008-64426.

[3.39] E. Tsuru, J. Agata, and Y. Nagata. Analytical approach for buckling resistance of UOE linepipe with orthogonal anisotropy under combined loading. In *Proceedings of the 8th International Pipeline Conference (IPC)*, Calgary, Alberta, Canada, 2010. IPC2010-31224.

[3.40] X. Li, L. Ji, W. Zhao, and H. Li. Key issues should be considered for application of strain-based designed pipeline in China. In *Proceedings of the 17th International Offshore and Polar Engineering Conference (ISOPE)*, pages 3054–3056, Lisbon, Portugal, 2007.

[3.41] J. Zhou, D. Taylor, and D. Hodgkinson. Further large-scale implementation of advanced pipeline technologies. In *Proceedings of the 7th International Pipeline Conference (IPC)*, Calgary, Alberta, Canada, 2008. IPC2008-64472.

[3.42] Y.Y. Wang, M. Liu, J. Gianetto, and B. Tyson. Considerations of linepipe and girth weld tensile properties for strain-based design of pipelines. In *Proceedings of the 8th International Pipeline Conference (IPC)*, Calgary, Alberta, Canada, 2010. IPC2010-31376.

[3.43] P. Ludwik. *Elemente der Technologischen Mechanic*. Verlag Julius Springer, Berlin, 1909. 32 pages. In German.

[3.44] W. Ramberg and W.R. Osgood. Description of stress-strain curves by three parameters. Technical report, National Advisory Committee for Aeronautics, 1943. Technical note No. 902. 13 pages.

[3.45] J.H. Hollomon. Tensile deformation. *Transactions of the AIME*, 162:268–290, 1945.

[3.46] E. Voce. The relationship between stress and strain for homogeneous deformation. *Journal of the Institute of Metals*, 74:537–562, 1948.

[3.47] H.W. Swift. Plastic instability under plane stress. *Journal of the Mechanics and Physics of Solids*, 1(1):1–18, 1952.

[3.48] D.C. Ludwigson. Modified stress-strain relation for FCC metals and alloys. *Metallurgical Transactions*, 2:2825–2828, 1971.

[3.49] C.H. Crussard and B. Jaoul. Contribution à l'étude de la forme des courbes de traction des métaux et à son interprétation physique. *Revue de Métallurgie*, 47(8):589–600, 1950. In French.

[3.50] K.G. Samuel. Limitations of Hollomon and Ludwigson stress-strain relations in assessing the strain hardening parameters. *Journal of Physics D: Applied Physics*, 39(1):203–212, 2006.

[3.51] J.R. Low and F. Garofalo. Precision determination of stress-strain curves in the plastic range. *Proceedings of the Society for Experimental Stress Analysis*, 4(2):16–24, 1947.

[3.52] P.G. Nelson and J. Winlock. A method of determining the percentage elongation at maximum load in the tension test. *ASTM Bulletin*, pages 53–55, 1949.

[3.53] K. Ono. Strain-hardening equations and uniform strain. *Metallurgical Transactions*, 3:749–751, 1972.

[3.54] H.J. Kleemola and M.A. Nieminen. On the strain-hardening parameters of metals. *Metallurgical Transactions*, 5:1863–1866, 1974.

[3.55] R.E. Reed-Hill, W.R. Cribb, and S.N. Monteiro. Concerning the analysis of tensile stress-strain data using $\log(\mathrm{d}\sigma/\mathrm{d}\epsilon)$ versus $\log(\sigma)$ diagrams. *Metallurgical Transactions*, 4:2665–2667, 1973.

[3.56] H.N. Hill. Determination of stress-strain relations from the offset yield strength values. Technical report, National Advisory Committee for Aeronautics, 1944. Technical note No. 927. 6 pages.

[3.57] U.F. Kocks. Laws for work-hardening and low-temperature creep. *Journal of Engineering Materials and Technology - Transactions of the Asme*, 98(1):76–85, 1976.

[3.58] H. Mecking and U.F. Kocks. Kinetics of flow and strain-hardening. *Acta Metallurgica*, 29(11):1865–1875, 1981.

[3.59] M. Milititsky, N. De Wispelaere, R. Petrov, J.E. Ramos, A. Reguly, and H. Hanninen. Characterization of the mechanical properties of low-nickel austenitic stainless steels. *Materials Science and Engineering A - Structural Materials Properties Microstructure and Processing*, 498(1-2):289–295, 2008.

[3.60] R. Markandeya, S. Nagarjuna, D.V.V. Satyanarayana, and D.S. Sarma. Correlation of structure and flow behaviour of Cu-Ti-Cd alloys. *Materials Science and Engineering A - Structural Materials Properties Microstructure and Processing*, 428(1-2):233–243, 2006.

[3.61] *Oil & gas pipeline systems, CSA Z662*. Canadian Standards Association, Ontario, Canada, 2007.

[3.62] *Welding of Pipelines and Related Facilities, API 1104*. American Petroleum Institute, Washington, USA, 2007.

[3.63] Y. Shinohara, Y. Madi, and J. Besson. A combined phenomenological model for the representation of anisotropic hardening behavior in high strength steel line pipes. *European Journal of Mechanics A/Solids*, 29(6):917–927, 2010.

[3.64] M. Guagnelli, J. Ferino, E. Anelli, and G. Mannucci. High strength linepipes with enhanced deformability. In *Proceedings of the 17th International Offshore and Polar Engineering Conference (ISOPE)*, pages 2055–2062, Lisbon, Portugal, 2007.

[3.65] A.C. Bannister, J.R. Ocejo, and F. Gutierrez-Solana. Implications of the yield stress/tensile stress ratio to the SINTAP failure assessment diagrams for homogeneous materials. *Engineering Fracture Mechanics*, 67(6):547–562, 2000.

[3.66] M. Koçak, S. Webster, J.J. Janosch, R.A. Ainsworth, and R. Koers, editors. *Fitness for service procedure, FITNET , MK8, vol. I: procedure.* GKSS Research Centre, ISBN 978-3-940923-00-4, 2008.

[3.67] R. Denys, S. Hertelé, W. De Waele, and A. Lefevre. Estimate of Y/T ratio and uniform elongation capacity of pipeline steels from yield strength. In R. Denys, editor, *Proceedings of the 5th International Conference on Pipeline Technology*, Ostend, Belgium, 2009.

[3.68] R. Denys, P. De Baets, A. Lefevre, and W. De Waele. Material tensile properties in relation to the failure behavior of girth welds subject to plastic longitudinal strains. In *Proceedings of the International Conference on Application and Evaluation of High-Grade Linepipes in Hostile Environments*, pages 159–172, 2002.

[3.69] D. Rudland, G. Wilkowski, Y.Y. Wang, D. Horsley, B. Rothwell, and A. Glover. Development of a procedure for the calculation of J-R curves from pressed-notch drop weight tear test specimens. In *Proceedings of the 4th International Pipeline Conference (IPC)*, Calgary, Alberta, Canada, 2002. IPC02-27028.

[3.70] S. Hertelé, R. Denys, and W. De Waele. Full range stress-strain relation modelling of pipeline steels. *Journal of Pipeline Engineering*, 8(3):213–221, 2009.

[3.71] S. Höhler, S. Zimmerman, H. Brauer, and H. Löbbe. Work hardening properties of high-frequency-induction (HFI) welded line pipe: parameters for assessment of multi-axial load histories. In *Proceedings of the 5th International Conference on Pipeline Technology*, Ostend, Belgium, 2009.

[3.72] A.W. Bowen and P.G. Partridge. Limitations of the Hollomon strain-hardening equation. *Journal of Physics D: Applied Physics*, 7(7):969–978, 1974.

[3.73] W.B. Morrison. Effect of grain size on the stress-strain relationship in low-carbon steel. *Transactions of the ASM*, 59:824–845, 1966.

[3.74] B.K. Jha, R. Avtar, V.S. Dwivedi, and V. Ramaswamy. Applicability of modified Crussard-Jaoul analysis on the deformation-behavior of dual-phase steels. *Journal of Materials Science Letters*, 6(8):891–893, 1987.

[3.75] A.S. Podder, D. Bhattacharjee, and R.K. Ray. Effect of martensite on the mechanical behavior of ferrite-bainite dual phase steels. *Iron and Steel Institute of Japan (ISIJ) International*, 47(7):1058–1064, 2007.

[3.76] M. Umemoto, Z.G. Liu, S. Sugimoto, and K. Tsuchiya. Tensile stress-strain analysis of single-structure steels. *Metallurgical and Materials Transactions A - Physical Metallurgy and Materials Science*, 31(7):1785–1794, 2000.

[3.77] Y. Tomita and K. Okabayashi. Tensile stress-strain analysis of cold-worked metals and steels and dual-phase steels. *Metallurgical Transactions A - Physical Metallurgy and Materials Science*, 16(5):865–872, 1985.

[3.78] M. Atkinson. Strain-hardening behavior of polycrystalline iron and low-carbon steels - a statistical analysis. *Metallurgical Transactions A - Physical Metallurgy and Materials Science*, 15(6):1185–1192, 1984.

[3.79] K.T. Park, C.S. Lee, and D.H. Shin. Strain hardenability of ultrafine grained low carbon steels processed by ECAP. *Reviews on Advanced Materials Science*, 10(2):133–137, 2005.

[3.80] J.W. Simmons. Influence of nitride (Cr_2N) precipitation on the plastic-flow behavior of high-nitrogen austenitic stainless-steel. *Scripta Metallurgica et Materialia*, 32(2):265–270, 1995.

[3.81] E.P. Klier and C.P. Gazzara. Stress-strain properties of selected titanium. *ASTM Bulletin*, 59:1015–1028, 1959.

[3.82] S.N. Monteiro and R.E. Reed-Hill. Empirical analysis of titanium stress-strain curves. *Metallurgical Transactions*, 4(4):1011–1015, 1973.

[3.83] J. Man, M. Holzmann, and B. Vlach. Microstrain region and transition to macrostrain in 9.9 percent polycrystalline copper. *Physica Status Solidi*, 19(2):543–553, 1967.

[3.84] C. Schwink and W. Vorbrugg. Experimentelle und theoretische untersuchungen zum plastischen verhalten kubisch-flachenzentrierter vielkristalle. *Zeitschrift fur Naturforschung Part A-Astrophysik Physik und Physikalische Chemie*, A 22(5):626–642, 1967. In German.

[3.85] G. Zankl. Magnetische und elektronenmikroskopische untersuchungen zum plastischen verhalten von vielkristallinem nickel. *Zeitschrift fur Naturforschung Part A - Astrophysik Physik und Physikalische Chemie*, A 18(7):795–809, 1963. In German.

[3.86] K.V.U. Praveen, G.V.S. Sastry, and V. Singh. Work hardening behavior of the Ni-Fe based superalloy IN 718. In *International Symposium of Research Students on Material Science and Engineering*, Chennai, India, 2004.

[3.87] *Standard test method for tensile strain-hardening exponents (n-values) of metallic sheet materials, ASTM E 646-00.* ASTM International, West Conshohocken, USA, 2000.

[3.88] V. Schwinn, P. Fluess, A. Liessem, and J. Schroeder. Concepts of grade X100 for high toughness and strain based design application. In *Proceedings of the 18th International Offshore and Polar Engineering Conference (ISOPE)*, pages 27–32, Vancouver, Canada, 2008.

[3.89] M. Macdonald, J. Rhodes, and G.T. Taylor. Mechanical properties of stainless steel lipped channels. In *Proceedings of the 15th International Specialty Conference on Cold-Formed Steel Structures*, pages 673–686, Missouri, USA, 2000.

[3.90] E. Mirambell and E. Real. On the calculation of deflections in structural stainless steel beams: an experimental and numerical investigation. *Journal of Constructional Steel Research*, 54(1):109–133, 2000.

[3.91] K.J.R. Rasmussen. Full-range stress-strain curves for stainless steel alloys. *Journal of Constructional Steel Research*, 59(1):47–61, 2003.

[3.92] L. Gardner and D.A. Nethercot. Experiments on stainless steel hollow sections - Part 1: Material and cross-sectional behaviour. *Journal of Constructional Steel Research*, 60(9):1291–1318, 2004.

[3.93] L. Gardner and M. Ashraf. Structural design for non-linear metallic materials. *Engineering Structures*, 28(6):926–934, 2006.

[3.94] K. Abdella. Inversion of a full-range stress-strain relation for stainless steel alloys. *International Journal of Non-Linear Mechanics*, 41(3):456–463, 2006.

[3.95] J. Chen and B. Young. Stress-strain curves for stainless steel at elevated temperatures. *Engineering Structures*, 28(2):229–239, 2006.

[3.96] W.M. Quach, J.G. Teng, and K.F. Chung. Three-stage full-range stress-strain model for stainless steels. *Journal of Structural Engineering*, 134(9):1518–1527, 2008.

[3.97] L. Gardner, A. Insausti, K.T. Ng, and M. Ashraf. Elevated temperature material properties of stainless steel alloys. *Journal of Constructional Steel Research*, 66(5):634–647, 2010.

[3.98] H.A. Saab and D.A. Nethercot. Modeling steel frame behavior under fire conditions. *Engineering Structures*, 13(4):371–382, 1991.

[3.99] S. Hertelé, W. De Waele, and R. Denys. A generic stress-strain model for metallic materials with two-stage strain hardening behaviour. *International Journal of Non-Linear Mechanics*, 46(3):519–531, 2011.

[3.100] S. Hertelé, W. De Waele, R. Denys, and M. Verstraete. Full-range stress-strain behaviour of contemporary pipeline steels: Part I. Model description. *International Journal of Pressure Vessels and Piping*, 92:34–40, 2012.

[3.101] U. Zerbst, R.A. Ainsworth, and K.H. Schwalbe. Basic principles of analytical flaw assessment methods. *International Journal of Pressure Vessels and Piping*, 77(14-15):855–867, 2000.

[3.102] S. Hertelé, W. De Waele, R. Denys, and M. Verstraete. Full-range stress-strain behaviour of contemporary pipeline steels: Part II. Estimation of model parameters. *International Journal of Pressure Vessels and Piping*, 92:27–33, 2012.

[3.103] S. Hertelé, W. De Waele, and R. Denys. Determination of full range stress-strain behavior of pipeline steels using tensile characteristics. In *Proceedings of the 8th International Pipeline Conference (IPC)*, Calgary, Alberta, Canada, 2010. IPC2010-31291.

[3.104] J. Chattopadhyay. Improved J and COD estimation by GE/EPRI method in elastic to fully plastic transition zone. *Engineering Fracture Mechanics*, 73(14):1959–1979, 2006.

Chapter 4

Development of a finite element model of large scale pipe tension tests

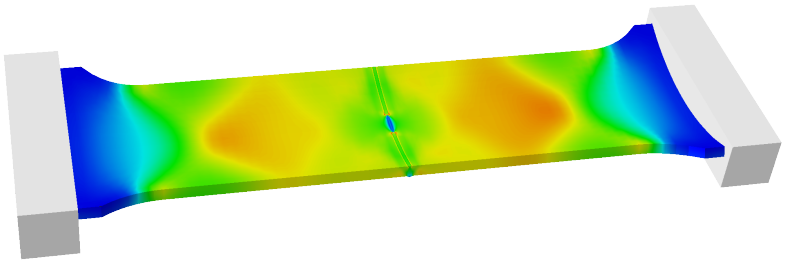

Contour plot of longitudinal strain in a tensile loaded curved wide plate specimen.

4.1 Goal

As discussed in section 2.3.2, the deformation capacity of a girth welded pipe is influenced by many interacting factors involving geometry, materials and loading conditions. To date, the specific influences of all factors and their interactions are not yet fully understood. To enable a systematic investigation in the performed and future research, a fully parametric Python software code has been developed which automatically creates, processes and postprocesses finite element models of large scale girth weld tension tests using the software package *ABAQUS*® (version 6.10 and higher). Concretely, this script provides the ability to choose between a CWP test (section 2.4.2) or a FSP test (section 2.4.1) and allows to investigate all assumed key parameters.

Apart from the possibility to perform parametric studies, the development of the finite element model serves two additional purposes:

- In combination with an experimental validation, the general possibilities and restrictions of finite element modelling in a strain based context can be revealed. In particular, the following question can be addressed:

  'To what extent can finite element modelling serve as a predictive tool and, hence, as a valid alternative to experimental testing?'

  This question is highly relevant, as most existing analytical strain based flaw assessment procedures (section 2.6) have somehow been based upon or tuned to finite element results.

- The finite element model can assist in the optimization of both test configurations (CWP and FSP) in terms of geometry and instrumentation, and can facilitate the interpretation of their results.

This chapter is devoted to the construction and analysis of CWP and FSP models by the parametric Python script. First, section 4.2 highlights the general requirements that correspond with the nature of the investigated problem. Then, section 4.3 is devoted to the creation of models with a fixed flaw size under a monotonically increasing applied global displacement. Section 4.4 finally discusses the implementation of ductile tearing, starting from models with a fixed flaw size.

It will be shown that a numerical model of a structural problem with a high degree of complexity can be constructed by applying a '*divide and rule*' approach: different challenges are separately dealt with at subsequent stages, which are superposed in a way that allows for the creation of a fully integrated numerical model.

4.2 General requirements

The investigated problem is highly specific, as it involves a combination of both fracture mechanics (to cover ductile tearing) and plasticity (to cover collapse). Both analysis types introduce specific requirements, which may be conflicting. This section provides an overview which first focuses on fracture mechanics (section 4.2.1), and subsequently deals with plasticity (section 4.2.2).

4.2.1 Requirements for fracture mechanics analysis

A numerical fracture mechanics analysis involves solving the stress and strain fields near a sharp (crack) or blunt (flaw) tip. As both fields are prone to large gradients near the flaw tip, precautions have to be taken in terms of mesh configuration and density.

Based on rules of good practice provided in [4.1, 4.2], a top-down decision strategy has been composed for numerical flaw tip modelling (figure 4.1). This strategy applies to meshes with hexagonal elements, which generally have a higher performance over other three-dimensional continuum element types. Some aspects in this strategy deserve more explanation.

- A small strain analysis ignores geometric nonlinearities in the calculations, by formulating the elements in the original configuration (prior to deformation) throughout the entire simulation. As a result, analysis speed is drastically increased and convergence more easily attained. The introduced linearization error is negligible for 'small' deformations but becomes pronounced for 'large' deformations. For more details regarding this aspect, see section 4.2.2.

- In case of small strain assumptions, exact solutions of the near-tip stress and strain distributions can be approximated by modelling a perfectly sharp crack tip with a so-called 'spider web mesh' (figure 4.3(a)), thereby collapsing the elements that contact the crack tip into wedges. Depending on the material behaviour (linear elastic, elastic-perfectly plastic or power law hardening), different element types and settings are to be chosen for. In particular, the following aspects are important:

  - Element type: first order or second order;
  - Collapsed nodes can either be duplicated (and, hence, will diverge from each other) or specified to remain attached to each other;
  - In case of second order elements, the node positions on the edges that point towards the crack tip are specified by a factor $0 < \tau < 1$, as shown in figure 4.2. Depending on the desired analysis, different τ-values are advised.

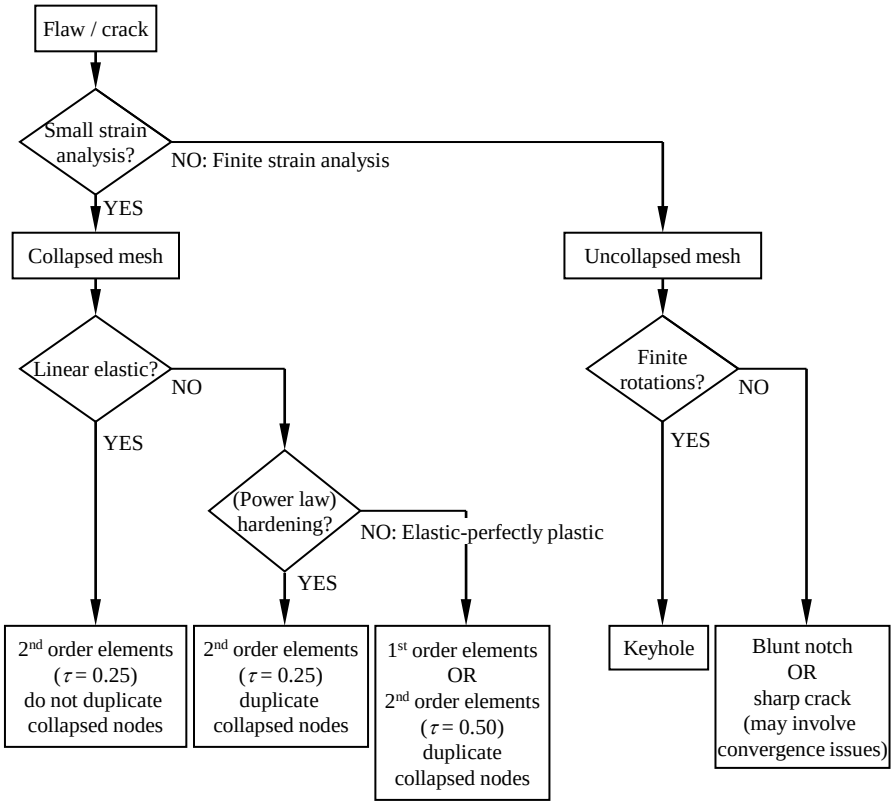

Figure 4.1: Top-down decision tree for crack tip meshing [4.1, 4.2].

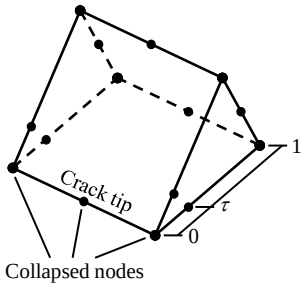

Figure 4.2: Collapsed second order crack tip element with definition of τ.

- In case of finite strain assumptions and absence of significant bending, two configurations can be chosen for: a crack with a sharp tip and uncollapsed mesh (i.e. no spider web mesh) or with a blunt tip and a spider web mesh

(figure 4.3(b)). Whereas the former may show convergence issues, a suited initial crack tip radius ρ_i has to be chosen for the latter. Two approaches can be followed to this respect:

- According to [4.2], if a perfectly sharp crack is aimed at, the crack tip should blunt out more than four times ρ_i. A similar but more conservative blunting requirement of five times ρ_i is proposed in [4.3]. Depending on the application aimed at, initial radius values are typically within the order of magnitude of micrometres (e.g. 2.5 μm [4.4]) or even less [4.5].
- If a blunt flaw is aimed at rather than a sharp crack, ρ_i can be deliberately chosen to correspond with the physical flaw. This has for instance been applied in the development of a FAD-based correction for flaw acuity in [4.6, 4.7].

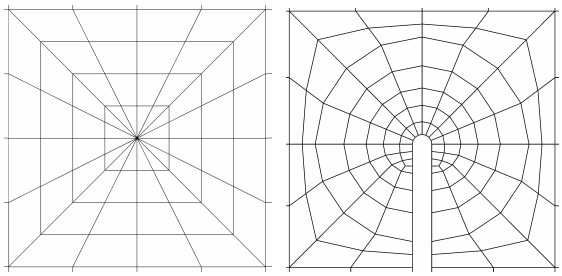

Figure 4.3: Example spider web meshes: (a) collapsed mesh around sharp crack, (b) uncollapsed mesh around a blunt flaw.

Recalling that a strain based flaw assessment using CWP or FSP tests may involve large plastic deformations and is mostly a problem of tension rather than bending, figure 4.1 has led to the choice to model the considered weld flaw as an initially blunt notch with a spider web mesh near the flaw tip (as in figure 4.3(b)).

4.2.2 Requirements for plasticity analysis

As already briefly mentioned in section 4.2.1, a small strain analysis introduces significant errors when large plastic deformations occur. A particular implication of the geometric linearizations made in a small strain analysis is that localized necking cannot be simulated. This is illustrated by a simulated CWP test result in figure 4.4(a), where geometric non-linearities cause the weld to collapse at 0.045 remote strain. In addition, remote stress (same figure) and deformations (figure 4.5) are poorly predicted without the incorporation of

non-linear geometric effects. Hence, if the incorporation of plastic collapse is aimed at, non-linear geometric effects[1] have to be taken into account. Such setting is also referred to in literature as a 'finite strain analysis'. Note that crack driving force (CMOD in the case of figure 4.4(a)) is well predicted without geometrical non-linearities, up to the gradual initiation of weld collapse. Similar observations have been made for CTOD.

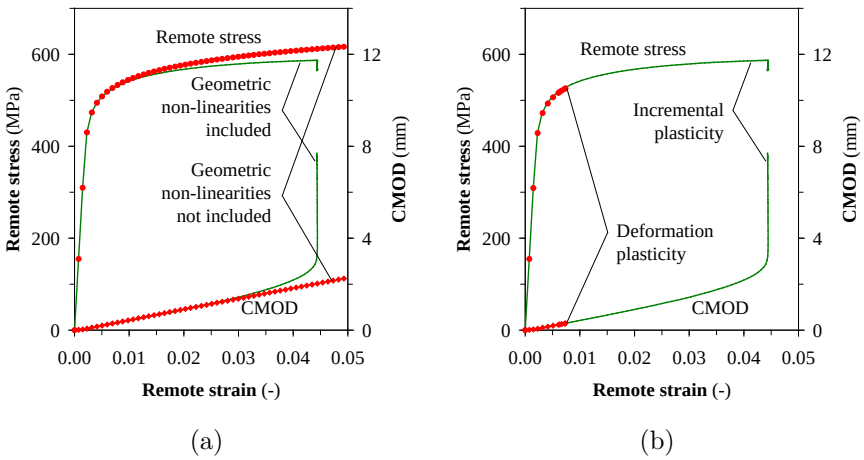

Figure 4.4: Comparison of CWP simulation results (a) with and without incorporation of geometric non-linearities, and (b) with deformation plasticity and incremental plasticity.

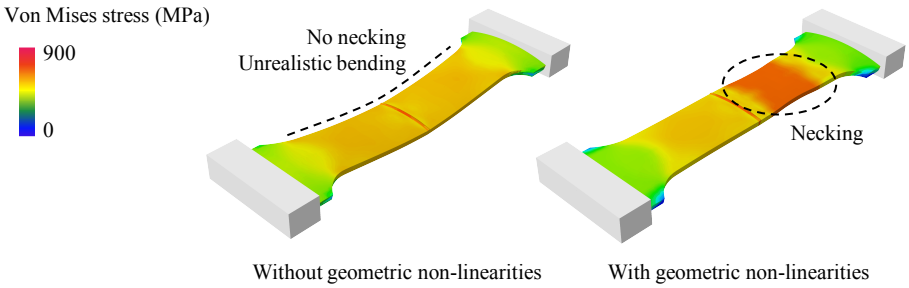

Figure 4.5: Unrealistic deformations are observed if geometrical non-linearities are not taken into account.

[1]Note: non-linear geometric effects are referred to in *ABAQUS*® as 'nlgeom'.

The incorporation of non-linear geometric effects may hamper the simulation convergence. A key influence to this respect was found to be the formulation of non-linear material behaviour. On the one hand, such behaviour can be modelled as elastic-plastic on the basis of a pointwise stress-strain curve definition ('incremental plasticity'). On the other hand, a non-linear but fully elastic formulation which follows the Ramberg-Osgood equation (Eq. (3.15)) can be readily chosen in $ABAQUS^{®}$ ('deformation plasticity'). Deformation plasticity is computationally more efficient since the result is not history dependent, and is expected to give results similar to incremental plasticity in cases of uniaxial tension. More important for the examined problem, however, is that deformation plasticity was found to produce severe convergence problems due to a poor treatment of the high element distortions near the flaw tip. These problems were not observed for simulations with materials that adopt incremental plasticity. An illustration is given in figure 4.4(b): the simulation with deformation plasticity behaves similar to that with incremental plasticity but fails to converge at a remote strain of roughly 0.0075.

The required adoption of incremental plasticity under incorporation of non-linear geometric effects has consequences for the numerical calculation of J. This calculation is based upon a contour integral which, in order to be path independent, requires a strain energy density w from which stresses can be uniquely derived as $\sigma_{ij} = \partial w / \partial \epsilon_{ij}$. This assumption is valid for deformation plasticity but not for incremental plasticity. As a consequence, the numerically calculated J integral becomes path dependent if the contour path crosses the plastic zone originating from the notch tip [4.8]. This is often inevitable for strain based assessments, where global plasticity is not uncommon. Therefore, if calculating crack driving force (J in particular) is the sole purpose of the simulation, the incorporation of non-linear geometric effects (which implies an incremental plasticity formulation for convergence reasons) is disadvised.

Summarizing the above, non-linear geometric effects have to be incorporated to simulate plastic collapse phenomena. To enhance convergence in such case, an incremental plasticity definition of plastic material behaviour is advised. This implies that numerical calculations of J may become path dependent. If the sole purpose of the simulation is to predict J (and not plastic collapse), a small strain analysis is justified.

4.3 Starting point: model with fixed flaw size

4.3.1 General structure

As already briefly mentioned in section 4.1, the finite element models are created, processed and postprocessed on the basis of a parametric Python script which communicates with the finite element software package $ABAQUS^{®}$ (fi-

gure 4.6). The script requires a user-defined text file that assigns values to all necessary model parameters, and eventually produces an output text file which can be easily analyzed using spreadsheet software. The major challenge is situated in the preprocessing part, i.e. creating the desired geometry and mesh for a proper analysis. Processing and postprocessing are fairly straightforward and not further elaborated in this dissertation. For more details regarding these aspects, the reader is referred to [4.9].

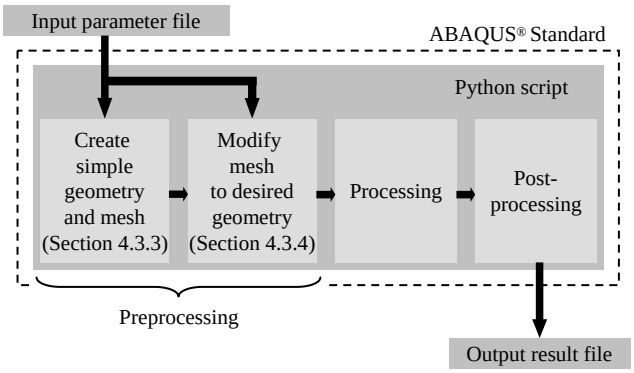

Figure 4.6: General structure of the parametric Python scripting approach.

To address the challenge of creating the desired configuration (section 4.3.2), preprocessing has been separated into two distinct stages. First, the script creates and meshes an approximation of the desired model with a simplified weld and specimen geometry (section 4.3.3). The mesh of the approximate geometry is then modified to the desired shape using nodal coordinate transformations (section 4.3.4).

4.3.2 Specifications of the model

To clarify the following, a right-handed Cartesian coordinate system (x, y, z) is introduced in figure 4.7. Although this figure specifically shows a CWP specimen, the same definition applies for an FSP specimen.

Both considered configurations (CWP and FSP specimen) are symmetrical in the transverse direction, the symmetry plane intersecting the center of the flaw. Hence, the introduction of appropriate boundary conditions allows to model one half of the geometry ($x > 0$), resulting in a reduction of calculation time. Note that a quarter model with an additional symmetry plane through the girth weld (line $A - A$ in figure 4.7) has not been chosen for, since both pipe sections can differ in geometry and/or material properties. An additional

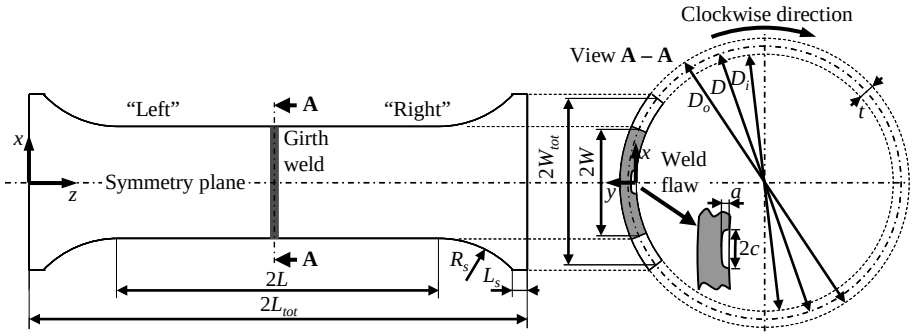

Figure 4.7: Graphical introduction of geometrical parameters.

advantage of a half model over a quarter model is the capability to model HAZ flaws.

Residual stresses have not been implemented into the model for reasons explained in the first paragraph of section 2.3.2 and given the existence of a pragmatic correction on strain capacity (section 2.6.2.1). This simplification has been widely adopted for numerical strain based assessments in literature (e.g. [4.10–4.14]). The representativeness of numerical results assuming an absence of residual stresses will be shown by experimental validations in chapter 7.

The half model is geometrically characterized in terms of four categories:

- pipe geometry: (nominal) outer diameter D_o and thickness t; derived quantities are the inner diameter D_i and average diameter D;
- test specimen geometry: half total length L_{tot} (CWP and FSP specimen), and half length of the prismatic section L, half total width at mid-thickness W_{tot}, half width at mid-thickness of the prismatic section W, shoulder radius R_s, shoulder runout length L_s (CWP specimen only);
- weld geometry;
- flaw position, geometry and size.

Two of the four abovementioned categories (weld and flaw characteristics) require a more elaborate description, separately given in the following two sections.

4.3.2.1 Weld geometry

The weld geometry is graphically summarized in figure 4.8.

For simplicity, the heat-affected zones at both sides of the weld are assumed to have a constant and equal width l_{HAZ}. Further, the weld geometry can be characterized by five features: a possible wall thickness difference between the connected pipe sections, a possible weld misalignment, the weld root and cap profile, the fusion line profile, and a potentially heterogeneous weld metal.

First, the possible occurrence of a wall thickness difference (δ_t) between two pipes has to be bridged by the weld. If the left pipe has a thickness t, the right pipe is assigned a thickness $t + \delta_t$. Second, weld misalignment is defined as the y-distance between the inner-diameter surfaces of both pipe sections, denoted as h.

Third, each proper weld has a certain volume of excessive root and cap material (also referred to as root penetration and cap reinforcement, respectively). Due to the narrowness of the weld root opening, the amount of excessive root material is not included in the model. The weld cap reinforcement, however, can be significant and is described by a longitudinal profile f_c as in figure 4.8. This profile is function of a normalized z-coordinate ζ (0 at the 'left' side of the weld cap, 1 at the 'right' side of the weld cap).

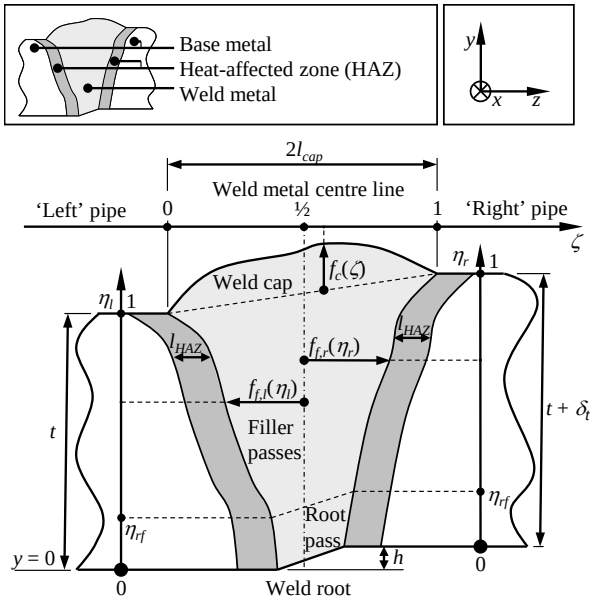

Figure 4.8: Graphical definition of weld geometry.

Fourth, the fusion line profiles at each side of the weld deviate from being perfectly straight. Introducing normalized y-coordinates η_l and η_r which are 0 at the inner diameter surface and 1 at the outer diameter surface of the left and the right pipe sections respectively, the fusion lines can be expressed by functions $f_{f,l}(\eta_l)$ (left fusion line) and $f_{f,r}(\eta_r)$ (right fusion line) as in figure 4.8.

Finally, it has been chosen for to divide the weld into two separate zones, which can be appointed different material properties. The border between both zones is characterized by a parameter η_{rf}, by defining a line which connects the points $\eta_l = \eta_{rf}$ and $\eta_r = \eta_{rf}$. The additional freedom introduced may address different phenomena.

- In practice, a softer filler material is often chosen for the weld root pass to reduce the susceptibility to hydrogen cracking and consequently improve weldability [4.15].

- The thermal cycles exhibited on existing weld passes by the application of new weld passes may cause a continuous evolution of strength properties in the thickness direction. This evolution might to some limited extent be discretized into two different zones of homogeneous material properties. Since this discretization involves a strong simplification compared with actual weld heterogeneity, it should rather be seen as a first, approximate tool to investigate weld flaws in localized weaker or stronger weld metal.

- In case of a repaired weld, the mechanical properties of the repair weld may significantly differ from those of the original weld [4.16].

4.3.2.2 Flaw position and shape

The finite element model is confined to surface flaws (i.e. embedded flaws are not covered). A distinction is made between two fundamentally different flaw locations: at the weld metal center ($\zeta = 0.5$) or near the weld fusion line ($\zeta = 0$ or 1). For instance, the former case might represent a lack of penetration, whereas the latter may represent a lack of fusion.

Apart from its position, the surface flaw is characterized by its size and shape. Parameters that define the size are the flaw length $2c$ and depth a. Due to the assumed symmetry, only half of the flaw length (c) is modelled. As regards the shape, one of the two following simplifications is generally made in literature:

- a flaw with constant depth, except at its ends where quarter circles deflect the flaw tip to the surface;

- a semi-elliptical flaw.

Whereas the former geometry is easier to obtain in terms of meshing, the latter has more theoretical relevance as most existing fracture mechanics relations for surface flaws have been based upon a semi-elliptical shape.

4.3.3 Stage 1: creating a simplified, approximate geometry

In the first preprocessing stage, a flat geometry of uniform thickness is built and meshed. This flat plate contains a weld with a simplified geometry characterized as follows: perfectly straight fusion lines (oriented according to the through-thickness direction), no excessive root and weld cap material, no weld misalignment.

At this stage, the CWP and FSP specimens differ at two points (figure 4.9):

- For the CWP panel, end shoulders have to be included in the flat plate.
- For the CWP panel, symmetry is defined at the longitudinal (yz) mid-plane only. For the FSP coupon, symmetry has to be additionally defined for the plane opposite to this mid-plane. Indeed, in the second preprocessing stage (section 4.3.4), a coordinate transformation that creates the pipe geometry will bend this plane over 180 degrees to end up in the yz plane. The additional symmetry condition is therefore required to 'close' the pipe.

Figure 4.9 also shows that one end plane is clamped (all rotations and displacements are restricted) whereas the other end plane is translated in the z-direction (with zero displacement in the x and y directions). These boundary conditions have been obtained by connecting the specimen end planes with two rigid end blocks (not shown on the figure). To evaluate whether the influence of the simplified boundary conditions on the simulation result, two alternatives have been considered:

- The specimen is pinned instead of clamped (rotations of the end planes around the x-axis are not impeded);
- The end blocks behave linear elastically instead of being fully rigid.

A comparison of results has indicated that the simulated CMOD response is unsensitive to the exact boundary condition.

A partitioning strategy has been designed and optimized to serve two purposes:

- A fine, spider web flaw tip mesh should be combined with a coarse specimen body mesh. Whereas the former is key to obtaining accurate crack driving force calculations, the latter is required to maintain an acceptable computation time.

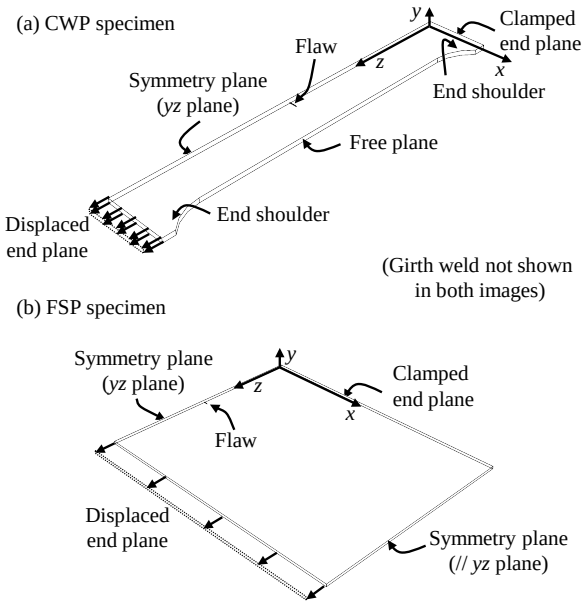

Figure 4.9: Specific features and boundary conditions for a CWP specimen and an FSP specimen.

- The user should be able to choose between a WMC flaw or an HAZ flaw.

The first purpose is achieved by embedding the fine flaw tip mesh into a so-called 'flaw block'. The partitions and mesh strategies in this flaw block are designed to gradually simplify the relatively complex flaw tip mesh, going away from the flaw. Eventually, a regular rectangular mesh is achieved, which can be easily connected to the coarsely meshed remainder of the specimen (figure 4.10).

The second purpose is achieved by differently allocating the weld metal and HAZ material properties over the partitions near the flaw. Figure 4.11 illustrates how, with the same partitioning scheme but different material allocations, both (a) a WMC and (b) an HAZ flaw can be achieved.

The mesh consists of three-dimensional hexagonal continuum elements. In a mesh convergence study, the best trade-off between numerical accuracy and computation time has been found for linear elements with reduced integration [2]. Further, the mesh densities at all partitions can be modified on the basis of parameters which are specified in the input file. This allows the user to create models which serve a particular purpose. In particular, the mesh density of the spider web mesh near the flaw tip can be set very fine on the one hand (figure

[2]Note: this element type is denoted 'C3D8R' in $ABAQUS^{®}$.

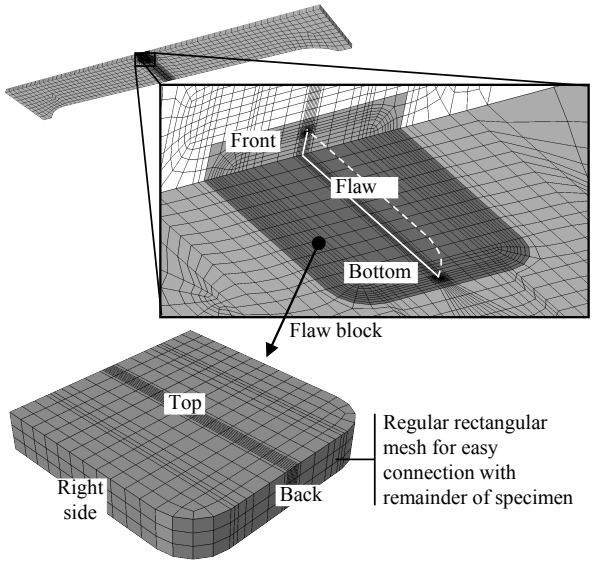

Figure 4.10: The flaw is embedded in a flaw block which easily connects with the remainder of the specimen.

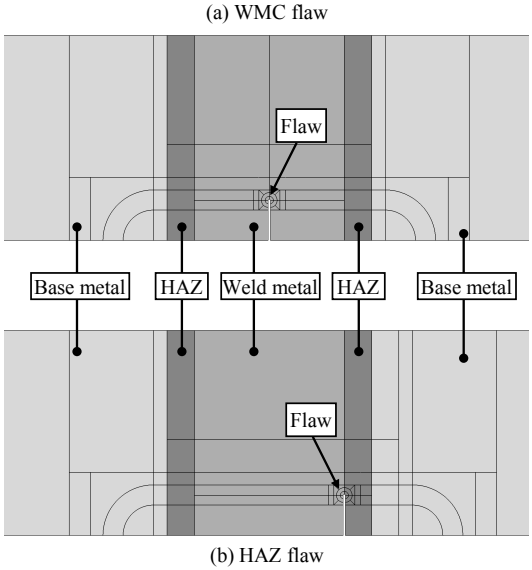

Figure 4.11: Both a WMC flaw and an HAZ flaw can be generated using the same partitioning strategy but different material allocations and well-chosen partition locations.

4.12(a)) to obtain accurate near-tip stress-strain field results for constraint calculations (see for example [4.17]). On the other hand, quantities as CTOD, CMOD and J are obtained with sufficient accuracy from a less fine spider web mesh (figure 4.12(b)) which requires less computation time.

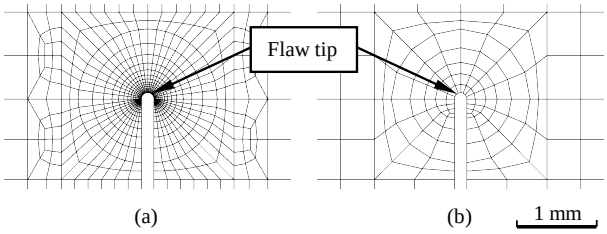

Figure 4.12: (a) Fine and (b) coarse spider web mesh around the flaw tip.

Three predefined density parameter sets have been developed for CWP specimens, aiming to obtain either 'very fast but less accurate', 'fast and fairly accurate' or 'highly accurate but slow' calculations of J, CTOD, CMOD and tensile force (as a function of the applied strain level). These predefined settings are summarized in table 4.1 and illustrated in figure 4.13 for an example 'fast and fairly accurate' mesh. Table 4.2 provides corresponding typical numbers of elements, nodes, degrees of freedom (DOFs), computational time and numerical calculation errors of tensile force and CMOD. The computational times and errors were deduced from comparison with an extremely fine (more than 80,000 nodes) reference simulation, for one arbitrary configuration with fixed geometry and materials.

4.3.4 Stage 2: transforming the simplified geometry to the desired geometry

To obtain the desired geometry with all specifications discussed in section 4.3.2, the mesh of the simplified geometry generated according to section 4.3.3 is modified using a succession of nodal coordinate transformations. These are functions which calculate translation vectors $\Delta\vec{P}(\Delta x, \Delta y, \Delta z)$ for all nodes $\vec{P}(x, y, z)$ to obtain updated node positions $\vec{P}' = \vec{P} + \Delta\vec{P}$ with coordinates (x', y', z'):

$$(x', y', z') = (x + \Delta x, y + \Delta y, z + \Delta z) \tag{4.1}$$

Six nodal coordinate transformations have been implemented, each of which modifies a different geometrical feature and is denoted with a particular subscript:

1. the curved character of the pipe ($\Delta\vec{P}_p$);

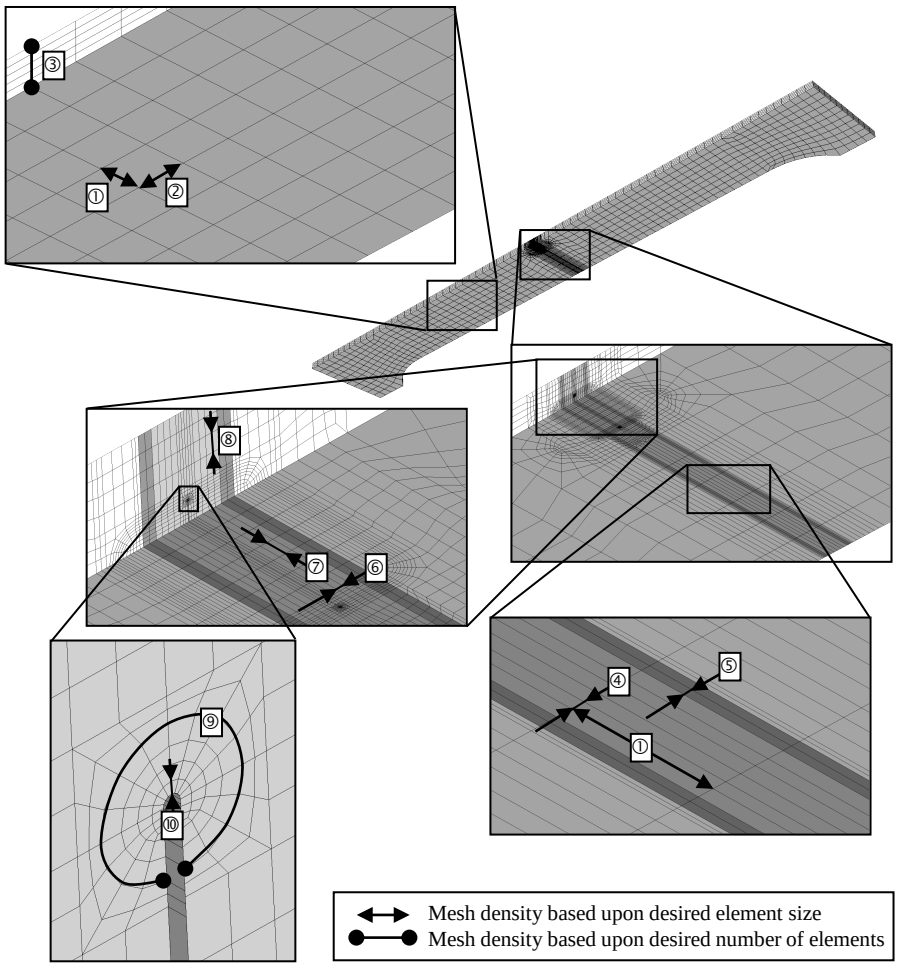

Figure 4.13: Illustration of a 'fast and fairly accurate' mesh, with indications of the mesh parameters from table 4.1.

2. the profile of the weld fusion line ($\Delta\vec{P}_f$);
3. the profile of the weld cap reinforcement ($\Delta\vec{P}_c$);
4. weld misalignment ($\Delta\vec{P}_m$);
5. thickness difference ($\Delta\vec{P}_t$);
6. flaw shape ($\Delta\vec{P}_s$).

A complete mathematical overview of the first five abovementioned transformations is provided in [4.18], whereas the flaw shape transformation $\Delta\vec{P}_s$ is

Table 4.1: Predefined mesh density settings for CWP specimens.

Setting		**Very fast but less accurate**	**Fast and fairly accurate**	**Highly accurate but slow**
Nr. ⋆	Based on †	Desired value ‡		
1	element size	$W/4$	$W/8$	$W/16$
2	element size	$L/12$	$L/25$	$L/50$
3	number of elements	2	4	8
4	element size	5.00 mm	2.50 mm	1.25 mm
5	element size	2.0 mm (or 0.5 mm §)	1.0 mm (or 0.5 mm §)	0.5 mm (or 0.3 mm §)
6	element size	2.0 mm	1.0 mm	0.5 mm
7	element size	4.0 mm	3.0 mm	2.0 mm
8	element size	6.0 mm	3.0 mm	1.5 mm
9	number of elements	16	16	24
10	element size	$1.5\rho_i$	$1.5\rho_i$	$1.5\rho_i$

⋆ See figure 4.13 for the meaning of each number.

† If 'element size', the values represent a distance (mm).
If 'number of elements', the values represent a number.

‡ Actual values may slightly differ due to discretization effects.
If so, mesh density is always finer than desired.

§ Value for the heat-affected zone which contains a flaw
(in case of a HAZ flaw only).

fully elaborated in [4.9]. By means of illustration, section 4.3.4.1 develops the curvature transformation equations for $\Delta\vec{P}_p$. Then, a brief overview of the other transformations is given in section 4.3.4.2. Next, the order of execution of the different coordinate transformations is dealt with in section 4.3.4.3.

4.3.4.1 Example: creating pipe curvature

The curved character of the pipe is obtained by virtually 'rolling' the originally flat plate over a rigid cylindrical mandrel with a diameter D_i (the inner diameter of the pipe) and a longitudinal axis parallel with the z-direction (figure 4.14). Using some basic trigonometry, this is mathematically expressed as follows:

Table 4.2: Typical properties of CWP simulations with predefined mesh settings.

Setting	Very fast but less accurate	Fast and fairly accurate	Highly accurate but slow
Mesh properties			
Nr. of elements	5,000–10,000	10,000–17,000	35,000–45,000
Nr. of nodes	6,000–13,000	12,000–21,000	40,000–53,000
Nr. of DOFs	18,000–39,000	36,000–63,000	120,000–159,000
Approximate relative computational time (%) ⋆			
	15	25	100
Approximate numerical error (%)			
Tensile force	0.50	0.10	0.03
CMOD	3.50	0.60	0.10

⋆ Relative to the 'highly accurate but slow' setting.

$$\Delta\vec{P}_p = \begin{pmatrix} \Delta x_p \\ \Delta y_p \\ \Delta z_p \end{pmatrix} = \begin{pmatrix} \left(\frac{D_i}{2} + y\right)\sin\left(\frac{2x}{D_i}\right) - x \\ \left(\frac{D_i}{2} + y\right)\cos\left(\frac{2x}{D_i}\right) - \left(y + \frac{D_i}{2}\right) \\ 0 \end{pmatrix} \tag{4.2}$$

The half width of the flat plate prior to the coordinate transformation, W_{flat}, should be chosen to obtain the eventually desired geometry. In case of a CWP coupon with a half width W defined at mid-thickness (figure 4.14), the following relation can be shown:

$$W_{flat} = \frac{D_i}{2}\arcsin\left(\frac{2W}{D}\right) \tag{4.3}$$

For the FSP coupon, W_{flat} should equal half the circumference of the circle that represents the inner surface of the pipe:

$$W_{flat} = \frac{\pi D_i}{2} \tag{4.4}$$

4.3.4.2 Brief overview of other coordinate transformations

First, figure 4.15 illustrates examples of the four implemented weld transformations ($\Delta\vec{P}_f$, $\Delta\vec{P}_c$, $\Delta\vec{P}_m$, $\Delta\vec{P}_t$) that contribute to describing all features presented in figure 4.8. All weld transformations are performed in the plane of a weld macrography (parallel with the yz plane), i.e. there is no translation in the width (x) direction.

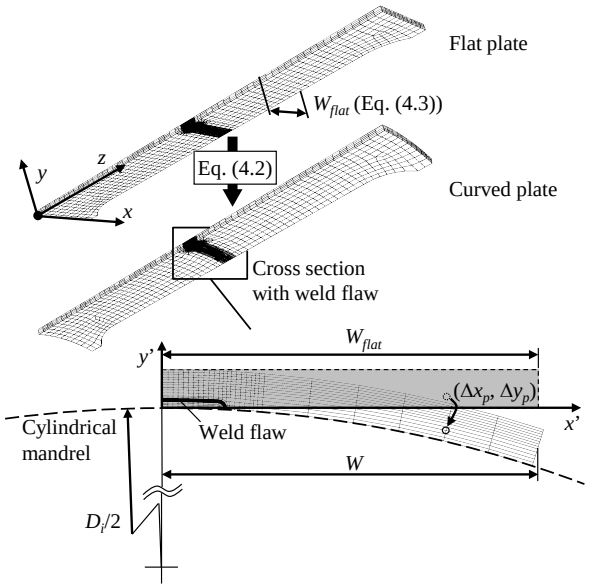

Figure 4.14: Transformation of a flat plate into a curved plate.

Second, figure 4.16 illustrates the flaw shape transformation ($\Delta\vec{P}_s$) which changes the flaw with constant depth created in stage 1 (section 4.3.3) to a semi-elliptical shape. This coordinate transformation is performed in planes parallel with the xy plane, i.e. there is no translation in the longitudinal (z) direction. Since the mesh in the near vicinity of the flaw tip is transformed, specific precautions have been taken in the definition of $\Delta\vec{P}_s$ to avoid mesh distortions of an unwanted nature.

4.3.4.3 Choosing the order of execution of different transformations

To provide a graphical overview in the following, a block scheme representation of Eq. (4.1) is presented in figure 4.17.

Since different coordinate transformations have to be executed, unwanted interactions can occur. Important in this respect is the choice of node coordinates input to each specific transformation. These coordinates may for instance refer to the simplified initial geometry, but also to a geometry which was already changed by other coordinate transformations. A well-chosen order of execution is required to obtain the desired output.

Apart from being undesired in most cases, interactions between different coordinate transformations may be useful to change specific aspects of the resulting geometry. For instance, different types of misalignment between two welded

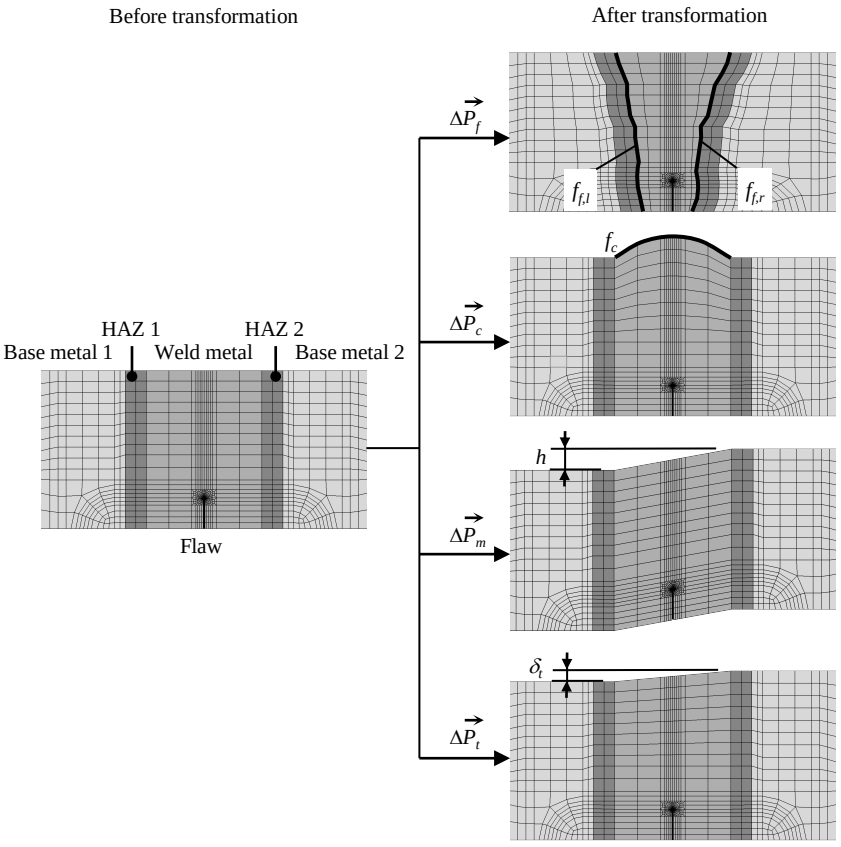

Figure 4.15: Overview of weld transformations.

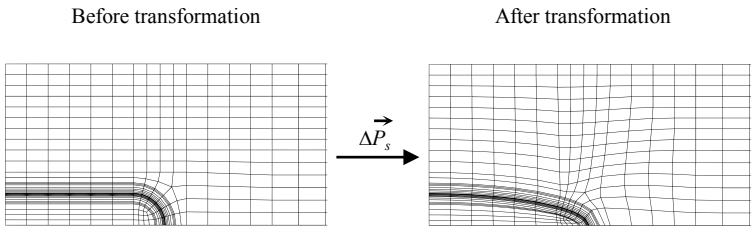

Figure 4.16: Change of flaw shape from constant depth to semi-elliptical.

pipes can be obtained [4.18]:

- Misalignment due to slightly different pipe diameters; this is obtained by performing the misalignment transformation $\Delta\vec{P}_m$ *prior to* the pipe

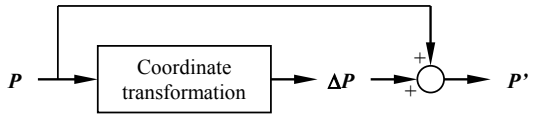

Figure 4.17: Graphical representation of a nodal coordinate transformation according to Eq. (4.1).

curvature transformation $\Delta\vec{P}_p$.

- High-low misalignment between pipes with identical diameters; this is obtained by performing $\Delta\vec{P}_m$ *after* $\Delta\vec{P}_p$.

By means of illustration, the full transformation scheme for a high-low misalignment configuration is shown in figure 4.18.

Figure 4.19 illustrates that the combination of the developed weld coordinate transformations can be used to obtain highly accurate representations of actual weld geometries.

4.4 Modelling of ductile tearing

Previous sections have focused on the creation of finite element models with a fixed flaw size. Since the failure of sufficiently tough structures under strain based conditions is majorly influenced by ductile tearing (section 2.3.1), this phenomenon must somehow be incorporated into the model. This section first critically compares different techniques to model ductile tearing, leading to a motivated selection of the eventually adopted method (section 4.4.1). Then, the concrete implementation of ductile tearing into the script is elaborated.

4.4.1 Modelling techniques

4.4.1.1 Damage modelling: Gurson-Tvergaard-Needleman model

The most widely applied damage model for ductile failure is the Gurson-Tvergaard-Needleman (GTN) model, which has its foundations in [4.19–4.21]. It aims to describe the physical process behind ductile failure, i.e. the nucleation, growth and eventual coalescence of voids. These voids can be unmistakably observed in a post-mortem macrography of stable weld crack extension (figure 4.20).

In the GTN model, the void volume fraction f is introduced as a damage parameter. Tvergaard and Needleman [4.21] proposed that above a critical

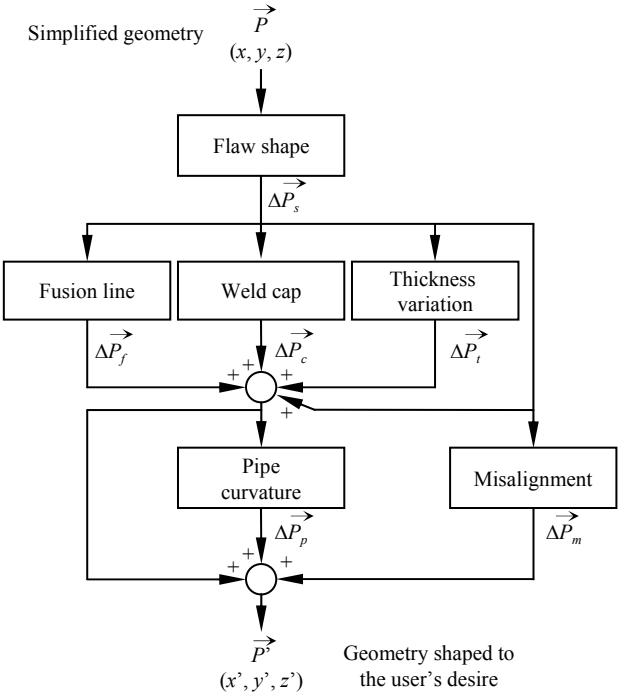

Figure 4.18: Example order of execution of coordinate transformations.

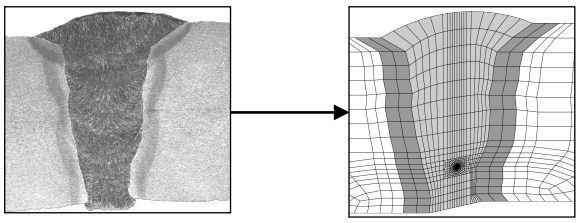

Figure 4.19: Weld macrographies can be represented with a high degree of detail.

value f_c, this fraction should be converted to an 'effective' value $f^\star$ which exceeds the 'actual' value f, to address the increasing importance of coalescence effects. An element fails when f reaches a critical value f_F. The calculation of the evolution of f involves a four-parameter algorithm, a key parameter of which is the initial void volume fraction f_0. This value can be identified from a metallographic investigation by counting the fraction of non-metallic inclusions [3].

[3]For instance, literature mentions CaS, TiN, MgO and Al_2O_3 as the most observed metal-

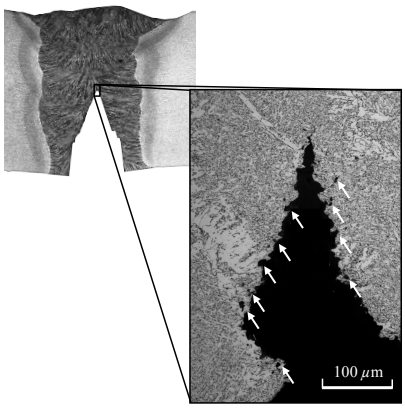

Figure 4.20: The physical nature of ductile tearing: a coalescence of nucleated and grown voids.

Apart from being related to element failure, $f^\star$ is included into the yield function as follows:

$$\left(\frac{\sigma_{Mises}}{\sigma_0}\right)^2 + 2q_1 f^\star \cosh\left(\frac{3}{2}q_2\frac{\sigma_h}{\sigma_0}\right) - \left(1 + q_1^2 f^{\star 2}\right) = 0 \tag{4.5}$$

with σ_{Mises} the Von Mises equivalent stress, σ_0 the yield stress, σ_h the hydrostatic stress, and q_1 and q_2 two GTN model parameters. Basically, the Von Mises stress required for plastic flow decreases as σ_m and/or $f^\star$ increase. Eq. (4.5) is Tvergaard's [4.20] modification to Gurson's original yield function [4.19], which assumed $q_1 = q_2 = 1.0$. Whereas q_2 is often assumed 1.0, q_1 is typically taken between 1.0 and 1.5 [4.2].

The GTN algorithm requires a total of eight parameters which hampers its practical applicability and requires extensive small-scale testing for parameter calibration. In addition, three other challenges can be put forward. First, the outcome of the GTN damage model is highly mesh dependent. Apart from this dependence, a very fine mesh is needed which drastically increases computational time. Second, it may be challenging to relate the model parameters to an experimental representation of ductile tearing in the form of a crack growth resistance curve. Third, the GTN damage model as implemented in *ABAQUS*® is uncapable to capture softening under pure shear [4.24]. In [4.23], shear fractures were found to be dominated by small secondary voids that nucleated from fine precipitates of Fe_3C and martensite-austenite constituents. This may reduce the applicability of the implemented GTN model to high strength line

lic inclusions for grade X100 line pipe steels [4.22, 4.23].

pipe steels such as X100, given their microstructure and the low constraint level of tension loaded pipelines which promotes shear rupture.

In contrast, the GTN model has the unmistakable advantage of being based upon microstructural physics which significantly increases its possibilities. In particular:

- The path of ductile tearing is readily predicted, without requiring additional assumptions.
- The influence of σ_m in Eq. (4.5) reflects that the GTN model can inherently take into account crack tip constraint effects [4.25, 4.26].
- The effect of residual stresses on ductile tearing resistance can be investigated. For instance, damage modelling in [4.27] indicated that tensile residual stresses decrease the crack initiation resistance, but their effect fades out as the crack propagates.

4.4.1.2 Cohesive zone modelling

Cohesive zone modelling assumes a predefined crack propagation path or zone ('process zone') ahead of the crack tip, in which zero-thickness cohesive elements are added as an interface between continuum elements. These cohesive elements are characterized by a 'separation law', which correlates the local normal or shear stress with a certain separation. The latter is highly similar to CTOD.

The history of cohesive zone modelling goes back to as early as the 1960's, when Dugdale [4.28] and Barenblatt [4.29] used a similar approach in analytical strip yield models. Throughout time, many linear and non-linear separation laws have been developed, as indicated in figure 4.21 [4.30].

The application of cohesive zone modelling is attractive as its algorithm is fairly straightforward and intuitive from an engineering point of view. Nevertheless, some objections can be made:

- It is challenging to estimate the separation parameters (e.g. T_0, δ_0, Γ_0, figure 4.21) that comply with experimentally measured failure behaviour obtained from notched tensile tests or fracture mechanics specimens [4.31]. To obtain a good representation of reality, inverse modelling is required [4.30]. As a consequence, much of the intuitiveness is lost.
- The separation parameters are dependent of crack tip constraint [4.32].
- In the most straightforward application of cohesive modelling, a crack path is prescribed and cohesive elements are added in this prescribed path only. As a consequence, crack path predictions become impossible. To

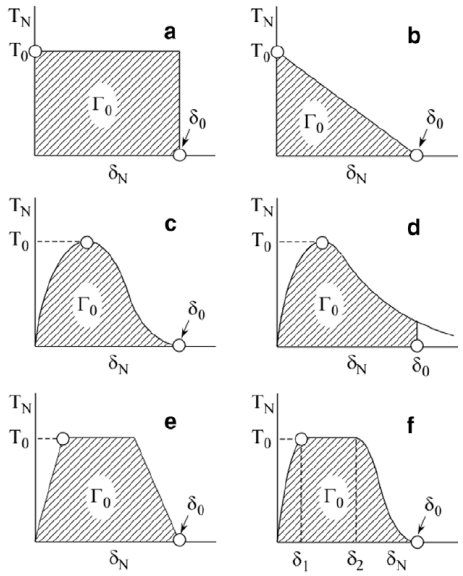

Figure 4.21: Different possible separation laws for cohesive zone modelling [4.30]. In this figure, T_N is the normal tensile stress, δ_N the normal separation, and Γ_0 the separation energy.

overcome this anomaly, cohesive elements can be added at the interfaces of all elements in a *volume* rather than a surface. However, this involves other issues such as the requirement of a very fine and computationally intensive mesh, since the crack propagation path is obliged to coincide with element boundaries (see e.g. figure 4.22 [4.33]).

4.4.1.3 Extended finite element modelling

The extended finite element modelling (X-FEM) method, first reported in 1999 by Belytschko and Black [4.34], addresses the limitation of methods such as cohesive zone modelling that crack propagation should follow element edges (2D) or surfaces (3D). In X-FEM, a crack is allowed to intersect edges of elements, whose nodes are enriched with Heaviside degrees of freedom to allow for discontinuous displacement jumps.

Major advantages of the X-FEM approach are that mesh dependency is strongly reduced, and that crack propagation need not follow a pre-described path. As a consequence, it can be used to predict crack propagation direction in a continuous way.

On the other hand, crack propagation parameters are dependent of constraint.

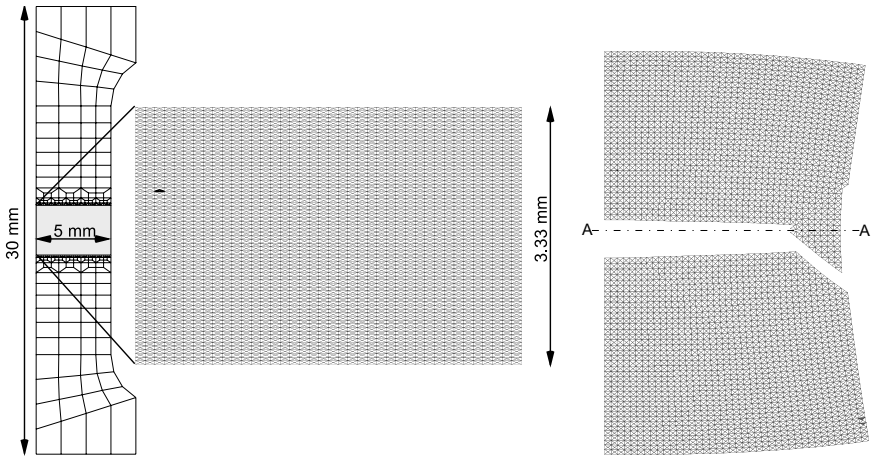

Figure 4.22: Replication of cup and cone fracture in a round bar tensile test: (a) model mesh, (b) fracture path. Taken from [4.33].

The major limitation of X-FEM for the developed finite element model, however, is that its implementation in *ABAQUS*® (version 6.10) is based upon linear elastic material behaviour [4.2]. This implementation is unsuited for the incorporation of advanced plasticity which is aimed at in this dissertation.

4.4.1.4 The mapping approach

The mapping approach is a pragmatic alternative to the abovementioned approaches which – all of them – incorporate ductile tearing within a single simulation. Mapping simply interpolates between results of several simulations with fixed but different crack sizes. The tangency criterion (section 2.2.5) is applied to identify failure due to unstable crack extension. Figure 4.23 illustrates the mapping methodology for application within a strain based context (i.e. deformation controlled loading).

Concretely, the following four steps are followed.

1. Finite element models with flaws of different depths a_i (starting from the initial flaw depth a_0 and alternatively characterized by $\Delta a_i = a_i - a_0$) are built and calculated (figure 4.23(a)). Note that next to flaw depth a, flaw length $2c$ could also be gradually increased. However, the remainder of this dissertation assumes a constant flaw length in accordance with numerically and experimentally observed crack shape developments for long shallow flaws under tension [4.35] (figure 4.24) [4].

[4]Note that this has also been confirmed by experience with CWP testing at Laboratory

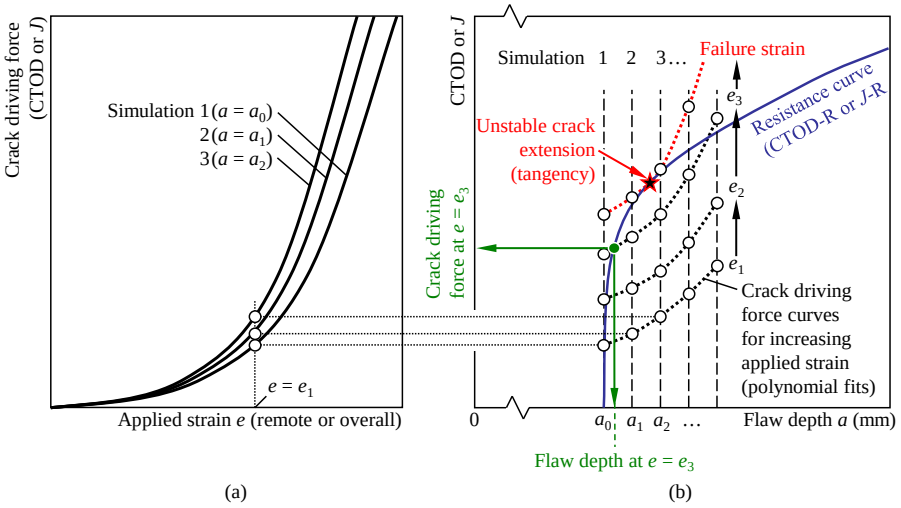

Figure 4.23: Graphical explanation of the mapping approach.

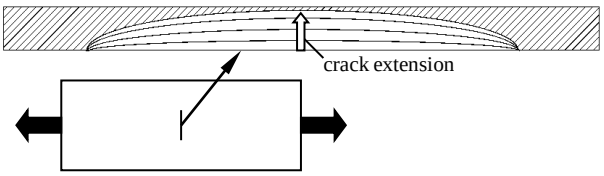

Figure 4.24: Crack shape development of long shallow flaws under tension, according to [4.35].

2. Crack driving force (CTOD or J) values for all simulated flaw extensions a_i corresponding with an equal applied (remote or overall) strain are connected in polynomial fits, to form so-called 'crack driving force curves' (dotted lines in figure 4.23(b)).

3. At each applied strain level, the flaw depth and crack driving force are obtained from intersection between its crack driving force curve and a (CTOD-R or J-R) tearing resistance curve. For instance, figure 4.23(b) indicates the flaw depth and crack driving force at an applied strain e_3 (green circle). Next to this, tensile load is obtained from interpolation between simulation results, the interpolation factor depending on the flaw depth (not shown in the figure). For instance, the tensile load at an applied strain e_3 follows from interpolation between the simulations with

Soete where, notwithstanding rare exceptions, flaw length extension is mostly negligible.

flaw depths a_0 and a_1.

4. Unstable crack extension is announced by means of tangency between the crack driving force curve and the tearing resistance curve (red star in figure 4.23(b)). The corresponding strain level ('failure strain') is an indication of strain capacity.

Since crack growth is not explicitly included in the simulations (where flaw depth has a fixed value a_i), two questions arise:

1. Is the mapping approach justified?
2. If justified, what are (dis)advantages over other modelling methods resulting from the approach?

As regards the first question, Østby [4.36] proved that the mapping approach with the tangency criterion yields conservative results with respect to strain capacity. The reason is that mapping does not incorporate energy dissipation due to the plastic wake which is formed as a crack extends. As a result more energy is readily translated into crack driving force, which becomes overestimated [4.37]. The validity of the mapping approach is further promoted by noting that the determination of J-R curves from single specimen SENB [4.38] and SENT [4.39] tests is based upon an approximate analysis which adopted the mapping approach [4.40].

As regards the second question, the following **advantages** can be put forward.

- The mapping approach is highly pragmatic as it directly uses an experimentally measured crack growth resistance curve. No model parameters have to be tuned by inverse modelling.
- The mapping approach can be applied without modifications to the existing model with fixed flaw size (section 4.3).
- Although a limited set of flaw depths a_i is modelled in the mapping approach, its numerical accuracy is promoted by polynomially fitting (rather than linearly connecting) the obtained results to form crack driving force curves.
- If desired, a crack propagation direction may be imposed by performing nodal coordinate transformations, similar to section 4.3.4. Consequently, in contrast with the GTN damage model and cohesive zone modelling, the mapping approach does not require an extremely fine crack tip mesh.

On the other hand, the mapping approach involves some **disadvantages**.

- In contrast with the GTN damage model, effects of constraint are not explicitly described and should be incorporated by the input of a constraint representative CTOD-R or J-R curve (see section 4.4.1.5).

- The direction of crack propagation is not predicted during the simulation itself and, therefore, requires a user-defined criterion. Although the physical mechanisms behind crack path deviation have not yet been fully clarified, Igi et al. indicated that the distribution of equivalent plastic strain around the flaw tip may play a role (figure 4.25 [4.41]). An alternative approach (based on fracture mechanics principles rather than plasticity) adopts the crack path extension direction which is characterized by the largest energy release rate [4.42].
- Possibilities for crack path deviation are practically impossible in the case of HAZ flaws, since such flaws are forced to follow the fusion line in the finite element model (figure 4.11(b)).

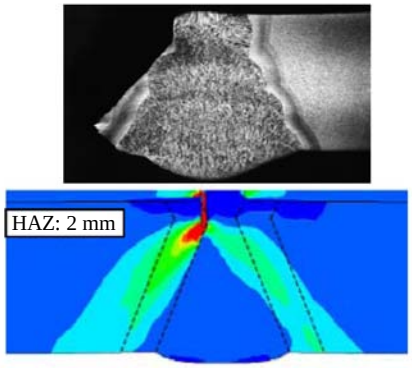

Figure 4.25: The observed direction of crack path deviation (above) corresponds with the area that shows the highest simulated equivalent plastic strain (below) [4.41].

4.4.1.5 Choice of method

Comparing all considered methods for modelling of ductile tearing, a high degree of pragmatism was put forward as a key requisite. As a result, the mapping approach (including the tangency criterion) has been chosen for in this work.

To address the abovementioned disadvantages of this method, the following can be noted.

- As regards the measurement of a representative tearing resistance curve, clamped SENT tests have recently been found to represent the constraint

level of (pressurized) pipes [4.26, 4.43–4.47] and CWP specimens [4.48], both under tension.

- The prediction of crack propagation direction has not been investigated in this research and is advised for future research. For the remainder of this work, cracks are assumed to propagate in the through-thickness direction for WMC flaws and along the fusion line for HAZ flaws. Note that a similar approach has been followed in reported numerical studies, such as [4.12, 4.14, 4.49]. Fairchild et al. reported that the assumption of through-thickness crack extension yields conservative results [4.49].

4.4.2 Implementation of the mapping approach

As regards the practical application of the mapping approach, two different methods (parallel and serial) have been implemented (figure 4.26).

4.4.2.1 Parallel implementation

A first method performs different simulations in **parallel** (figure 4.26(a)). Their results are used to calculate crack driving force curves for application of the mapping approach (see figure 4.23), whose intersections with the tearing resistance curve lead to responses of crack driving force (CTOD(e) or $J(e)$), flaw depth $a(e)$ and tensile load $F(e)$ as a function of applied (remote or overall) strain e. Then, two failure modes (unstable crack extension and plastic collapse) are identified as follows:

- Unstable crack extension follows from the tangency criterion. Since the analysis of simulations involves discretized strain increments, the corresponding failure strain is conservatively estimated as the last strain level which has a crack driving force curve that intersects the tearing resistance curve (figure 4.27).

- Plastic collapse (and its corresponding failure strain) follows from the observation of a maximum tensile load, which indicates the initiation of a necking phenomenon.

The strain capacity of the simulated configuration is then obtained as the minimum of both abovementioned failure strains, as also adopted by Kibey et al. [4.13].

4.4.2.2 Serial implementation

A second method adopts a **serial** execution scheme (figure 4.26(b)). Starting from a simulation with the initial flaw depth a_0, the following steps are followed.

1. A finite element model is created.

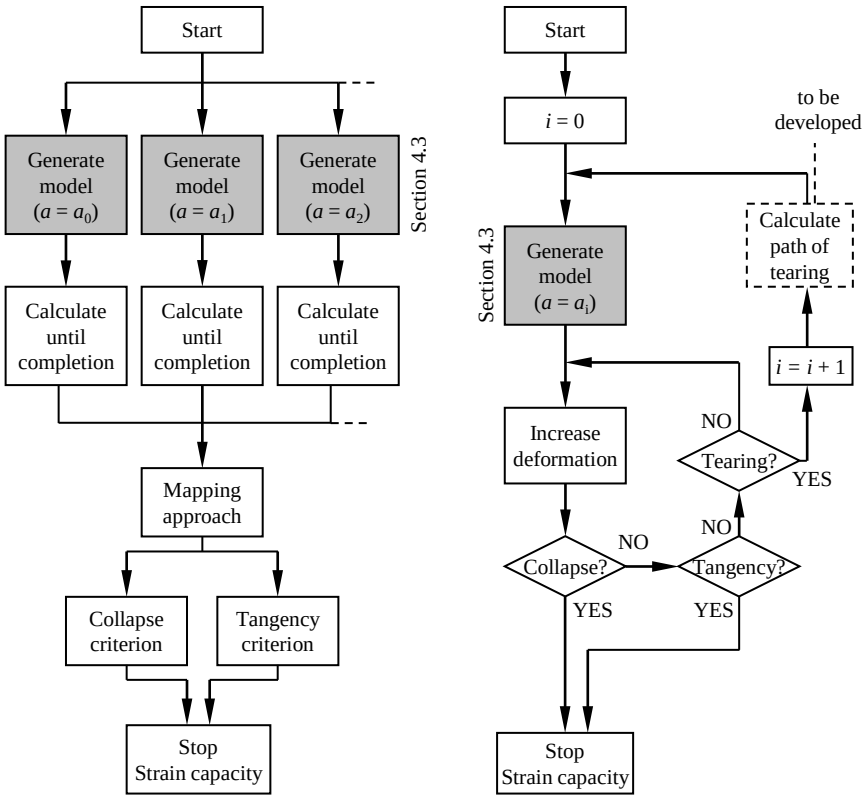

Figure 4.26: Two possible implementation methods of the mapping approach: (a) parallel, (b) serial.

2. The applied end plane displacement (i.e. applied strain) is increased.
3. After each strain increment, it is checked whether or not a drop in tensile load is observed.
   (a) If so, failure occurs due to plastic collapse.
   (b) If not, it is checked whether or not the crack driving force (CTOD or J) exceeds the tearing resistance for the simulated flaw depth.
      i. If not, the procedure goes back to step 2.
      ii. If so, it is checked whether or not tangency occurs (figure 4.27). Note that this check is only possible after two flaw depths have been simulated (i.e. starting from a_1).

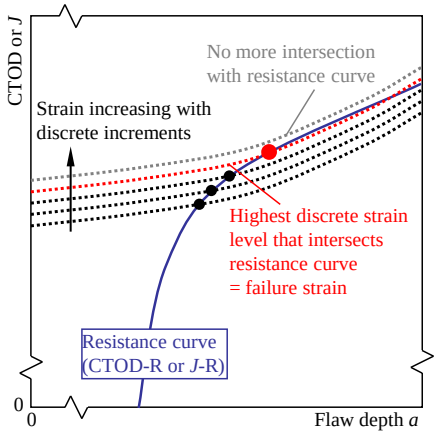

Figure 4.27: Numerical implementation of the tangency criterion.

A. If so, failure occurs due to unstable crack extension.
B. If not, the flaw size is increased with a predefined flaw growth increment from a_i to a_{i+1} and the procedure goes back to step 1.

If available, a procedure can be executed after step 'B' to calculate a deviation path of tearing for WMC flaws (recall related difficulties for HAZ flaws as noted in section 4.4.1.4). Even though such procedure has not been developed in this research, the possibility for its implementation in future work has been explicitly included in a master Python script.

4.4.2.3 Comparison

In contrast with the serial method, the parallel method does not have a feedback loop which allows to modify the direction of crack path deviation. As a consequence, the parallel simulation method is only suited for analyses where assumptions with regard to the path of tearing are made prior to the analysis. A major advantage of parallel simulation executions, however, is a potential reduction of computational time.

4.5 Summary and conclusions

This chapter has presented the development of a parametric finite element model for large scale pipe (panel) tension tests. The developed Python script allows to describe both CWP and FSP specimens. Particular is the 'divide and rule' approach followed: each challenge is separately tackled at a certain stage of the modelling process. A concrete overview is provided in table 4.3, where

all challenges are accompanied by the adopted solutions and corresponding references to the text.

Table 4.3: '*Divide and rule*' approach for creation of finite element models.

Challenge	Approach	Section
Finite-strain fracture mechanics calculations	Spider web mesh at blunt flaw tip	4.2.1
Plasticity analysis	Non-linear geometrical effects, incremental plasticity	4.2.2
Specimen type (CWP or FSP)	Parametric geometry and boundary conditions	4.3.3
Flaw location (WMC or HAZ)	Same partitioning, different material allocations	4.3.3
Numerical accuracy, computation time	Parametric mesh density, possibly predefined	4.3.3
Fine flaw tip in coarse body mesh	Flaw block with regular interface mesh	4.3.3
Pipe curvature	Nodal coordinate transformation	4.3.4
Weld profile (fusion lines, weld cap)	Nodal coordinate transformation	4.3.4
Thickness variation	Nodal coordinate transformation	4.3.4
Misalignment	Nodal coordinate transformation	4.3.4
Type of misalignment	Order of execution of node coordinate transformations	4.3.4
Flaw shape	Nodal coordinate transformation	4.3.4
Ductile tearing	Mapping approach	4.4.2
Direction of crack path deviation	Nodal coordinate transformation in serial execution of mapping	4.4.2

Summarizing table 4.3, the following points deserve particular attention.

- The combination of plasticity and fracture mechanics requires a finite strain analysis which adopts incremental plasticity to describe material behaviour. Other approaches are either unable to predict plastic collapse (small strain analysis instead of finite strain analysis) or prone to convergence issues (deformation plasticity instead of incremental plasticity).
- The flexibility to choose between a CWP or a FSP specimen on the one hand, and between a WMC or a HAZ flaw on the other hand, has been

obtained with a minimum of effort by including boundary conditions and material allocation in the decision-making process of the parametric script.

- Mesh density is parametrically defined, which particularly allows to choose between relatively fine and coarse spider web meshes near the flaw tip. Whereas the former may be required for constraint research purposes, the latter suffices for accurate determinations of crack driving force. Further, three predefined mesh density settings have been developed for the CWP specimen (table 4.1), allowing for different trade-offs between numerical accuracy and computational time.

- Nearly all user-defined geometrical specifications are achieved by the execution of purpose-specific nodal coordinate transformations in a well-chosen order.

- Ductile tearing is modelled by the pragmatic mapping approach, which interpolates between simulations with different fixed flaw depths. The mapping approach has been theoretically justified.

Accepting that finite element modelling relies upon a set of assumptions, the following concrete limitations and restrictions are identified.

Limitations with respect to analysis

- If non-linear geometrical effects are accounted for, an incremental plasticity formulation is required to facilitate analysis convergence. As a consequence, J becomes path independent and is therefore prone to a problematic contour integral convergence. In such case, CTOD appears a more appropriate crack driving force quantity to extract.

- Although the possibility for its implementation has been foreseen, no procedure has been developed to determine the direction of crack path deviation.

Limitations with respect to geometry

Although the development of new (or modification of existing) nodal coordinate transformations can introduce additional geometrical features, the current model is restricted in some aspects, e.g.

- the weld does not have a root penetration,

- pipes are perfectly circular and equally aligned (i.e. weld misalignment due to pipe ovality and angular weld misalignment cannot be investigated).

Limitations with respect to material

Welds, heat-affected zones and line pipe steels consist of continuous transitions between heterogeneous microstructures. The finite element model, however, is confined to the definition of six homogeneous metals: two different homogeneous weld metals (near the root and near the cap), two homogeneous heat-affected zones and two homogeneous base metals (one at each side of the weld).

Despite its limitations, the possibilities of the developed model are at least comparable to those of most reported finite element models for strain based flaw assessment. Therefore, it is concluded that the developed finite element model addresses all requirements for

- *executing detailed parametric studies (see e.g. chapter 8), and*
- *supporting the interpretation of experimental results of large scale pipe tension (CWP and FSP) tests (see e.g. chapter 7).*

Bibliography

[4.1] Dassault Systèmes. *ABAQUS CAE User's manual (version 6.10)*, 2010.

[4.2] Dassault Systèmes. *ABAQUS Analysis User's manual (version 6.10)*, 2010.

[4.3] R.M. McMeeking and D.M. Parks. On criteria for J-dominance of crack tip fields in large-scale yielding. *ASTM STP 668, American Society for Testing and Materials*, pages 175–194, 1979.

[4.4] S. Cravero and C. Ruggieri. A two-parameter framework to describe effect of constraint loss on cleavage fracture and implications for failure assessments of cracked components. *Journal of the Brazilian Society of Mechanical Sciences and Engineering*, 15(4):403–412, 2003.

[4.5] N. O'Dowd. Computational fracture mechanics: numerical modelling of elastic-plastic, creep and residual stresses. In *Structural Integrity and Component Life Assessment – Post Experience Course*, Imperial College, London, UK, May 12-14, 2010.

[4.6] A.J. Horn. *Development of an engineering assessment procedure for predicting cleavage fracture from non-sharp defects using the Failure Assessment Diagram.* PhD thesis, University of Manchester, 2010.

[4.7] A.J. Horn and A.H. Sherry. An engineering assessment methodology for non-sharp defects in steel structures - Part I: Procedure development. *International Journal of Pressure Vessels and Piping*, 89:137–150, 2012.

[4.8] W. Brocks and I. Scheider. Numerical aspects of the path-dependence of the J-integral in incremental plasticity - How to calculate reliable J-values in FE analyses. Technical report, Institut für Werkstofforschung, GKSS-Forschungszentrum Geesthacht, 2001. Technical Note GKSS/WMS/01/08.

[4.9] S. Hertelé. Parametric finite element modelling of large-scale pipeline tests - Part I: Description of the model. Technical Report R/10/0619, Ghent University - Laboratory Soete, Ghent, Belgium, 2010. 101 pages.

[4.10] E. Østby. Fracture control - Offshore pipelines - New strain-based fracture mechanics equations including the effects of biaxial loading, mismatch and misalignment. In *Proceedings of the 24th International Conference on Offshore Mechanics and Arctic Engineering (OMAE)*, Halkidiki, Greece, 2005. OMAE2005-67518.

[4.11] K. Minnaar, P.C. Gioielli, M.L. Macia, F. Bardi, N.E. Biery, and W.C. Kan. Predictive FEA modeling of pressurized full-scale tests. In *Proceedings of the 17th International Offshore and Polar Engineering Conference (ISOPE)*, pages 3114–3120, Lisbon, Portugal, 2007.

[4.12] D.M. Duan, Y.Y. Wang, Y. Chen, and J. Zhou. Modeling and CMOD mapping of surface-cracked wide plates. In *Proceedings of the 7th International Pipeline Conference (IPC)*, Calgary, Alberta, Canada, 2008. IPC2008-64425.

[4.13] S.A. Kibey, K. Minnaar, W. Cheng, and X. Wang. Development of a physics-based approach for the prediction of strain capacity of welded pipelines. In *Proceedings of the 19th International Offshore and Polar Engineering Conference (ISOPE)*, pages 132–137, Osaka, Japan, 2009.

[4.14] N. Yoosef-Ghodsi, D.M. Duan, Q. Chen, R. Petersen, and C. Fan. Finite element analysis of flaw growth history. In *Proceedings of the 8th International Pipeline Conference (IPC)*, Calgary, Alberta, Canada, 2010. IPC2010-31418.

[4.15] N. Gubeljak. Fracture behaviour of specimens with surface notch tip in the heat affected zone (HAZ) of strength mis-matched welded joints. *International Journal of Fracture*, 100(2):155–167, 1999.

[4.16] D. Kozak, N. Gubeljak, P. Konjatić, and J. Sertić. Yield load solutions of heterogeneous welded joints. *International Journal of Pressure Vessels and Piping*, 86(12):807–812, 2009.

[4.17] X. Wang. Two-parameter characterization of elastic-plastic crack front fields: Surface cracked plates under tensile loading. *Engineering Fracture Mechanics*, 76(7):958–982, 2009.

[4.18] S. Hertelé, W. De Waele, R. Denys, M. Verstraete, and J. Van Wittenberghe. Parametric finite element model for large scale tension tests on flawed pipeline girth welds. *Advances in Engineering Software*, 47(1):24–34, 2012.

[4.19] A.L. Gurson. Continuum theory of ductile rupture by void nucleation and growth: Part I - Yield criteria and flow rules for porous ductile materials. *Journal of Engineering Materials and Technology*, 99(1):2–15, 1977.

[4.20] V. Tvergaard. Influence of voids on shear band instabilities under plane strain condition. *International Journal of Fracture Mechanics*, 17(4):389–407, 1981.

[4.21] V. Tvergaard and A. Needleman. An analysis of ductile rupture in notched bars. *Journal of Mechanics and Physics of Solids*, 32(6):461–490, 1984.

[4.22] B. Tanguy, T.T. Luu, G. Perrin, A. Pineau, and J. Besson. Plastic and damage behaviour of a high strength X100 pipeline steel: Experiments and modelling. *International Journal of Pressure Vessels and Piping*, 85(5):322–335, 2008.

[4.23] A. Nonn and C. Kalwa. Modelling of damage behaviour of high strength pipeline steel. 2010. www.tsa.ind.br/files/2010_modelling_of_damage.pdf (Accessed: December 17, 2011).

[4.24] K. Nahshon and J.W. Hutchinson. Modification of the Gurson model for shear failure. *European Journal of Mechanics A/Solids*, 27(1):1–17, 2008.

[4.25] J. Xu, Z.L. Zhang, E. Østby, B. Nyhus, and D.B. Sun. Effects of crack depth and specimen size on ductile crack growth of SENT and SENB specimens for fracture mechanics evaluation of pipeline steels. *International Journal of Pressure Vessels and Piping*, 86(12):787–797, 2009.

[4.26] N. Nourpanah and F. Taheri. Development of a reference strain approach for assessment of fracture response of reeled pipelines. *Engineering Fracture Mechanics*, 77(12):2337–2353, 2010.

[4.27] X.B. Ren, Z.L. Zhang, and B. Nyhus. Effect of residual stresses on ductile crack growth resistance. *Engineering Fracture Mechanics*, 77(8):1325–1337, 2010.

[4.28] D.S. Dugdale. Yielding of steel sheets containing slits. *Journal of the Mechanics and Physics of Solids*, 8(2):100–108, 1960.

[4.29] G.I. Barenblatt. The mathematical theory of equilibrium of cracks in brittle fracture. *Advances in Applied Mechanics*, 7:55–129, 1962.

[4.30] U. Zerbst, M. Heinimann, C. Dalle Donne, and D. Steglich. Fracture and damage mechanics modelling of thin-walled structures - An overview. *Engineering Fracture Mechanics*, 76(1):5–43, 2009.

[4.31] A. Cornec, I. Scheider, and K.H. Schwalbe. On the practical application of the cohesive model. *Engineering Fracture Mechanics*, 70(14):1963–1987, 2003.

[4.32] T. Siegmund and W. Brocks. The role of cohesive strength and separation energy for modelling of ductile fracture. *ASTM STP 1360*, pages 139–151, 2000.

[4.33] I. Scheider and W. Brocks. Simulation of cup-cone fracture using the cohesive model. *Engineering Fracture Mechanics*, 70(14):1943–1961, 2003.

[4.34] T. Belytschko and T. Black. Elastic crack growth in finite elements with minimal remeshing. *International Journal for Numerical Methods in Engineering*, 45(5):601–620, 1999.

[4.35] B. Brickstad and I. Sattari-Far. Crack shape developments for LBB applications. *Engineering Fracture Mechanics*, 67(6):625–646, 2000.

[4.36] E. Østby, C. Thaulow, and B. Nyhus. A new approach to ductile tearing assessment of pipelines under large-scale yielding. *International Journal of Pressure Vessels and Piping*, 84(6):337–348, 2007.

[4.37] S. Hertelé, W. De Waele, R. Denys, and M. Verstraete. Justification of the mapping approach for finite element modelling of ductile tearing. In *Proceedings of the 4th Conference on Sustainable Construction and Design*, pages 36–43, Ghent, Belgium, 2012. ISSN 2032-7471.

[4.38] *Standard test method for measurement of fracture toughness, ASTM E 1820-06*. ASTM International, West Conshohocken, USA, 2006.

[4.39] G. Shen, J.A. Gianetto, and W.R. Tyson. Measurement of J-R curves using single-specimen technique on clamped SE(T) specimens. In *Proceedings of the 19th International Offshore and Polar Engineering Conference (ISOPE)*, pages 92–99, Osaka, Japan, 2009.

[4.40] H.A. Ernst, P.C. Paris, and J.D. Landes. Estimations on J-integral and tearing modulus T from a single specimen test record. In R. Robert, editor, *Proceedings of ASTM STP 743, 13th Fracture Mechanics Conference*, pages 476–502, 1981.

[4.41] S. Igi, T. Sakimoto, N. Suzuki, R. Muraoka, and T. Arakawa. Tensile strain capacity of X80 under tensile loading with internal pressure. In *Proceedings of the 8th International Pipeline Conference (IPC)*, Calgary, Alberta, Canada, 2010. IPC2010-31281.

[4.42] H. Schütte. On curved crack paths in finite strain fracture mechanics. *International Journal of Fracture*, 166(1-2):145–151, 2010.

[4.43] W. Cheng, H. Tang, P.C. Gioielli, K. Minnaar, and M.L. Macia. Test methods for characterization of strain capacity: comparison of R-curves from SENT/CWP/FS tests. In R. Denys, editor, *Proceedings of the 5th International Conference on Pipeline Technology*, Ostend, Belgium, 2009.

[4.44] S. Kalyanam, G.M. Wilkowski, D.-J. Shim, F.W. Brust, Y. Hioe, G. Wall, and P. Mincer. Why conduct SEN(T) tests and considerations in conducting/analyzing SEN(T) testing. In *Proceedings of the 8th International Pipeline Conference (IPC)*, Calgary, Alberta, Canada, 2010. IPC2010-31631.

[4.45] E. Drexler, Y.Y. Wang, J.W. Sowards, and M.D. Dvorak. SE(T) testing of pipeline welds. In *Proceedings of the 8th International Pipeline Conference (IPC)*, Calgary, Alberta, Canada, 2010. IPC2010-31325.

[4.46] H. Tang, M. Macia, K. Minnaar, P. Gioielli, S. Kibey, and D. Fairchild. Development of the SENT test for strain-based design of welded pipelines. In *Proceedings of the 8th International Pipeline Conference (IPC)*, Calgary, Alberta, Canada, 2010. IPC2010-31590.

[4.47] M. Verstraete, W. De Waele, S. Hertelé, and Denys. Influence and evaluation of constraint on fracture toughness in pipeline research. In *Proceedings of the 4th Conference on Sustainable Construction and Design*, pages 25–35, Ghent, Belgium, 2012. ISSN 2032-7471.

[4.48] M. Verstraete, W. De Waele, S. Hertelé, and R. Denys. Constraint analysis of curved wide plate specimens. In *Proceedings of the 19th European Conference on Fracture (ECF19)*, Kazan, Russia, 2012. Accepted for publication.

[4.49] D.P. Fairchild, M.L. Macia, S. Kibey, X. Wang, V.R. Krishnan, F. Bardi, H. Tang, and W. Cheng. A multi-tiered procedure for engineering critical assessment of strain-based pipelines. In *Proceedings of the 21st International Offshore and Polar Engineering Conference (ISOPE)*, pages 698–705, Maui, Hawaii, USA, 2011.

Chapter 5

Development of the medium (curved) wide plate test

An instrumented medium wide plate specimen, mounted in a 2.5 MN universal test rig.

5.1 Goal

Despite the suitability of curved wide plate (CWP) tests for the development of strain based flaw assessment guidelines, their analysis has been mostly confined to the extraction of crack driving force (CMOD or CTOD) as a function of remote strain. This is indeed the prior output of interest since it allows to estimate strain capacity (section 2.4.2). Nevertheless, the evolutions of the two main mechanisms that eventually lead to failure in absence of brittle behaviour – plastic collapse and ductile tearing – are hard to quantify. As a consequence, a proper interpretation of the observed strain capacity may be challenging. This issue is complicated by the fact that the CWP test is not yet standardized for strain based purposes, which hampers the exchangeability of results obtained from different laboratories.

This chapter addresses the abovementioned shortcomings of current CWP testing practice. First, section 5.2 discusses an extension of the traditional instrumentation and test execution, aiming to quantify plasticity and ductile tearing. Then, section 5.3 elaborates on the development of a medium scale wide plate configuration, which has been used to optimize the measurement techniques. Section 5.4 finally shows that this configuration meets important requisites to achieve a representative and exchangeable test result, i.e.

- the occurrence and measurement of highly uniform fields of longitudinal strain, and,
- the possibility of remote strain measurements to represent this uniform longitudinal strain field.

5.2 Advanced instrumentation and test execution

Quantities that are typically recorded during CWP tests are summarized in table 5.1. As explained in section 2.4.2, these measurements allow to identify the occurrence of weld section collapse (load drops and CMOD increases drastically), gross section collapse (CMOD stabilizes and load drops) or a pop-through of the flaw (jump in CMOD).

In order to realize an improved understanding of plastic straining and ductile crack extension, the following measurements have been added to the wide plate testing procedure in this research:

- strain distributions over the specimen, using digital image correlation (section 5.2.1);
- ductile tearing, using the unloading compliance technique (section 5.2.2).

Table 5.1: Typical measurements in CWP testing for strain based design [5.1].

Quantity	Sensor	Aim
Tensile load	Load cell(s)	Calculation of longitudinal gross or net stress
CMOD or CTOD	(Double) clip gauge	Measure of crack driving force
Longitudinal strain	'Small' LVDTs or strain gauges	Measurement of remote strain
Longitudinal strain	'Large' LVDTs	Measurement of overall strain

5.2.1 Digital image correlation

Digital image correlation (DIC) is an optical measurement technique that allows for the quantification of full-field surface strain distributions, which are deduced from displacement distributions. Advantages over strain measurements through LVDTs or strain gauges are that information is gathered over an extended area rather than recording one single result, and that multiple strain components (longitudinal, transverse, shear) can be extracted. DIC measurements strongly enhance the potential for a proper interpretation and, in particular, for the experimental validation of finite element analysis results. For example, the added value of the DIC technique has been shown in literature for tension tests on wide center-notched thin aluminium panels [5.2, 5.3]. Preliminary DIC measurement results on CWP specimens and full scale pipe specimens have been reported in [5.4] and [5.5], respectively.

Note that, apart from DIC, other optical techniques have been implemented in the past to visualize full-field strain distributions in CWP specimens: moiré patterns and photoelasticity. Nevertheless, these techniques – as applied for CWP testing – have some restrictions compared to DIC:

- **Moiré fringe measurements** have been common practice for decades at Laboratory Soete (figure 5.1(a)), with an aim of characterizing the failure mode of CWP tests [5.6]. The applied technique was restricted to an analysis of *longitudinal* strain. Also, the measurements were performed *after* the test instead of on a regular basis during the test. As a consequence, *plastic* strains were measured rather than total strains.

- **Photoelastic measurements** during CWP tests have been performed by NIST [5.7, 5.8] (figure 5.1(b)). This technique is limited to the measurement of *principal* strains rather than the separate in-plane components of the strain tensor. Moreover, it is difficult to obtain quantitative measurements of strain (rather than a qualitative visualization of areas of strain concentration) and there are practical challenges with respect to the required application of a photosensitive film [5.9].

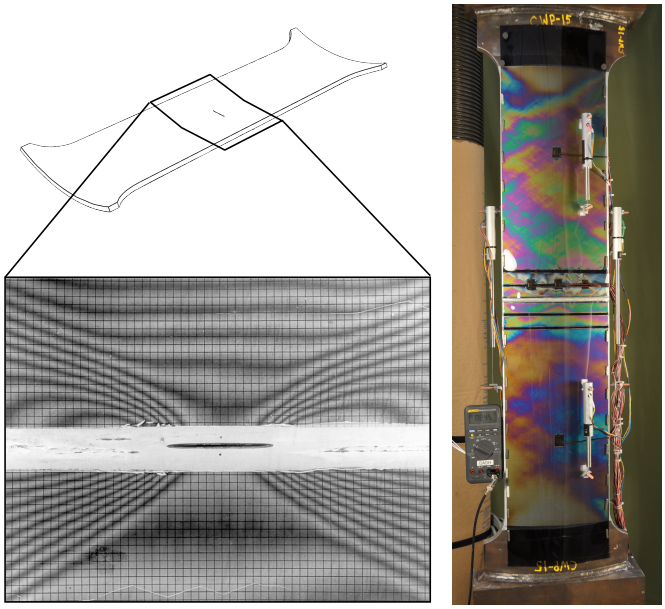

(a) (b)

Figure 5.1: (a) Moiré patterns recorded at Laboratory Soete. (b) Photoelastic patterns on CWP specimen, tested by NIST [5.7].

Necessary for the successful execution of a DIC measurement are:

1. a stereo vision system which records images of the area of interest at well-defined moments. This area of interest may be the entire specimen or a certain zone on this specimen (e.g. in close vicinity to the notch);
2. a random, high-constrast speckle pattern applied on the area of interest;
3. specific software for the post-processing of the recorded images.

Each component is separately discussed below, with a focus on its application in CWP tests.

5.2.1.1 Stereo vision system

The applied stereo vision system consists of two monochromatic 14 bit cameras with a resolution of 2452 by 2054 pixels (5 megapixels), provided by Limess Messtechnik & Software GmbH [5.10]. Both are connected to the control computer with the DIC processing software in a 'daisy chain' configuration to ensure a proper synchronisation between both cameras (figure 5.2). The same figure also shows the position of the stereo vision system with respect to the specimen: measurements have been performed with a view on the inner diameter

surface of the specimen, which is the surface that contains the applied notch mouth.

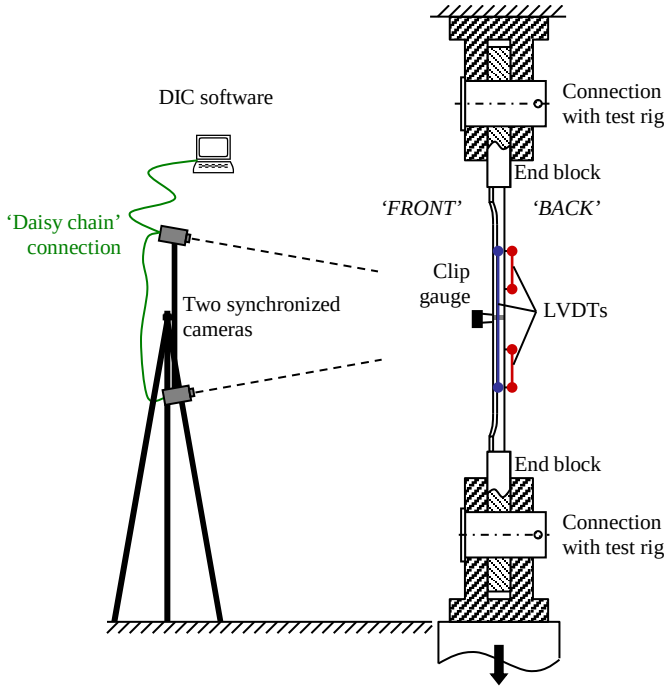

Figure 5.2: Stereo vision system for three-dimensional displacement measurements.

It can be noted that the use of two cameras allows to obtain positions and displacements in three dimensions. Hence, in addition to measuring strains in the two dimensions of the specimen surface, the DIC setup could also be used to accurately record the evolution of the specimen profile.

5.2.1.2 Speckle pattern

A proper DIC analysis requires images of a non-uniform high-contrast random speckle pattern applied on the specimen. Such pattern is generated by spraying a uniform white layer of paint and, after drying, projecting black paint droplets upon the specimen surface. The procedure has been optimized to aim for a speckle size of approximately 3 by 3 pixels, which is advised in [5.11] to achieve a good accuracy. This corresponds with speckles of 0.8 mm by 0.8 mm. Evidently, it is impossible to exactly meet this requirement given the random character of speckles obtained through the applied speckling method. Nevertheless, microscopic images of applied patterns (e.g. figure 5.3) revealed that the developed technique succeeds to achieve speckles whose size vary around

the desired order of magnitude. In addition to the size requirement, a sufficient number of speckles (covering about 50 % of the surface) is advisable. Further, a high contrast between black speckles and white background was achieved by proper lighting.

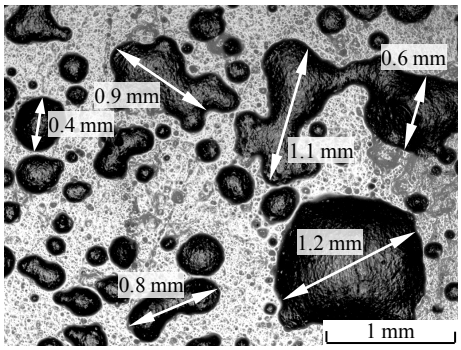

Figure 5.3: Microscopic view of speckles that closely approach the theoretically advised size.

Using the abovementioned speckling method, the standard deviation of measurement scatter is around 10^{-4} (0.01 %) strain. This value has been estimated by calculating the standard deviation of experimental data in the linear elastic region to a linear regression line (figure 5.4). The obtained value of 0.01 % strain is close to the specified optimal strain accuracy of the DIC system (0.005 % [5.12]), which indicates that the speckle pattern is close to optimal.

5.2.1.3 Post-processing software

The VIC3D software (2009 version) of Correlated Solutions Inc. [5.13] has been used to post-process the images obtained by the stereo vision system. The software algorithm aims to obtain the displacement field that yields the best correlation between the image of a deformed surface and a reference image of the undeformed surface. To quantify this correlation, a sum of squared differences is calculated for every investigated point, comparing the grey values of a square subset of pixels around the point in the reference image with the same – but transformed by an assumed displacement field – subset in the deformed image. The displacement of that point is then obtained by minimizing this sum of squared differences. From the obtained displacement field, in-plane strains can be calculated by means of differentiation.

An important parameter in the outcome of a DIC measurement is the size of the subset taken around an investigated point. As a rule of good practice, it is advised for the subset to roughly capture three speckles [5.11]. For the medium

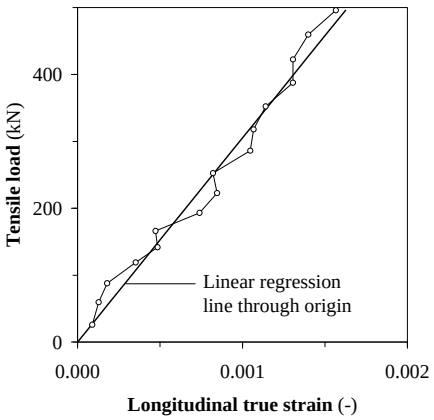

Figure 5.4: Strain-load plot in the linear elastic region of a wide plate test. Strain has been extracted from a DIC measurement at a random point in the prismatic part of the specimen.

wide plate tests, this advice led to the choice for a subset size of 21 by 21 pixels (figure 5.5).

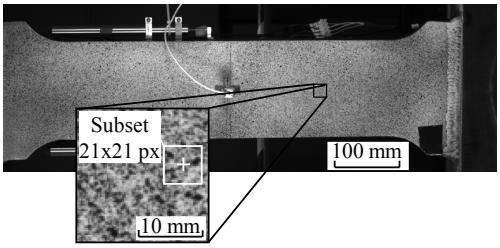

Figure 5.5: The subset size has been chosen to roughly capture three speckles.

5.2.2 Unloading compliance

The unloading compliance (UC) technique aims to relate the flaw size with the compliance (inverse of the stiffness) of the structural element, which is expected to increase if ductile tearing occurs. The 'unloading' compliance UC is defined as the inverse slope of the load-CMOD curve during an unloading-reloading cycle (figure 5.6(b)). These cycles are performed at discrete stages during the test (figure 5.6(a)).

The design and optimization of the unloading compliance method for the fur-

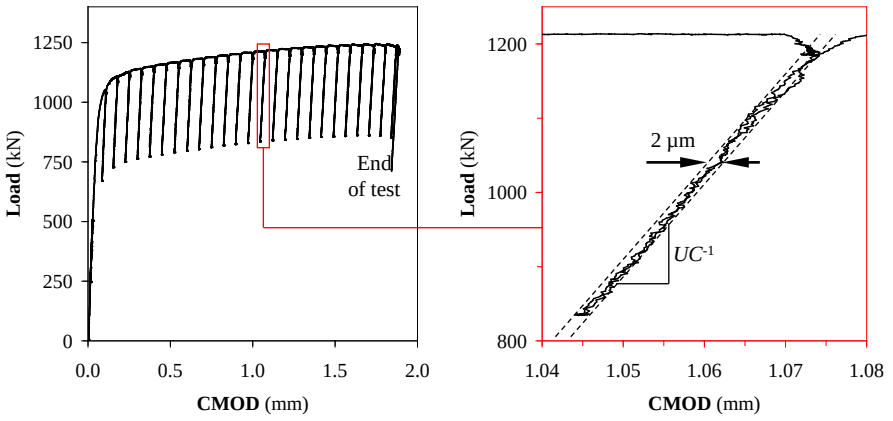

Figure 5.6: Unloading compliance technique, applied to a medium scale (section 5.3.2) CWP test: (a) global load-CMOD record, (b) detail of unloading-reloading cycle.

ther discussed medium wide plate test (see section 5.3.2) has been part of parallel doctoral research within Laboratory Soete, performed by Matthias Verstraete. Therefore, further details regarding the unloading compliance execution procedure are omitted in this dissertation. At this point, it suffices to mention that two particular challenges are related to the successful execution and analysis of an unloading compliance test result.

- An unloading compliance measurement is prone to scatter, which is to a great extent influenced by the accuracy of the clip gauge that measures CMOD. Figure 5.6(b) shows that an accuracy in the order of ± 1 μm is no luxury, given the low compliance of a CWP specimen. Similar accuracies are confirmed in literature [5.4, 5.14]. Bearing in mind that the full scale range of a CMOD clip gauge is typically in the order of 5 mm or more, this corresponds with a relative accuracy of $\pm$ 0.02 %. To achieve this, particular attention has to be devoted to analog and/or digital data filtering.

- The obtained evolution of unloading compliance has to be related to ductile tearing somehow. Whereas analytical relations have been developed for small-scale specimens (e.g. [5.15] for clamped SENT tests), such relations are inexistent for curved wide plate tests which are far more variable in terms of geometry. Therefore, a series of numerical (finite element) results is necessary to construct a case-specific relation between unloading compliance and flaw growth [5.16].

5.3 Design of test specimen geometry

5.3.1 Importance of the prismatic length-to-width ratio and lack of standardization

Whereas a wide plate specimen is restricted in length due to test rig limitations, it aims at representing a long pipeline section. When loaded in tension, the longitudinal strain field in a pipe section at a considerable distance from the girth weld is uniform. Hence, for the wide plate specimen to be representative for strain based assessments, it should ideally contain areas of uniform longitudinal strain at each side of the weld. In such case, the strain distribution near the flawed weld is not influenced by the specimen's end shoulders and their connection to end blocks.

To illustrate the challenge of obtaining an area of uniform strain, figure 5.7 depicts the longitudinal strain distribution in a medium wide plate specimen (see section 5.3.2), obtained through DIC. Two zones of fairly uniform longitudinal strain are beaconed by so-called 'strain hotspots' near the end shoulders and shear lines arising from the flaw. Only if remote strain measurements avoid both the strain hotspots and the shear lines, an unambiguous test result is achieved.

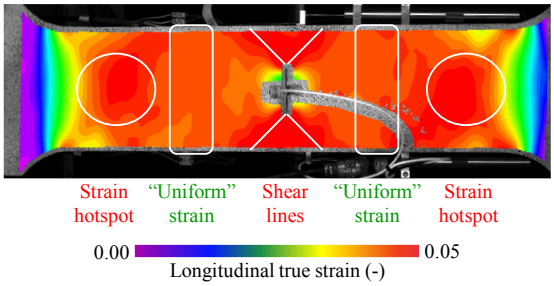

Figure 5.7: DIC measurement of longitudinal strain in a plastically deformed medium wide plate specimen.

To achieve a zone of uniform longitudinal strain in a CWP specimen, recent studies advise a prismatic length-to-width ratio L/W (recall figure 4.7 for the definitions of L and W) of at least 3 [5.4, 5.17, 5.18] [1]. Nevertheless, since

- the (C)WP test is not yet standardized for use in strain based flaw assessments of pipeline girth welds, and

[1] Note that this is more than the minimum L/W ratio 2 specified in the ASTM-standard E740 (2010) [5.19] for wide plate tests intended for the *stress based* flaw assessment of *plain* (i.e. unwelded) plates.

- its dimensions are mostly restricted by test rig limitations,

many different geometrical designs have been applied with prismatic length-to-width ratios ranging from 0.75 to 4.50 [5.1, 5.4, 5.14, 5.20–5.31] (table 5.2; to the author's knowledge). Note that the specimens adopted in [5.22] and [5.28] were only 50 mm and 90 mm wide respectively, which is small compared to common wide plate tests. Nevertheless, they have been included in the table because their purpose was also to investigate the crack driving force response in a strain based design context. Apart from table 5.2, other studies have reported wide plate tests for strain based assessments without explicitly mentioning the specimen geometry (e.g. [5.32, 5.33]).

Table 5.2: Overview of published wide plate specimen geometries for strain based assessment purposes (ordered by increasing prismatic length-to-width ratio L/W).

Author (year) [reference]	$2L$ (mm)	$2W$ (mm)	L/W (-)
Minami et al. (1995, 2011) [5.20, 5.21]	300	400	0.75
Motarjemi (2009) [5.22]	50	50	1.00
Ishikawa et al. (2004) [5.23]	300	200	1.50
Igi et al. (2007) [5.24]	300	200	1.50
Denys (1990) [5.25]	550	300	1.83
Igi et al. (2010) [5.26]	600	200	3.00
Igi et al. (2008) [5.27]	900	300	3.00
Denys et al. (2009) [5.1]	900	300	3.00
Fairchild et al. (2008) [5.4]	1000	300	3.33
Østby (2007) [5.28]	350	90	3.89
Richards et al. (2010) [5.29]	1016	254	4.00
Yoosef-Ghodsi et al. (2010) [5.14]	1400	350	4.00
Stephens et al. (2009, 2010) [5.30, 5.31]	1028	229	4.50

5.3.2 Test rig limitations and the medium (curved) wide plate specimen

The measurements explained in section 5.2 have – next to conventional measurements of tensile load, CMOD and strains – been performed on so-called 'medium' wide plate (MWP) specimens. The name of this specimen originates from the fact that it is smaller than most reported (curved) wide plate tests (typically 200 to 400 mm wide, table 5.2). The MWP specimen width $2W$ is 150 mm. Other dimensions are graphically summarized in figure 5.8(a). Similar to the specimens reported in [5.4], the MWP specimen has a prismatic length-to-width ratio of 3.33 which is close to three. Note that the term 'MWP' refers to both flat and curved wide plate specimens.

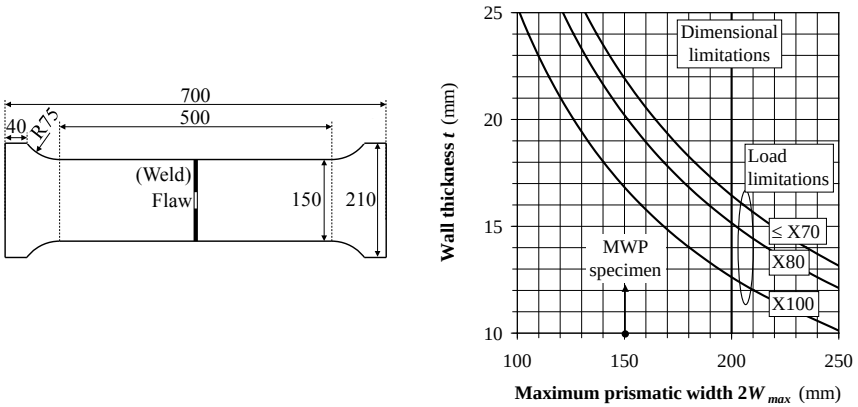

(a) (b)

Figure 5.8: Geometry of the MWP specimen (dimensions in mm) (a), related to the design limitations of the 2.5 MN test rig (b).

Apart from the desire to design a specimen with a prismatic length-to-width ratio of at least 3, the dimensions of the MWP specimen have been chosen with regard to the dimensional and structural limitations of Laboratory Soete's 2.5 MN test rig (figure 5.9, [5.34]). By postulating that the maximum load P_{max} = 2.5 MN should be sufficient to cause collapse in the pipe body – which is the ultimate failure mode of a wide plate specimen – the maximum allowable specimen width $2W_{max}$ can be related to the plate thickness t and steel grade, as follows:

$$2W_{max} = \frac{P_{max}}{R_{m,max}t} \tag{5.1}$$

with $R_{m,max}$ the maximum specified ultimate tensile strength of the steel grade (table 3.1). A width $2W$ = 150 mm has been chosen for the specimen to be applicable under a wide range of conditions (thickness and steel grade), see figure 5.8(b). This figure allows to quantify the possible necessity of choosing a narrower specimen in particular cases (e.g. 20 mm thick X100 panels).

For the sake of completeness, table 5.3 mentions measurement ranges and accuracies of 'typical' [2] measurements that have been performed during MWP tests (see chapter 6). The sensors that have been used for these measurements are depicted in figure 5.10.

[2] Recall table 5.1.

Figure 5.9: An MWP specimen welded to end blocks and mounted in Laboratory Soete's 2.5 MN universal test rig [5.34].

Given the modest dimensions of the MWP specimen compared to common CWP specimens, it should be seen as a medium scale fracture mechanics test specimen. The MWP specimen has been used within this research to investigate and optimize techniques to evaluate plastic straining and ductile tearing.

Table 5.3: Ranges and accuracies of 'typical' measurements for the performed MWP tests.

Sensor	Quantity	Range	Accuracy
Load cell	Tensile load	0 – 2500 kN	± 1 kN
Clip gauge	CMOD	0 – 5 mm	± 1 μm
Remote strain LVDTs	Elongation	0 – 10 mm	± 5 μm
Overall strain LVDTs	Elongation	0 – 90 mm	± 0.3 mm

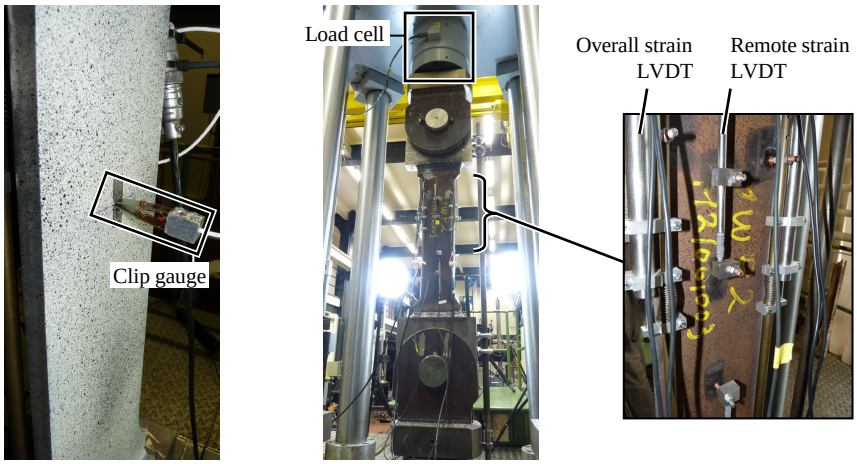

Figure 5.10: Sensors for 'typical' measurements (recall figure 5.2 for definition of 'front' and 'back' surfaces of specimen).

5.4 Measurement of remote strain on a medium wide plate specimen

As already illustrated in figure 5.7, the application of DIC allows to investigate the MWP specimen's feasibility to achieve zones of uniform remote strain. Notwithstanding its extended possibilities for strain analysis, the use of DIC as a routine application is hindered by two aspects. First, the implementation of more conventional strain measurements through LVDTs or strain gauges is far less labour intensive. Second, the applicability of DIC measurements during a wide plate test under sub-zero temperature is practically impossible, as the presence of cooling lugs and/or frost formation on the specimen strongly reduces or even eliminates the visibility of the speckle pattern.

To evaluate the performance of the MWP specimen, a finite element study has been executed which focuses on the uniformity of strain and on where to

ideally place 'conventional' remote strain sensors (LVDTs, strain gauges) on the specimen. Section 5.4.1 explains the applied analysis method. Next, section 5.4.2 elaborates on the simulation matrix. Results are discussed in section 5.4.3.

5.4.1 Analysis method

First, the uniformity of longitudinal strains has been investigated at different cross sections in the prismatic part of the specimen. Introducing a z_{45°-coordinate which is zero where 45 degree lines [3] starting from the flaw center intersect the specimen edges, these sections are characterized by: $z_{45^\circ} = 0$, 25, 50, 75 and 100 mm (figure 5.11). The area closer to the flaw ($z_{45^\circ} < 0$ mm) is considered to show a non-uniform strain distribution due to shear lines originating from the flaw. The area further from the flaw ($z_{45^\circ} > 100$ mm) is also assumed to strain non-uniformly due to the vicinity of the specimen shoulders. The validity of these statements is discussed in section 5.4.3.

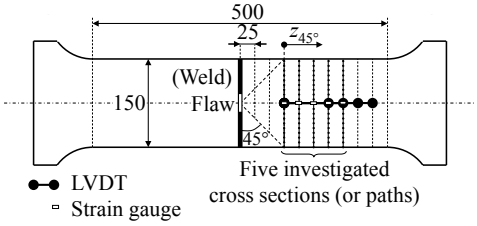

Cross section and strain gauge position z_{45° (mm)	0	25	50	75	100
LVDT gauge length* (mm)	75	100	125	150	

*All LVDT measurements start at $z_{45^\circ} = 0$ mm

Figure 5.11: Investigated configurations for remote strain measurement.

Since sub-surface strains cannot be readily observed experimentally, the analysis of each cross section has been confined to its intersection with the inner diameter specimen surface (further referred to as a 'path'). This simplification is built upon the assumption that, under pure tension, the strain distribution is uniform in the through-thickness direction. This assumption is experimentally validated in chapter 6 (sections 6.5.2.3). For each investigated path, the strain uniformity is further quantified by a dimensionless coefficient of variance c_v. It is defined as the standard deviation of longitudinal strain over the path divided by the average longitudinal strain.

[3] The choice for 45 degree lines has been adopted from the analytical slip line solution of through-wall center cracked tensile loaded (CCT) plates with perfectly plastic homogeneous material behaviour [5.35]. Similar slip lines have been assumed for part-through cracked plates under tension (e.g. in [5.36]). Further, experience with CWP testing has shown that shear lines originating from the flaw are mostly confined to the area $z_{45^\circ} < 0$ mm.

As deformation develops in the specimen during the test, c_v may be prone to changes. To obtain one single output value for every path, c_v is averaged over the simulation result as follows:

$$\bar{c_v} = \frac{\int_0^{\epsilon_{max}} c_v \mathrm{d}\epsilon}{\epsilon_{max}} \geq 0 \tag{5.2}$$

where ϵ_{max} – the strain capacity of the CWP specimen – represents failure (identified as the point of maximum load). The path with the lowest $\bar{c_v}$-value is interpreted as having the most uniform longitudinal strain distribution (the extreme case of a fully uniform strain field corresponding with $\bar{c_v} = 0$). The average true strain observed over that path is considered as the best possible measure of true remote strain ϵ_r and as an advisable location for strain gauges. It is further seen as a reference for other strain measurements and is denoted as $\epsilon_{r,ref}$.

Second, to quantify the ability of an LVDT to measure remote strain, its measurement $\epsilon_{r,meas}$ is compared to the reference measurement $\epsilon_{r,ref}$. Ideally, the ratio $\epsilon_{r,meas}/\epsilon_{r,ref}$ should approximate unity during the full course of the test. In total, four LVDT positions have been considered, all of which have an end point at $z_{45^\circ} = 0$ mm (figure 5.11). Note that some LVDTs exceed the assumed potential area of uniform strain (0 mm $< z_{45^\circ} <$ 100 mm). Longer LVDTs have also been considered since they produce signals with a lower relative strain measurement error, given their increased gauge length. In absence of other considerations, they are therefore preferred over LVDTs with a smaller gauge length.

5.4.2 Finite element study

Finite element simulations of MWP tests have been performed using the model discussed in chapter 4. To investigate a wide range of possible conditions, five parameters have been varied in a simulation matrix. These parameters relate to:

- specimen geometry: D_o/t,
- material characteristics: yield strength overmatch OM_{YS}, strain hardening exponent n (equal for both base and weld metal) under the assumption of Ramberg-Osgood stress-strain behaviour (Eq. (3.15)),
- relative flaw size: a/t, $2c/2W$.

Note that, despite the better ability of the 'UGent' model to represent high strength line pipe steels (chapter 3), the Ramberg-Osgood equation has been adopted for simplicity as the main aim of the parametric study was to obtain general trends rather than exact results.

A design of experiments (DOE) approach has been applied to reduce the number of simulations required for a statistically relevant analysis. For all five varied parameters, realistic 'low' and 'high' values have been chosen (table 5.4). Note that the 'high' value of D_o/t is infinite, which corresponds with a flat plate. In total, 16 simulations have been performed. Each simulation is characterized by a unique combination of 'low' and 'high' values (table 5.5). According to DOE theory, the simulation matrix has a resolution five which implies that main effects and two-factor interaction effects can be unambiguously identified.

Apart from the five varied parameters, all other parameters have been kept fixed for all simulations, notably:

- 0.2 % proof stress of base metal $R_{p0.2,base}$: 500 MPa;
- weld geometry: root opening 5 mm, bevel angle 10°, no weld cap reinforcement, no weld misalignment;
- flaw location (WMC), flaw shape (semi-elliptical), flaw tip radius (75 μm), flaw depth (3 mm).

Table 5.4: Values given to the five variable parameters

Parameter	**Low value ('–')**	**High value ('+')**
OM_{YS} (%)	0	20
n (-)	15 ($Y/T \approx 0.85$) *	25 ($Y/T \approx 0.93$) *
D_o/t (-)	40	∞ (flat plate)
a/t (-)	0.15 ($t = 20$ mm)	0.30 ($t = 10$ mm)
$2c/2W$ (-)	0.17 ($2c = 25$ mm)	0.33 ($2c = 50$ mm)

* Recall Eq. (3.28).

Table 5.5: Design-of-experiments simulation matrix

	Simulation number															
	1	2	3	4	5	6	7	8	9	10	11	12	13	14	15	16
OM_{YS}	–	–	–	–	–	–	–	–	+	+	+	+	+	+	+	+
n	–	–	–	–	+	+	+	+	–	–	–	–	+	+	+	+
D_o/t	–	–	+	+	–	–	+	+	–	–	+	+	–	–	+	+
a/t	+	–	+	–	+	–	+	–	+	–	+	–	+	–	+	–
$2c/2W$	+	–	–	+	–	+	+	–	–	+	+	–	+	–	–	+

5.4.3 Results and discussion

As mentioned in the beginning of section 5.4, results are investigated on two levels, separately discussed below: the possibility of the MWP specimen to produce areas of uniform longitudinal strain (section 5.4.3.1) and the measurements of differently positioned strain sensors (section 5.4.3.2).

5.4.3.1 Uniformity of strain distribution

Figure 5.12 depicts the obtained $\bar{c_v}$-values at the five different investigated paths for the 16 performed simulations. The following is observed:

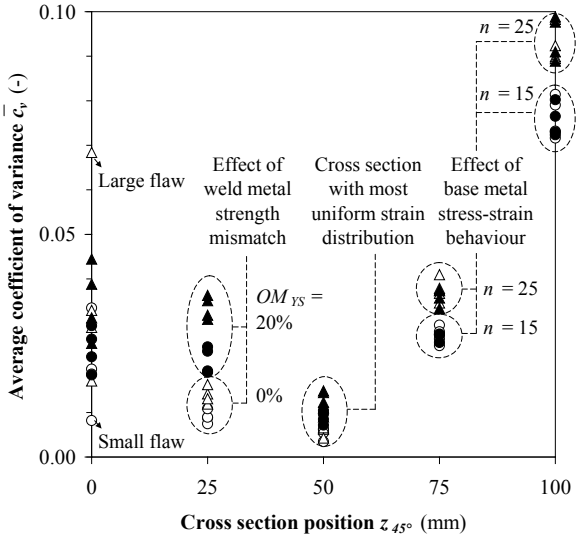

Figure 5.12: $\bar{c_v}$-values for the performed simulations.

- The cross section with the most uniform strain distribution systematically occurs near $z_{45°} = 50$ mm. For all 16 simulations, the average coefficient of variance observed there is below 0.02 which indicates a high degree of uniformity. As an example, figure 5.13 illustrates the strain distribution along the path with $z_{45°} = 50$ mm for the simulation with the highest observed $\bar{c_v}$-value (simulation 16, $\bar{c_v} = 0.015$). When the onset of necking is approached, the specimen tends to strain to a lesser extent at its sides. Nevertheless, a high strain uniformity is remarkable for most of the applied deformation.

- The non-uniformity near the strain hotspots ($z_{45°} = 75$ and 100 mm) is mostly determined by the strain hardening behaviour of the base metal

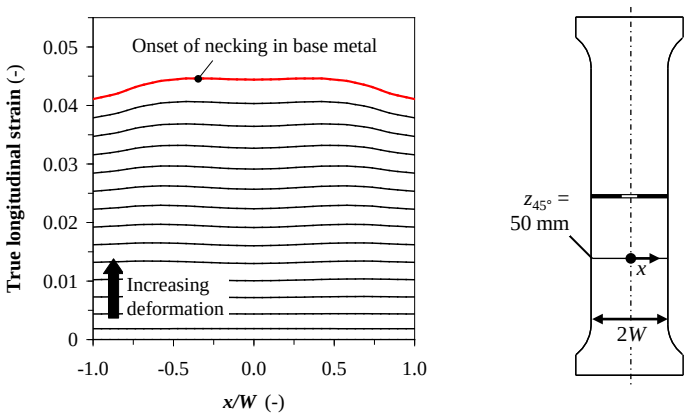

Figure 5.13: Strain distribution along $z_{45^\circ} = 50$ mm path for simulation with the highest observed $\bar{c_v}$-value (simulation 16), up to the onset of necking in the base metal (gross section collapse).

(n), distinguished in figure 5.12 by means of different marker shapes (circular or triangular).

- At a position $z_{45^\circ} = 0$ mm, a major factor of influence seems to be the flaw size, relative to the cross section surface. This position may be too close to the flawed section to perform a remote strain measurement using strain gauges.
- At $z_{45^\circ} = 25$ mm all simulations with $OM_{YS} = 20$ % (black filled markers) have a higher $\bar{c_v}$-value than those with $OM_{YS} = 0$ % (unfilled markers), which indicates a local influence of weld strength overmatch. This is a consequence of different strain distributions, as illustrated in figure 5.14. Whereas the specimens with zero weld yield strength overmatch tend to show pronounced near-shoulder strain hotspots similar to figure 5.7, the overmatching specimens are characterized by more widespread zones of strain concentration (figure 5.14).
- Plate curvature (D_o/t) has not been observed to play a significant role (not shown in figure 5.12).

Overall, given the high strain uniformity at $z_{45^\circ} = 50$ mm (and fair strain uniformity at $z_{45^\circ} = 25$ and 75 mm), the MWP specimen is found suitable for strain based assessment purposes.

5.4.3.2 Influence of sensor position on strain measurement

First, if strain gauges are applied, they should be placed in an area of highly uniform longitudinal strain. From section 5.4.3.1, the position $z_{45^\circ} = 50$ mm

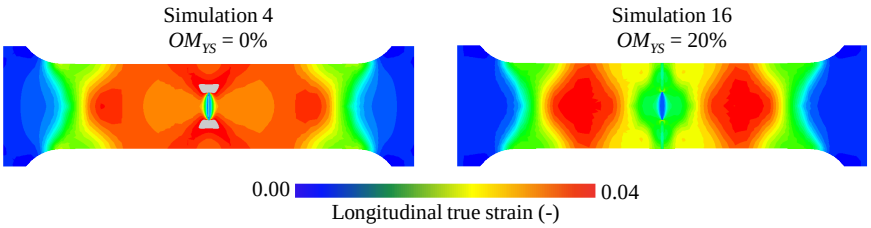

Figure 5.14: Weld strength overmatch has a pronounced effect on the strain distribution in an MWP specimen.

can be advised. Given the local character of a strain gauge measurement, it seems appropriate to place multiple strain gauges on this path and average their outcome. Hereby, it is advisable not to place strain gauges near the specimen sides, where local unevenness (e.g. if the specimen is burnt out of a pipeline) may introduce parasitic strain concentrations. A minimum of three strain gauges is arbitrarely proposed near $x/W = -0.5, 0.0, 0.5$ (recall figure 5.13 for the definition of x).

Second, to evaluate the representativeness of the four LVDT measurements considered in figure 5.11, figures 5.15(a) to (d) depict the evolution of $\epsilon_{r,meas}/\epsilon_{r,ref}$ for different LVDTs, showing a representative selection of simulations. From section 5.4.3.1, OM_{YS} and n have been identified as the key influences on the strain distribution within the specified simulation matrix. Hence, four simulations have been selected from table 5.5 including all possible combinations between these two parameters (simulations 1, 7, 13 and 16). The other twelve simulations perform similarly. Figure 5.15 indicates that the 100 mm long LVDT has the highest representativeness for determination of strain capacity, as its measurement is highly similar to $\epsilon_{r,ref}$ during the full course of all simulations.

Finally it can be noted that – assuming that longitudinal strain does not depend on through-thickness position – it is advised to place strain sensors on the surface which is not recorded by digital image correlation cameras, as this enables a maximum visibility of the speckle pattern.

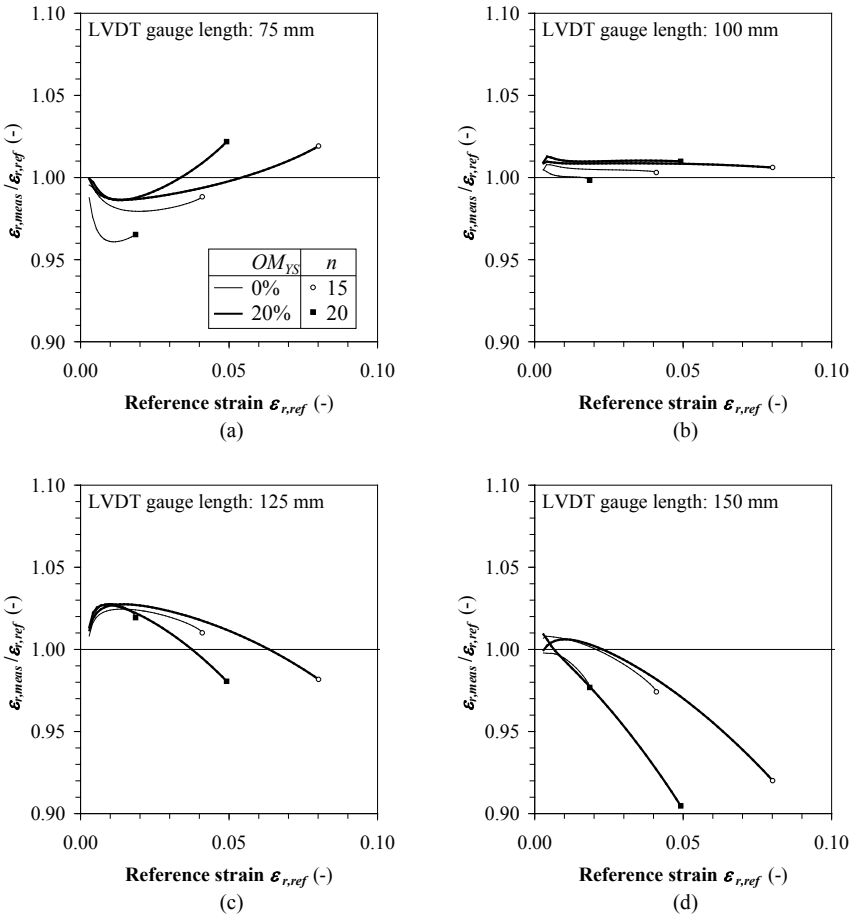

Figure 5.15: Remote strain calculations by LVDT measurements: selection of representative finite element simulation results.

5.5 Summary and conclusions

This chapter has elaborated on the development of a medium scale (curved) wide plate specimen, with particular attention to its instrumentation and geometry.

First, two measurement techniques have been discussed which provide additional useful data over more conventional measurements (load, strain, crack driving force) in a CWP specimen:

- Full-field three-dimensional displacements and surface strain distributions are quantified using digital image correlation (DIC) on images recorded

by a stereo vision system. Particular attention has been given to the achievement of suitable speckle patterns. Important parameters for the sake of accuracy are the size of the speckles, the number of speckles and the contrast between the speckles and the uniformly coloured background layer.

- The unloading compliance (UC) technique has been implemented for the quantification of ductile tearing. Concretely, the specimen is partially unloaded and reloaded at discrete stages, and ductile tearing related to the observed compliance. Required for the successful execution of an UC analysis are a highly accurate CMOD measurement, and a set of finite element analyses which relate the measured compliance with the amount of ductile tearing.

Second, the absence of a standardized procedure for CWP testing has led to a wide variety between test configurations. The estimation of a representative strain capacity is influenced by the prismatic length-to-width (L/W) ratio. Observed variations in L/W-ratio strongly reduce the exchangeability of test results obtained at different laboraties. Aiming to perform medium scale wide plate tests on a 2.5 MN test rig, a specimen has been developed with a prismatic length-to-width ratio of 3.33. A finite element study has shown that this specimen is suited for strain based assessment of flawed pipe girth welds, as

- a zone of highly uniform longitudinal strain is achieved in the specimen, and

- this uniform strain can be accurately measured using conventional sensors (LVDTs, strain gauges).

Concretely, the specimen geometry and advised positions for strain sensors are graphically summarized in figure 5.16.

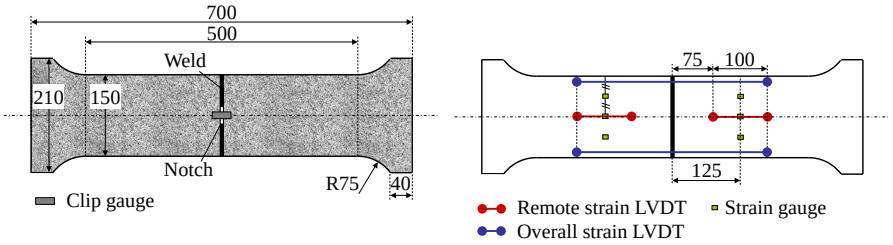

Figure 5.16: The MWP specimen and advised positions for strain measurements: (a) inner diameter surface with notch, (b) outer diameter surface.

The results of the presented study can be extrapolated to other, similar wide plate specimen designs. In particular, if allowed by the dimensional and structural limitations of the test rig,

- *the MWP geometry and sensor configuration can be readily scaled to larger CWP specimens, and/or*
- *a larger prismatic length-to-width ratio can be chosen for to obtain a larger zone of uniform longitudinal strain.*

Bibliography

[5.1] R. Denys and A. Lefevre. UGent guidelines for curved wide plate testing. In R. Denys, editor, *Proceedings of the 5th International Conference on Pipeline Technology*, Ostend, Belgium, 2009.

[5.2] J.D. Helm, M.A. Sutton, and S.R. McNeill. Deformations in wide, center-notched, thin panels, part I: three-dimensional shape and deformation measurements by computer vision. *Optical Engineering*, 42(5):1293–1305, 2003.

[5.3] J.D. Helm, M.A. Sutton, and S.R. McNeill. Deformations in wide, center-notched, thin panels, part II: finite element analysis and comparison to experimental measurements. *Optical Engineering*, 42(5):1306–1320, 2003.

[5.4] D.P. Fairchild, W. Cheng, S.J. Ford, K. Minnaar, N.E. Biery, A. Kumar, and N.E. Nissley. Recent advances in curved wide plate testing and implications for strain-based design. *International Journal of Offshore and Polar Engineering*, 18(3):161–170, 2008.

[5.5] W. Cheng, H. Tang, P.C. Gioielli, K. Minnaar, and M.L. Macia. Test methods for characterization of strain capacity: comparison of R-curves from SENT/CWP/FS tests. In R. Denys, editor, *Proceedings of the 5th International Conference on Pipeline Technology*, Ostend, Belgium, 2009.

[5.6] R. Denys and A. Lefevre. Failure characterisation of a girth weld with surface-breaking flaw under tensile load. In R. Denys, editor, *Proceedings of the 5th International Conference on Pipeline Technology*, Ostend, Belgium, 2009.

[5.7] http://www.nist.gov/mml/materials_reliability/structural_materials/pipeline-safety.cfm. Accessed: December 25, 2011.

[5.8] Y.Y. Wang, M. Liu, T. Weeks, M. Richards, D. McColskey, and D. Horsley. Broad perspectives of girth weld tensile strain response. In *Proceedings of the 8th International Pipeline Conference (IPC)*, Calgary, Alberta, Canada, 2010. IPC2010-31369.

[5.9] Timothy 'Dash' Weeks (NIST, Boulder, Colorado, USA). Personal communication (2012).

[5.10] Limess Messtechnik & Software GmbH, www.limess.com. Accessed: February 20, 2012.

[5.11] M.A. Sutton, J.J. Orteu, and H.W. Schreier. *Image correlation for shape, motion and deformation measurements. Basic concepts, theory and applications*. Springer, 2009. 364 pages. ISBN 978-0-387-78746-6.

[5.12] http://www.correlatedsolutions.com/index.php/products/vic-3d-2009. Accessed: August 2, 2010.

[5.13] Correlated Solutions Inc., www.correlatedsolutions.com. Accessed: February 20, 2012.

[5.14] N. Yoosef-Ghodsi, D.M. Duan, Q. Chen, R. Petersen, and C. Fan. Finite element analysis of flaw growth history. In *Proceedings of the 8th International Pipeline Conference (IPC)*, Calgary, Alberta, Canada, 2010. IPC2010-31418.

[5.15] G. Shen, J.A. Gianetto, and W.R. Tyson. Measurement of J-R curves using single-specimen technique on clamped SE(T) specimens. In *Proceedings of the 19th International Offshore and Polar Engineering Conference (ISOPE)*, pages 92–99, Osaka, Japan, 2009.

[5.16] K. Minnaar, P.C. Gioielli, M.L. Macia, F. Bardi, N.E. Biery, and W.C. Kan. Predictive FEA modeling of pressurized full-scale tests. In *Proceedings of the 17th International Offshore and Polar Engineering Conference (ISOPE)*, pages 3114–3120, Lisbon, Portugal, 2007.

[5.17] Y.Y. Wang, M. Liu, Y. Chen, and D. Horsley. Effects of geometry, temperature, and test procedure on reported failure strains from simulated wide plate tests. In *Proceedings of the 6th International Pipeline Conference (IPC)*, Calgary, Alberta, Canada, 2006. IPC2006-10497.

[5.18] S. Hertelé, W. De Waele, R. Denys, J. Van Wittenberghe, and M. Verstraete. Investigation of pipe strain measurements in a curved wide plate specimen. In *Proceedings of the 8th International Pipeline Conference (IPC)*, Calgary, Alberta, Canada, 2010. IPC2010-31292.

[5.19] *Standard practice for fracture testing with surface-crack tension specimens, ASTM E 740-03.* ASTM International, West Conshohocken, USA, 2010.

[5.20] F. Minami, M. Ohata, M. Toyoda, T. Tanaka, K. Arimochi, A.G. Glover, and T.H. North. The effect of weld metal yield strength on the fracture behaviour of girth welds in Grade 550 pipe. In R. Denys, editor, *Proceedings of the 2nd International Conference on Pipeline Technology*, pages 441–461, Ostend, Belgium, 1995.

[5.21] F. Minami, Y. Takashima, and M. Ohata. Constraint-based assessment of CTOD toughness requirement for high-strain line pipe. *International Journal of Offshore and Polar Engineering*, 21(2):129–140, 2011.

[5.22] A. Motarjemi. Strain-based engineering critical assessment (ECA) of partially mismatched girth welds. In R. Denys, editor, *Proceedings of the 5th International Conference on Pipeline Technology*, Ostend, Belgium, 2009.

[5.23] R. Ishikawa, S. Endo, S. Igi, A.G. Glover, D. Horsley, M. Ohata, and M. Toyoda. Ductile fracture behaviour of girth-welded joints and strain-based design for high-strength pipeline. In R. Denys, editor, *Proceedings of the 4th International Conference on Pipeline Technology*, volume 1, pages 81–98, Ostend, Belgium, 2004.

[5.24] S. Igi and N. Suzuki. Tensile strain limits of X80 high-strain pipelines. In *Proceedings of the 17th International Offshore and Polar Engineering Conference (ISOPE)*, pages 3081–3087, Lisbon, Portugal, 2007.

[5.25] R. Denys. Wide plate testing of weldments, part II - Wide-plate evaluation of notch toughness. *ASTM STP 1058*, pages 157–228, 1990.

[5.26] S. Igi, T. Sakimoto, N. Suzuki, R. Muraoka, and T. Arakawa. Tensile strain capacity of X80 under tensile loading with internal pressure. In *Proceedings of the 8th International Pipeline Conference (IPC)*, Calgary, Alberta, Canada, 2010. IPC2010-31281.

[5.27] S. Igi, T. Sadasue, T. Kubo, N. Ishikawa, and N. Suzuki. Effect of crack geometry and tensile properties on tensile strain limit of X80 linepipe. In *Proceedings of the 18th International Offshore and Polar Engineering Conference (ISOPE)*, pages 79–85, Vancouver, Canada, 2008.

[5.28] E. Østby. Fracture control - Offshore pipelines JIP proposal for strain-based fracture assessment procedure. In *Proceedings of the 17th International Offshore and Polar Engineering Conference (ISOPE)*, pages 3238–3245, Lisbon, Portugal, 2007.

[5.29] M. Richards, T. Weeks, D. McColskey, B. Wang, and Y.Y. Wang. Fatigue pre-cracking curved wide plates in bending. In *Proceedings of the 8th International Pipeline Conference (IPC)*, Calgary, Alberta, Canada, 2010. IPC2010-31468.

[5.30] M.J. Stephens, T. Randy, R.T. Petersen, Y.Y. Wang, and D. Horsley. An experimental basis for improved strain-based design models. In *Proceedings of the 19th International Offshore and Polar Engineering Conference (ISOPE)*, pages 29–35, Osaka, Japan, 2009.

[5.31] M. Stephens, R. Petersen, Y.Y. Wang, R. Gordon, and D. Horsley. Large scale experimental data for improved strain-based design models. In *Proceedings of the 8th International Pipeline Conference (IPC)*, Calgary, Alberta, Canada, 2010. IPC2010-31396.

[5.32] A.C. Bannister, J.R. Ocejo, and F. Gutierrez-Solana. Implications of the yield stress/tensile stress ratio to the SINTAP failure assessment diagrams for homogeneous materials. *Engineering Fracture Mechanics*, 67(6):547–562, 2000.

[5.33] C. Dallam, S. Huysmans, R. Denys, and V. van der Mee. Design criteria for X80 pipe welding: process and strength effects on weld performance in wide plate tests. In R. Denys, editor, *Proceedings of the 5th International Conference on Pipeline Technology*, Ostend, Belgium, 2009.

[5.34] http://www.tribology-fatigue.ugent.be/05_a_mts.shtml. Accessed: October 26, 2011.

[5.35] S. Hao, A. Cornec, and K.-H. Schwalbe. Plastic stress-strain fields and limit loads of a plane strain cracked tensile panel with a mismatched welded joint. *International Journal of Solids and Structures*, 34(3):297–326, 1997.

[5.36] Y. Lei. Use of local and global limit load solutions for plates with surface cracks under tension. *International Journal of Pressure Vessels and Piping*, 84(9):545–559, 2007.

Chapter 6

Curved wide plate and medium wide plate test results

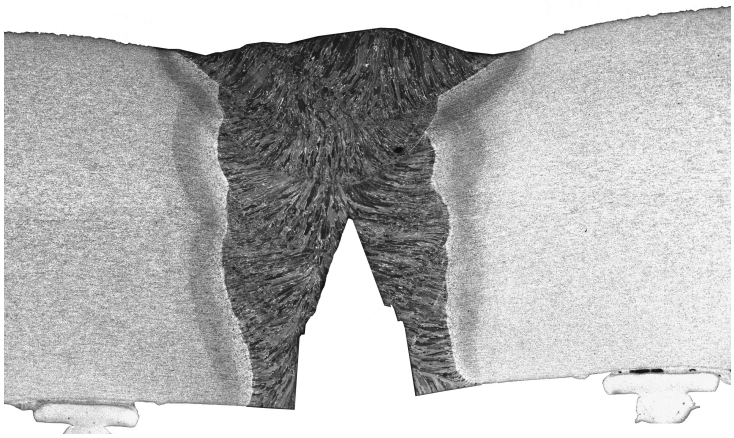

Post-mortem sectioning of an MWP-tested girth weld reveals two important failure mechanisms: plastic collapse and stable ductile tearing.

6.1 Goal

Curved or medium wide plate testing involves a vast number of variables which affect the outcome of the test. Each combination of input materials, geometry, instrumentation and testing conditions produces a unique output and corresponding interpretation. To gain feeling with potential outcomes and issues, an experimental study is an absolute necessity.

This chapter reports on six wide plate test results. Of these, two CWP tests have been adopted from earlier research outside the framework of this dissertation. The other four tests involved MWP specimens and have been intendedly performed for this research.

Throughout this and following chapters, the experimental results will prove to reveal a number of influences and evaluate a set of hypotheses. Of particular interest is the following.

- Although six test results do not suffice for a profound parametric study and are challenging to compare, effects of weld strength overmatch, base metal heterogeneity, flaw dimensions and flaw location will be shown.

- The experimental results allow for a critical comparison between overall and remote strain measurements under different conditions.

- The medium wide plate test results will show the ability of DIC and unloading compliance measurements to obtain a better interpretation of the failure mechanisms.

- The experimental results allow for a critical experimental validation of the finite element model elaborated in chapter 4. To this respect, the MWP tests play a particular role as these tests involved a DIC measurement of surface strain distributions. The experimental validation of the finite element model is treated in chapter 7.

This chapter is structured as follows. First, section 6.2 summarizes major characteristics of all six tests. Then, sections 6.3 and 6.4 elaborate on the two investigated CWP tests (further denoted CWP-1 and CWP-2 respectively). Emphasis is put on 'traditional' measurements of stress, strain and CMOD. Next, sections 6.5 and 6.6 thoroughly discuss the results of the MWP test program. Concretely, section 6.5 explains two MWP tests with specimens extracted from a flat plate and section 6.6 deals with tests on girth weldments produced in the field. Particular attention goes to the DIC and unloading compliance measurements. Conclusions are drawn in section 6.7.

6.2 Experimental program

The experimental program was defined with the aim of including a wide variety of geometrical and material properties. Major characteristics of all six wide plate tests are given in table 6.1. Noteworthy is the coverage of different

- specimen geometries (two different CWP configurations and the MWP geometry; flat plates and curved plates),
- line pipe steel grades (X65 to X80), thermal treatments (uncoated and as-coated) and yielding behaviours (continuous or discontinuous),
- weld types (no weld, manual FCAW weld, mechanized GMAW weld) and yielding behaviours (continuous or discontinuous),

Table 6.1: Overview of investigated wide plate tests.

Specimen type	**CWP**		**MWP**			
Test	**1**	**2**	**F-1**	**F-2**	**C-1**	**C-2**
Section	6.3	6.4	6.5		6.6	
Conditions						
Temperature	-20 °C	-20 °C	RT ⋆		RT ⋆	
Pipe geometry †						
D_o (mm)	1,067 (42")	610 (24")	flat		1,219 (48")	
t (mm)	19.8	15.0	14.6		13.7	
D_o/t (-)	54	41	—		89	
Specimen geometry †						
$2W$ (mm)	200	270	150		150	
$2L$ (mm)	600	900	500		500	
L/W (-)	3.00	3.33	3.33		3.33	
Notch properties †						
a (mm)	3	3	3		3	
$2c$ (mm)	50		25	50	40	
$2ca/2Wt$ (-)	0.038	0.037	0.034	0.068	0.058	
Location	WMC		base metal		WMC	HAZ
Pipe metal properties						
API 5L grade	X80	X65	X65		X70	
Coated?	yes	no	no		yes	
Yielding	continuous	continuous	discontinuous		discontinuous	
Weld (metal) properties						
Weld type	GMAW	FCAW	no weld		GMAW	
Misalignment	no	no	—		yes	
Yielding	continuous	discontinuous	—		discontinuous	

⋆ RT: room temperature.

† See figure 4.7.

- notch locations (base metal, HAZ, WMC) and sizes (between 3.4 % and 6.8 % of the unflawed cross section).

Apart from table 6.1, the following adds belief to the coverage of a wide range of properties. Overmatch levels between 0 % (tests on plain base metal) and 46.6 % (OM_{YS}), 38.1 % (OM_{FS}) or 31.2 % (OM_{TS}) were included. The investigated base metals have Y/T ratios between 0.82 and 0.89 and uniform elongations between 0.079 (7.9 %) and 0.161 (16.1 %).

6.3 Curved wide plate test: GMAW welded X80 pipes (CWP-1)

6.3.1 Material and specimen

CWP-1 was sampled from a girth weldment connecting X80 pipe pups with an outer diameter 1,067 mm (42") and a wall thickness 19.8 mm. The test temperature was -20 °C. The test and the supporting small-scale tests were performed in 2009 at Corus RD&T (nowadays Tata Steel RD&T), Swinden Technology Centre, Rotherham, UK within the framework of the LINESPEC project funded by the Research Fund for Coal and Steel (RFCS) [6.1]. The pipes were GMAW welded, as visible in figure 6.1. Both pups originally belonged to one pipe which was cut in two, after which both parts were bevelled and subsequently joined again by girth welding. A 50 mm long by 3 mm deep notch was produced by electrical discharge machining at the weld metal center, thereby producing a notch tip radius of 150 μm. The notch was rectangularly shaped (i.e. had a constant depth of 3 mm).

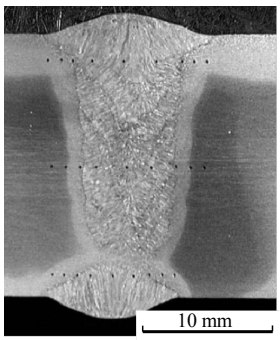

Figure 6.1: GMAW welded X80 pipes: weld section with 10 kgf Vickers hardness indentations after 2 % nital etching.

Table 6.2 gives an overview of major strength and toughness properties, further

discussed below.

Table 6.2: Mechanical properties for CWP specimen of GMAW welded X80 pipes.

Property	**BM**		**HAZ**	**WM**
Temperature	RT ⋆	-20 °C †	RT ⋆	-20 °C
Stress-strain properties (average)				
Yielding	continuous	continuous		continuous
$R_{p0.2}$ (MPa)	590	621		756
R_m (MPa)	687	718		860
Y/T (-)	0.86	0.86		0.88
e_m (-)	0.079	0.079		0.092
OM_{YS} (%) ‡				21.7
OM_{FS} (%) ‡				20.7
OM_{TS} (%) ‡				19.8
10 kgf Vickers (HV10) hardness properties (average)				
Root side	244		273	300
Mid-thickness	218		223	280
Cap side	248		252	272
Average	237		249	284
Toughness properties (minimum / average)				
CTOD (mm) §				0.040 / 0.075

⋆ RT: room temperature.

† values obtained from the FITNET temperature correction (Eq. (6.1)).

‡ overmatch values deduced from temperature corrected base metal properties.

§ obtained from nine $B \times 2B$ SENB tests.

Base metal ('BM') stress-strain properties were determined at room temperature at both sides of the girth weld using longitudinal full thickness strip ('L-FS') specimens (figure 6.2). A high homogeneity is observed since both sides originated from the same pipe. The base metal shows a round-house yielding behaviour. Figure 6.2 also shows transversal weld metal ('WM') stress-strain properties, obtained in the near vicinity of the CWP specimen on the basis of a 4.5 mm diameter round-bar ('T-RB') all weld metal tensile test extracted at mid-thickness, performed at -20 °C.

The different temperatures of the base metal and weld metal tensile tests do not allow for a direct quantitative determination of weld strength overmatch. Therefore, the empirical FITNET [6.2] temperature correction for yield strength $\Delta\sigma_T$ (MPa) was applied to the *full* [1] stress-strain curves of the base metal tensile tests:

[1] This involves the pragmatic assumption that a yield strength temperature correction can be extrapolated to all stress-strain data points.

$$\Delta\sigma_T\,(\text{MPa}) = \frac{10^5}{491 + 1.8T\,(^\circ\text{C})} - 189 \tag{6.1}$$

The resulting corrected strength values ($\Delta\sigma_T$ = 31 MPa for T = -20 °C) are also provided in table 6.2 and have been used for the determination of weld strength overmatch levels.

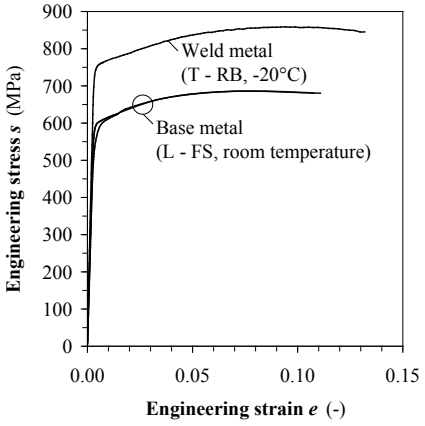

Figure 6.2: GMAW welded X80 pipes: base and weld metal stress-strain curves.

10 kgf Vickers hardness tests (HV10) were performed near the weld root, the weld cap, and at mid-thickness. The HAZ near the weld root was significantly harder than its adjacent pipe metal. Apart from the weld root location, HAZ and pipe metal hardness properties were similar. From the fact that hardness values are an indicator of strength (more specifically, ultimate tensile strength R_m [6.3]), the high degree of weld strength overmatch is confirmed.

SENB fracture toughness tests indicated a fairly low weld metal fracture toughness (CTOD) of 0.040 mm (minimum) / 0.075 mm (average) at -20 °C.

Figure 6.3 shows the specimen geometry and positions of LVDTs for measurement of remote strain e_r and overall strain e_o. Note that overall strain was measured from two LVDTs at opposite surfaces of the specimen, and remote strain was measured on the notched surface of both base metals. Further, CMOD and tensile load were recorded.

6.3.2 CWP test result

Despite the low weld metal toughness, CWP-1 failed due to gross section collapse. After the test, the specimen was cooled to liquid nitrogen temperature

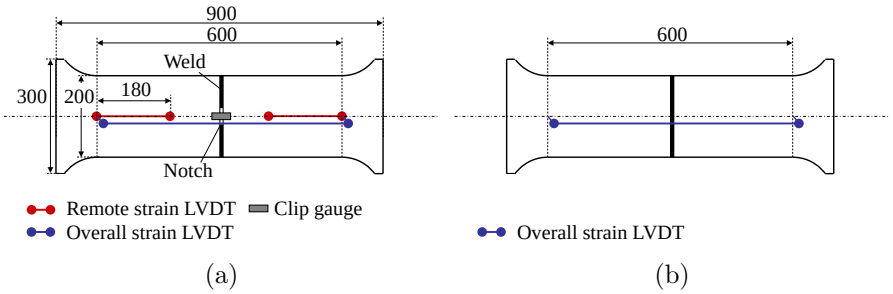

Figure 6.3: Geometry and instrumentation of CWP-1: (a) inner diameter surface, (b) outer diameter surface

and broken open in a brittle way to view the notch. Visual inspection (figure 6.4) and optical microscopy did not reveal any ductile tearing.

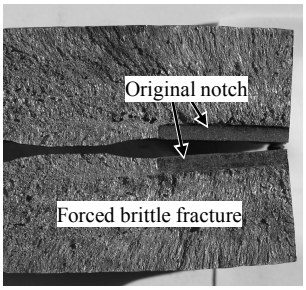

Figure 6.4: CWP-1: A view on the electrical discharge machined notch after forced brittle fracture does not indicate ductile tearing.

The relative response of both welded plates is reflected in their evolution of remote strain, visualized on the basis of a further called 'remote strain heterogeneity plot' (figure 6.5(a)). Near a remote strain level of 0.06, the corresponding LVDTs saturated and further measurements became unvalid. Nevertheless, the remarkable correspondence between both base metals' remote strains up to that level confirms the abovementioned base metal homogeneity. Given the saturation of the remote strain LVDTs, the overall strain is further used for discussion of the CWP test result. Note that overall strain (averaged from both LVDTs at opposite surfaces, $e_{o,avg}$) tends to be slightly smaller than remote strain (figure 6.5(b)).

Figure 6.6 shows the evolution of gross stress s and CMOD as a function of average overall strain. Comparison between the s-$e_{o,avg}$ curve and the temperature corrected base metal stress-strain curves indicates a fair correspondence,

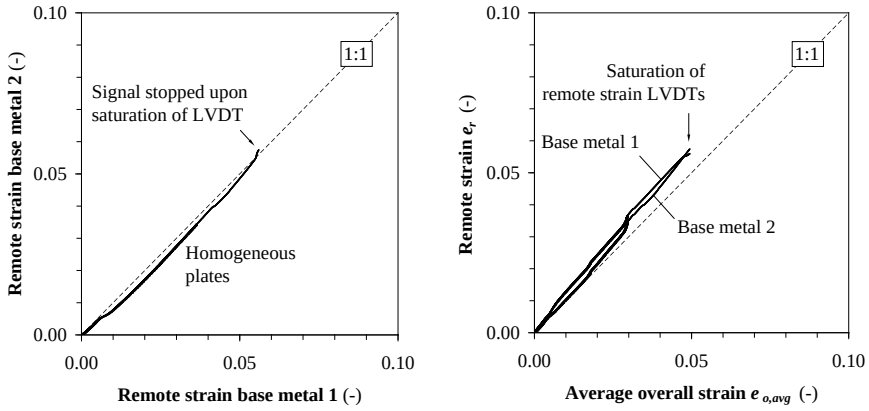

Figure 6.5: CWP-1: (a) Remote strain heterogeneity plot; (b) Prior to saturation of the remote strain LVDTs, remote strains are larger than overall strain.

given the approximate nature of Eq. (6.1).

The observed CMOD response (figure 6.6) is – apart from its initial behaviour – mostly characterized by a fairly constant slope up to the point of base metal necking. The slight kink around 0.03 overall strain could be attributed to instrumentation and is therefore not related to material behaviour. Note that CMOD keeps rising even after the occurrence of maximum tensile force, a phenomenon which has been observed before in [6.4] and which is not yet fully understood. A hypothesis in [6.4] was that the crack grows even beyond the achievement of maximum load. It can be noted that this observation is further investigated using finite element analysis in section 7.3.1.1.

It is challenging to estimate a strain capacity value from the test data as five discrete peaks of equal maximum load have been recorded. These peaks occur at $e_{o,avg} = 0.059$, 0.060, 0.063, 0.066 and 0.067 overall strain, thereby covering a range of 0.008 average overall strain. Note that CMOD keeps rising even after the occurrence of the last maximum tensile force peak, a phenomenon which has been observed before in [6.4] and which is not yet fully understood. Concretely, assuming a strain capacity of 0.063 (the average of the five overall strains at maximum load), the eventual CMOD (1.34 mm) exceeds its value at strain capacity (1.24 mm) with 8 %.

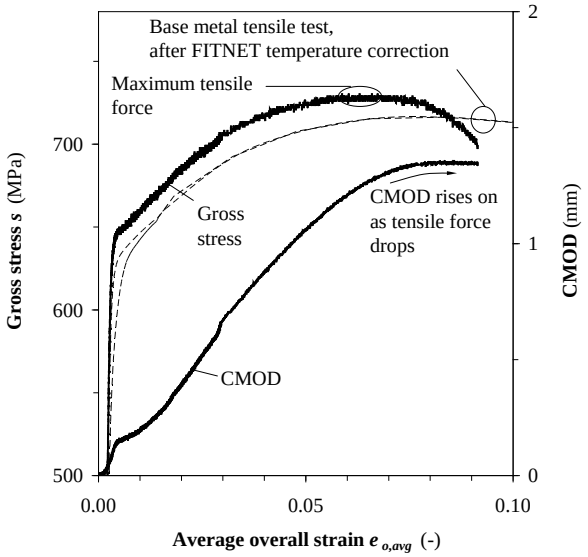

Figure 6.6: CWP-1: CMOD and load response.

6.4 Curved wide plate test: FCAW welded X65 pipes (CWP-2)

6.4.1 Material and specimen

CWP-2 tested a girth weldment between two X65 pipe pups with 610 mm (24") outside diameter and 15 mm wall thickness. The test was performed on Laboratory Soete's 8 MN tensile test rig [6.5] at a monitored temperature of -20 °C. The girth weld procedure was designed for research purposes and not intended for application in the field. Similar to CWP-1 (section 6.3.1), both pups originated from the same pipe. No ageing heat treatment was applied. The girth weld consisted of a soft GTAW [2] root pass, followed by FCAW filler passes (figure 6.7). An exceptionally high weld cap reinforcement (roughly 4.5 mm) is particularly observed. The weld is not misaligned.

The CWP specimen contained a 50.0 mm long by 3.0 mm deep surface notch, milled centrally into the WMC root in two steps, the final step using a 150 μm thick saw blade (blade diameter 63 mm).

Strength and toughness properties are summarized in table 6.3 and discussed below.

[2]Gas tungsten arc welding.

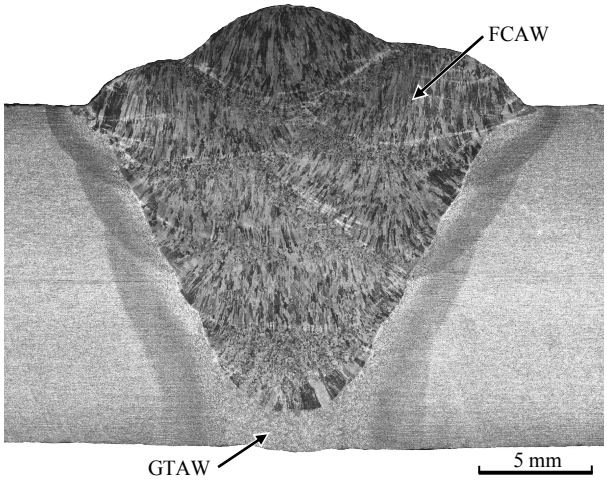

Figure 6.7: FCAW filler and cap welded X65 pipes with GTAW root weld pass: section of weld after 2 % nital etching.

At both sides of the weld, base metal properties were determined at room temperature using longitudinal full thickness strip ('L-FS') specimens (figure 6.8). As was also the case for CWP-1 (section 6.3.1), the base metals are highly homogeneous due to their identical origin.

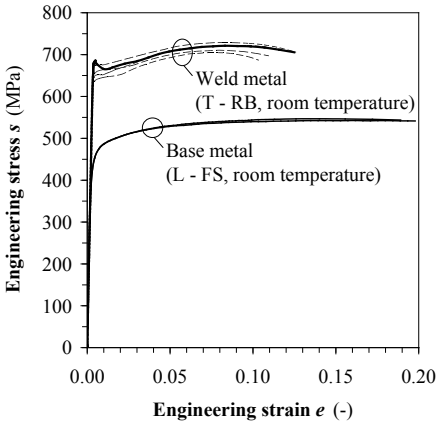

Figure 6.8: FCAW welded X65 pipes: base and weld metal stress-strain curves.

Transversal weld metal stress-strain properties have been obtained for different o'clock positions on the basis of 6 mm diameter round-bar ('T-RB') all weld

Table 6.3: Mechanical properties for CWP specimen of FCAW welded X65 pipes.

Property	**BM**	**HAZ**	**WM** ⋆
Stress-strain properties (average) †			
Yielding	continuous		discontinuous
$R_{p0.2}$ (MPa)	451		661
R_m (MPa)	548		719
Y/T (-)	0.82		0.92
e_m (-)	0.137		0.081
e_L (-)	—		0.015
OM_{YS} (%)			46.6
OM_{FS} (%)			38.1
OM_{TS} (%)			31.2
10 kgf Vickers (HV10) hardness properties (average)			
Root side	192	190	188 (GTAW)
Mid-thickness	170	178	240
Cap side	187	208	246
Average	183	192	243
Toughness properties (minimum / average)			
CTOD (mm) ‡			0.090 / 0.095

⋆ unless otherwise specified, data represent the FCAW weld metal.

† obtained from tensile tests at room temperature.

‡ obtained from three $B \times 2B$ SENB tests at -20 °C.

metal tensile tests, sampled in the weld metal center at mid-thickness (FCAW filler passes). The resulting stress-strain curves (figure 6.8) indicate a high degree of o'clock heterogeneity in terms of yield and ultimate tensile strength (varying over roughly 50 MPa) and Lüders elongation e_L (ranging between 0.005 and 0.025). The stress-strain curve corresponding with the specimen sampled most adjacent to the CWP panel is indicated with a bold solid line; other weld metal curves are thin and dashed. The small-scale tensile tests indicate an exceptionally high degree of weld strength overmatch (on average 46.6 % for $R_{p0.2}$ and 31.2 % for R_m).

10 kgf Vickers hardness tests (HV10) were performed near the weld root and the weld cap, and at mid-thickness. The results confirm the high degree of FCAW weld strength overmatch (table 6.3). Further, no HAZ softening was observed and the hardness of the GTAW root pass was found similar to that of the base metal.

Specimen geometry and LVDT positions were chosen according to figure 6.9. Two LVDTs measured overall strain e_o at both sides of the specimen, whereas two other LVDTs recorded remote strain e_r on the notched inner diameter

surface for each base metal. Further, the specimen was instrumented with a clip gauge for CMOD measurement and tensile load was recorded. Strain gauges were not used.

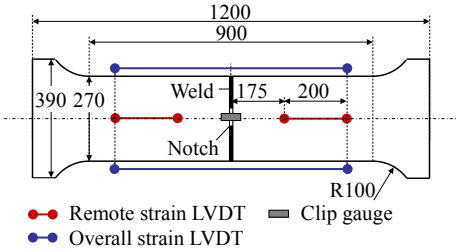

Figure 6.9: CWP-2: Specimen geometry and positions of sensors (inner diameter surface).

SENB fracture toughness tests indicated a moderate weld metal fracture toughness (CTOD) of 0.090 mm (minimum) / 0.095 mm (average) at -20 °C.

6.4.2 CWP test result

CWP-2 failed due to gross section collapse. A post-mortem section of the notched weld reveals that, apart from some minor ductile tear initiation, no significant crack extension had occurred (figure 6.10).

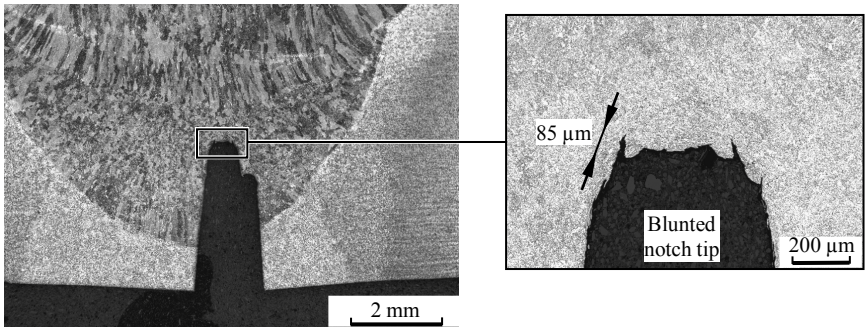

Figure 6.10: CWP-2: Post mortem image of notched weld after 2 % nital etching.

The abovementioned homogeneity of both welded plates is reflected in their remote strain heterogeneity plot (figure 6.11(a)). Apart from the obvious absence of heterogeneity, this plot also indicates the failure mode and location, as deformations eventually concentrate into one plate ('base metal 1' in the figure).

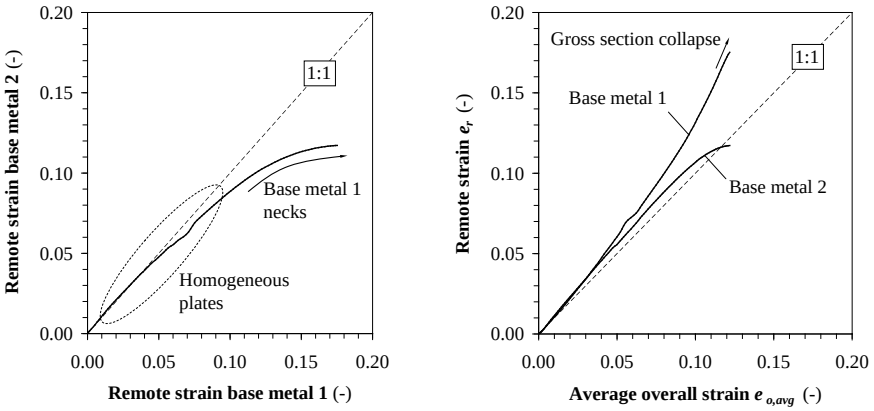

(a) (b)

Figure 6.11: CWP-2: (a) Remote strain heterogeneity plot; (b) Prior to necking, remote strains are larger than overall strain.

Figure 6.12 shows the monitored evolution of gross stress and CMOD against remote strain, averaged between both plates ($e_{r,avg}$). The following is observed.

- Similar to CWP-1 (section 6.3.2) the base metal behaved stronger during the CWP test than during small-scale tensile testing. Application of the FITNET temperature correction on the small-scale tensile test results (Eq. (6.1)) gives a near to perfect correspondence between the base metal stress-strain responses of the CWP test and the corrected tensile tests. Hence, the increased base metal strength of CWP-2 can be fully attributed the sub-ambient test temperature.
- At the initial remote yielding stage (average remote strain below 0.02), CMOD seems to stabilize towards a value not exceeding 0.15 mm. Between 0.02 and 0.06 average remote strain, however, an abrupt slope increase occurs. Gradually CMOD stabilizes again which marks the development of gross section collapse. In agreement with CWP-1 but more pronounced, the saturation of CMOD is delayed to a strain level beyond the occurrence of maximum tensile force.

At the point of failure, the remote strains at both sides of the girth weld were 0.094 and 0.109. These values are lower than the base metal's uniform elongation (table 6.3). This observation may be a consequence of the reduced test temperature which has a detrimental effect on ductility.

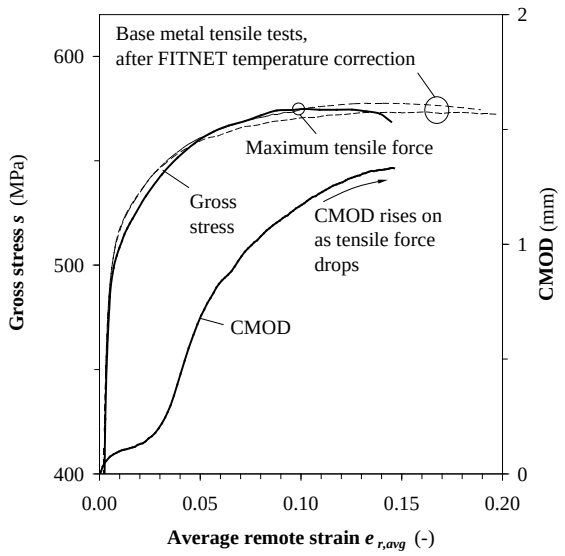

Figure 6.12: CWP-2: CMOD and load response.

6.5 Flat medium wide plate tests: plain X65 plate (MWP-F-1 and MWP-F-2)

6.5.1 Material and specimen

As a first step in gaining experience with MWP testing, specimens were extracted from 14.6 mm thick flat X65 plates without weld. Stress-strain behaviour is summarized in table 6.4 and depicted in figure 6.13. Particularly notable is a highly pronounced Lüders plateau. Note that figure 6.13 shows only one of six obtained stress-strain curves, which were found highly similar with respect to strength and strain characteristics.

Eventually, two flat plate MWP tests (MWP-F-1 and MWP-F-2) with geometry and instrumentation according to figure 5.16 (apart from strain gauges, which were not applied) were performed at room temperature on Laboratory Soete's 2.5 MN test rig (figure 5.9). These tests only differ in the size of the notch applied (3 mm × 25 mm and 3 mm × 50 mm, respectively). The notch was milled centrally into the specimen with a procedure equal to that used for notching specimen CWP-2 (section 6.4.1).

Table 6.4: Stress-strain properties of plain X65 plate.

Property	Value
Yielding	discontinuous
$R_{p0.2}$ (MPa)	443
R_m (MPa)	537
Y/T (-)	0.83
e_m (-)	0.161
e_L (-)	0.026

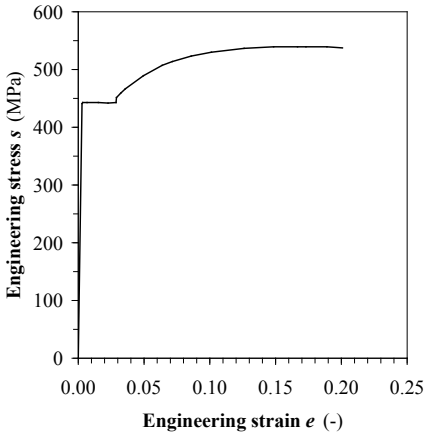

Figure 6.13: X65 plate: stress-strain curve.

6.5.2 MWP test results

Compared with CWP-1 (section 6.3) and CWP-2 (section 6.4), the analysis of the executed MWP tests additionally involves DIC and unloading compliance measurements. For the sake of clarity, this section is separated into four aspects:

1. failure and post mortem analysis,
2. DIC analysis,
3. load, strain and CMOD responses,
4. unloading compliance analysis.

6.5.2.1 Failure and post mortem analysis

MWP-F-1 failed due to net section collapse. To protect equipment, the test was stopped after the achievement of maximum load but before an actual unstable rupture event occurred. MWP-F-2 was ended prior to the observation of

maximum load due to an unforeseen bug in the control software. Nevertheless, a high degree of plasticity was achieved and MWP-F-2 was also very close to net section collapse. This failure mode should be of no surprise for both tests as plain metal without weld was tested.

The occurrence of net section (flaw ligament) collapse and significant ductile tearing in MWP-F-1 becomes clear from a post mortem cross section of the notch. The final crack depth was 4.8 mm. Ductile tearing was also observed in MWP-F-2, showing a final crack depth 4.3 mm.

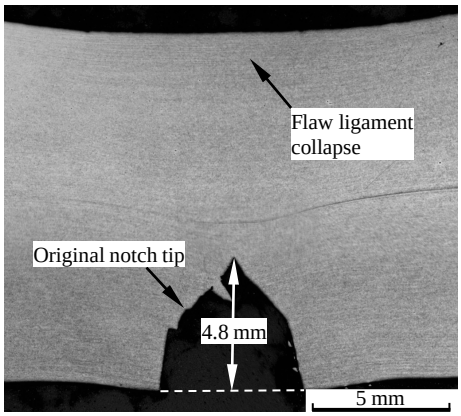

Figure 6.14: MWP-F-1: Post mortem image of notched section after 2 % nital etching.

6.5.2.2 DIC analysis

Figure 6.15 shows a DIC analysis of longitudinally oriented strain in MWP-F-1 and MWP-F-2. For each contour plot, the central location of the notch is indicated by the position of the clip gauge. Four typical strain patterns can be identified throughout the test:

1. The specimens deform linear elastically and strain concentrations originate from the specimen shoulders (subfigures (a)). At this point, the DIC result is to a large extent blurred due to the relative importance of measurement scatter with respect to the actual (i.e. low) strain level.

2. Lüders bands originate from the area of highest stress concentration (subfigures (b)). For MWP-F-2, this area was the notched section. For MWP-F-1, the notch was sufficiently small for Lüders bands to initiate from one of the shoulders rather than the notch.

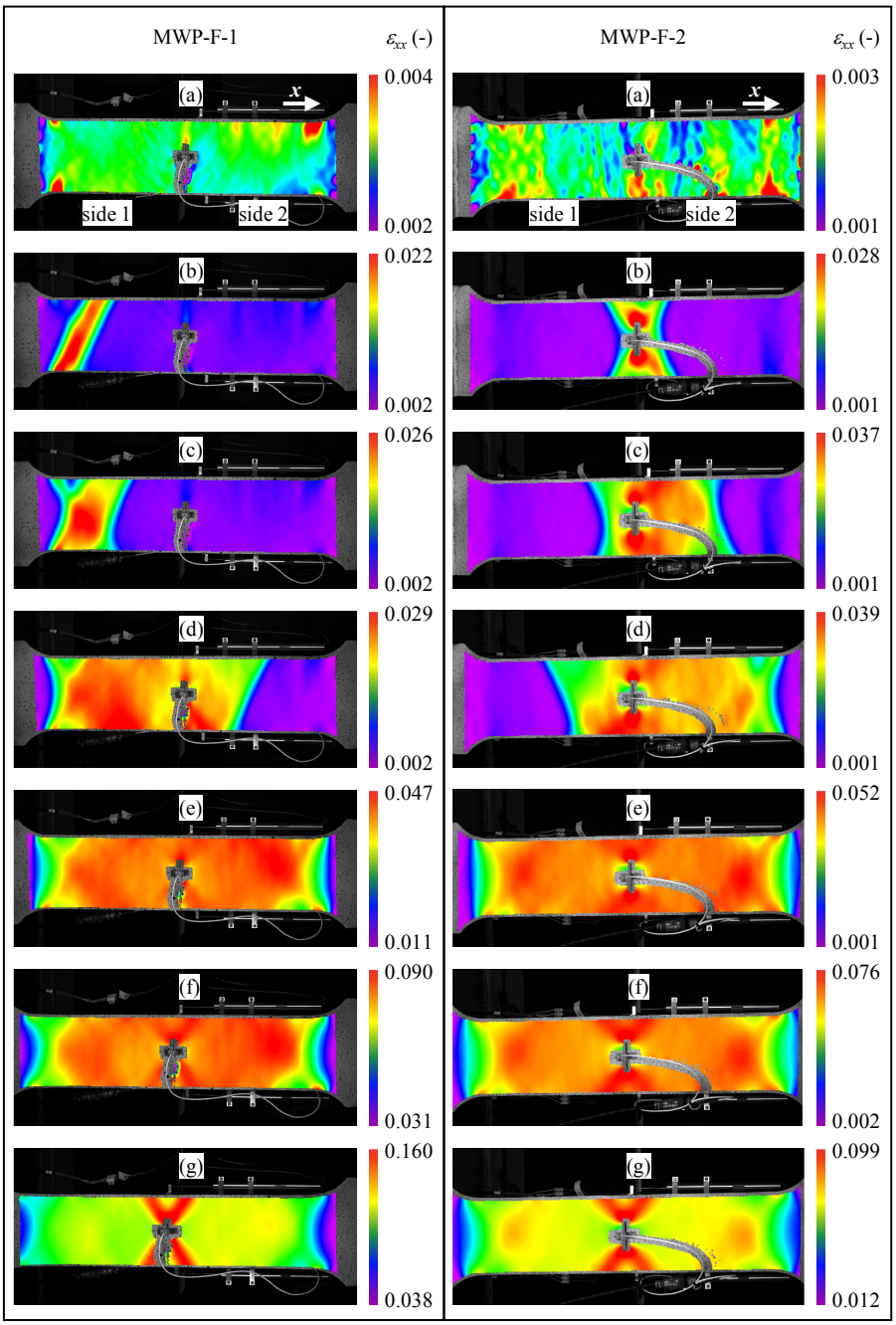

Figure 6.15: MWP-F-1 (left) and MWP-F-2 (right): Evolution of longitudinal strain obtained from digital image correlation.

3. After the full development (subfigures (c) and (d)) of the Lüders bands, the specimens strain fairly uniform (subfigures (e) and (f)). Strain concentrations are observed near the notch and at strain hotspots close to the shoulders. Similar hotspots were also observed in numerical simulations of evenmatching girth welds (see figure 5.14, left).

4. Eventually, deformations increasingly concentrate in shear lines originating from the notch (subfigures (g)). This observation announces a net section collapse phenomenon.

In quantitative terms, the DIC measurement indicates an average remote strain level of 0.141 at net section collapse for MWP-F-1. A similar measurement could not be performed for MWP-F-2, as it did not reach failure.

6.5.2.3 Load, strain and CMOD responses

First, figure 6.16(a) compares the remote strain measurements of the LVDTs at both sides of the notch. After completion of the development of Lüders bands, both sides deform in a similar manner. This is logical as they represent material from the same plate.

Second, by illustration for MWP-F-1, figure 6.16(b) confirms the trend of figures 6.5(b) and 6.11(b) that overall strain tends to underestimate remote strains (with obvious exception of the discontinuous yielding phenomenon). Around 0.09 strain, however, the remote strain LVDTs reached their point of saturation. This is also reflected in figure 6.17, which compares the measurement of one such LVDT with a 'virtual LVDT' measurement from DIC analysis, performed between the same end points but at the opposite surface of the specimen.

Next to the confirmation of LVDT saturation, figure 6.17 motivates two important statements.

- The agreement between DIC analysis and LVDT measurements can be seen as a validation of the DIC measurement technique (or vice versa).

- Strains at opposite surfaces of the panel are highly similar, which justifies the simplification of analyzing strain uniformity in cross sections on the basis of a surface path in section 5.4.1.

Both statements are confirmed by similar comparisons for the other performed MWP tests.

Next, figure 6.18 compares the CMOD responses of both flat plate MWP tests. This figure confirms net section collapse as a (near to) failure mechanism, as CMOD progressively rises after the discontinuous yielding phenomena. Further, MWP-F-2 showed higher CMOD values for a fixed remote strain, due to its larger notch length (50 mm, compared to 25 mm for MWP-F-1).

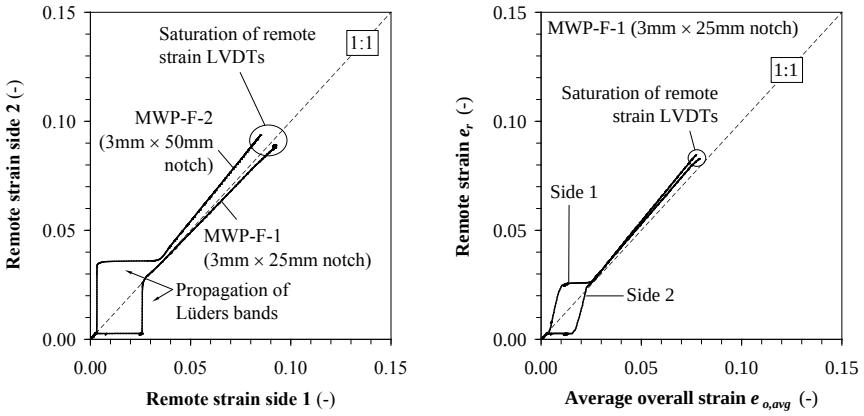

Figure 6.16: (a) MWP-F-1 and MWP-F-2: Remote strain heterogeneity plots; (b) MWP-F-1: Prior to saturation of the remote strain LVDTs, remote strains are larger than overall strain.

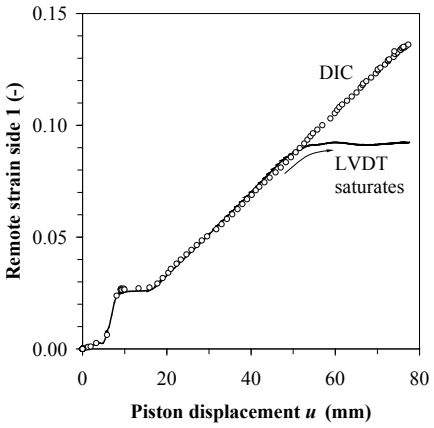

Figure 6.17: A comparison between LVDT and DIC measurements indicates the accuracy of the DIC system and reveals a saturation of the remote LVDT voltage signal.

Finally, figure 6.19 illustrates for MWP-F-2 that the evolution of gross stress against the average remote strain follows the material's stress-strain behaviour to a large extent. Notwithstanding a minor difference with respect to the Lüders elongation, yield strength and strain hardening agree. No temperature correction is necessary as tensile tests and MWP tests were both performed

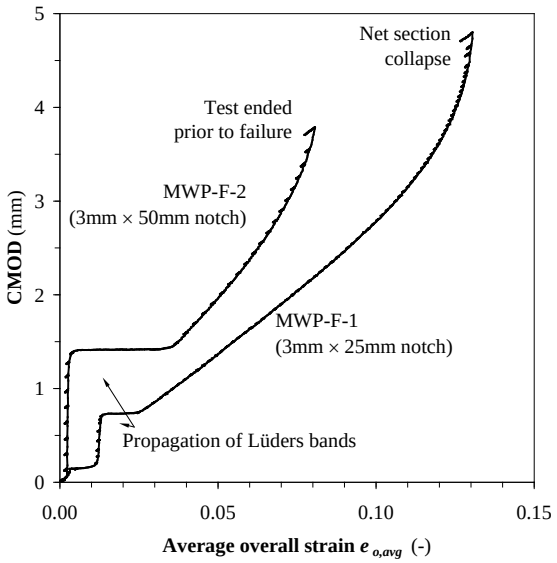

Figure 6.18: MWP-F-1 and MWP-F-2: CMOD responses.

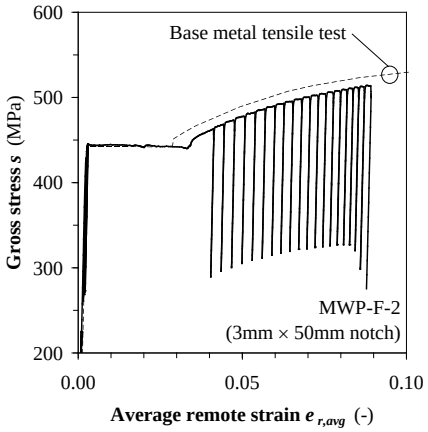

Figure 6.19: MWP-F-2: Gross stress and remote strain reflect the material's stress-strain behaviour obtained from small scale tensile tests.

at room temperature. Moreover, quasistatic conditions were respected. For instance, the MWP specimens were deformed at a piston displacement rate of 0.75 mm/min. The remote strain measurements indicated strain rates below $1.3 \cdot 10^{-3}$ min^{-1} and stress rates below 120 MPa/min during (un)loading.

These observed strain and stress rates satisfy criteria for the fulfilment of quasi-static conditions. For instance, ASTM E8M (2004) [6.6] prescribes stress rates between 69 and 690 MPa/min and, assuming $E = 206900$ MPa, strain rates between $0.3 \cdot 10^{-3}$ and $3.3 \cdot 10^{-3}$ min^{-1} for linear elastic loading of tensile test specimens.

6.5.2.4 Unloading compliance responses

The unloading compliance responses of MWP-F-1 and MWP-F-2 were prone to a high amount of scatter due to a poor data acquisition strategy which introduced a low frequency signal aliased from the 50 Hz electricity circuit. Their analysis did not lead to useful results and is therefore omitted from this text.

6.6 Curved medium wide plate tests: GMAW welded X70 pipes (MWP-C-1 and MWP-C-2)

6.6.1 Material and specimen

After the execution of flat MWP tests for the development of the experimental procedure, two curved MWP tests (MWP-C-1 and MWP-C-2) were performed at room temperature on a GMAW girth weld connecting X70 pipes ($D_o =$ 1,219 mm, $t = 13.7$ mm). Again, specimen geometry and instrumentation were taken from figure 5.16, apart from strain gauges which were not applied. The tests were performed at a piston displacement rate of 0.70 mm/min.

A representative etched section reveals a narrow gap weld with a width of slightly over 5 mm at mid-thickness and a misalignment of nearly 1 mm (figure 6.20). Both specimens were notched 3 mm deep and 40 mm long using the same procedure as for CWP-2, MWP-F-1 and MWP-F-2. The major distinction between MWP-C-1 and MWP-C-2 is found in the location of their notch: whereas MWP-C-1 was notched at the weld metal center, the notch of MWP-C-2 targeted the coarse grained HAZ.

The tested girth weld was taken from a field pipe joint and therefore involved coated pipes. Remarkable is the presence of heterogeneity between both pipes, reflected in their average tensile characteristics (table 6.5) obtained from three stress-strain diagrams per pipe (figure 6.21).

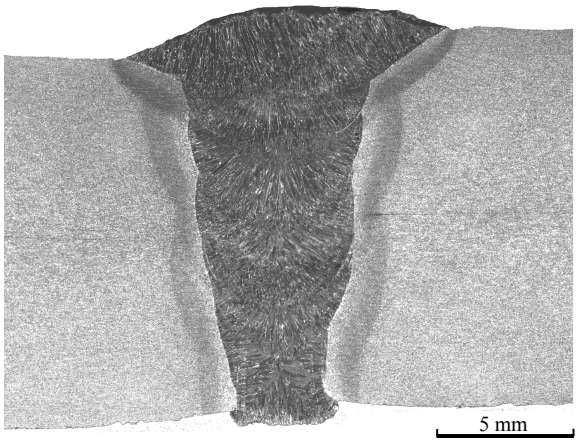

Figure 6.20: GMAW welded X70 pipes: section of weld after 2 % nital etching.

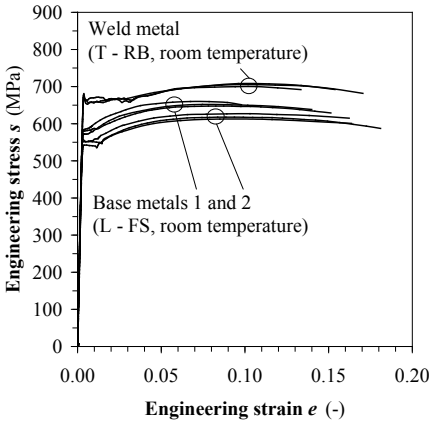

Figure 6.21: GMAW welded X70 pipes: base and weld metal stress-strain curves.

The sampling of a field girth weld with heterogeneous pipes necessitates a more extensive characterization of material properties, compared with specimens where both pipe pups originate from the same pipe and are girth welded back together solely for research purposes (such as CWP-1 and CWP-2). As a result, the evaluation of the test result becomes more challenging.

As a consequence of the pipe-to-pipe heterogeneity, it is impossible to characterize the weld metal on the basis of one single value for OM_{YS} and OM_{TS}. Based on three all weld metal tensile tests (5 mm diameter round bars) ex-

Table 6.5: Mechanical properties for MWP specimen of GMAW welded X70 pipes.

Property	**BM 1** ⋆	**HAZ 1**	**WM** ⋆	**HAZ 2**	**BM 2** ⋆
Stress-strain properties (average)					
Yielding	discontinuous		discontinuous		discontinuous
$R_{p0.2}$ (MPa)	572		659		550
R_m (MPa)	653		705		616
Y/T (-)	0.88		0.93		0.89
e_m (-)	0.080		0.105		0.101
e_L (-)	0.005		0.024		0.015
OM_{YS} (%) †			15.2 / 19.8		
OM_{FS} (%) †			11.3 / 17.0		
OM_{TS} (%) †			8.0 / 14.4		
5 kgf Vickers (HV5) hardness properties (average)					
Root side	231	242	253	233	221
Mid-thickness	219	222	239	225	202
Cap side	232	258	256	259	214
Average	227	241	249	239	212
Toughness properties (minimum / average)					
CTOD (mm) ‡			0.479 / 0.502		

⋆ BM: base metal, WM: weld metal.

† with respect to BM 1 / BM 2.

‡ obtained from three $B \times 2B$ SENB tests at -45 °C.

tracted at mid-thickness, the weld metal was found to overmatch both base metals but the actual overmatch levels significantly differ (table 6.5). Given the narrowness of the weld, particular care was given to the proper sampling of the round bar specimens. As advised in [6.7] for narrow gap welds, microstructures of circular cross sections from the round bars (one for each specimen) were verified after performing the tensile tests. None of the cross sections revealed any presence of HAZ material (e.g. figure 6.22).

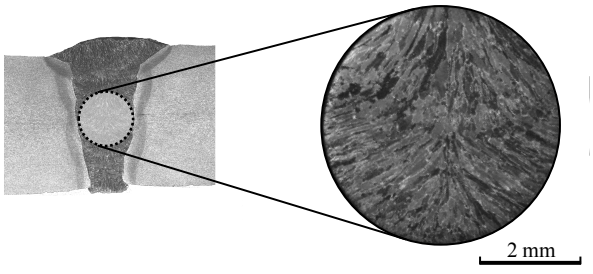

Figure 6.22: Cross sections of the round bar specimens for all weld metal tensile testing (right) indicate that the specimens have been extracted properly, as shown left.

5 kgf Vickers hardness traverses clearly identify the coarse grained heat-affected zones as the hardest areas of the weldment (figure 6.23). This is reflected in their microstructure which, in contrast with the ferritic-pearlitic base metal, is bainitic. It must be noted that the HAZ notch of MWP-C-2 was applied at the side of base metal 1, which is the strongest base metal.

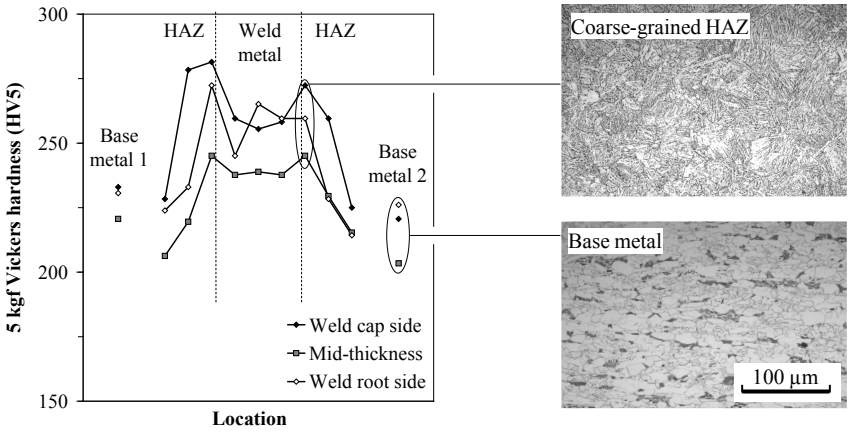

Figure 6.23: Typical observed HV5 hardness profile for MWP-C-1 and MWP-C-2 and corresponding microstructures.

Weld metal fracture toughness had been quantified prior to this research through SENB testing, and indicated remarkably high CTOD toughness values. HAZ fracture toughness data were not available prior to girth weld selection and have not been obtained afterwards as MWP-C-2 failed in a ductile manner (see the following section).

6.6.2 MWP test results

6.6.2.1 Failure and post mortem analysis

MWP-C-1 failed due to net section collapse and showed significant stable tearing (figure 6.24(a)). On the other hand, MWP-C-2 necked in the weakest base metal and ductile crack extension was much less pronounced (figure 6.24(b)). Both tests were stopped after a clear identification of maximum load and before unstable rupture.

Two additional notes can be made from figure 6.24.

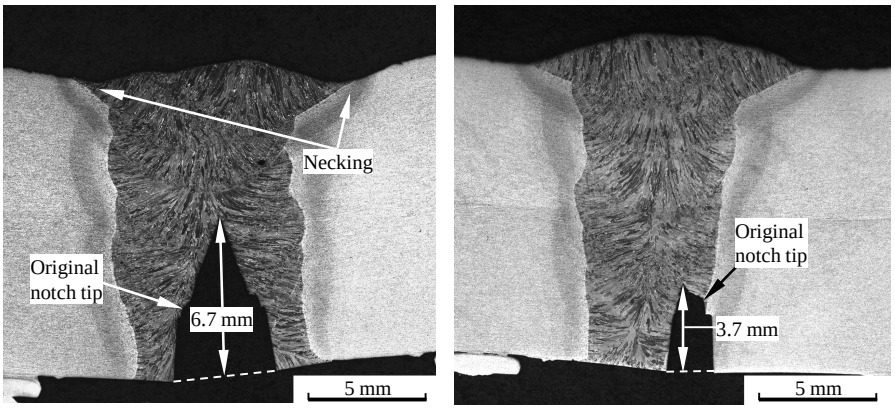

Figure 6.24: (a) MWP-C-1 and (b) MWP-C-2: Post mortem images of notched sections after 2 % nital etching.

- Figure 6.24(a) has been used in figure 4.20 to show the ductile tearing mechanism of void nucleation, growth and coalescence.
- The initial notch tip of MWP-C-2 missed the targeted coarse grained HAZ location with approximately 0.2 mm (figure 6.25). Together with the high HAZ hardness (figure 6.23), this may explain why ductile crack extension occured towards the weld rather than the fusion line. Consequently, the test result is questionable for qualification of HAZ flaw tolerance [6.7]. Nevertheless, it remains useful for the investigation of measurement techniques (further in this chapter) and validation of the finite element model (chapter 7).

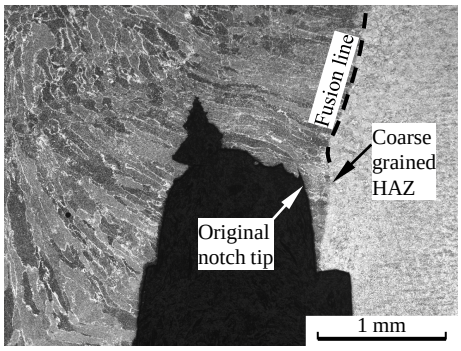

Figure 6.25: The notch of MWP-C-2 slightly missed the targeted coarse grained HAZ.

6.6.2.2 DIC analysis

Figure 6.26 depicts representative DIC contour plots of longitudinal strain throughout the progress of MWP-C-1 and MWP-C-2. The following can be noted:

1. Lüders bands originate from the notched weld into the weaker base metal 2 (subfigures (a)). These bands connect with strain concentrations at the corresponding specimen shoulder (subfigures (b)).
2. After the full development of Lüders bands in base metal 2, a pronounced

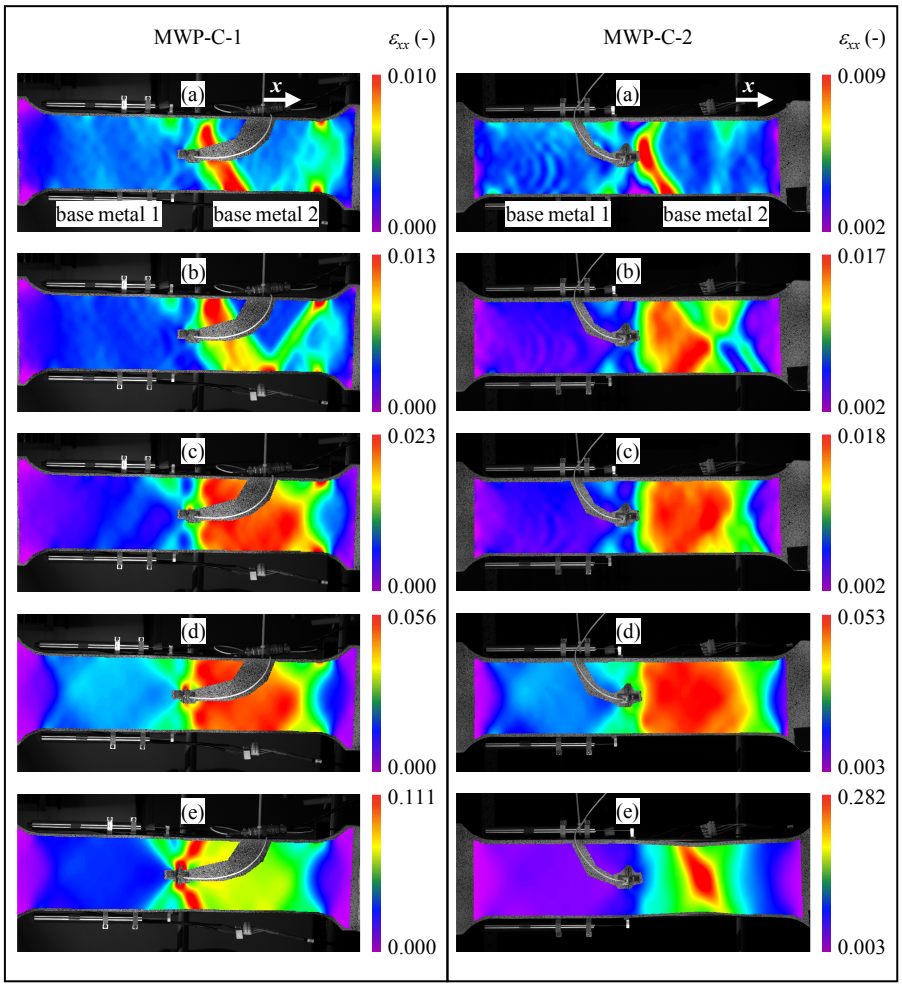

Figure 6.26: MWP-C-1 (left) and MWP-C-2 (right): Evolution of longitudinal strain obtained from digital image correlation.

effect of strength heterogeneity – as schematically shown in figure 2.7 – is unmistakable. A substantial fraction of the applied deformation is concentrated in base metal 2 (subfigures (c) and (d)). In this base metal, a strain hotspot is – although less pronounced than those in figure 6.15 – visible in MWP-C-1. On the other hand, the weakest plate of MWP-C-2 has a strain distribution which more closely represents that of figure 5.14 (right).

3. Eventually, net section collapse and global section collapse phenomena become clear for MWP-C-1 and MWP-C-2 respectively (subfigures (e)).

The tendency of MWP-C-1 towards net section collapse is announced between subfigures (c) and (d) as these two contour plots differ with respect to the following major observation. In subfigure (c), the notch is shielded from the remote strain in base metal 2. This is also reflected in figure 6.27, which shows the corresponding distribution of principal strain ϵ_1 in vicinity to the weld. In subfigure (d), however, strain concentration surrounding the notch tips has become more pronounced. This concentration breeds the shear lines that eventually lead to net section collapse. A similar evolution is not observed in MWP-C-2 where the notch stays shielded from remote strains – similar to figure 6.27 – until gross section collapse occurs. This is reflected in a comparison of the subfigures (d) of MWP-C-1 and MWP-C-2.

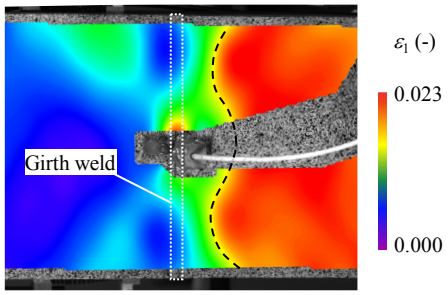

Figure 6.27: MWP-C-1: A strength overmatching weld shields the notch from the area of highest remote strains at base metal 2 (right from the dashed line).

6.6.2.3 Load, strain and CMOD responses

First, similar to the flat plate MWPs, gross stress as a function of remote strain represents the stress-strain behaviour of the material from tensile testing (e.g. figure 6.28). Note that, similar to CWP-F-1 and CWP-F-2, gross stress and remote strain rates agreed with the requirement of ASTM E8M during elastic (un)loading.

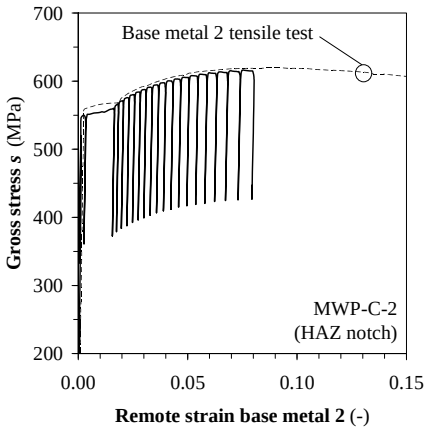

Figure 6.28: MWP-C-2: Gross stress reflects the material's stress-strain behaviour (shown for base metal 2).

Second, a remote strain heterogeneity plot (figure 6.29(a)) reflects the concentration of longitudinal strain into the weakest base metal. At failure (maximum load), the remote strain in base metal 2 is a factor 3.77 (MWP-C-1) and 4.95 (MWP-C-2) higher than that in base metal 1 (table 6.6).

Table 6.6: Remote strains at failure for MWP-C-1 and MWP-C-2.

Test	**Remote strain at failure (-)**			**Max./min. (-)**
	Base metal 1	Base metal 2	Average	
MWP-C-1	0.022	0.083	0.053	3.77
MWP-C-2	0.020	0.099	0.060	4.95

Note that the high degree of strain concentration in base metal 2 is the result of a fairly modest degree of strength heterogeneity. In particular, $R_{p0.2}$ and R_m differ by no more than 40 MPa between both base metals. Similar observations were also made in [6.8], where the remote strains in girth welded plates with merely 10 MPa difference in yield strength differed by a factor 1.5.

Recalling that API 5L (2007) [6.9] allows for yield strength variations of 150 MPa within the same line pipe steel grade and even higher variations for ultimate tensile strength (table 3.1), MWP-C-1 and MWP-C-2 unmistakably show that strength heterogeneity is a key factor to take into account for strain based flaw assessments.

It is clear that the analysis of a field weldment connecting two different pipes is far more complicated than that of the CWP and flat plate MWP tests discussed in sections 6.3 to 6.5. In particular, an overall strain measurement is no longer able to give a view on the strain distribution in both base metals (figure 6.29(b)). It rather approximates the average of the remote strains and thus provides intuition on the global deformation behaviour *for the specific combination of heterogeneous base metals tested*. This approximation involves a slight underestimation of the average remote strain. Note that figures 6.5(b), 6.11(b) and 6.16(b) also respect this statement, for special cases of weldments with homogeneous plates.

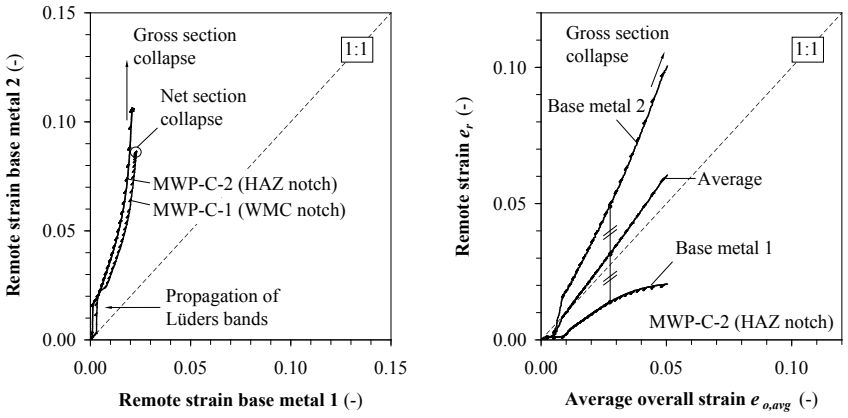

Figure 6.29: (a) MWP-C-1 and MWP-C-2: Remote strain heterogeneity plots indicate pronounced pipe-to-pipe heterogeneity; (b) MWP-C-2: Overall strain does not reflect the effect of heterogeneity.

Finally, comparing the CMOD evolutions of MWP-C-1 and MWP-C-2 as a function of overall strain, it becomes clear that both specimens initially responded similarly. However, starting from 0.02 overall strain, both CMOD responses progressively diverge and eventually indicate different failure modes.

6.6.2.4 Unloading compliance responses

Prior to executing MWP-C-1 and MWP-C-2, unloading compliance data acquisition was improved to avoid the anomalies encountered for MWP-F-1 and MWP-F-2 (section 6.5.2.4). The obtained unloading compliance responses (figure 6.31) indicate the following:

- The recorded unloading compliances are prone to scatter, but this scatter does not hamper the identification of clear trends.

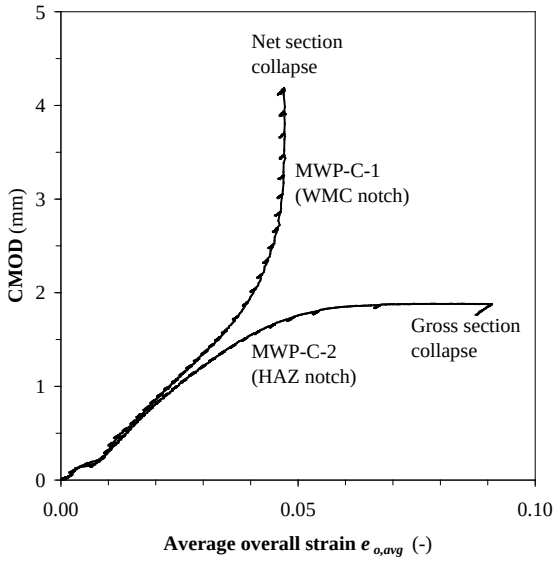

Figure 6.30: MWP-C-1 and MWP-C-2: CMOD responses.

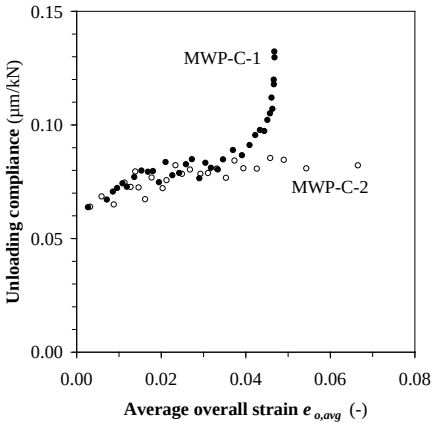

Figure 6.31: MWP-C-1 and MWP-C-2: Unloading compliance responses initially correspond and then indicate significant tearing in MWP-C-1.

- Initially, the unloading compliance responses measured for MWP-C-1 and MWP-C-2 correspond. Apparently, the position of the notch (WMC or HAZ) has no significant effect on unloading compliance prior to ductile tearing, if flaw dimensions are equal.

- Starting roughly between 0.03 and 0.04 overall strain (the exact value is hard to quantify), MWP-C-1 clearly diverges from MWP-C-2. Whereas the latter's unloading compliance saturates, the former indicates a progressive ductile tearing.

As deducing ductile crack extension from unloading compliance requires finite element analyses (section 5.2.2), its discussion is postponed to chapter 7. There, the obtained ductile tearing will be compared with the actual post mortem values (figure 6.24) to validate the coupled experimental-numerical method.

6.7 Summary and conclusions

This chapter has reported on six curved wide plate and medium wide plate tension tests, supported by small scale tests related to strength, hardness and toughness, and microstructure investigations. Section 6.2 has shown that these tests cover a wide range of possible configurations with respect to both geometry and material parameters.

Summarizing this chapter is not straightforward, as many observations are highly specific to the circumstances of the test investigated. Nevertheless, the following statements (most of which are confirmations of literature) can be summarized with respect to the **structural behaviour** of a wide plate test (be it an MWP specimen or a larger CWP specimen).

- Flaw size (more specifically flaw length, in this chapter) has a pronounced influence on crack driving force (MWP-F-1, MWP-F-2).
- Weld strength overmatch is confirmed as one of the key factors to obtain a high strain capacity, as it shields a weld flaw (or notch) from applied strains. This promotes gross section collapse as a failure mode, in which case the notched weld is no longer the weakest link of the structure (CWP-1, CWP-2, MWP-C-1).
- For similar degrees of flaw size and overmatch, however, the mechanism of failure may differ between a WMC and a HAZ notch (MWP-C-1, MWP-C-2). The reason hereof is at this point hypothesized to be a notch location dependent response of crack driving force.
- Tests on field weldments have indicated that base metals with heterogeneous strength properties add significant complexity to the analysis of wide plate tension test results. To this respect, the reporting of a remote strain heterogeneity plot (e.g. figure 6.29(a)) is advised as it visualises the effect of heterogeneity. For a moderate difference of 40 MPa between the yield strengths of both base metals, the weakest base metal in CWP-C-1 and CWP-C-2 strained roughly four to five times more than its stronger

neighbour. Since heterogeneity between pipes is a fact of life and – following API 5L – often even more pronounced, this added complexity has to be incorporated into a strain based flaw assessment.

Second, the following conclusions can be drawn regarding the **instrumentation** of a wide plate test.

- Overall strain e_o gives a slight underestimation of the average remote strain $e_{r,avg}$.
- Digital image correlation (DIC) analysis provides a sensible and robust view on the evolution of strain distributions and the corresponding process towards failure. In particular, it indicates whether the notch is shielded from applied strains or, alternatively, shows strain concentrations that breed shear deformation lines.
- Apart from providing intuition on the response of the weld notch, DIC analysis has been able to confirm the propagation of Lüders bands over discontinuously yielding base metals and, after development of these bands, the presence of strain hotspots similar to those observed in figure 5.14.
- A measurement of unloading compliance requires particular attention with respect to sensor accuracy and data sampling. If properly performed, it can significantly aid in the interpretation of the test result (MWP-C-1, MWP-C-2).

The presented results provide a broad basis for a thorough experimental validation in chapter 7 of the finite element model presented in chapter 4. Given the extended instrumentation of the medium wide plate tests, this validation will cover a wide range of aspects.

Bibliography

[6.1] ftp://ftp.cordis.europa.eu/pub/coal-steel-rtd/docs/synopsis_projects_2007-2010_en.pdf. Accessed: January 12, 2012.

[6.2] M. Koçak, S. Webster, J.J. Janosch, R.A. Ainsworth, and R. Koers, editors. *Fitness for service procedure, FITNET , MK8, vol. I: procedure*. GKSS Research Centre, ISBN 978-3-940923-00-4, 2008.

[6.3] *Metallic materials – Conversion of hardness values, ISO 18265*. International Organization for Standardization, Geneva, Switzerland, 2003.

[6.4] D.P. Fairchild, W. Cheng, S.J. Ford, K. Minnaar, N.E. Biery, A. Kumar, and N.E. Nissley. Recent advances in curved wide plate testing and implications for strain-based design. *International Journal of Offshore and Polar Engineering*, 18(3):161–170, 2008.

[6.5] http://www.tribology-fatigue.ugent.be/05_a_wideplate.shtml. Accessed: January 12, 2012.

[6.6] *Standard test methods for tension testing of metallic materials, ASTM E 8M-04*. ASTM International, West Conshohocken, USA, 2004.

[6.7] R. Denys and A. Lefevre. UGent guidelines for curved wide plate testing. In R. Denys, editor, *Proceedings of the 5th International Conference on Pipeline Technology*, Ostend, Belgium, 2009.

[6.8] Y.Y. Wang, M. Liu, T. Weeks, M. Richards, D. McColskey, and D. Horsley. Broad perspectives of girth weld tensile strain response. In *Proceedings of the 8th International Pipeline Conference (IPC)*, Calgary, Alberta, Canada, 2010. IPC2010-31369.

[6.9] *Specification for Line Pipe, API 5L, 44th edition*. American Petroleum Institute, Washington, USA, 2007.

Chapter 7

Validation of the finite element model

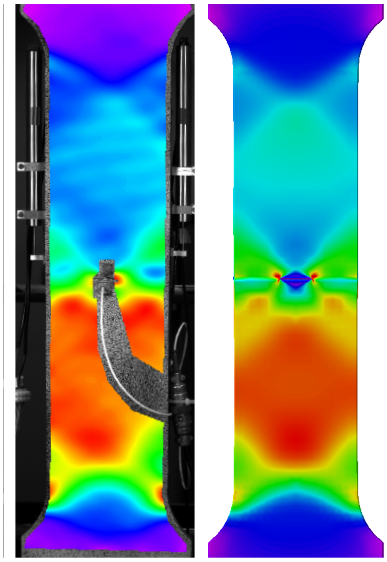

There is a pronounced agreement between experimentally observed (left) and numerically predicted (right) strain distributions in a medium wide plate specimen.

7.1 Goal

Chapter 4 elaborated on a finite element model of the curved wide plate and full scale pipe test under axial tension. This model has been used in chapter 5 to provide guidance for the design of a medium wide plate test and the interpretation of its results. However, the use of finite element results for design and analysis purposes is only justified if the numerical model has been thoroughly validated. Both analytical formulations and experimental results are used to this purpose in the current chapter. The former refers to fracture mechanics concepts explained in chapter 2, whereas the latter adopts results from chapter 6.

This chapter answers the following questions with respect to the validity of the finite element model:

- *Does it confirm crack driving force relations from literature?*
- *Is it capable of predicting experimentally observed crack driving force responses?*
- *Does the model allow to estimate ductile tearing?*
- *Is the model able to predict strain capacity?*
- *Do simulated strain distributions and remote strain measurements as observed in the experiments resemble the experimental ones?*

As a result, the presented validations should provide consciousness on the possibilities and limitations of finite element modelling in strain based flaw assessments.

First, section 7.2 provides a comparison with well established analytical crack driving force solutions for simplified configurations. Focus is put on K_I, J and CTOD. Then, section 7.3 provides a multidisciplinary comparison between simulations and experiments with a distinct focus on CMOD, ductile tearing and strain distributions. Section 7.4 summarizes and concludes.

7.2 Analytical validation

The analytical validation of K_I, J and CTOD is separately discussed in three subsections. It is important to note that all equations adopted from literature originated from finite element analyses. Hence, the analytical validation compares results of the developed finite element model with those of numerical models used in literature.

7.2.1 Linear elastic conditions (K_I)

Linear elastic conditions may at first sight seem irrelevant to the problem of strain based flaw assessments. Nevertheless, a validation under these conditions is an absolute necessity. Indeed, some routines for elastic-plastic flaw assessment require knowledge of linear elastic crack driving force (K_I or J_{el}), in particular the reference stress approach (section 2.2.3) and FAD approach (section 2.2.4). These concepts have been adopted in some strain based flaw assessment methods such as DNV-RP-F108 (section 2.6.2.1) and the strain based FAD (section 2.6.2.2). Moreover, if unsuccessful, it is unlikely that a more challenging elastic-plastic validation will prove satisfactory.

Linear elastic crack driving force solutions for K_I (or equivalently $J_{el} = K_I^2/E'$, Eq. (2.8)) have been derived for simplified configurations that can be described by the finite element model. These solutions generally assume plain base metal, which is in the model represented as an evenmatching [1] weldment without geometrical weld reinforcement. Further, analytical solutions typically apply for sharp defects (cracks) that are semi-elliptical in a cylindrical coordinate system originating from the pipe center (figure 7.1(a)), or in a Cartesian coordinate system for flat geometries (figure 7.1(b)). Each position on the crack tip is then uniquely defined by an angle ϕ as shown in the same figure. Particular positions are where the flaw tip touches the surface ($\phi = 0$ and $\phi = \pi$) and the deepest point of the flaw ($\phi = \pi/2$). Because of symmetry reasons, crack driving force is evaluated for one half of the crack ($0 \leq \phi \leq \pi/2$).

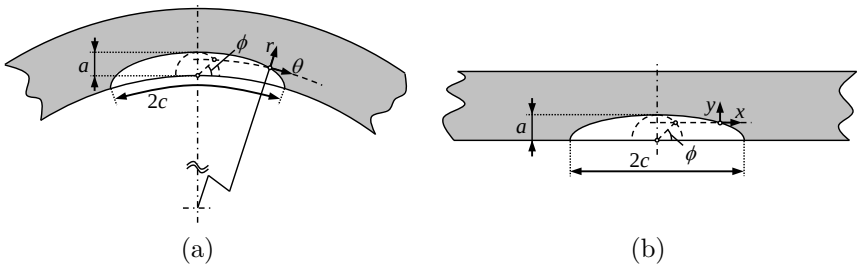

Figure 7.1: Definition of flaw tip position ϕ for (a) curved geometries, and (b) flat geometries.

Note that in figure 7.1(a), $2c$ is defined as the arc length of the crack rather than its projected length. This definition corresponds to literature used for the analytical validation. Moreover, it is nearly identical to the projected horizontal flaw length definition (as used for the experiments in chapter 6).

Two simplified geometries have been investigated and are separately discussed

[1] i.e. base metal, HAZ and weld metal properties are identical.

below: a flat plate (section 7.2.1.1) and a full pipe (section 7.2.1.2), both subjected to uniaxial tension.

7.2.1.1 Flat plate under uniaxial tension

Newman and Raju's equation [7.1] is universally accepted for the calculation of K_I in surface cracked flat plates under tension. This equation gives normalized stress intensity factors K_I/σ as a function of a, $2c$, t, $2W$ and ϕ. Application limits are:

$$\begin{cases} 2c/a \geq 2 \\ a/t \leq \min\left(1.25\left(a/c + 0.6\right), 1\right) \end{cases} \tag{7.1}$$

Two configurations have been compared with the Newman-Raju equation, both of which are covered by its application limits (table 7.1). These geometries were chosen for the following reasons:

- The first configuration ('plate A') has plate and flaw dimensions which are not uncommon for curved wide plate testing. The corresponding mesh is depicted in figure 7.2.
- The second configuration ('plate B') is also used for the analytical validation under elastic-plastic conditions (section 7.2.2) and therefore validated for K_I as a starting point.

Table 7.1: Considered flat plates for the validation of K_I.

Geometry	$2L$ (mm)	$2W$ (mm)	t (mm)	$2c$ (mm)	a (mm)
Plate A	1,200	300	15	50	3
Plate B	480	120	15	30	3

The material was modelled purely linear elastic, with a Young's modulus E of 206,900 MPa and a Poisson coefficient $\nu = 0.3$. Given the assumption of linear elasticity, non-linear geometrical effects were not taken into account. Plate length $2L$ was chosen four times the plate width $2W$, aiming to obtain an area of uniform longitudinal stress and strain. The initial crack tip radius ρ_i was taken 2.5 μm from considerations given in section 4.2.1. Mesh density parameters were set to achieve a 'fast and fairly accurate' numerical result (section 4.3.3). The half models of plates A and B consist of respectively 14,386 and 11,536 elements. The spider web mesh contains 19 contours. An end plane displacement corresponding with a remote tensile stress of approximately $\sigma = 200$ MPa was imposed. Note that this value was arbitrarily chosen and does not influence the result under linear elastic conditions as K_I is normalized against σ. End plane rotations were allowed to avoid the introduction of a

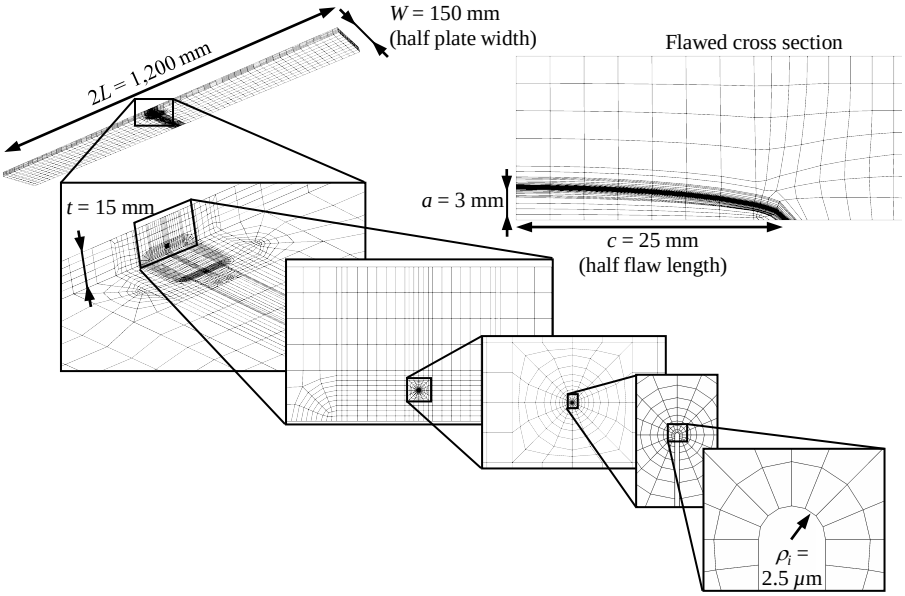

Figure 7.2: Mesh of half model of 'plate A'.

remotely applied bending moment. K_I was derived from J contour integral evaluation as readily applicable in $ABAQUS^{®}$ (version 6.10 and above [7.2]), along the outer spider web contour. A proper convergence of K_I towards this contour has been observed. The applied gross stress σ was obtained as the tensile load corresponding to the applied deformation, divided by the initial cross section.

Figure 7.3 compares the finite element results for plates A and B with their analytical K_I/σ-values from the Newman-Raju equation, as a function of $\phi/(\pi/2)$. At the deepest point of the crack ($\phi/(\pi/2) = 1$) the difference between the finite element results and the Newman-Raju solution is merely 0.7 % for plate A and 2.2 % for plate B (relative to the analytical solution). Towards the plate surface ($\phi/(\pi/2) \to 0$) the agreement is less pronounced, which results from the mesh distortion in that area (figure 7.3, mesh fragment in dotted rectangular). This mesh distortion is created by the nodal coordinate transformation $\Delta\vec{P}_s$ that shapes the semi-elliptical flaw (section 4.3.4.2) and is independent of the mesh density settings chosen for (section 4.3.3). Also, there is a point on the crack front where K_I does not respect the overall trend of the other positions. This point was in both models located on the partitioning interface between two areas with a different meshing strategy (as indicated in the shown mesh fragment).

Nevertheless, the overall trend agrees and, since the position $\phi/(\pi/2) = 1$ is the main point of interest for large scale tension tests on flawed girth welds (recall figure 4.24), the plate validation under linear elastic conditions is considered successful.

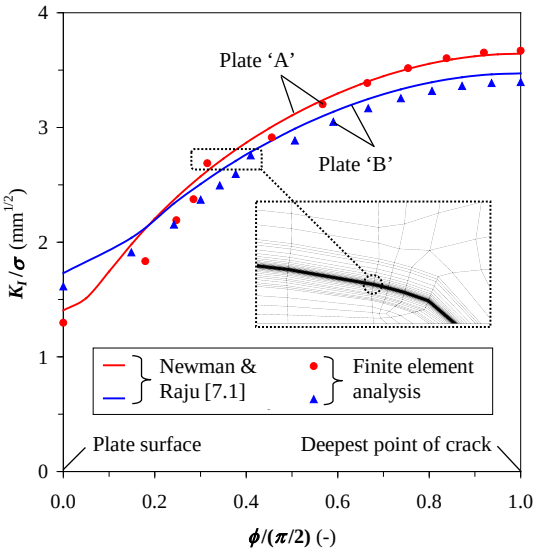

Figure 7.3: Comparison of K_I/σ between linear elastic finite element simulations of flat plates and the Newman-Raju equation.

7.2.1.2 Full pipe under uniaxial tension

Whereas the Newman-Raju equation covers the entire crack front, similar extended solutions are to the author's knowledge not available for part-through circumferentially cracked pipes. Nevertheless, solutions have been proposed for the deepest point of the crack ($\phi = \pi/2$) and where the crack meets the surface ($\phi = 0$). Focus is given to pipes cracked along the inner diameter surface.

Adopted in this section are solutions of Zahoor [7.3] and of Bergman [7.4]. First, Zahoor [7.3] proposed a closed-form solution for K_I/σ at $\phi = \pi/2$, given by

$$\frac{K_I}{\sigma} = F\sqrt{\frac{\pi a}{Q}} \tag{7.2}$$

where

$$Q = 1.464\left(\frac{a}{c}\right)^{1.65} \tag{7.3}$$

and

$$F = 1 + Q^2 \left[0.02 + \frac{2c}{t} \left(0.0103 + 0.00617 \frac{2c}{t} \right) \right. \\ \left. + 0.0035 \left(1 + 0.7 \frac{2c}{t} \right) \left(\frac{D_o - t}{2t} - 5 \right)^{0.7} \right] \quad (7.4)$$

Application limits are:

$$\begin{cases} 0.2 \leq a/t \leq 0.8 \\ 3 \leq 2c/a \leq 12 \\ 11 \leq D_o/t \leq 41 \end{cases} \quad (7.5)$$

Second, Bergman [7.4] proposed tabulated K_I solutions for $\phi = 0$ and for $\phi = \pi/2$, covering geometries within the following boundaries:

$$\begin{cases} 0.0 \leq a/t \leq 0.8 \\ 2 \leq 2c/a \leq 32 \\ 12 \leq D_o/t \leq 22 \end{cases} \quad (7.6)$$

Two cracked pipes have been considered (table 7.2). Whereas 'pipe A' is covered by the application limits of both Zahoor's and Bergman's solutions, a second configuration ('pipe B') has a more critical flaw length. This pipe is only covered by Bergman's solution.

Table 7.2: Considered pipes for the validation of K_I.

Geometry	$2L$ (mm)	D_o (mm)	t (mm)	$2c$ (mm)	a (mm)
Pipe A	1,320	330	15	12	3
Pipe B	1,320	330	15	48	3

Pipe length $2L$ was chosen four times the outer diameter D_o to eliminate boundary condition effects on K_I. Material properties were equal to those of section 7.2.1.1. Additionally, similar choices were made with respect to the initial crack tip radius ρ_i, mesh density, end plane displacement, allowance for end plane rotations and extraction of K_I. The half models of pipes A and B have respectively 19,520 and 26,538 elements. Figure 7.4 depicts the mesh of pipe B.

Figure 7.5 plots the resulting comparison. Similar to the validation for flat plates, a remarkable agreement is found at the deepest point of the crack ($\phi/(\pi/2) = 1$). The maximum difference is observed between the finite element

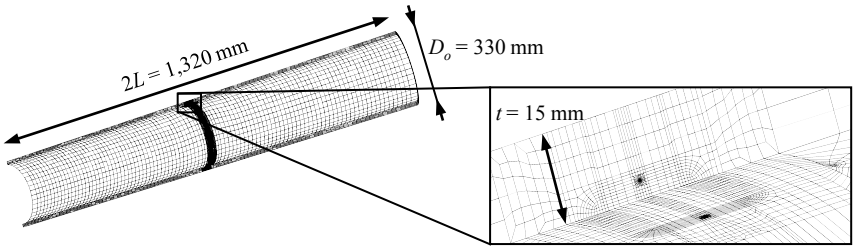

Figure 7.4: Mesh of half model of 'pipe B'.

result and the Zahoor equation for pipe A (1.8 % relative to Zahoor's solution). On the other hand, K_I is poorly predicted on the pipe surface ($\phi = 0$). Similar to the observations in section 7.2.1.1, mesh distortion is believed to be the cause of this local inaccuracy.

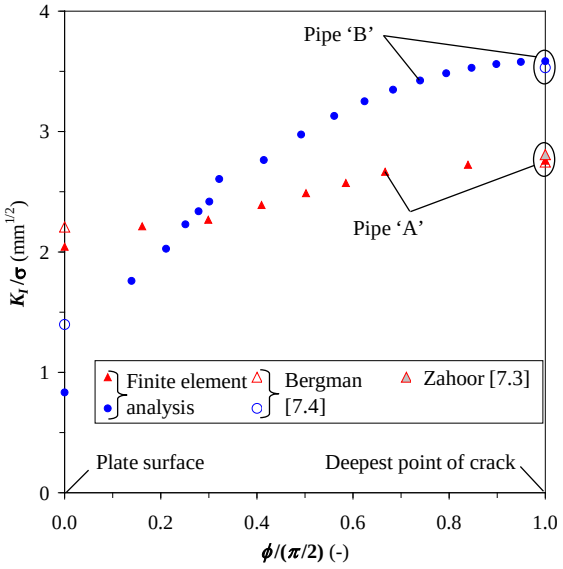

Figure 7.5: Comparison of K_I/σ between linear elastic finite element simulations of pipes and solutions from literature.

7.2.2 Elastic-plastic conditions (J)

This section considers five published studies for the validation of J: Boothman et al. [7.5], Yagawa et al. [7.6] (with corrections in [7.7]), McClung et al. [7.8],

Lei [7.9] and Wang [7.10]. These studies cover semi-elliptically flawed flat plates (without weld) under tension. However, assuming that the accuracy of J is mostly related to the quality of the mesh, a successful validation for plates is considered to also cover pipes. This statement is not objected by the validation of K_I (section 7.2.1), which proved promising for both configurations.

Note that, for all five adopted studies, non-linear geometrical effects were discarded as this strongly promotes the contour independence of far-field J (section 4.2.1). Likewise, the presented validation simulations also assume a small scale yielding analysis.

The first abovementioned study (Boothman et al. [7.5]) involves a prediction of J at the deepest point of the crack in an infinitely wide plate under tension, as a function of the remotely applied strain ϵ_r. The governing equations were based on a set of finite element simulations with sufficiently large dimensions ($2W/2c = 20$, $2L/2t = 20$) to avoid finite size effects. Material was modelled as $\epsilon/\epsilon_0 = (\sigma/\sigma_0)^n$ in the plastic region. The following relation resulted:

$$\frac{J}{G_y} = \begin{cases} \left(\frac{\epsilon_r}{\epsilon_0}\right)^2 & \frac{\epsilon_r}{\epsilon_0} \leq 0.8 \\ 0.64 + \left(\frac{\epsilon_r}{\epsilon_0} - 0.8\right) \frac{J_{fp}-0.64}{0.2} & 0.8 \leq \frac{\epsilon_r}{\epsilon_0} \leq 1.0 \\ J_{fp} + S_{fp}\left(\frac{\epsilon_r}{\epsilon_0} - 1.0\right) & 1.0 \leq \frac{\epsilon_r}{\epsilon_0} \leq 10.0 \end{cases} \tag{7.7}$$

with

$$G_y = Y^2 \pi \sigma_0 \epsilon_0 a \tag{7.8}$$

where Y is taken from Eq. (2.3) and can for instance be obtained using the Newman-Raju equation (section 7.2.1.1). Further,

$$J_{fp} = \min\left(0.9 + 6a/t; 1.5\right) \tag{7.9}$$

$$S_{fp} = \min\left(1.5 + 24{,}173.0\left(a/t - 0.05\right)^{3.6}; 2.0\right) \tag{7.10}$$

Boothman et al. targeted shallow cracks by formulating the following limitations:

$$\begin{cases} 3.5 \leq 2c/a \leq 10.0 \\ 0.05 \leq a/t \leq 0.15 \end{cases} \tag{7.11}$$

Note that Eq. (7.7) is material independent and was developed to approximately cover a wide range of possible power law hardening materials, with an emphasis on exponents $n \geq 5$ (figure 7.6 [7.5]).

To investigate the agreement between predicted J responses and the solution of Boothman et al., a wide plate ('plate C') with dimensions as given in table

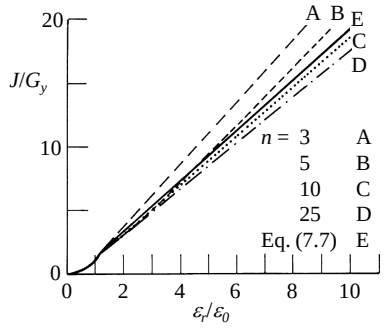

Figure 7.6: Eq. (7.7) aims to cover a wide range of material behaviours. Taken from [7.5].

7.3 was simulated. Since the best correspondence is found for $n = 10$ in figure 7.6, this value was adopted for the simulated material. Further $E = \sigma_0/\epsilon_0$ was taken 206,900 MPa and $\sigma_0 = 500$ MPa. Remote strain ϵ_r was extracted at a cross section of highly uniform longitudinal strain. Further details with respect to crack tip radius, mesh density, end plane rotations and extraction of J correspond with section 7.2.1.1. The model contains 14,496 elements.

Table 7.3: Considered flat plate for the validation of J on the basis of [7.5].

Geometry	$2L$ (mm)	$2W$ (mm)	t (mm)	$2c$ (mm)	a (mm)
Plate C	2,400	600	20	30	3

The resulting J response shows a remarkable agreement with the equations of Boothman et al. (figure 7.7).

As regards the other four considered studies [7.6–7.10], it can be noted that the validation of J under elastic-plastic conditions can be reduced to a validation of its plastic component J_{pl}. Indeed, the previous section (7.2.1) has shown that K_I is properly predicted and, given Eq. (2.8), the same applies for J_{el}. All four studies have provided solutions for J_{pl} under the form of h_1 factors through Eq.(2.10) as a function of a/t, $2c/a$, n and ϕ, thereby assuming Ramberg-Osgood material behaviour (Eq. (2.6)) and $2W/2c = 4$.

Since each study has particular limits of validity, a configuration which is covered by all four has been chosen for the validation. This resulted in the geometry (and mesh) of 'plate B' (table 7.1) and a material with $E = 206{,}900$ MPa, $\sigma_0 = 500$ MPa and $n = 10$. The parameter α in Eq. (2.6) was chosen in a way that equalizes σ_0 with the 0.2 % proof stress. h_1 was derived from the following

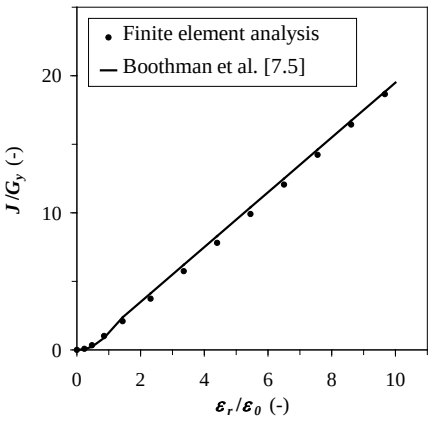

Figure 7.7: Finite element results and Eq. (7.7) agree.

relation, which can be shown from Eqs. (2.6) and (2.10):

$$h_1 = \frac{J - J_{el}}{t\sigma\left(\epsilon_r - \sigma/E\right)} \tag{7.12}$$

with J_{el} derived from the Newman-Raju equation (section 7.2.1.1), and σ and ϵ_r obtained in a cross section with uniform longitudinal stress and strain. Note that, for the conversion of Newman-Raju's K_I to J_{el}, plane strain conditions were assumed, i.e. $E' = E/(1-\nu^2)$ in Eq. (2.8). The obtained h_1 converges as the applied deformation becomes plastic (figure 7.8), which indicates the capability of Eq. (2.10) to describe J_{pl}. The h_1-values for the largest simulated deformation (corresponding with approximately 0.053 true remote strain) were compared with [7.6–7.10] (figure 7.9). The agreement is unmistakable and mostly pronounced in comparison with the most recent studies [7.9, 7.10], which are likely to be more accurate than the older studies [7.6–7.8].

Summarizing figures 7.7 and 7.9, calculated J-values are in strong correspondence with literature, which concludes its analytical validation.

7.2.3 Comparison between CTOD and J

As explained in section 2.2.1, J and CTOD are theoretically related through Eq. (2.7) which requires a dimensionless m-factor typically between 1 and 2. Østby [7.11] examined this relation through finite element analyses and found that m is approximately related to Y/T as follows:

$$m = 3.87 - 2.64\frac{Y}{T} \tag{7.13}$$

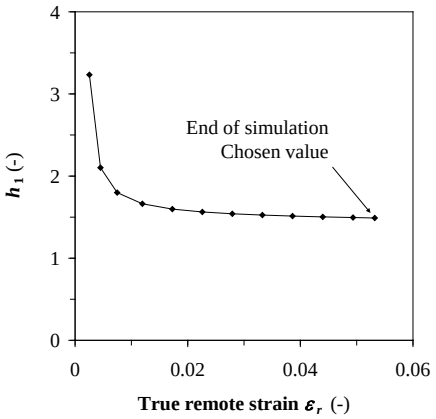

Figure 7.8: h_1 converges as remote strain becomes plastic.

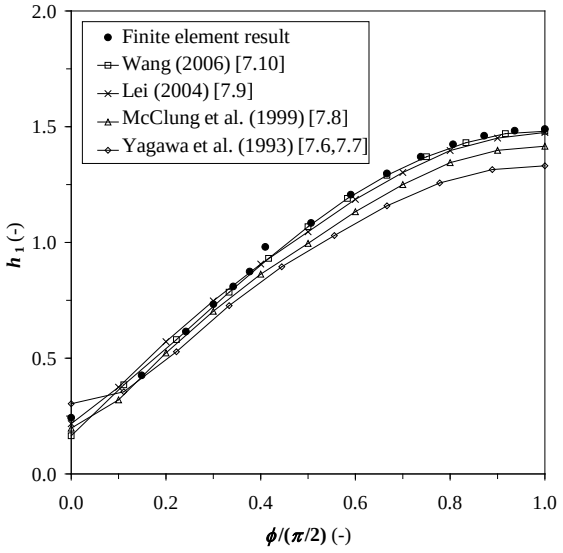

Figure 7.9: Finite element results agree with h_1 factors tabulated in [7.6–7.10].

Eq. (7.13) is valid for $0.82 \leq Y/T \leq 0.93$. Assumptions for its development were that the material exhibits small scale yielding according to the following stress-plastic strain (σ-ϵ_{pl}) law:

$$\frac{\sigma}{\sigma_0} = \left(1 + \frac{\epsilon_{pl}}{\epsilon_0}\right)^n \tag{7.14}$$

Further, the equation was derived for tension loaded pipes with a circumferential surface crack along the outer surface, with finite length $2c$ and constant depth a.

For comparison with Eq. (7.13), a set of finite element simulations of sharply cracked ($\rho_i = 2.5$ μm) flat plates with the geometry and crack dimensions of 'plate A' (table 7.1) were performed. Ramberg-Osgood stress-strain behaviour (Eq. (2.6)) was assumed with different strain hardening exponents, in order to achieve different Y/T-values. In this respect, Y/T was varied from 0.82 to 0.93 in steps of 0.01. Further, $E = \sigma_0/\epsilon_0$ and σ_0 were kept fixed at 206,900 MPa and 500 MPa and α was chosen for σ_0 to correspond with the 0.2 % proof stress. Different boundary conditions (end plane rotations freely allowed or inhibited) and crack front shapes (semi-elliptical or with a constant depth) were investigated and appeared not to significantly influence the resulting m-values. CTOD was extracted in accordance with the 90° intercept method (figure 2.1).

The results show that m converges in the small scale yielding area (figure 7.10(a), $0.005 \leq \epsilon_r \leq 0.020$), which confirms the proportionality between J and CTOD. Further, m decreases as Y/T increases. Adopting m-values observed near 0.02 true remote strain, the trend fairly agrees with Eq. (7.13) (figure 7.10(b)). Given the validation of J in section 7.2.2, the current result adds credibility to the validity of CTOD values calculated by the finite element model using the 90° intercept method.

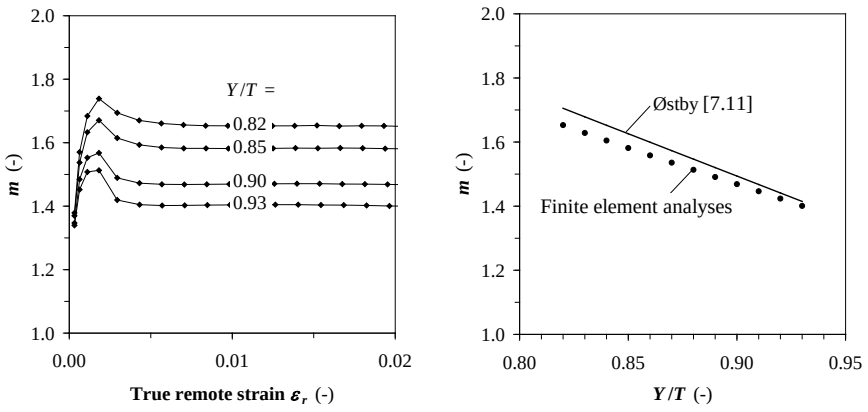

Figure 7.10: (a) m converges for small scale yielding and decreases with increasing Y/T, and (b) this trend fairly agrees with Østby [7.11].

7.3 Experimental validation using curved and medium wide plate tests

This section describes experimental validations of different aspects relevant to curved or medium wide plate testing. All experimental results discussed in chapter 6 are used throughout the following. A similar approach has been followed for all validation simulations, with respect to the definition of materials, geometry, instrumentation, meshing and boundary conditions.

All **materials** were modelled to harden isotropic according to the Von Mises yield criterion, in accordance with common practice for finite element analysis in strain based design of pipelines [7.12].

- The **base metals' stress-strain properties** were iteratively adapted starting from (temperature corrected) small scale tensile test results, to obtain a good representation of experimental gross stress s versus either average overall strain $e_{o,avg}$ or remote strains e_r of both base metals. Hereby, $e_{o,avg}$ was used for the tested *homogeneous* weldments (CWP-1 and 2) and plain plates (MWP-F-1 and 2). e_r on the other hand was used for both base metals separately in the *heterogeneous* weldments (MWP-C-1 and 2), aiming to replicate figure 6.29(a). Focus was put on the region prior to maximum load.

- **HAZ properties** were scaled from the corresponding base metal properties, proportionally to their ratio of average Vickers hardness. The scaling was performed uniformly over the entire stress-strain curve and hence applies to both yield strength and ultimate tensile strength in particular.

- **Weld metal stress-strain properties** were initially adopted from all weld metal tensile test results. If necessary (i.e. for CWP-2), the FITNET temperature correction for stress (Eq. (6.1)) was applied over the full plastic strain range. Possible influences of the definition of weld metal constitutive behaviour have been investigated for CWP-2.

Note that stress-strain properties are input into the finite element model on the basis of true quantities (ϵ and σ) rather than engineering quantities (e and s). The conversion equations Eqs. (3.1) and (3.2) lose validity upon the occurrence of localized deformations. In a pragmatic attempt to address this shortcoming, Ling [7.13] stated that the true stress-strain behaviour beyond necking (ϵ_m, σ_m) can be situated between two extremes: a power law extrapolation (lower bound) and a linear extrapolation (upper bound). Curves between these extremes are characterized by a weighted average with a weight factor $\alpha' \in [0;1]$, mathematically described as follows:

$$\sigma = \sigma_m \left[\alpha' \left(1 + \epsilon - \epsilon_m\right) + \left(1 - \alpha'\right) \left(\frac{\epsilon}{\epsilon_m} \right)^{\epsilon_m} \right] \tag{7.15}$$

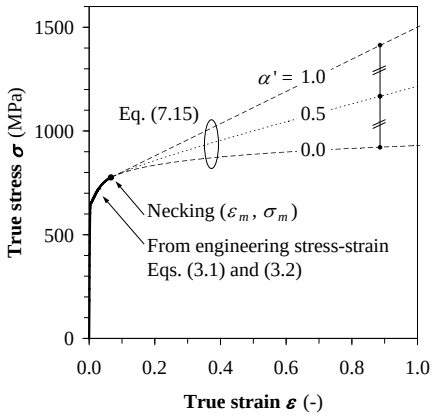

Figure 7.11: Post-necking stress-strain behaviour as defined by Ling [7.13].

The influence of post-necking stress-strain behaviour has been investigated for CWP-1, by simulating three cases (figure 7.11): $\alpha' = 0.0$ (power law extrapolation), 0.5 (average extrapolation) and 1.0 (linear extrapolation). A convergence study indicated that extrapolations up to 2.0 (200 %) true strain were sufficient.

The **geometries** of the simulated specimens and welds have been replicated from the information available. Notches were given their actual initial tip radius and were assumed semi-elliptically (with exception of CWP-1, whose electrical discharge machined notch is better represented as having a constant depth, figure 6.4). Further, the **instrumentation** was replicated as follows. 'Virtual' LVDTs were introduced in the specimen models in accordance with their actual mounting positions for the experiments. Accordingly, a CMOD measurement was performed by a 'virtual' clip gauge, mounted in a similar way as in the experiments.

Similar to the simulations for the analytical validation, **meshing** has been performed to obtain 'fast but fairly accurate' results. In terms of **boundary conditions**, the end planes were impeded to rotate.

Attention is given to the following aspects of CWP and MWP testing in separate sections:

- CMOD response and strain capacity (section 7.3.1),

- the relation between unloading compliance and ductile tearing (section 7.3.2),
- the strain distribution in the specimen and resulting measurement of remote strain (section 7.3.3).

7.3.1 CMOD response and strain capacity

7.3.1.1 CWP-1

As mentioned above, three validation simulations have been evaluated for CWP-1, each with a different α'-value (0.0, 0.5, 1.0). Note that CWP-1 is particularly suited to investigate the influence of α', as no significant ductile tearing occurred. Hence, the experiment should be fully replicated by one simulation with fixed flaw size.

First, figure 7.12 showsn an unmistakable correspondence in the evolution of s against $e_{o,avg}$.

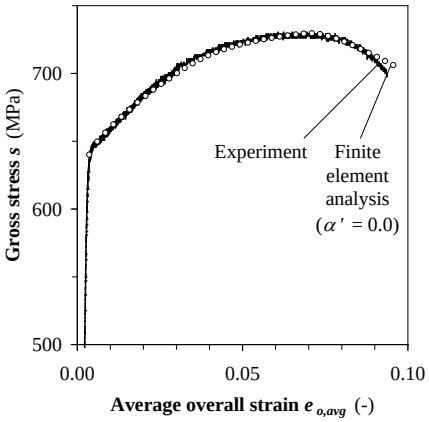

Figure 7.12: CWP-1: Gross stress - overall strain responses agree.

Second, the CMOD responses obtained are in strong general agreement with the experimentally obtained response prior to necking (figure 7.13). Apart from the kinks around 0.005 and 0.03 strain, the slopes of the simulated CMOD curves represent that of the experiment.

However, the three simulated results differ in terms of collapse behaviour. Whereas the case $\alpha' = 0.0$ nearly overlaps with the experiment and $\alpha' = 0.5$ also satisfies, the case $\alpha' = 1.0$ strongly disagrees. This is also reflected in the

observed average remote and overall strains at maximum load, given in table 7.4.

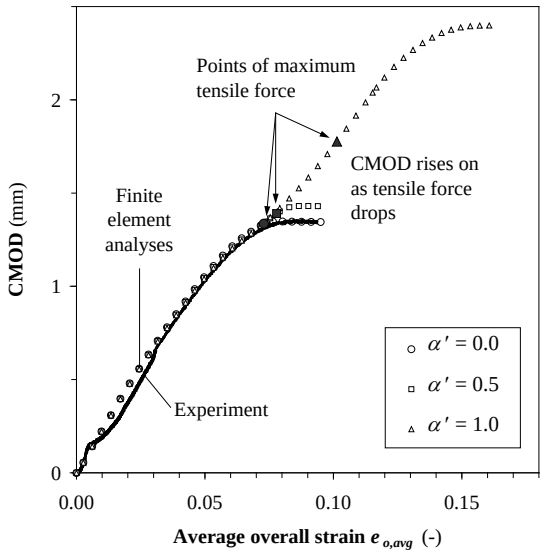

Figure 7.13: CWP-1: Experimental and simulated CMOD responses correspond prior to necking.

Table 7.4: Simulations of CWP-1: average strains at maximum load.

α'	0.0	0.5	1.0
$e_{r,avg}$	0.075	0.079	0.100
$e_{o,avg}$	0.071	0.076	0.098

Adopting average overall strain as strain capacity, the numerically observed values are in disagreement with the experimentally observed values (between 0.059 and 0.067, see section 6.3.2). Moreover, its value is strongly influenced by the value of α' chosen for. To this respect, it is important to note that Ling disadvises Eq. (7.15) for the *prediction* of failure strain, since 'a slight variation in elongation or even a small numerical disturbance can cause significant differences in the calculated fracture strain' [7.13]. The use of Eq. (7.15) should rather be seen as a pragmatic attempt to *describe* experimentally observed results.

Summarizing the validation of CWP-1, an input of proper geometrical and material characteristics may result in an accurately predicted CMOD response. Nevertheless, a prediction of strain capacity is far more challenging and strongly sensitive to post-necking yield behaviour.

Accepting the dependency of predicted strain capacity on post-necking stress-strain behaviour and given the satisfactory agreement for CWP-1 with $\alpha' = 0.0$, similar power law extrapolations were assumed for all further validations without additional consideration.

Finally worth mentioning is that, similar to the experiment, a CMOD rise is numerically observed after the occurrence of maximum load (figure 7.13). The CMOD rise during collapse depends on α' and is unrealisticly high for $\alpha' = 1.0$. For $\alpha' = 0.0$ and 0.5 respectively, CMOD rises 1 % and 3 % relative to its value at maximum tensile force.

In [7.14], a hypothesis for the CMOD rise throughout gross section collapse was that the crack extends even beyond the achievement of maximum load. Since the performed finite element simulations do not incorporate ductile tearing, figure 7.13 suggests that other effects may (additionally) come into play. In this respect, it was found that the restraint of the collapsing base metal increases the lateral compression in the weld due to compatibility effects. At a moderate drop of axial tensile load (e.g. 1 %, figure 7.14), this compression results in a net increase of the Von Mises equivalent stress in the flaw ligament, which is related to plasticity. As a consequence of the increased plasticity near the flaw tip, CMOD rises after the initiation of necking. Eventually, CMOD stabilizes since the Von Mises equivalent stress near the flaw tip is reduced again when the drop in axial load overcompensates the rise in compressive stress.

7.3.1.2 CWP-2

Challenging for this case was the description of the weld, because of two reasons:

- Two distinct welding processes (GTAW for the root pass and FCAW for the filler passes) with significantly different resulting strength characteristics are involved.
- A high degree of strength heterogeneity was observed for the FCAW weld metal (figure 6.8).

With respect to these points, simulation results have been compared with and without incorporation of the GTAW root pass. In the latter case, the root pass properties were defined identical to the properties of the filler passes. Comparing both approaches, results were found to be marginally influenced by the GTAW root pass, given its limited area and the fact that most of the notch

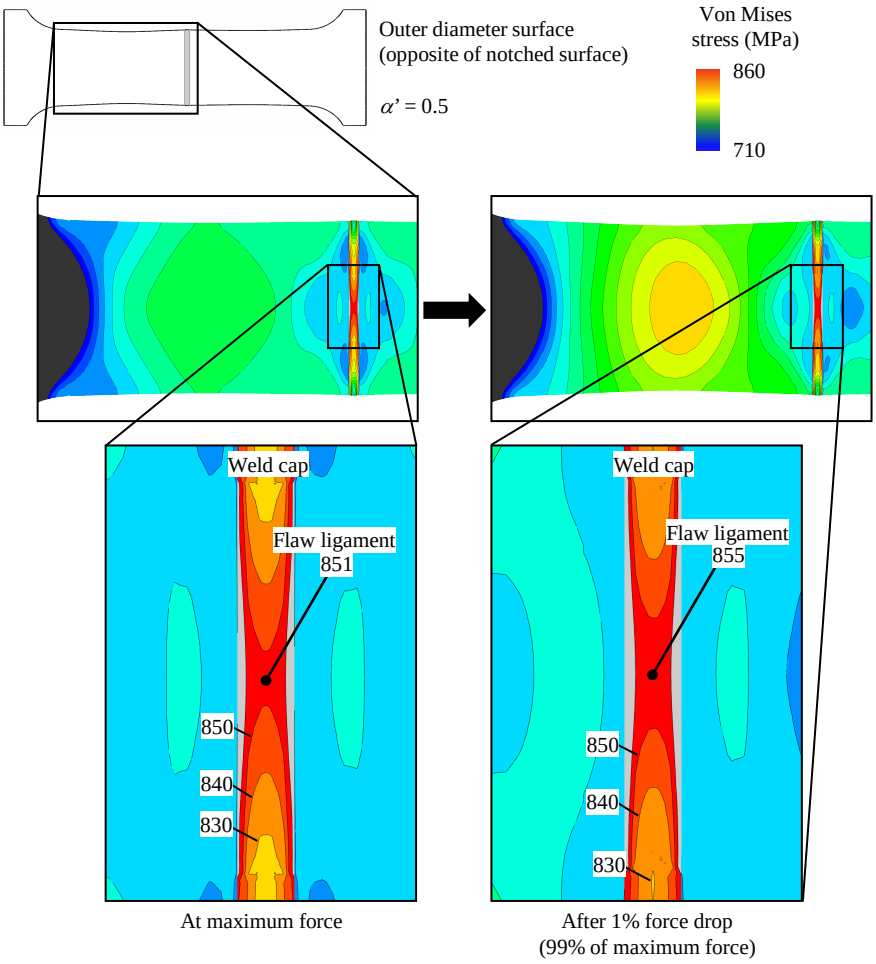

Figure 7.14: Lateral restraint of the necking base metal causes an increase of Von Mises stress from 851 MPa (maximum load) to 855 MPa (99 % of maximum load) in the weld cap surface of the flaw ligament (shown for $\alpha' = 0.5$).

tip is surrounded by FCAW material. The stress-strain behaviour of the all weld metal tensile test sampled closest to the CWP specimen (bold solid curve in figure 6.8) was adopted. Hereby, the Lüders plateau was initially considered flat and the true Lüders elongation ϵ_L was taken 0.02.

Although showing a proper correspondence for small (plastic) deformations, the resulting CMOD responses significantly diverge for overall strains above 0.015 (figure 7.15). As a first attempt to resolve this divergence, all input parameters

were varied between ranges that can be justified from scatter observed for the experiment. For instance, (a) lower and upper bound weld metal stress-strain properties were chosen with respect to figure 6.8, (b) weld geometry was varied on the basis of multiple etched weld sections, (c) notch depth was slightly adapted to the finally observed value, thereby incorporating the effect of the observed small ductile tear. None of the abovementioned measures could at this point explain why experiment and simulation diverge for large strains.

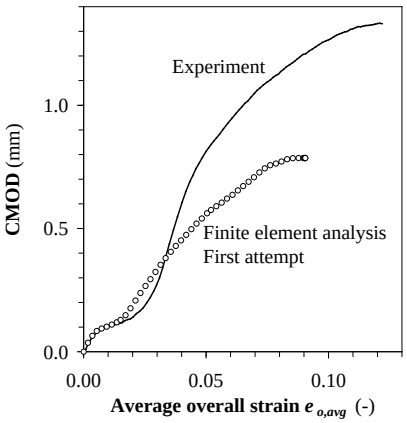

Figure 7.15: CWP-2: CMOD responses of experiment and simulation diverge around 0.015 overall strain.

A closer investigation of the simulation result revealed that the moment of divergence ($e_{o,avg} = 0.015$) is very close to the point where the plastic zone originating from the notch tip reaches the opposite surface ($e_{o,avg} = 0.018$). This is illustrated in figure 7.16, a criterion of equivalent plastic > 0.0001 being adopted for the identification of the plastic zone. From that moment, through-thickness Lüders bands in the weld may be much less restrained in their development, which promotes notch tip blunting and a corresponding steep increase in CMOD. If so, the divergence between simulation and experiment is likely due to the particular description given to the Lüders plateau.

The investigation of the plastic behaviour of discontinuously yielding structures has a recent history. To the author's knowledge, advanced numerical representations of Lüders bands were first reported in 1996 [7.15], where it was suggested to model a gradual softening behavior instead of a flat yield plateau. In terms of true stress and strain, the shape of the Lüders plateau in this so-called **'up-down-up' approach** is defined by its elongation ϵ_L, its negative slope E_L, and the average stress σ_0 (figure 7.17). Related with ϵ_L and E_L is the softening stress range $\Delta\sigma_L$. To obtain an equal amount of plastic energy

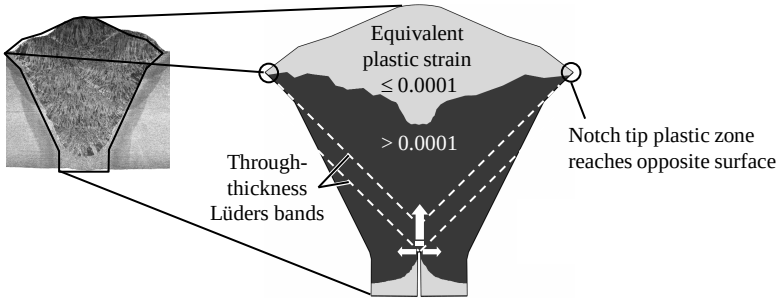

Figure 7.16: CWP-2: Contour plot of equivalent plastic strain at $e_{o,avg} = 0.018$.

dissipation as the experimental curve, the average stress is approximately chosen as the experimental lower yield point σ_0. Beyond the yield plateau, the model stress-strain curve is fit again to the measured curve.

The 'up-down-up' approach has been applied to describe Lüders bands for various problems related to pipeline or piping integrity, such as the uniaxial tension of line pipe steel strips [7.16], bending of seamless pipe [7.17], and bending of steel tubes [7.18–7.20]. For all mentioned studies, inverse modelling was required to find an appropriate value for E_L. A wide range of resulting values has been reported, down to as low as -9,190 MPa [7.18]. Hereby, $\Delta\sigma_L$ reached values roughly between 20 % and 30 % of σ_0. An additional challenge is obtaining a converging solution for the problem, which may require extremely small calculation increments to resolve the local instabilities that occur.

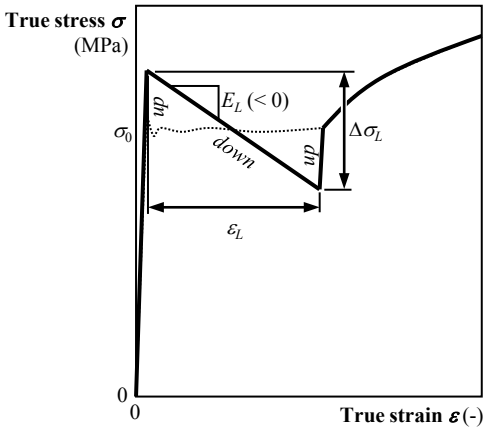

Figure 7.17: Up-down-up approach for modelling materials with a Lüders plateau.

The up-down-up approach for description of Lüders bands is a phenomenological tool which requires inverse modelling to achieve correspondence with experimental behaviour. In such case, the role of finite element modelling as a predictive tool for strain capacity may be questioned.

To investigate the possibility to obtain better numerical descriptions of the experimentally observed CMOD response, the up-down-up approach was applied in six simulations. Two negative slopes E_L were considered (-4,000 and -8,000 MPa) in combination with three true Lüders elongations (0.01, 0.02, 0.03). Of these six simulations, the closest match was achieved for E_L = -8,000 MPa and $\epsilon_L = 0.02$ ($\Delta\sigma_L = 160$ MPa ≈ 23 % of σ_0), and is shown in figure 7.18. This result describes the sharp increase in CMOD observed after 0.02 overall strain. Nevertheless, a good representation is still confined to overall strains below 0.035. Subsequent attempts to obtain better descriptions over the entire strain range were not taken. Nevertheless, figure 7.18 indicates that an iterative up-down-up approach may indeed be required to obtain a result which represents reality in presence of materials with a Lüders plateau.

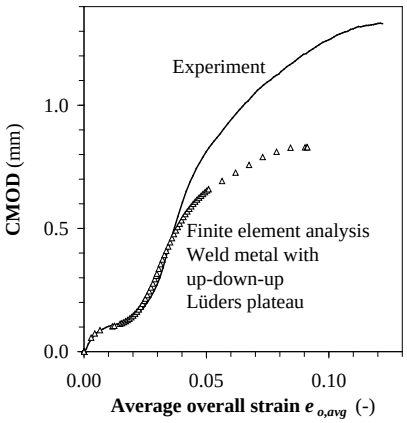

Figure 7.18: CWP-2: The up-down-up approach for description of the weld metal Lüders plateau gives a significantly better result.

7.3.1.3 MWP-F-1 and MWP-F-2

Even though the configurations of MWP-F-1 and MWP-F-2 are easy to describe (fully homogeneous flat plates without weld), two factors strongly complicate the interpretation of their CMOD responses: the pronounced Lüders plateau

of the material and the occurrence of ductile tearing [2].

The experimental CMOD responses of MWP-F-1 and MWP-F-2 were compared with two simulations for each test: a simulation with the initial notch depth, and one with the final depth from post mortem investigation (e.g. figure 6.14 for MWP-F-1). This approach of comparing an experiment with fixed flaw size simulations is referred to in literature as **'CMOD mapping'**. The following is observed (figure 7.19):

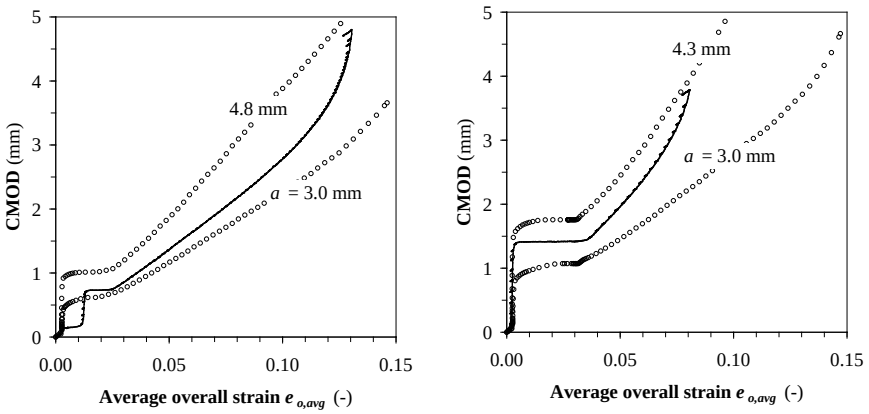

(a) (b)

Figure 7.19: Experimental and simulated CMOD responses: (a) MWP-F-1, (b) MWP-F-2.

- A significant disagreement is found at the stages of discontinuous yielding. This should not surprise, as simulated crack driving force responses in this region are known to be extremely sensitive to small changes in the (near to zero) slope and length of the modelled Lüders plateau, even without application of the up-down-up approach [7.5].
- Beyond discontinuous yielding, the experimental CMOD responses are fully bounded by the corresponding simulations with lower and upper bound flaw depth.
- Towards the ends of the tests, the experimental CMOD responses approach the simulated CMOD response with the final flaw depth obtained from post mortem investigation (4.8 mm and 4.3 mm for MWP-F-1 and MWP-F-2, respectively). *Assuming* that the technique of 'CMOD mapping' is justified, this adds belief to the representativeness of the finite

[2]Recall that monitoring the development of ductile tearing through unloading compliance was unsuccessful for MWP-F-1 and MWP-F-2 (section 6.5.2.4).

element model. Note that the validity of the CMOD mapping approach is still under discussion. For instance, it was not fully satisfactory in [7.21] but provided promising agreements in [7.22], where its resulting ductile tearing predictions were found comparable with unloading compliance analysis. In the latter's case, CMOD mapping was favoured given that it 'requires less experimental and computational effort than does the unloading compliance technique' [7.22].

7.3.1.4 MWP-C-1 and MWP-C-2

Of all performed validations, those of MWP-C-1 and MWP-C-2 were the most challenging because these configurations involved all aspects that complicate the interpretation of the simulation results: base metal heterogeneity, discontinuous yielding, ductile tearing, weld misalignment, different flaw locations and different failure modes.

From preliminary attempts, it became clear that the CMOD response is highly sensitive to base metal heterogeneity. Therefore, base metals were iteratively adapted in a first validation stage to obtain a proper representation of the *actual* remote strain heterogeneity plot. The result is shown in figure 7.20.

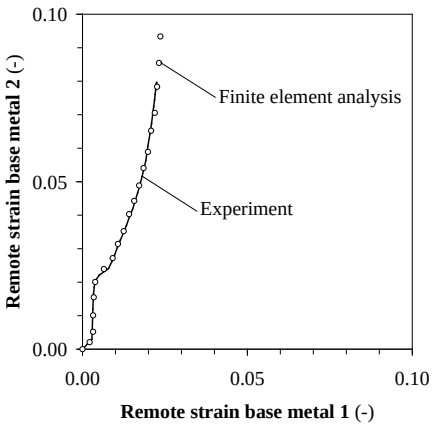

Figure 7.20: Special care has been given to a proper representation of base metal heterogeneity.

Given the occurrence of ductile tearing, a second stage consisted of performing multiple simulations with different fixed flaw depths. Figures 7.21 and 7.22 compare simulated with experimental CMOD responses for respectively MWP-C-1 and MWP-C-2, and indicate the following:

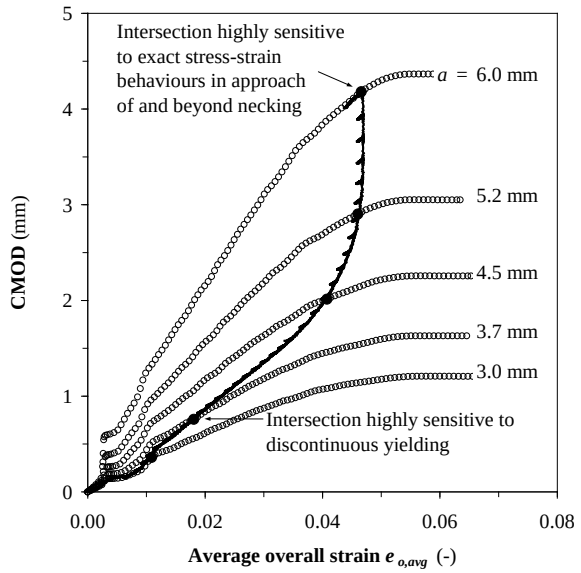

Figure 7.21: MWP-C-1: CMOD is well predicted prior to ductile tearing, and CMOD mapping predicts a final crack depth of 6.0 mm.

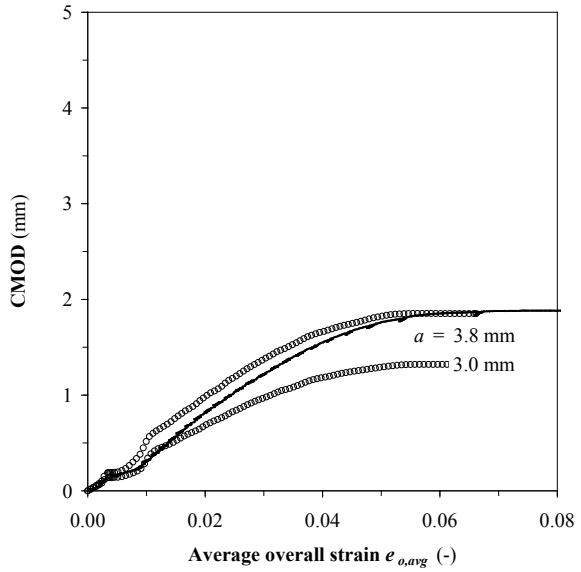

Figure 7.22: MWP-C-2: CMOD is well predicted prior to ductile tearing, and CMOD mapping predicts a final crack depth of 3.8 mm.

- Similar to the previously discussed validations, there is a strong initial agreement between the experiments and the corresponding simulations with $a = 3.0$ mm.
- Above 0.01 average overall strain, the experiments deviate from the simulations with $a = 3.0$ mm, which indicates an initiation of ductile tearing.
- Application of the CMOD mapping approach indicates a final crack depth of $a = 6.0$ mm for MWP-C-1 and $a = 3.8$ mm for MWP-C-2. These values are close to the actual final crack depths observed from post mortem macrography: 6.7 mm and 3.7 mm respectively (figure 6.24).
- Comparing figure 7.21 with figure 7.22, the crack driving responses of MWP-C-1 and MWP-C-2 are similar for both $a = 3.0$ mm and $a = 3.7$ mm. As a consequence, their different failure behaviour is assumed to be caused by a different ductile tearing resistance of the sampled microstructures.

By means of illustration, figure 7.23 depicts the deformed weld at the end of the simulation of MWP-C-1, with $a = 6.0$ mm. Clearly visible is that strain concentrations from the crack tip head towards the weakest base metal, and that the crack ligament has significantly necked.

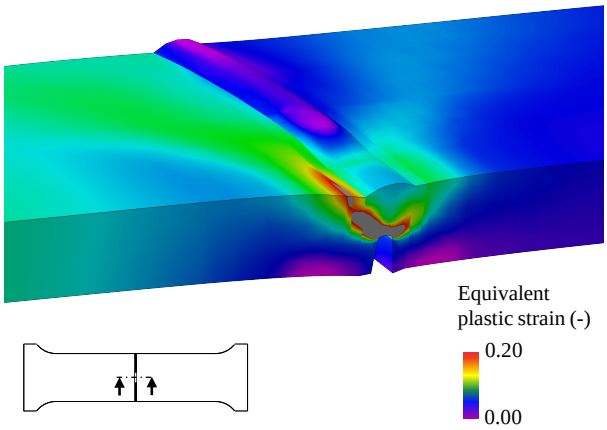

Figure 7.23: MWP-C-1 with $a = 6.0$ mm: Severe deformations occur near the notch tip and in the weld.

7.3.2 Ability to predict ductile tearing through CMOD mapping and unloading compliance

First, CMOD mapping allows for an estimation of the evolution of crack extension as illustrated in figure 7.21. The intersections of the experimental CMOD

response and simulated responses (solid black circles) indicate the average overall strains at which simulated flaw depths (3.7 mm, 4.5 mm, 5.2 mm, ...) are achieved. Given the limited tearing for CWP-1, CWP-2 and MWP-C-2 and the absence of unloading compliance data for MWP-F-1 and MWP-F-2, CMOD mapping has only been applied for MWP-C-1.

Despite the simplicity of the CMOD mapping concept, some critical remarks can be put forward.

- Prior to 0.04 average overall strain, the crack extension obtained from CMOD mapping is highly sensitive to small changes in experimental and numerical results. This sensitivity follows from the fairly similar slopes of the experimental and simulated CMOD responses. For instance, the $e_{o,avg}$-value corresponding with 0.7 mm crack extension (3.7 mm crack depth) is strongly influenced by the input discontinuous yielding behaviours (Lüders elongations) of base and weld metals, which determine the 'horizontal' and 'vertical' offsets of the numerical CMOD response after the full development of Lüders bands. This highlights the importance of knowing the *actual* properties (whether related to material, geometry or other aspects) to allow for proper interpretations.

- Similar to the discussion of figure 7.13, the predicted final crack depth is strongly influenced by the involved stress-strain behaviours near and beyond necking.

- As further discussed for the unloading compliance method, the numerical accuracy of the finite element model is reduced for high CMOD values.

Second, the experimental unloading compliance responses of MWP-C-1 and MWP-C-2 (figure 6.31) have been translated into crack extension responses through unloading compliance mapping. This technique is explained in [7.23] and has also been adopted in other studies (e.g. [7.22]). In brief terms, simulations with fixed flaw depths and unloading cycles are performed to create a relation between crack depth and unloading compliance, as a function of applied strain (figure 7.24 (a)). This so-called 'unloading compliance transfer function' is highly sensitive to minor changes of wall thickness and Young's modulus [7.23], and therefore typically offset ('anchored') to agree with the first unloading compliance record (figure 7.24 (b)).

Figure 7.25 depicts the unloading compliance map obtained for MWP-C-1. Simulations were unable to replicate the observed initial rise (prior to 0.01 average overall strain) of unloading compliance. Therefore, in contrast with [7.22, 7.23], the unloading compliance map was vertically translated to anchor the simulation with $a = 3.0$ mm to the *crack initiation point* rather than the first unloading compliance record (figure 7.24 (d)). This crack initiation

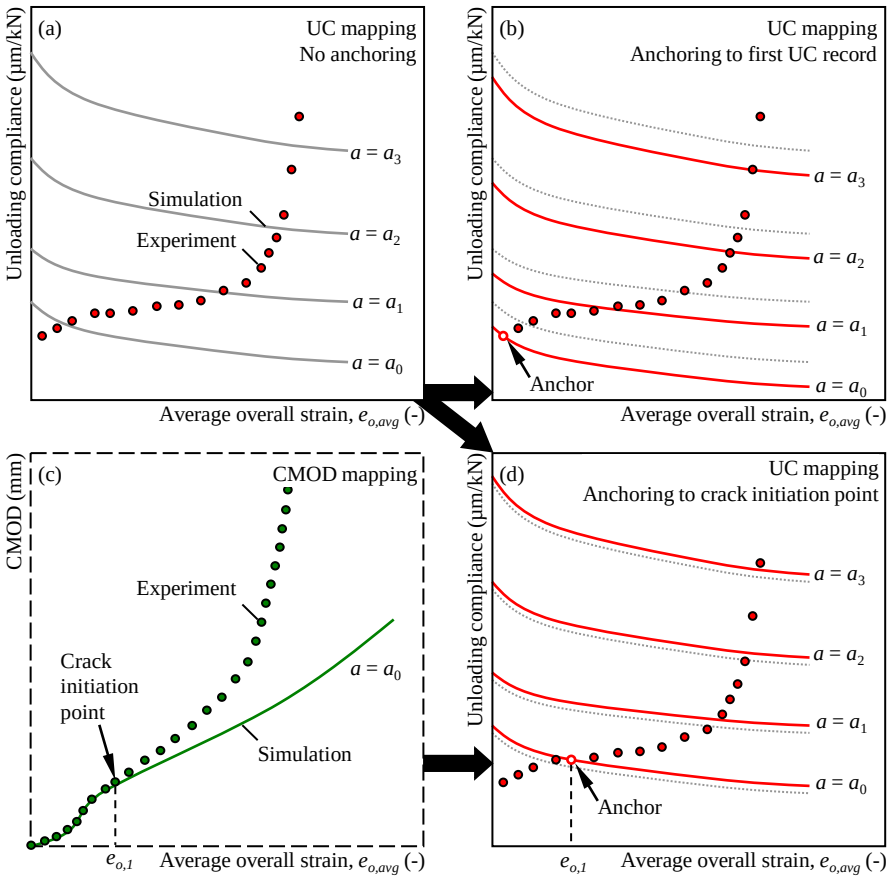

Figure 7.24: Schematical explanation of two different unloading compliance (UC) anchoring methods.

point was derived from CMOD mapping (figure 7.24 (c)), which indicated this point to be slightly above 0.01 average overall strain (recall figure 7.21). Crack depth was subsequently estimated for every unloading compliance datapoint by means of interpolation. Attempts to explain the initial evolution of unloading compliance are part of parallel PhD research performed by Matthias Verstraete, and have not been made within the framework of this dissertation.

For high crack depths (6.0 mm and above), the unloading compliance map tends to show irregular patterns. This phenomenon is assumed to result from the severe mesh distortion in the weld upon the achievement of high CMOD values. By means of illustration, figure 7.26 represents the end of the simulation with $a = 7.5$ mm. In particular, zero energy deformations have been

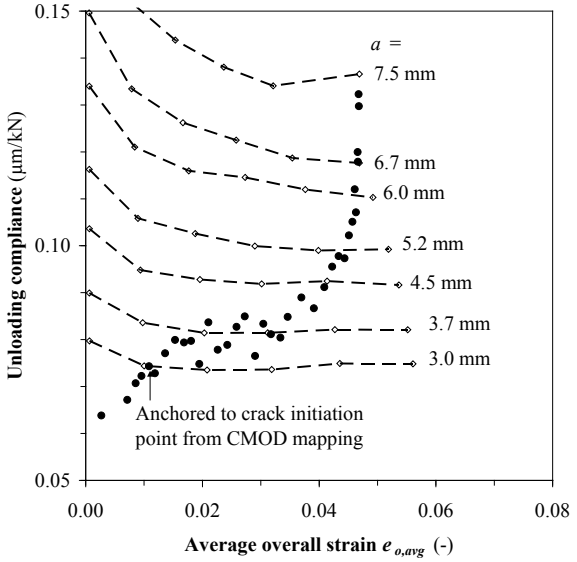

Figure 7.25: MWP-C-1: Unloading compliance map, anchored to the point of crack initiation according to CMOD mapping.

introduced into some notch tip elements, recognizable by the zigzag pattern of their edges ('hourglassing'). Hence, a proper accuracy of the unloading compliance map for high CMOD values is unlikely. Note that, whereas the adopted element type (eight-node bricks with reduced integration) is indeed susceptible to hourglassing [7.2], analyses with other element types failed to converge under severe deformation and/or required significantly higher calculation times.

Notwithstanding the questionable validity of the CMOD mapping and the unloading compliance methods for situations of 'high' CMOD, both approaches predict the final crack depth of MWP-C-1 with a fair (but far from optimal) accuracy. Moreover, the predicted evolutions of crack size as a function of $e_{o,avg}$ agree (figure 7.27). Even though the accuracy of the clip gauge was in the order of ± 1 μm (figure 5.6), the crack depths determined from unloading compliance are within a scatter band of roughly ± 0.5 mm. A further improvement of unloading compliance measurements in MWP tests is therefore desirable.

Similar to MWP-C-1, the unloading compliance mapping approach gives a rough indication of the actual crack extension of 0.7 mm for MWP-C-2 (figure 7.28). Given the abovementioned scatter band of ± 0.5 mm for calculated crack depths, no attempts have been made to describe this limited development of tearing as a function of $e_{o,avg}$.

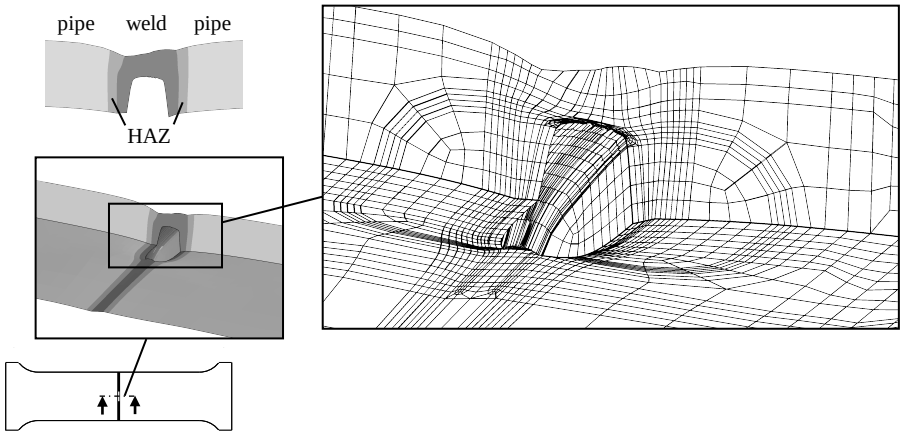

Figure 7.26: MWP-C-1 with $a = 7.5$ mm: The spider web severely distorts towards the end of the simulation.

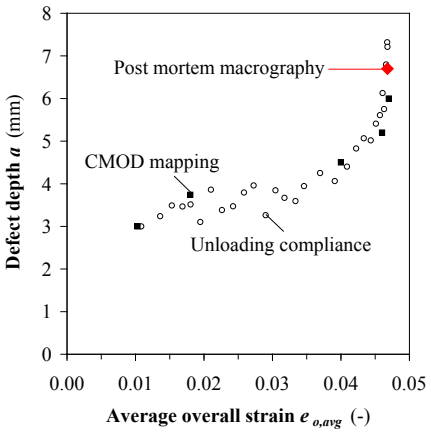

Figure 7.27: MWP-C-1: Crack extensions obtained through CMOD mapping and unloading compliance agree with post mortem macrography.

Whereas this section has shown the potential of both the CMOD mapping and the unloading compliance approach, their proper execution requires knowledge of all actual properties related to material, geometry and boundary conditions. In addition, both methods may become inaccurate for high CMOD values, as the mesh around the flaw tip severely distorts. Further, the CMOD mapping approach may be highly sensitive to small changes in model input, and significant scatter was observed for the unloading compliance approach.

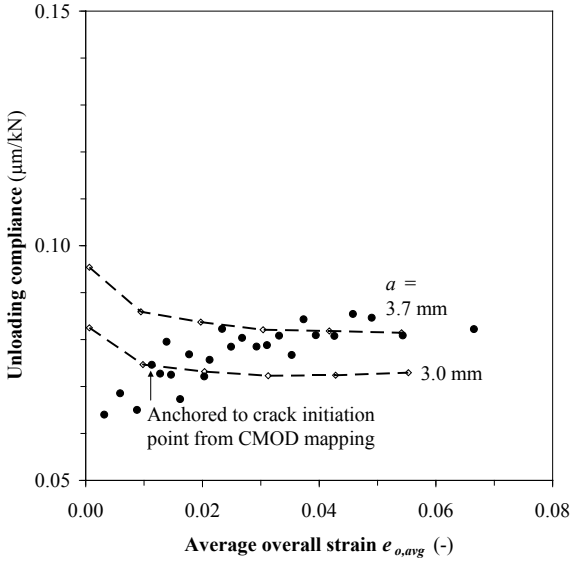

Figure 7.28: MWP-C-2: An unloading compliance map indicates a crack extension of roughly 0.7 mm.

7.3.3 Strain distribution in wide plate specimen and remote strain measurement

The DIC measurements performed on the MWP specimens allow for a qualitative and quantitative comparison of experimentally observed and numerically predicted strain distributions.

First, a clear agreement is qualitatively found from a visual comparison of strain contour plots after the development of Lüders bands. For instance, figure 7.29 compares distributions of first principal strain (ϵ_1) at similar strain levels, for (a) MWP-F-2 and (b) MWP-C-1. Of particular interest is the confirmation of strain hotspots which possibly influence LVDT measurements of remote strain. Note that the propagation of Lüders bands is not accurately predicted by the finite element simulations, whose material definitions did not involve an up-down-up approach (sections 7.3.1.3 and 7.3.1.4). Therefore, comparative contour plots in the discontinuous yielding stage do not agree.

Second, the predicted location and extent of strain hotspots has been quantitatively confirmed by comparing longitudinal strain over a path located at the specimens' mid-width. Figure 7.30 shows an example result, extracted for MWP-F-2 at one side of the notch.

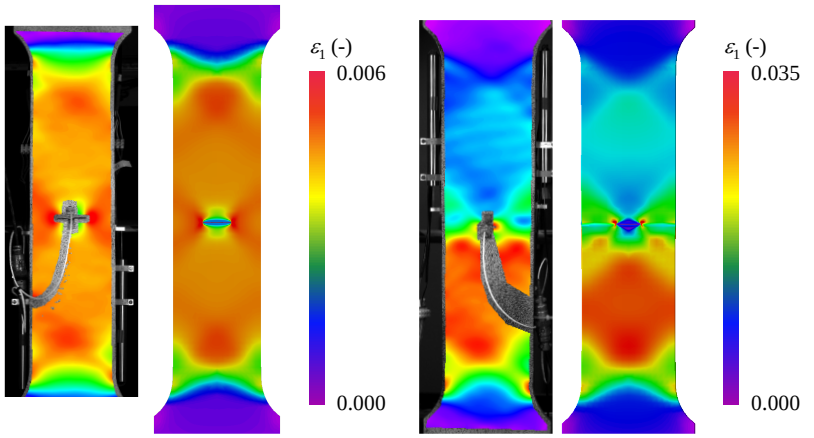

Figure 7.29: Illustrative comparison of experimentally measured and numerically obtained strain contour plots: (a) MWP-F-2, (b) MWP-C-1.

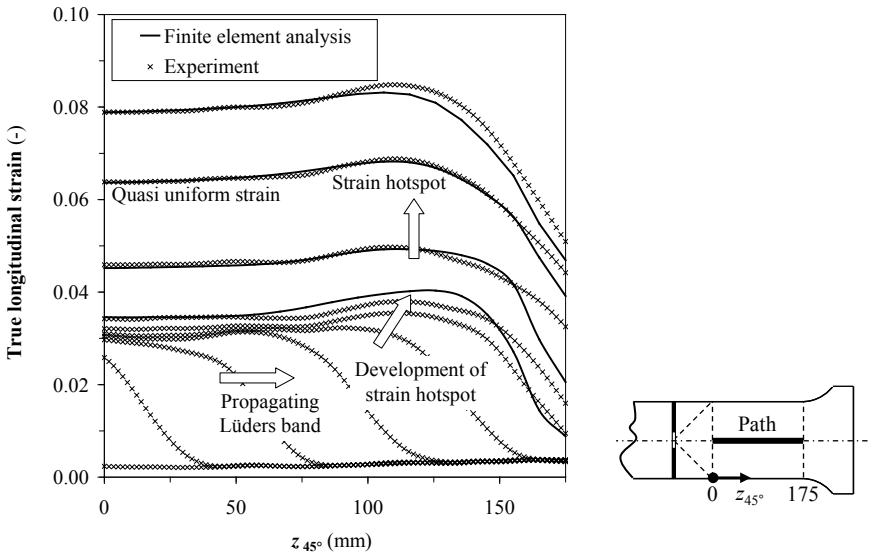

Figure 7.30: MWP-F-2: Observed and simulated longitudinal strain distributions.

Given the poor numerical representation of discontinuous yielding, numerical results in figure 7.30 are confined to strains above the Lüders elongation. The finite element model properly predicts the experimentally observed strain hotspot. Note that the agreement vanishes close to the shoulders (say, $z_{45°} >$

125 mm). Other boundary conditions (linear elastic end blocks and/or allowance of end plane rotations) have been attempted but could not explain this observation. It is suggested that a reason may be the combination of a pronounced biaxial stress state near the shoulders and base metal anisotropy. Indeed, the finite element result indicates a biaxiality ratio (transversal stress divided by longitudinal stress) of typically 0.2 in the shoulder area. In such case, effects of anisotropy may not be captured by the finite element model, which assumes isotropic strength properties. Nevertheless, the area $z_{45^\circ} > 125$ mm is not of particular interest for the presented study and the finite element result is considered acceptable.

Apart from qualitative visual examinations (e.g. figure 7.29) and quantitative investigations of strain distributions (e.g. figure 7.30), a third strain field validation involved a comparison of remote strain measurements. Similar to section 5.4.3.2, this comparison was performed on the basis of a relative remote strain $\epsilon_{r,meas}/\epsilon_{r,ref}$ for different LVDTs (figure 5.11), where $\epsilon_{r,ref}$ was averaged from the cross section with the lowest $\bar{c_v}$-value. In contrast with Eq. (5.2), the integral for calculation of c_v for this validation did not involve the discontinuous yielding stage given its poor numerical representation.

By means of illustration, figure 7.31 compares the experimental response of MWP-F-1 and MWP-F-2 with the simulated evolution of $\epsilon_{r,meas}/\epsilon_{r,ref}$ for MWP-F-2 (denoted as 'finite element analysis'). With exception of the LVDT measurement represented in subfigure (d), highly similar trends are observed between experimental and numerical remote strain measurements. The poor agreement for the 150 mm gauge length LVDT can be appointed to the discrepancy in strain distribution observed for $z_{45^\circ} > 125$ mm. Note that figure 7.31 indicates that LVDTs with gauge lengths 75, 100 and 125 mm perform properly for MWP-F-1 and MWP-F-2. This contrasts with figure 5.15, where the 100 mm gauge length LVDT clearly outperformed the other ones. Since figure 5.15 represents round house yielding materials, it is hypothesized that the strain distributions from MWP-F-1 and MWP-F-2 were influenced by the discontinuous yielding stage even after completion of this stage.

Summarizing this section, the finite element model accurately predicts strain distributions in the base metals, remote from the specimen shoulders and after completion of a possible discontinuous yielding stage. In particular, this validation has confirmed the performance of remote strain LVDT measurements, among which those advised in section 5.4.3.2.

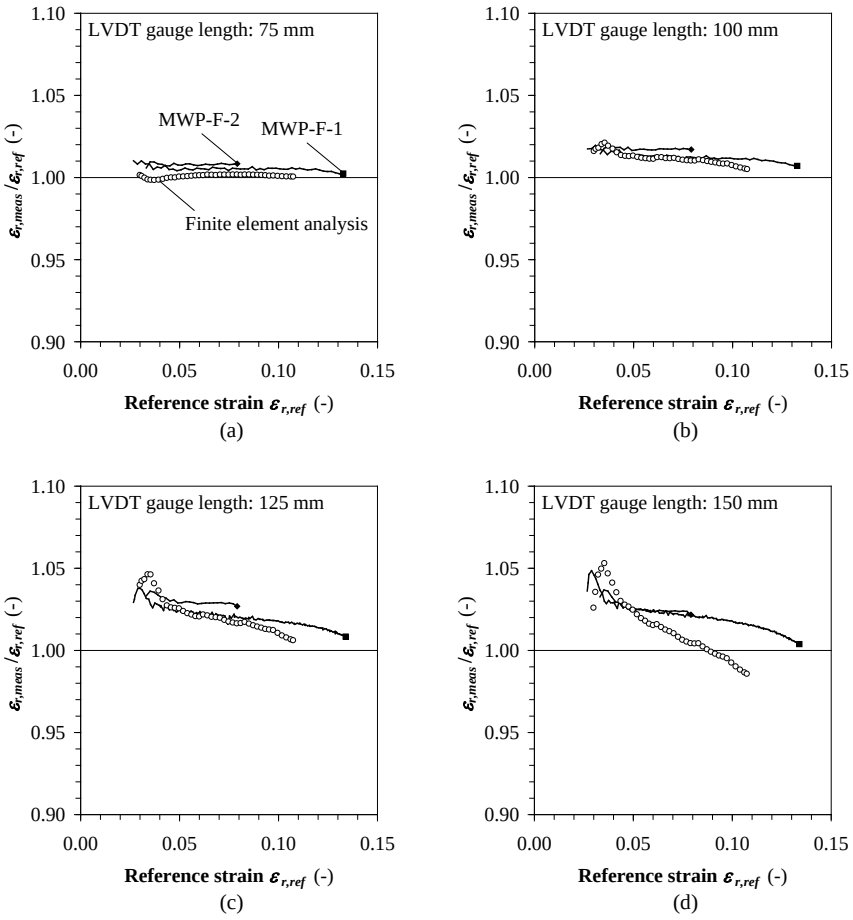

Figure 7.31: MWP-F-1 and MWP-F-2: Remote strain calculations agree with finite element analysis for the LVDTs with 75 mm, 100 mm and 125 mm (a-c) gauge length.

7.4 Summary and conclusions

This chapter has presented a critical, multidisciplinary validation of the finite element model presented in chapter 4. This validation was based upon analytical crack driving force relations and the experimental results from chapter 6.

The analytical validation confirmed the similarity of obtained crack driving force responses to those reported in literature. Attention has been given to K_I under linear elastic conditions, and to J and CTOD under elastic-plastic

conditions. The analytical validation showed that the model's potential to perform crack driving force analyses is considered comparable to that of other finite element models adopted in literature.

Even if in accordance with published analytical relations, the numerical representation of experimentally observed structural responses is far from obvious. Whereas analytical validations are mostly based upon highly simplified configurations (i.e. absence of a weld, simplified material behaviour), realistic structures involve many more aspects which should be accurately translated into the finite element model. The following challenges have been identified for numerical modelling from a predictive point of view:

- Even if the crack driving force response (qualitatively expressed in the form of CMOD) is properly predicted, post necking true stress-strain behaviour may influence the predicted strain capacity (validation of CWP-1, section 7.3.1.1).
- The presence of weld metal exhibiting a Lüders plateau has significantly complicated the validation of CWP-2. An up-down-up approach was required for the description of discontinuous yielding. This technique involves inverse modelling and is therefore inapplicable for predictive modelling purposes.
- For the simulations of MWP-C-1 and MWP-C-2, the result proved to be strongly dependent on a proper representation of base metal heterogeneity. This reflects that knowledge of *actual* material properties is essential [7.24], which introduces severe challenges to predictive modelling.

CMOD responses of CWP tests without significant tearing have been successfully replicated up to average overall strain levels of 0.04 (CWP-2) and above (CWP-1). A CMOD rise beyond base metal necking was found to be caused by an increased plasticity at the flaw ligament. This increase is explained by the lateral restraint arising from the collapsing base metal.

Estimations of ductile tearing through CMOD mapping and unloading compliance mapping were fairly successful but sensitive to model inputs and, as regards the latter approach specifically, to CMOD measurement scatter. Also, the anchor point of the unloading compliance transfer function had to be chosen on the basis of the CMOD mapping result rather than simply the first unloading compliance record as adopted in literature (figure 7.24).

Strong overall agreements were readily found for the strain distributions in the base metals. In particular, the predicted extent and location of strain hotspots has been experimentally confirmed, and numerical measurements of remote strain have been validated for the LVDT configuration advised in chapter 5.

Experiments and simulations are complementary: the combination of both adds value to the interpretation of each. In particular, finite element modelling is suited to reveal qualitative trends of influence factors rather than predict actual strain capacities. Experiments, on the other hand, are the one and only tool to verify whether the numerical outcomes of a finite element study are reflected in reality.

Bibliography

[7.1] J.C. Newman and I.S. Raju. Stress-intensity factor equations for cracks in three-dimensional finite bodies subjected to tension and bending loads. Technical report, National Aeronautics and Space Administration, 1984. NASA Technical Memorandum 85793, NASA.

[7.2] Dassault Systèmes. *ABAQUS Analysis User's manual (version 6.10)*, 2010.

[7.3] A. Zahoor. Closed form expressions for fracture mechanics analysis of cracked pipes. *Journal of Pressure Vessel Technology-Transactions of the ASME*, 107(2):203–205, 1985.

[7.4] M. Bergman. Stress intensity factors for circumferential surface cracks in pipes. *Fatigue & Fracture of Engineering Materials & Structures*, 18(10):1155–1172, 1995.

[7.5] D.P. Boothman, M.M.K. Lee, A.R. Luxmoore, and J.D.G. Sumpter. *J*-estimation for semi-elliptical surface cracks in wide plates under direct tension. *Fatigue & Fracture of Engineering Materials & Structures*, 21(3):333–346, 1998.

[7.6] G. Yagawa, Y. Kitajima, and H. Ueda. 3-Dimensional fully plastic solutions for semielliptic surface cracks. *International Journal of Pressure Vessels and Piping*, 53(3):457–510, 1993.

[7.7] G. Yagawa, Y. Kitajima, and H. Ueda. Three-dimensional fully plastic solutions for semi-elliptical surface cracks (erratum vol. 53, pg. 457, 1993). *International Journal of Pressure Vessels and Piping*, 74(1):77–80, 1997.

[7.8] R.C. McClung, G.G. Chell, Y.-D. Lee, D.A. Russell, and G.E. Orient. Development of a practical methodology for elastic-plastic and fully plastic fatigue crack growth. Technical report, National Aeronautics and Space Administration, 1999. NASA/CR-1999-209428. 112 pages.

[7.9] Y. Lei. *J*-integral and limit load analysis of semi-elliptical surface cracks in plates under tension. *International Journal of Pressure Vessels and Piping*, 81(1):21–30, 2004.

[7.10] X. Wang. Fully plastic *J*-integral solutions for surface cracked plates under biaxial loading. *Engineering Fracture Mechanics*, 73(11):1581–1595, 2006.

[7.11] E. Østby. Fracture control - Offshore pipelines - New strain-based fracture mechanics equations including the effects of biaxial loading, mismatch and misalignment. In *Proceedings of the 24th International Conference on Offshore Mechanics and Arctic Engineering (OMAE)*, Halkidiki, Greece, 2005. OMAE2005-67518.

[7.12] Y. Shinohara, Y. Madi, and J. Besson. A combined phenomenological model for the representation of anisotropic hardening behavior in high strength steel line pipes. *European Journal of Mechanics A/Solids*, 29(6):917–927, 2010.

[7.13] Y. Ling. Uniaxial true stress-strain after necking. *AMP Journal of Technology*, 5:37–48, 1996.

[7.14] D.P. Fairchild, W. Cheng, S.J. Ford, K. Minnaar, N.E. Biery, A. Kumar, and N.E. Nissley. Recent advances in curved wide plate testing and implications for strain-based design. *International Journal of Offshore and Polar Engineering*, 18(3):161–170, 2008.

[7.15] S. Beissel and T. Belytschko. On patterns of deformation in phase transformations and Lüders bands. *International Journal of Solids and Structures*, 33(12):1689–1707, 1996.

[7.16] S. Kyriakides and J.E. Miller. On the propagation of Lüders bands in steel strips. *Journal of Applied Mechanics - Transactions of the ASME*, 67(4):645–654, 2000.

[7.17] M. Carr, I. MacRae, and D. Bruton. Local buckling of pressurized seamless linepipe: results of the SAFEBUCK JIP. In R. Denys, editor, *Proceedings of the 5th International Conference on Pipeline Technology*, Ostend, Belgium, 2009.

[7.18] F. Aguirre, S. Kyriakides, and H.D. Yun. Bending of steel tubes with Lüders bands. *International Journal of Plasticity*, 20(7):1199–1225, 2004.

[7.19] S. Kyriakides, A. Ok, and E. Corona. Localization and propagation of curvature under pure bending in steel tubes with Lüders bands. *International Journal of Solids and Structures*, 45(10):3074–3087, 2008.

[7.20] J.F. Hallai and S. Kyriakides. On the effect of Lüders bands on the bending of steel tubes. Part II: Analysis. *International Journal of Solids and Structures*, 48(24):3285–3298, 2011.

[7.21] D.M. Duan, Y.Y. Wang, Y. Chen, and J. Zhou. Modeling and CMOD mapping of surface-cracked wide plates. In *Proceedings of the 7th International Pipeline Conference (IPC)*, Calgary, Alberta, Canada, 2008. IPC2008-64425.

[7.22] N. Yoosef-Ghodsi, D.M. Duan, Q. Chen, R. Petersen, and C. Fan. Finite element analysis of flaw growth history. In *Proceedings of the 8th International Pipeline Conference (IPC)*, Calgary, Alberta, Canada, 2010. IPC2010-31418.

[7.23] K. Minnaar, P.C. Gioielli, M.L. Macia, F. Bardi, N.E. Biery, and W.C. Kan. Predictive FEA modeling of pressurized full-scale tests. In *Proceedings of the 17th International Offshore and Polar Engineering Conference (ISOPE)*, pages 3114–3120, Lisbon, Portugal, 2007.

[7.24] R. Denys, W. De Waele, and A. Lefevre. Effect of pipe and weld metal post-yield characteristics on plastic straining capacity of axially loaded pipelines. In *Proceedings of the 5th International Pipeline Conference (IPC)*, Calgary, Alberta, Canada, 2004. IPC04-0768.

Chapter 8

Influence of weld strength mismatch and base metal constitutive properties on strain capacity

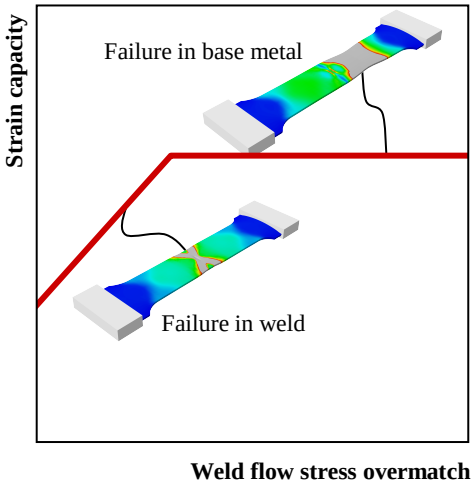

A parametric finite element study indicated that strain capacity is bilinearly related to weld flow stress overmatch.

8.1 Goal

The literature review of chapter 2 and the experimental results of chapter 6 have indicated that base metal strength characteristics are of major importance to strain capacity. This chapter investigates effects of weld strength mismatch, base metal constitutive behaviour and base metal heterogeneity on strain capacity. This is done by means of theoretical considerations and a parametric study using the finite element model elaborated in chapter 4 and validated in chapter 7. This validation was mostly based on MWP test results, which required the test setup elaborated in chapter 5. To obtain a high freedom in the parametric description of base metal strength characteristics, the 'UGent' stress-strain model developed in chapter 3 is adopted. In summary, results from all previous chapters are the fundaments of this chapter.

Two expressions that will be used throughout the chapter are introduced at this point.

- *Base metal heterogeneity* refers to a situation where both base metals are homogeneous, but have different properties. This expression thus refers to pipe-to-pipe heterogeneity and neglects in-pipe heterogeneity (section 3.3.3).
- A *homogeneous weldment* refers to a weldment where no base metal heterogeneity is present. It does not address the mechanical properties of the weld metal, which may be mismatched relative to the base metal properties.

First, section 8.2 deals with the influence of different weld strength overmatch definitions on the *strain capacity* of a homogeneous weldment. Section 8.3 then reveals and explains the observations on the level of *crack driving force response*. Finally, section 8.4 shows how base metal heterogeneity can change strain capacity by means of 'thought experiments' based upon a set of theoretical assumptions.

8.2 Influence of weld strength overmatch on strain capacity

To date, three definitions have been explicitly adopted for weld strength overmatch in a strain based context:

- yield strength overmatch OM_{YS} (Eq. (2.12));
- ultimate tensile strength overmatch OM_{TS} (Eq. (2.17));
- flow stress overmatch OM_{FS} (Eq. (2.18)).

It was already pointed out in section 2.3.2 that there is no consensus regarding the following question: '*Which is the most relevant weld strength overmatch definition in the framework of a strain based flaw assessment?*'. In an attempt to answer this question, an elaborate parametric finite element study of CWP tension tests has been performed using the model of chapter 4.

Section 8.2.1 elucidates the design of the parametric simulation program. Since the influence of base metal heterogeneity is further discussed in section 8.4, homogeneous weldments are assumed at this point. General observations are made in section 8.2.2. Section 8.2.3 discusses the results. Section 8.2.4 concludes with a framework for a strain capacity equation based upon weld strength overmatch.

8.2.1 Simulation program

The following aspects are separately covered:

1. geometrical properties of pipe, weld and flaw,
2. geometry and simulated instrumentation of the CWP specimens,
3. material stress-strain properties,
4. mesh design, and,
5. incorporation of ductile tearing.

8.2.1.1 Geometrical properties of pipe, weld and flaw

Pipe outer diameter D_o and thickness t were fixed at respectively 1,000 mm and 15 mm. The initial flaws were 50 mm long and 3 mm deep. The flaw shape was semi-elliptical with an initial notch tip radius $\rho_i = 75$ μm. Stable crack extension was accounted for as further explained in section 8.2.1.3.

Three different combinations of weld geometry and flaw location were assumed:

- a 'narrow gap' weld with a WMC flaw (figure 8.1(a));
- a 'wide bevel' weld with a WMC flaw (figure 8.1(b));
- the same 'wide bevel' with a HAZ flaw (figure 8.1(c)).

Note that both narrow gap and wide bevel welds have been investigated given the distinction between automatic and manual welds (figure 1.8). The considered combinations allow for a comparison between different weld geometries (figure 8.1(a) versus (b)) and between different flaw locations (figure 8.1(b) versus (c)).

Misalignment and wall thickness variations between both base metals have not been taken into account.

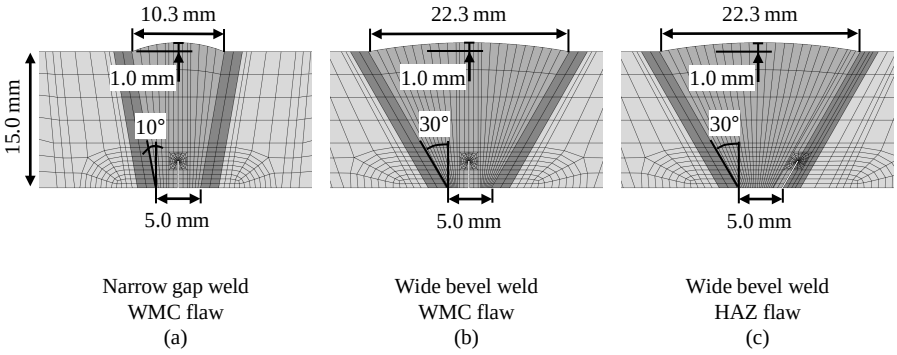

Figure 8.1: Different weld geometries and flaw locations have been considered.

8.2.1.2 Specimen geometry and simulated instrumentation

The parametric study was performed on 300 mm wide CWP specimens with fixed geometry and instrumentation according to the 'UGent guidelines for curved wide plate testing' [8.1] (figure 8.2). Note that the specimen has a prismatic length-to-width ratio $L/W = 3$. Strain analysis was based upon nodal displacements corresponding with remote strain LVDTs located at mid-width on the inner diameter surface, with end points as shown in the figure.

CTOD was extracted as a crack driving force measure in accordance with the 90 degree intercept method (figure 2.1). CTOD was preferred over J given the latter's contour convergence problems due to the incorporation of non-linear geometrical effects (section 4.2.2).

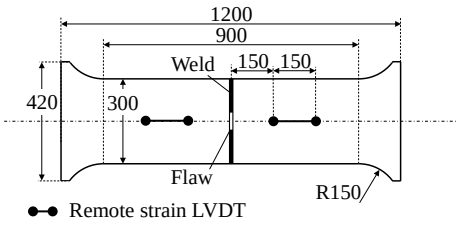

Figure 8.2: Assumed CWP specimen geometry and positions for remote strain measurement are in accordance with [8.1].

8.2.1.3 Material stress-strain properties

Homogeneous weldments were considered as defined in section 8.1. For convenience, base metal yield strength $R_{p0.2,base}$ was kept constant at 500 MPa. The

weld metal was modelled by a Ramberg-Osgood equation corresponding with a Y/T-ratio 0.90. Heat-affected zone stress-strain properties were assumed equal to those of the base metals. All materials were given a Young's modulus $E =$ 206,900 MPa.

The following material properties were varied to investigate effects of OM_{YS}, OM_{TS}, OM_{FS}, base metal uniform elongation e_m and base metal stress-strain curve shape:

- **Y/T-ratio of base metal**;
  This ratio was given realistic values 0.85, 0.90 and 0.93.
- **Ultimate tensile strength R_m of weld metal**;
  This characteristic was varied in order to set OM_{YS} and/or OM_{TS} to 0 %, 10 % or 20 %. Combining this variation with the abovementioned variation of base metal Y/T-ratio, wide ranges of strength overmatch levels were covered and are provided in table 8.1.

Table 8.1: Considered ranges for weld strength overmatch levels (in %).

Characteristic	OM_{YS}	OM_{TS}	OM_{FS}
Minimum value	-3.2	-5.6	-3.0
Maximum value	27.1	24.0	23.2

- **Constitutive model equation and uniform elongation e_m of the base metals**.
  The base metal was first modelled with the Ramberg-Osgood equation (Eq. (3.15)) which implies a uniform elongation e_m dependent on Y/T through Eq. (3.18). Next, the 'UGent' model was adopted to obtain larger uniform elongations, a difference of 0.02 with Ramberg-Osgood's e_m being aimed at. Overall, uniform elongations between 0.042 (4.2 %) and 0.093 (9.3 %) were covered. From comparison with figure 3.21(b), all considered Y/T-e_m couples are representative for contemporary line pipe steels. The difference between Ramberg-Osgood and 'UGent' curve shapes is illustrated for the base metal with $Y/T = 0.85$ in figure 8.3 (in this figure, the models' true stress-strain curves were converted into engineering stress and strain values up to the point of necking).

The resulting matrix of investigated material combinations is specified in table 8.2. This table represents thirty different combinations, each one characterized by its base metal stress-strain model – Ramberg-Osgood ('RO') or 'UGent' ('UG') – and the number in the first column. Each number represents a specific combination of weld strength overmatch levels. In the following, material combinations will be denoted as follows: RO-1, UG-1, RO-2, ..., UG-14, RO-15, UG-15.

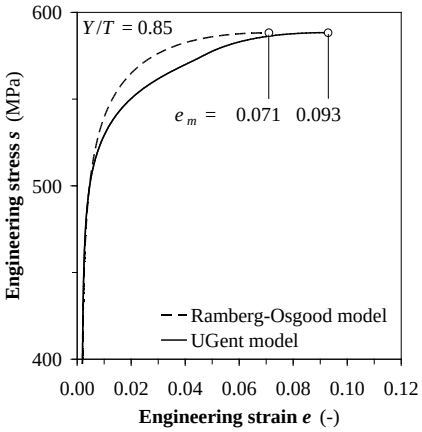

Figure 8.3: Example stress-strain relations used (base metal with $Y/T = 0.85$; up to the point of necking).

Table 8.2: Overview of simulated base metal constitutive characteristics and weld strength mismatch levels.

Number	Base metal characteristics			Weld strength overmatch characteristics		
	Y/T (-)	e_m (-)		OM_{YS} (%)	OM_{TS} (%)	OM_{FS} (%)
		RO ⋆	UG ⋆			
1	0.85	0.071	0.093	0.0	-5.6	-3.0
2				10.0	3.9	6.7
3				20.0	13.3	16.4
4				5.9	0.0	2.7
5				16.5	10.0	13.0
6				27.1	20.0	23.2
7	0.90	0.053	0.074	0.0	0.0	0.0
8				10.0	10.0	10.0
9				20.0	20.0	20.0
10	0.93	0.042	0.064	0.0	3.3	1.73
11				10.0	13.7	11.9
12				20.0	24.0	22.1
13				-3.2	0.0	-1.6
14				6.5	10.0	8.3
15				16.1	20.0	18.1

⋆ RO: Ramberg-Osgood model, UG: 'UGent' model

It can be noted that post necking stress-strain behaviour was modelled by means of a power law extrapolation ($\alpha' = 0$ in Eq. (7.15)).

8.2.1.4 Mesh design

Mesh density was chosen to obtain 'fast but fairly accurate' results (section 4.3.3). This resulted in finite element models consisting of 10,896 to 16,125 elements.

8.2.1.5 Incorporation of ductile tearing

Ductile tearing was assumed to merely increase the flaw depth a (i.e. flaw depth $2c$ was kept constant). To this purpose, the mapping approach has been implemented using the flow chart of figure 4.26(a). Four different fixed flaw depths were simulated: from the initial flaw depth $a_0 = 3.0$ mm up to 4.5 mm in discrete steps of 0.5 mm. The investigated flaw depth range of 1.5 mm sufficed to cover stable ductile tearing up to failure for all performed simulations.

Ductile tearing resistance was modelled on the basis of a power law CTOD-R curve equation similar to that used in ExxonMobil's flaw assessment procedure [8.2]:

$$\text{CTOD} = \delta \, (\Delta a)^{\eta} \tag{8.1}$$

For the inclined HAZ flaw from figure 8.1(c), Δa represented the projection of ductile tearing on the through-thickness direction. The following CTOD-R curve parameters were arbitrarily adopted from [8.3]: $\delta = 1.1$ and $\eta = 0.6$. The resulting resistance curve is depicted in figure 8.4. From comparison with a CTOD-R curve 'envelope' given in [8.3] (covering weld metals as well as heat-affected zones), the adopted curve may be interpreted as corresponding with a moderate ductile tearing resistance.

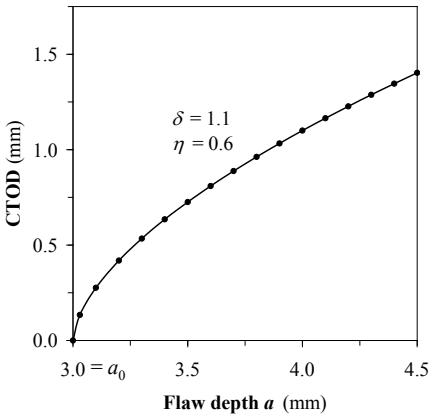

Figure 8.4: CTOD-R curve with $\delta = 1.1$, $\eta = 0.6$ and $a_0 = 3$ mm.

8.2.2 General observations

In total, 360 simulations have been performed for the parametric study (3 variants of weld geometry and flaw location × 30 material definitions × 4 different flaw depths, or: 90 configurations × 4 different flaw depths). All ninety simulated configurations failed due to one of both mechanisms (recall figure 2.2):

- local (i.e. flaw ligament) net section collapse, resulting in unstable crack extension by means of the tangency approach,
- global collapse, resulting in a stabilization of crack driving force.

Both observed failure mechanisms are briefly discussed below. Note that global net section collapse (i.e. collapse of the entire flawed weld resulting in a drop of tensile load) did not occur, since flaw ligament collapse was promoted by ductile tearing and typically occurred prior to maximum load.

First, figure 8.5 shows an example outcome of the ductile tearing and mapping approach for a configuration that failed in the flaw ligament. As tearing propagates (b), CTOD rapidly increases (a) until unstable crack extension eventually occurs (c) at a remote strain of 0.053. The final stable tear Δa is 1.15 mm (i.e. the flaw depth at the onset of unstable crack extension is 4.15 mm).

Second, for specimens that failed due to gross section collapse rather than unstable crack extension, a general observation was that remote strains tended to exceed the base metals' uniform elongation upon achievement of maximum load. Since uniform elongation represents maximum load in a small scale tensile test, this observation does not appear realistic and may be due to a high sensitivity of uniform elongation to small numerical inaccuracies in the finite element model (recall the discussion in section 7.3.1.1) or due to geometrical boundary effects of the CWP specimen. The actual reason has not been revealed within this research. However, regardless of the cause, it is suggested to conservatively introduce both base metals' uniform elongation in the following alternative definition of strain capacity e_{max}:

$$e_{max} = \frac{\min\left(e_{r,1}, e_{m,1}\right) + \min\left(e_{r,2}, e_{m,2}\right)}{2} \qquad \text{at peak load} \tag{8.2}$$

where the indices '1' and '2' represent both base metals. If remote strain at maximum load does not exceed uniform elongation, strain capacity simply reduces to the average remote strain at peak load:

$$e_{max} = \frac{e_{r,1} + e_{r,2}}{2} \qquad \text{at peak load} \tag{8.3}$$

The experimental results from chapter 6 have shown that, in such case, the proposed definition is in close agreement with the more common definition for strain capacity, being overall strain e_o at peak load (section 2.4.2).

(a)

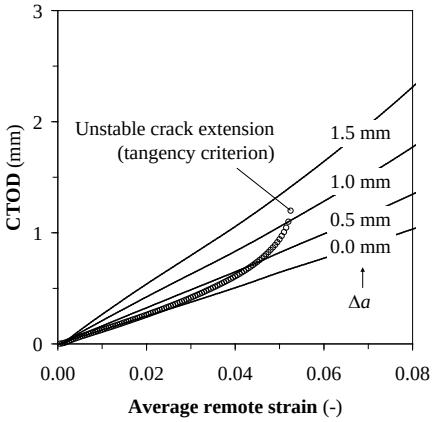

(b)

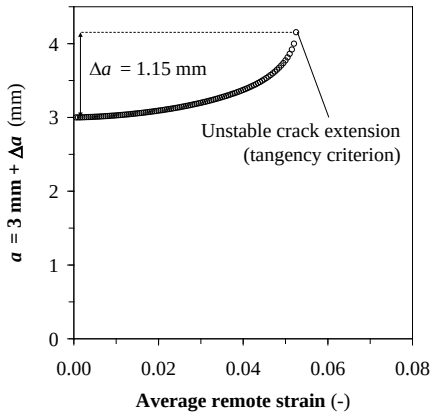

(c)

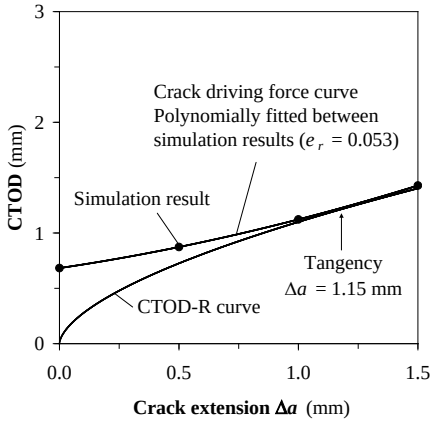

Figure 8.5: Illustrative result of the mapping approach for ductile tearing (narrow gap weld with WMC flaw, material combination 'UG-5').

Since the simulations of section 8.2.1 involve homogeneous weldments, $e_{r,1}$ is equal to $e_{r,2}$ (simply denoted e_r) and $e_{m,1}$ is equal to $e_{m,2}$ (simply denoted e_m). Eq. (8.2) thus reduces to $e_{max} = \min(e_r, e_m)$ at peak load. A relative strain capacity e_{max}/e_m is introduced. Its upper bound 1 marks gross section collapse.

8.2.3 Results and discussion

8.2.3.1 Influence of weld strength overmatch definition on strain capacity

This section focuses on detailed results of the narrow gap weld – WMC flaw combination (figure 8.1(a)). Results for the other weld-flaw configurations are in qualitative agreement and are compared in section 8.2.3.2.

First, figure 8.6(a) plots influences of different weld strength overmatch definitions on the simulated relative strain capacities e_{max}/e_m. The following is observed.

- As expected, a global trend of increasing relative strain capacity is observed as weld strength overmatch (whether it be OM_{YS}, OM_{TS} or OM_{FS}) increases.

- The quantitative effect of OM_{YS} on e_{max}/e_m is vague as figure 8.6(a1) is strongly scattered. The strongest relation with relative strain capacity (i.e. least amount of scatter) is observed for ultimate tensile strength overmatch OM_{TS} (figure 8.6(a2)).

- However, OM_{TS} and e_m are not the only parameters that characterize the influence of base metal stress-strain behaviour on e_{max} since figure 8.6(a2) is still scattered.

- Results from simulations with equal base metal Y/T and weld strength overmatch but different uniform elongation ('RO' simulations (triangles) versus 'UG' simulations (circles)) differ as for instance indicated with ellipses in figure 8.6(a3). Since both models represent different stress-strain curve *shapes*, e_{max}/e_m is hypothesized to be additionally influenced by the base metal's actual strain hardening behaviour. This effect is not quantified by any of the three investigated overmatch definitions, which are deduced from a limited number of strength characteristics.

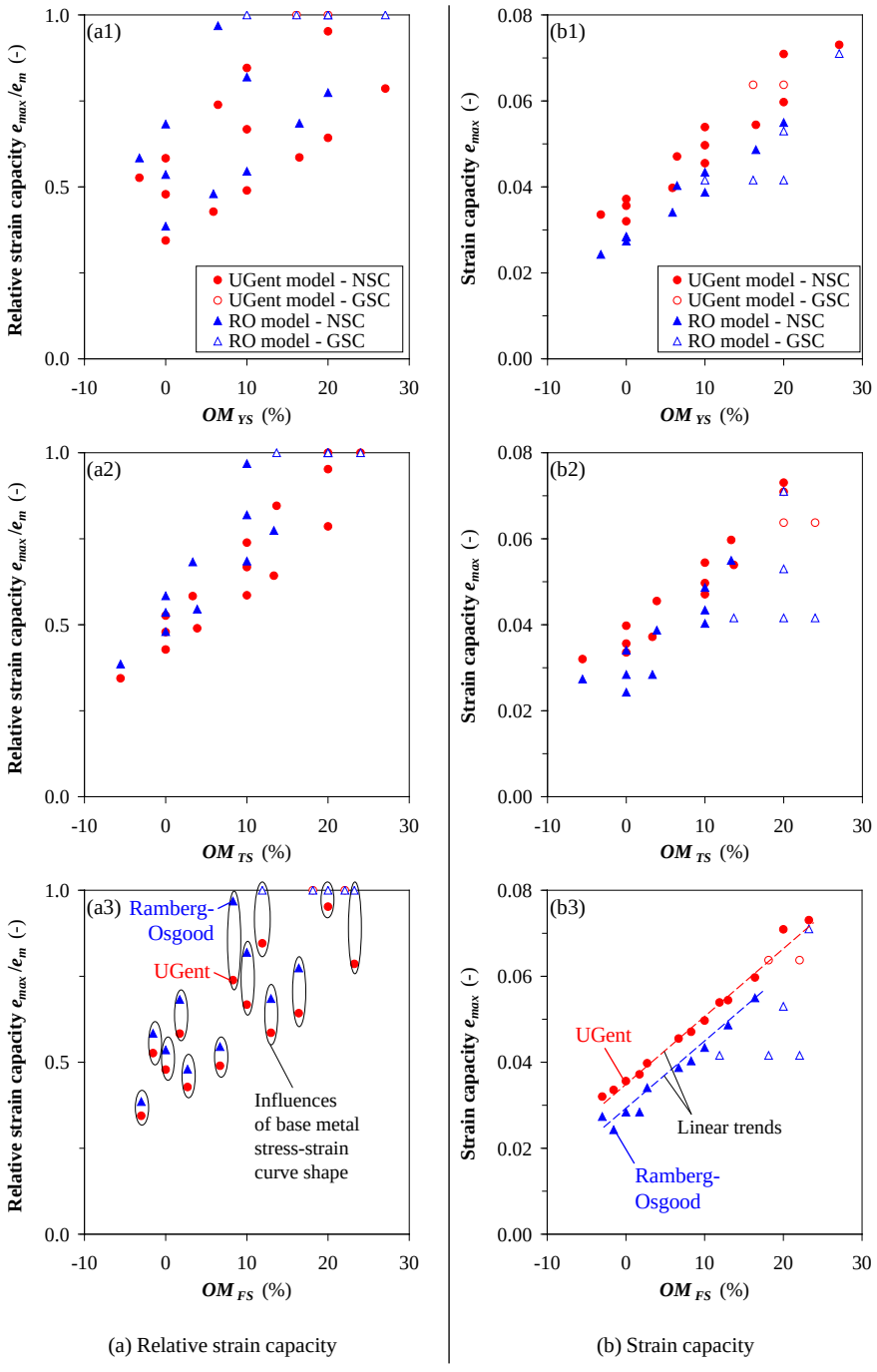

Figure 8.6: Influences of different weld strength overmatch definitions on (relative) strain capacity.

- The effect of stress-strain curve shape is considerable, as differences in relative strain capacity between base metals described by the Ramberg-Osgood and the 'UGent' model ('RO-i' versus 'UG-i', $i = 1 \ldots 15$) were observed up to as much as 0.23 (or 23 %) in figure 8.6(a3). Similar maximum differences were observed for the wide bevel weld (24 % for the WMC flaw, 21 % for the HAZ flaw).

It must be emphasized that, according to figure 8.6(a3), using the standardized Ramberg-Osgood model as a constitutive law for line pipe steel material (e.g. based upon Y/T through Eq. (3.28)) may produce highly unconservative estimations of relative strain capacity.

Since none of the weld strength overmatch definitions OM_{YS}, OM_{TS}, OM_{FS} appears to unambiguously predict relative strain capacity e_{max}/e_m, their ability to predict strain capacity e_{max} without normalization against uniform elongation has also been investigated (figure 8.6(b)). The following is revealed:

- Given the scatter in figures 8.6(b1) and (b2), OM_{YS} and OM_{TS} are again incapable of uniquely representing the influence of base metal stress-strain behaviour on e_{max}.

- In contrast, figure 8.6(b3) indicates that, as long as gross section collapse (open markers) is not reached, OM_{FS} is by far the most appropriate characteristic to quantify the effect of weld strength overmatch on strain capacity. Clear and approximately linear trends are observed. Given the definition of strain capacity (Eq. (8.2)), the linear trend is cut off at the base metal's uniform elongation upon attainment of gross section collapse.

- Similar to figure 8.6(a3), the actual near-to-linear relation between strain capacity and OM_{FS} depends on the stress-strain model adopted for the base metal (triangles versus circles), indicating an influence of uniform elongation and/or stress-strain curve shape. It can be noted that the linear trends for both the Ramberg-Osgood model and the 'UGent' model appear to be parallel in this study.

8.2.3.2 Influence of weld geometry and flaw location on strain capacity

The observations from figure 8.6 are confirmed for the other investigated weld geometry (wide bevel weld) containing either a WMC (figure 8.1(b)) or a HAZ (figure 8.1(c)) flaw. Indeed, clear trends are again observed for strain capacity as a function of weld flow stress overmatch OM_{FS}. Figure 8.7 plots these

trends for simulations where base metal was described by the 'UGent' stress-strain model (UG-1 to UG-15). For clarity, points of gross section collapse have been omitted. Figure 8.7 indicates that the actual relation between OM_{FS} and e_{max} is influenced by weld geometry and flaw location:

- A wider (and strength overmatching) weld yields higher strain capacities. This is in agreement with [8.4, 8.5] where welds with a wider bevel preparation were found to have an increased shielding effect against remotely applied strains.
- Focusing on the wide bevel weld, the strain capacity of HAZ flawed specimens is less sensitive to OM_{FS} than that of WMC flawed specimens, given the slightly lower slope of the former's linear trend. However, this effect is limited and it is unclear whether or not it is coincidental. Moreover, this comparison is rather theoretical since the tearing resistance behaviours of microstructures in the heat-affected zone and the weld are most likely different.

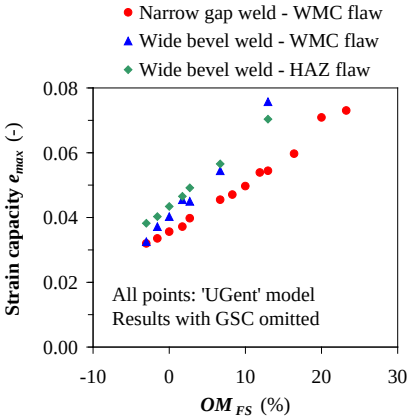

Figure 8.7: The relation between OM_{FS} and e_{max} is influenced by weld geometry and flaw location.

8.2.4 Conclusion and framework for strain capacity equation

From the strong trends observed in figures 8.6(b3) and 8.7, the following strain capacity equation structure can be deduced (figure 8.8):

$$e_{max} = \min\left(e_{max,0} + C \cdot OM_{FS}, e_m\right) \qquad \text{for } OM_{FS} > 0 \tag{8.4}$$

where $C(>0)$ is an overmatch sensitivity factor and $e_{max,0}$ is the strain capacity for an evenmatching ($OM_{FS} = 0$ %) girth weld with, apart from OM_{FS}, equal properties. Since the parametric study was mostly aimed at representing strength overmatching welds, cases with $OM_{FS} < 0$ are excluded from the validity range of Eq. (8.4). Besides, strength undermatching weldments are disadvised and rejected in most strain based flaw assessment equations (recall section 2.6.3).

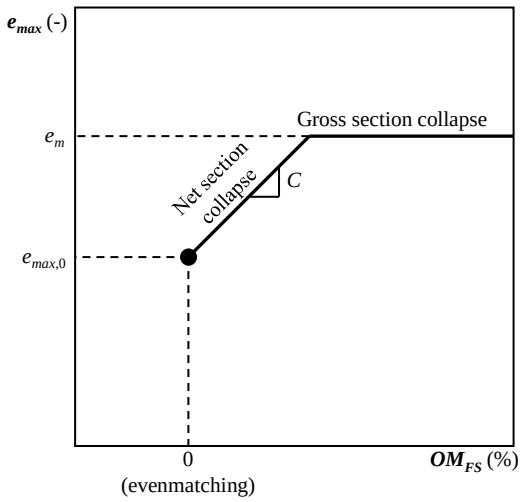

Figure 8.8: Graphical representation of the proposed framework for strain capacity estimation (Eq. (8.4)).

The structure of Eq. (8.4) is in agreement with the empirical UGent strain capacity equation of Denys et al. [8.6] (section 2.6.3.4), which also predicts a linear dependency of strain capacity on OM_{FS} (Eq. (2.23)). Hence, results obtained from a large experimental curved wide plate test database confirm the numerically predicted trends (and vice versa).

Eq. (8.4) merely provides a general framework since $e_{max,0}$ and C are influenced by many parameters (e.g. flaw dimensions and location, biaxiality due to internal pipe pressure, ductile tearing resistance, weld geometry, stress-strain curve shape), and their knowledge is required for the quantitative application of Eq. (8.4).

Two final notes deserve particular future research efforts.

- Since local (flaw ligament) collapse was the only net section collapse phe-

nomenon observed in the parametric study, it may be useful to evaluate the performance of Eq. (8.4) in presence of global (weld section) collapse. For instance, this failure mode might change the slope C or even introduce a third linear branch to the equation.

- In section 8.2.3.1 it was noted that the observed slopes of the linear ascending trends between e_{max} and OM_{FS} appear to be similar for Ramberg-Osgood and 'UGent' modelled base metals. This raises the hypothesis that C is not (strongly) affected by the constitutive behaviour of the base metal.

8.3 Influences of weld strength overmatch and base metal constitutive behaviour on crack driving force

It section 8.2 it was pointed out that weld strength overmatch and base metal constitutive properties are major influences to strain capacity. Strain capacity results from the equilibrium between crack driving force and ductile tearing. Since ductile tearing has been assumed constant in section 8.2 (figure 8.4), effects on strain capacity have to result from changes in crack driving force response. These changes are investigated in this section using results of the parametric study from section 8.2.

The discussion is separated into two sections, covering influences on crack driving force of

- weld strength overmatch (section 8.3.1), and,
- base metal constitutive behaviour (section 8.3.2).

8.3.1 Weld strength overmatch

Comparing simulations with different weld strength overmatch levels (and equal Y/T, e_m, weld geometry, flaw location) confirms the knowledge (section 2.3.2.1) that weld strength overmatch has a beneficial effect on crack driving force response. By means of illustration, figure 8.9 depicts CTOD responses from simulations with a WMC flawed wide bevel weld and material combinations UG-1 to UG-6 (base metal $Y/T = 0.85$, $e_m = 0.093$). Crack driving force is decreased as weld overmatch (e.g. expressed as OM_{FS}) increases. As a result, the connection with the highest weld strength overmatch ($OM_{FS} = 23.2$ %) shows gross section collapse which indicates that the weld is no longer the weakest structural link.

In figure 6.27, weld strength overmatch was shown to 'shield' the weld from the remote strain field. This is confirmed in figure 8.10, which depicts contour

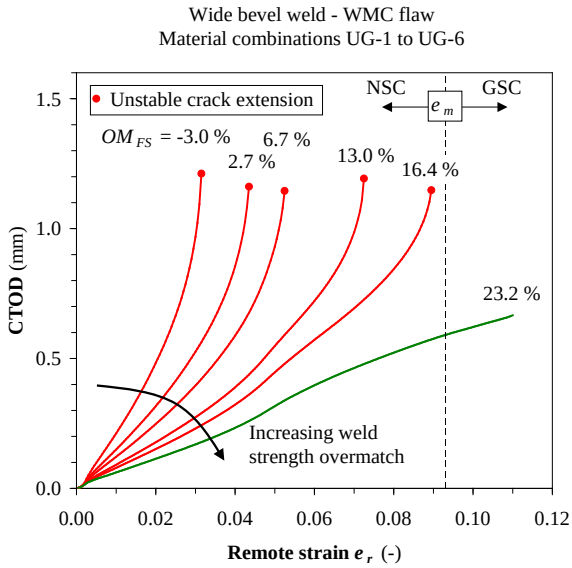

Figure 8.9: CTOD response decreases as weld strength overmatch (expressed here as OM_{FS}) increases.

plots of first principal strain ϵ_1 for increasing weld strength overmatch levels (selection of four configurations from figure 8.9). Note that all contour plots have been taken from simulations with an equal flaw depth ($a = 4.0$ mm). The remote strains corresponding with all four contour plots are similar. However, the strain fields near the flawed weld strongly differ. Whereas the notch in the weld with OM_{FS} = -3.0 % is clearly 'attacked' by shear lines of strain concentration, the weld with OM_{FS} = 23.2 % 'protects' the area in close vicinity to the notch.

8.3.2 Base metal constitutive behaviour

Influences of the base metal's Y/T-ratio and uniform elongation e_m have been evaluated on the arbitrary basis of the WMC flawed narrow gap weld.

First, starting from material combination RO-8 as a reference, a reduction of Y/T from 0.90 to 0.85 was investigated by:

- decreasing OM_{TS} and keeping OM_{YS} constant (RO-2),
- keeping OM_{TS} constant and increasing OM_{YS} (RO-5).

These decreases in base metal Y/T-ratio are linked with a corresponding increase in base metal uniform elongation (from 0.053 to 0.071).

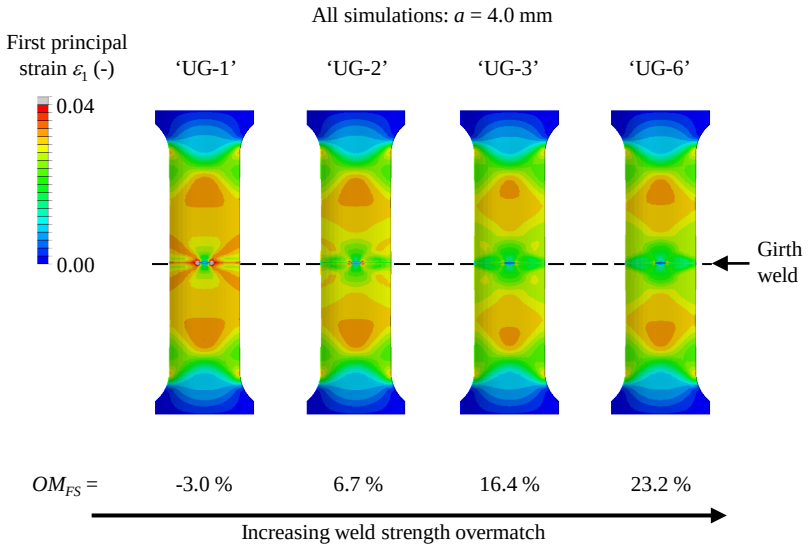

Figure 8.10: Weld strength overmatch shields the effect from applied strains.

Figure 8.11(a) shows that the effect of a change in Y/T can be either positive or negative, given the related effects on weld strength overmatch. In qualitative terms, the findings of section 8.3.1 are confirmed: an increase in weld strength overmatch (OM_{YS}, RO-5) corresponds with a lower CTOD response and vice versa (decrease in OM_{TS}, RO-2).

Second, to eliminate the possible effect of the change in e_m, figure 8.11(b) shows a similar comparison between UG-8 (instead of RO-8), RO-2 and RO-5. The corresponding base metals have highly similar uniform elongations: 0.074 (UG-8) and 0.071 (RO-2 and RO-5). Here too, it is challenging to identify a 'unique' influence of Y/T. Note that figure 8.11(b) appears to show a clear overall connection between CTOD responses of simulations with equal OM_{TS} and e_m. Referring back to the scatter in figure 8.6(a2), however, this observation is considered coincidential rather than systematic.

Third, the effect of uniform elongation e_m is illustrated in figure 8.12, which depicts two CTOD responses obtained from HAZ flawed wide bevel welds with equal overmatch levels and Y/T-values. Both responses agree up to 0.01 remote strain. Beyond this strain range, however, a clear divergence is observed. At the point where the simulation with Ramberg-Osgood modelled base metals (RO-13) fails ($e_r = 0.030$, CTOD = 1.1 mm):

- its remote strain is 0.009 (or 30 % of 0.03) lower than that of simulation UG-13 at an equal CTOD level,

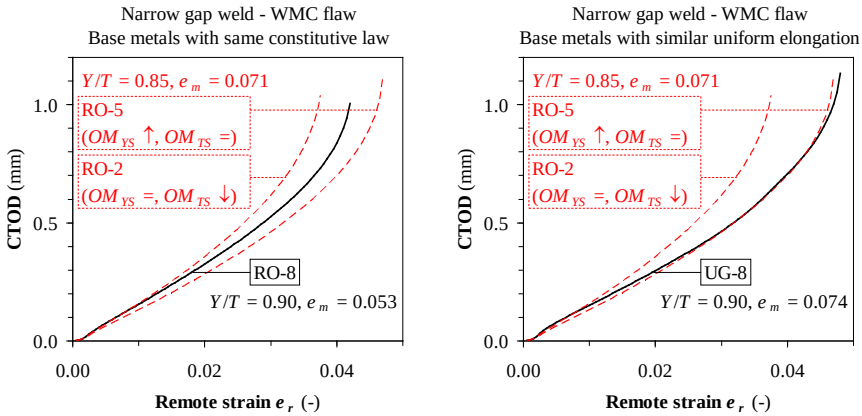

Figure 8.11: Influences of changes in base metal Y/T on CTOD response are related to other factors such as weld strength overmatch and uniform elongation.

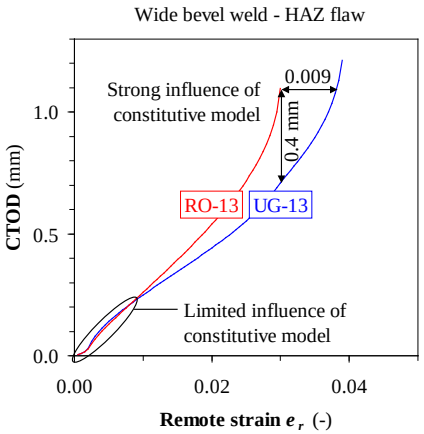

Figure 8.12: CTOD response is significantly influenced by e_m (or, equivalently, by the constitutive model assumed).

- its CTOD is 0.40 mm (or 36 % of 1.1 mm) higher than that of simulation UG-13 at an equal remote strain level.

Figures 8.11 and 8.12 emphasize the importance of properly representing the base metal's constitutive behaviour for strain based flaw assessment purposes. The Ramberg-Osgood model is limited in this respect, given

- *its dependency between Y/T and e_m (figure 3.21(b)), and,*
- *its description of strain hardening behaviour on the mere basis of one fixed strain hardening exponent n.*

Hence, figures 8.11 and 8.12 indicate that the potential improvement in assessment accuracy can be drastically increased by using the 'UGent' stress-strain model.

8.4 Influence of base metal heterogeneity on strain capacity

Section 8.2 has indicated that effects of weld strength mismatch properties on strain capacity can be characterized in terms of Eq. (8.4) for flawed girth welds connecting homogeneous base metals. However, the experimental results of two medium wide plate tests (MWP-C-1 and MWP-C-2, section 6.6) have indicated that effects of moderate base metal heterogeneity on the distribution of strains can be substantial and should be taken into account for an accurate assessment. It is unclear at this point how to incorporate these effects since Eq. (8.4) assumes both girth welded pipes to have

- an identical uniform elongation;
- an identical flow stress and, hence, a unique OM_{FS}-value which simultaneously describes weld strength overmatch with respect to both base metals.

Given the possible extent of its observed effects, the quantification of base metal heterogeneity effects is strongly advised for future research. This section provides a theoretical basis for such inquiry.

First, section 8.4.1 introduces assumptions that are necessary for the theoretical study. Then, effects of heterogeneity are investigated relative to a reference girth weld joint which has homogeneous base metal properties. Starting from this reference homogeneous weldment, heterogeneous joints are obtained by varying one of the base metals' strength properties (i.e. the other base metal has fixed properties). The discussion is separated into two possible cases: the reference joint fails in the weld (section 8.4.2) or in one of the base metals (section 8.4.3). Section 8.4.4 summarizes and concludes.

8.4.1 Assumptions

Four assumptions are necessary for the following and are summarized below.

Assumption 1:
The investigated problem is uniaxial

This assumption implies that the influence of transverse normal and shear stresses (biaxiality) is not taken into account. As a consequence, the structural problem can be investigated on the basis of uniaxial stress-strain properties as obtained from tensile tests. Effects of a biaxial stress state due to internal pressure (pressurized FSP tests only) or compatibility between heterogeneous materials under plastic deformation (both CWP and pressurized FSP tests) should deserve due consideration in a more advanced model.

Assumption 2:
Failure is governed by the weakest structural link in terms of load bearing capacity

Although investigated in a strain based context, the structural problem of a girth weldment under tension is governed by its weakest link in terms of load bearing capacity. This statement directly follows from the transfer of tensile load P through all cross sections of the entire specimen according to the principle of action-reaction (Newton's third law, figure 8.13).

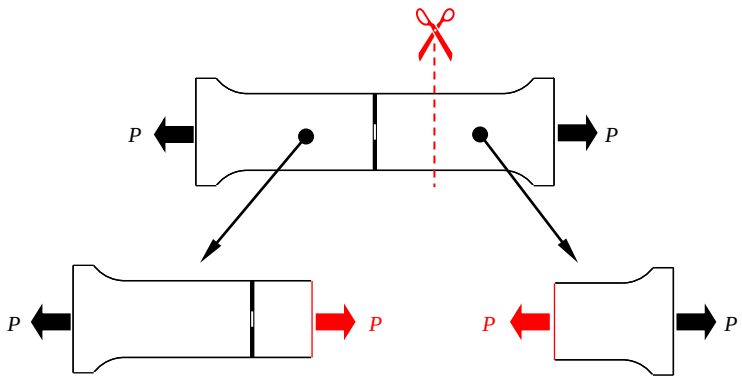

Figure 8.13: The principle of action-reaction implies that every cross section (including that which contains a weld flaw or notch) faces the applied tensile load P.

Three load bearing capacities will be considered in the model: that of the weld ($P_{max,WM}$) and those of both base metals ($P_{max,BM,1}$ and $P_{max,BM,2}$). Hence, possible HAZ softening is neglected. The load bearing capacity of the weld

is assumed constant throughout the increase of applied strain. This implies that ductile tearing is not taken into account and failure corresponds with global (weld section) collapse or gross section collapse. From the weakest link principle, the load bearing capacity P_{max} of the entire weldment follows from:

$$P_{max} = \min\left(P_{max,WM}, P_{max,BM1}, P_{max,BM2}\right) \tag{8.5}$$

Failure in the weld is characterized by $P_{max,WM} < P_{max,BM,1}$ and $P_{max,WM} < P_{max,BM,2}$, whereas failure in one of the base metals implies that its load bearing capacity is smaller than that of the weld and of the other base metal.

Assumption 3:
Base metal heterogeneity is uniform over the entire stress-strain curve

This assumption narrows the investigation to one specific case of base metal heterogeneity, where the difference in engineering stress is constant over the full strain hardening range and symbolized by Δs (figure 8.14). Note that engineering quantities are more relevant for the investigated problem since engineering stress is linearly proportional to the applied load, which relates to the load bearing capacity discussed in assumption 2.

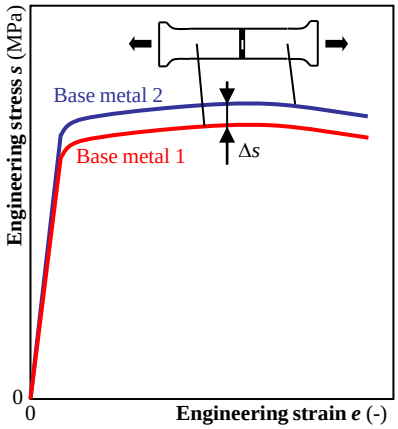

Figure 8.14: The assumed base metal heterogeneity is uniquely characterized by a constant difference in strength Δs between both base metals.

The following types of heterogeneity are particularly excluded from the following discussion:

- one base metal is initially weaker, but gradually exceeds the other's strength (intersecting stress-strain curves);

- both base metals have equal strength characteristics (yield strength, ultimate tensile strength), but a different stress-strain curve shape and/or uniform elongation.

Since the uniform elongations of both base metals are assumed equal, both are denoted as e_m. It should be noted that the assumption of equal uniform elongations may not reflect actual trends in stress-strain properties of line pipe steels, since figure 3.21(a) has indicated that uniform elongation tends to decrease as $R_{p0.2}$ increases.

Assumption 4:
Remote strain cannot exceed the uniform elongation of its corresponding base metal

In section 8.2.2, it was mentioned that simulated remote strains at maximum load exceeded the base metal's uniform elongation e_m in case of gross section collapse. To address this observation an alternative definition of strain capacity (Eq. (8.2)) was proposed, which by nature cannot exceed e_m. Here, it is assumed that a remote strain equal to e_m implies a collapse of the corresponding base metal. Hence, Eq. (8.2) reduces to Eq. (8.3).

8.4.2 First thought experiment: reference (homogeneous) weldment fails in the weld

In this and the following section, it is arbitrarily assumed that base metal '1' and weld metal have constant properties. Base metal '2' is varied and characterized on the basis of Δs (figure 8.14), a positive value corresponding with base metal '2' being stronger than base metal '1' and vice versa. As a consequence of these choices and assumption 1, the load bearing capacities of weld metal ($P_{max,WM}$) and base metal '1' ($P_{max,BM,1}$) are constant. This is obviously not the case for base metal '2', whose load bearing capacity linearly varies with Δs.

This section focuses on cases where the homogeneous reference weldment ($\Delta s = 0$) fails in the flawed weld section. A graphical summary is provided in figure 8.15.

Given that failure occurs in the weld for the homogeneous connection, load bearing capacities are related as follows for $\Delta s = 0$:

$$P_{max} = P_{max,WM} < P_{max,BM,1} = P_{max,BM,2} \qquad (\Delta s = 0) \qquad (8.6)$$

First, if the strength of base metal '2' is increased ($\Delta s > 0$), the weld remains the weakest link since $P_{max,BM,2}$ increases and hence:

$$P_{max} = P_{max,WM} < P_{max,BM,1} < P_{max,BM,2} \qquad (\Delta s > 0) \qquad (8.7)$$

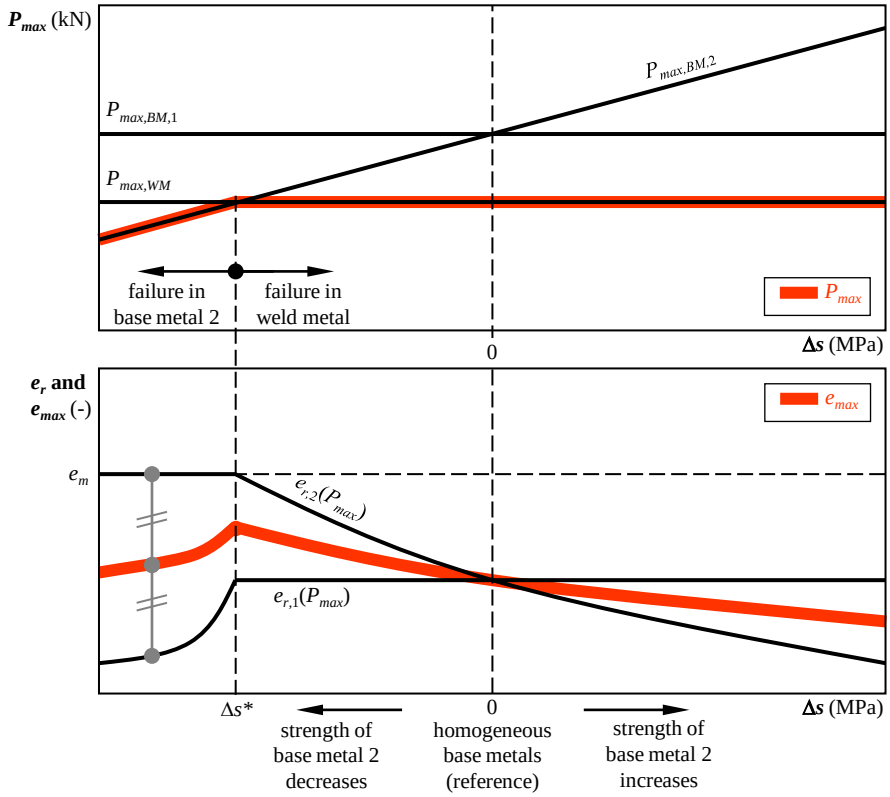

Figure 8.15: Evolution of load bearing capacity and strain capacity as a function of heterogeneity, the reference (homogeneous) case corresponding with failure in the weld.

As a consequence, P_{max} remains constant. The corresponding strain capacity e_{max}, however, decreases since the remote strain in base metal '2' upon maximum load $e_{r,2}(P_{max})$ is reduced due to its increasing strength. The extent of this decrease as a function of Δs depends on the stress-strain curve shape of base metal '2' (recall figure 2.7, which shows a similar dependency on stress-strain curve shape).

Second, when the strength of base metal '2' is decreased relative to the homogeneous connection ($\Delta s < 0$), the discussion can be partially reversed: strain capacity initially increases as the remote strain upon failure $e_{r,2}(P_{max})$ is increased. At a certain point $\Delta s^{\star}$, however, base metal '2' becomes the weakest link rather than the weld. In this case, load bearing capacities become related

as follows:

$$P_{max} = P_{max,BM,2} < P_{max,WM} < P_{max,BM,1} \qquad (\Delta s < \Delta s^{\star}) \qquad (8.8)$$

At this point, the failure mode has switched to gross section collapse and the uniform elongation e_m is achieved in base metal '2'. If the strength of base metal '2' further drops, the load bearing capacity of the structure P_{max} reduces and hereby causes a decrease of the remote strain obtained in base metal '1'. As a consequence, the strain capacity of the structure reduces. This reduction is non-linear, since the 'shape' of the $e_{r,1}$-Δs curve for $\Delta s < \Delta s^{\star}$ is related to the stress-strain curve shape of the strongest base metal 1 (figure 8.16).

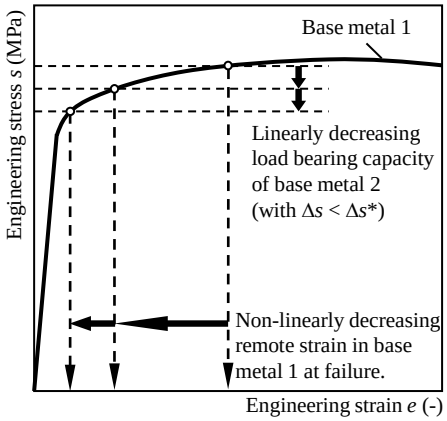

Figure 8.16: A linear reduction in load bearing capacity introduces non-linear effects for remote strain at failure and, hence, strain capacity.

8.4.3 Second thought experiment: reference (homogeneous) weldment fails in one of the base metals

This section focuses on cases where the homogeneous reference weldment ($\Delta s = 0$) fails in one of the base metals [1]. A graphical summary is provided in figure 8.17.

Given that failure does not occur in the weld for the homogeneous connection, the following relations apply for $\Delta s = 0$:

$$P_{max} = P_{max,BM,2} = P_{max,BM,1} < P_{max,WM} \qquad (\Delta s = 0) \qquad (8.9)$$

Since $P_{max,BM,1}$ and $P_{max,WM}$ are constants, this equation implies that failure will never occur in the weld if Δs is varied. Indeed, the relation $P_{max,BM,1} <$

[1] Theoretically, the weldment with $\Delta s = 0$ can fail in *both* base metals simultaneously. In reality, however, necking is evidently confined to one base metal.

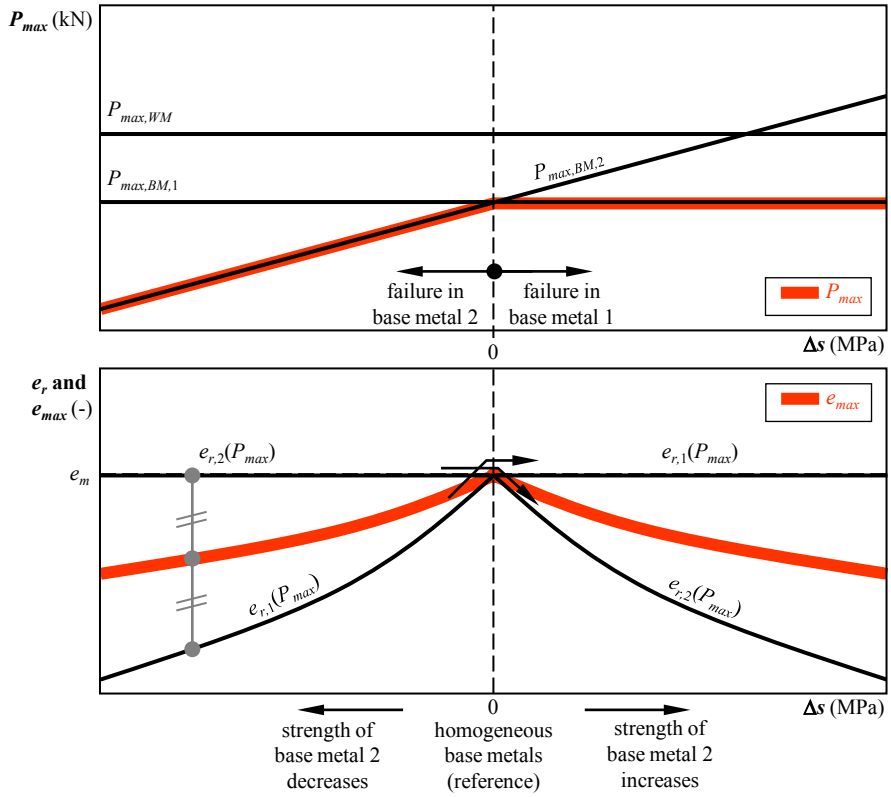

Figure 8.17: Evolution of load bearing capacity and strain capacity as a function of heterogeneity, the reference (homogeneous) case corresponding with failure in one of the base metals.

$P_{max,WM}$ remains unaltered. Δs rather has an influence on which base metal fails, as it determines the strength difference between both.

The strain capacity e_{max} of a homogeneous weldment that fails in the base metal is simply equal to e_m. The introduction of base metal heterogeneity (whether it be $\Delta s < 0$ or $\Delta s > 0$) implies that the strongest base metal will not achieve its uniform elongation upon peak load. As a consequence, base metal heterogeneity is always detrimental to strain capacity for this case.

8.4.4 What is 'the' worst case base metal combination?

Table 8.3 summarizes figures 8.15 and 8.17 and shows that, under the assumptions made, the effect of base metal heterogeneity on strain capacity can be either positive or negative depending on the situation investigated.

Table 8.3: Hypothesized effects of base metal heterogeneity on strain capacity.

Failure location (homogeneous base metals)	Figure	Effect on e_{max} for	
		$\Delta s > 0$ and increasing	$\Delta s < 0$ and decreasing
Weld metal	8.15	$\searrow$	$\nearrow, \searrow$ †
Base metal	8.17	$\searrow$	$\searrow$

† depending on the position of Δs with respect to $\Delta s^{\star}$

At first sight, the ambiguous effects in table 8.3 do not allow for a straightforward answer to the question which is the worst possible combination of base metals within their production scatter range. Nevertheless, a closer investigation reveals the following statements.

- Whether failure is governed by the weld or by one of the base metals, strain capacity reduces as the strength properties of the strongest base metal are increased ($\Delta s > 0$ and increasing). This implies that a worst case material combination *must* include a base metal at the *upper* end of the strength range.
- Given that one of the base metals must have strength properties at the upper end of their statistical distribution, the following can be noted for the *other* base metal:
  - If failure occurs in the base metal, the worst case corresponds with the highest possible degree of base metal heterogeneity according to figure 8.17. This case corresponds with the softer base metal being located at the *lower* end of the strength range.
  - If failure occurs in the weld, however, the worst case corresponds with fully homogeneous base metals ($\Delta s = 0$) according to figure 8.15. Indeed, as long as $\Delta s > \Delta s^{\star}$ (i.e. the weld is the weakest link), decreasing the softest base metal's strength ($\Delta s < 0$ and decreasing) has a positive effect on strain capacity.

As a conclusion, there are at least two potential worst case material combinations (figure 8.18) which should be separately considered. The first (figure 8.18(a)) causes highly different remote strains in both base metals and thereby reduces the ability of strain capacity to achieve the uniform elongation. Note that this phenomenon has been observed in tests MWP-C-1 and MWP-C-2 (see table 6.6). The second combination (figure 8.18(b)) yields the lowest possible weld metal strength overmatch levels with respect to both base metals and consequently reduces strain capacity in cases of weld failure.

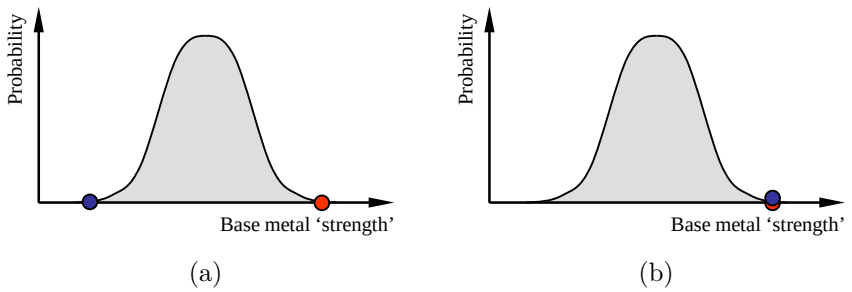

Figure 8.18: There are at least two potential worst case base metal combinations with respect to strain capacity.

Figure 8.18(a) is more likely to be a worst case base metal combination if weld strength overmatch is increased, since this promotes gross section collapse. On the other hand, the probability of figure 8.18(b) being a worst case combination increases if weld strength overmatch is decreased (which promotes net section collapse).

It must be noted that the definition of base metal 'strength' in figure 8.18 is vague. Since the thought experiments assumed that both base metals strain harden in an equal manner (but at different stress levels, related by Δs), it is not yet clear how to extrapolate the findings to more realistic situations where base metal strain hardening behaviours and uniform elongations differ. Further, since the considerations made are based upon a set of simplifying assumptions, an extensive validation is required and advised for future research.

8.5 Summary and conclusions

This chapter has addressed effects of weld strength overmatch, base metal constitutive behaviour and base metal heterogeneity on the strain capacity of a flawed girth weldment. Whereas the first two aspects have been investigated by means of a parametric finite element study, the third aspect was discussed on the basis of theoretical thought experiments.

First, the parametric finite element study revealed that commonly used weld strength overmatch definitions (based upon yield strength or ultimate tensile strength values) explain a trend of increasing strain capacity as overmatch increases. However, this trend is scattered for both definitions, which thus have a limited capability of describing overmatch effects. An alternative definition based upon flow stresses (OM_{FS}) is far more closely related to strain capacity. An approximate linear trend is observed, which is cut off to a strain capacity corresponding with the base metal uniform elongation. Apart from weld

strength overmatch effects the parametric study has indicated effects of weld geometry and flaw location, which are not yet quantified.

The observations led to the development of an analytical framework for strain capacity based upon weld flow stress overmatch (Eq. (8.4)). This framework is in agreement with the strain capacity equation of Denys et al. [8.6] which also adopts OM_{FS} as a weld strength overmatch measure. The quantification of the parameters that define Eq. (8.4) is advised for future research.

Second, the base metals' uniform elongation and yield-to-tensile ratio (and, as a consequence, stress-strain curve shape) were found to influence strain capacity.

Significant errors can be introduced if base metals are modelled with the Ramberg-Osgood model, which fails to separate the effects of Y/T from those of e_m. The 'UGent' model does not show this limitation and is therefore advised for application in numerical strain based flaw assessments.

Third, starting from simplifying assumptions, the analytical thought experiments related to base metal heterogeneity have proven that there are at least two potential worst case base metal combinations with respect to strain capacity. One intuitively logical combination involves homogeneous base metals at the upper end of the strength distribution (figure 8.18(b)). Another combination involves base metals with a high degree of heterogeneity (figure 8.18(a)), which strongly reduces the development of longitudinal strain in the strongest base metal. This effect has also been observed in the experiments MWP-C-1 and MWP-C-2, reported in chapter 6.

It can be concluded that some far from obvious but significant effects of stress-strain properties (both base metal and weld metal) are not (fully) accounted for in current analytical flaw assessment procedures.

Bibliography

[8.1] R. Denys and A. Lefevre. UGent guidelines for curved wide plate testing. In R. Denys, editor, *Proceedings of the 5th International Conference on Pipeline Technology*, Ostend, Belgium, 2009.

[8.2] S. Kibey, X. Wang, K. Minnaar, M.L. Macia, D.P. Fairchild, W.C. Kan, S.J. Ford, and B. Newbury. Tensile strain capacity equations for strain-based design of welded pipelines. In *Proceedings of the 8th International Pipeline Conference (IPC)*, Calgary, Alberta, Canada, 2010. IPC2010-31661.

[8.3] D.P. Fairchild, M.L. Macia, S. Kibey, X. Wang, V.R. Krishnan, F. Bardi, H. Tang, and W. Cheng. A multi-tiered procedure for engineering critical assessment of strain-based pipelines. In *Proceedings of the 21st International Offshore and Polar Engineering Conference (ISOPE)*, pages 698–705, Maui, Hawaii, USA, 2011.

[8.4] R. Denys. Weld metal strength mismatch: past, present and future. In *Proceedings of the International Symposium to Celebrate Prof. Masao Toyoda's Retirement from Osaka University*, pages 115–148, Osaka, Japan, 2008.

[8.5] R. Denys, S. Hertelé, and M. Verstraete. Strain capacity of weak and strong girth welds in axially loaded pipelines. In *Proceedings of the International Pipeline Technology Conference (IPTC)*, pages 116–124, Beijing, China, 2010.

[8.6] R. Denys, S. Hertelé, M. Verstraete, and W. De Waele. Strain capacity prediction for strain-based pipeline designs. In *Proceedings of the Internal Workshop on Welding of High Strength Pipeline Steels*, Araxá, Brazil, 2011. CBMM.

Chapter 9

Conclusions and recommendations for future research

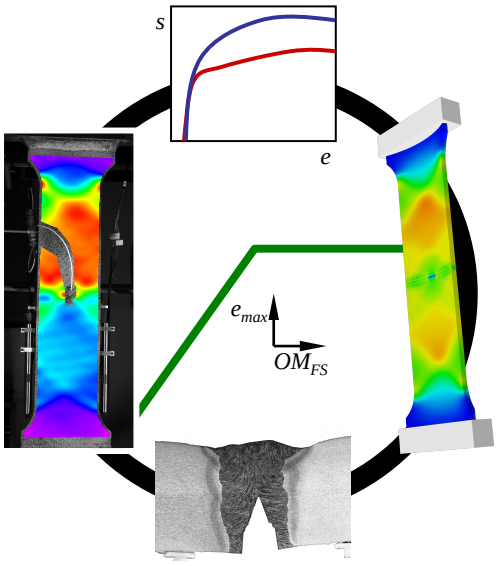

When it all comes together ...

9.1 General conclusions

9.1.1 Summary

This dissertation has elaborated on the development of experimental, numerical and analytical tools for the investigation of tensile strain capacity of surface flawed pipeline girth welds. Particular attention has been given to effects of base metal stress-strain properties and weld strength mismatch in the presence of sufficient toughness to avoid brittle failure.

Current analytical strain based flaw assessment procedures show limitations with respect to conservativeness, sensitivity to inputs and/or the coverage of key parameters. As a consequence, experimental and numerical studies remain essential for strain based engineering critical assessments of girth weld flaws. In the performed research, effort has been devoted to the development and optimization of tools for both approaches.

The curved wide plate (CWP) tension test has been used as a basis for all investigations. Compared with full scale (pressurized) pipe testing, it requires a pressure correction factor for strain capacity. On the other hand, the CWP test allows for the surrounding small scale characterization of material properties. The CWP test has first been replicated in a finite element model and in a medium scale test specimen variant with advanced instrumentation and analysis possibilities. The test results validated the finite element model, which was finally used to investigate effects of stress-strain properties on the strain capacity of a flawed girth weldment. In this respect, a 'UGent' stress-strain model was developed. This model proved essential for the advanced parametric description of contemporary line pipe steels.

The obtained numerical and experimental results have revealed

- *that a proper flaw assessment requires accurate input of base metal stress-strain properties (including yield-to-tensile ratio and uniform elongation);*
- *that weld flow stress overmatch is a key beneficial factor for strain capacity;*
- *how to best define this overmatch in terms of pipe and weld strength characteristics;*
- *that base metal heterogeneity can have a significant impact on strain capacity, which is not yet quantified.*

The following sections 9.1.2 and 9.1.3 provide systematic answers to the research questions posed at the end of chapter 1.

9.1.2 Methodology used in this work

9.1.2.1 Numerical developments

A parametric finite element model has been developed with the aim to describe curved wide plate and full scale (pressurized) pipe (FSP) tension tests. The Python script that constructs the models allows to geometrically reproduce actual test specimens with a high degree of representativeness and with a minimum of effort to the user. Ductile tearing is included. As a result, it is possible to perform level three assessments according to ExxonMobil's flaw assessment procedure [9.1].

Sound calculations of load, deformations and crack driving force under remote plastic straining require an incorporation of non-linear geometrical effects and an incremental plasticity formulation. In such circumstances, the quantification of crack driving force by means of crack tip opening displacement (CTOD) is preferred over J as the latter has a problematic contour integral convergence. CTOD is obtained by applying the 90 degree intercept method.

The Python scripting technique allows to easily choose between different specimen types (CWP, FSP) and different flaw locations (weld metal center or heat-affected zone), and to modify geometrical aspects related to pipe, weld and flaw by application of nodal coordinate transformations on the meshed structure. Moreover, different predefined mesh density settings can be chosen for, depending on the desired trade-off between numerical accuracy and calculation time.

A justified mapping algorithm using simulations with fixed but different flaw dimensions provides a pragmatic solution to the incorporation of stable ductile tearing. Moreover, it allows for a prediction of unstable crack extension by application of the tangency criterion.

9.1.2.2 Experimental developments

A medium scale wide plate (MWP) test specimen and procedure have been developed, with emphasis on specimen geometry and the implementation and optimization of two advanced measurement techniques. Digital image correlation (DIC) provides an optical measurement of full field surface strain distributions, and unloading-reloading sequences allow for an estimation of ductile tearing through unloading compliance (UC) analysis. Both techniques facilitate a proper interpretation of test results, particularly their evolution towards failure.

Application of digital image correlation requires a random speckle pattern applied on the specimen surface. An optimized spray painting technique allows to obtain a sufficient density of speckles that approximate the desired size, thereby promoting the accuracy of the DIC strain measurement. With the optimized speckling technique, the standard deviation of strain measurement scatter could be limited to 10^{-4} (or 0.01 %) strain.

Proper unloading compliance measurements imply highly accurate clip gauge measurements of CMOD (crack mouth opening displacement). A clip gauge accuracy of ± 1 μm allowed for crack extension measurements within a scatter band of ± 0.5 mm.

The advanced measurements were of vital importance to the validation of the finite element model, which was then used to:

- confirm the ability of the MWP specimen (with a prismatic length-to-width ratio 3.33) to obtain fields of highly uniform longitudinal strain;
- derive suited positions for 'conventional' remote strain sensors (LVDTs, strain gauges).

The resulting specimen and instrumentation design is summarized in figure 5.16.

9.1.2.3 Analytical developments

Two analytical approaches have been developed to investigate influences of base metal stress-strain characteristics on the strain capacity of a curved wide plate specimen: the 'UGent' stress-strain model and a framework for strain capacity prediction based on weld strength mismatch.

First, a new 'UGent' stress-strain model (figure 3.23) was developed with a focus on the proper representation of high strength line pipe steels. This 'UGent' constitutive law allows for the independent variation of yield-to-tensile ratio and uniform elongation by proper choices of its parameters, and is therefore particularly suited for parametric finite element studies. In this respect, different procedures have been developed for the estimation of suited 'UGent' model parameters. Among these, an analytical procedure requires knowledge of the 1.0 % proof stress, whose acquisition from tensile test results is advised.

Second, a parametric finite element study has been executed to develop an analytical framework for the influence of weld strength mismatch on strain capacity. This study adopted the 'UGent' stress-strain model to additionally investigate effects of base metal stress-strain curve – and, in particular, yield-to-tensile ratio and uniform elongation.

9.1.2.4 Theoretical considerations

Theoretical thought experiments have been performed to create awareness of possible influences of base metal heterogeneity on strain capacity. The considerations were based upon a set of simplifying assumptions which require future validation.

9.1.3 Main results

9.1.3.1 Characterization and effects of stress-strain behaviour of line pipe steels

Longitudinal stress-strain properties of line pipe steels should be obtained for a strain based girth weld flaw assessment. Full-thickness strip specimens provide average properties of the entire pipe wall and are therefore advised over smaller round bar specimens. Tensile test specimens should be sampled from as-coated steel (or steel which has undergone a thermal cycle that simulates the pipe coating process).

Ample tensile testing is required to characterize pipe steel heterogeneity. The resulting distribution of stress-strain properties allows to identify potential worst case pipe combinations with respect to strain capacity:

- both girth welded pipes are in the upper end of the strength range;
- one pipe is at the upper end of the strength range, the other at the lower end;
- the line pipe steel has a low uniform elongation (often combined with a high yield-to-tensile ratio).

Note that this list is not necessarily complete and may expand under additional considerations of e.g. HAZ toughness and susceptibility to HAZ softening.

The 'UGent' stress-strain model provides significantly improved descriptions of line pipe steels with a yield-to-tensile ratio above 0.80, compared with the widely applied Ramberg-Osgood model. A particular advantage of the 'UGent' model is its ability to independently vary uniform elongation, yield-to-tensile ratio and stress-strain curve shape, which is required to represent a wide range of line pipe steels.

9.1.3.2 Weld strength mismatch effects on strain capacity

A finite element based parametric study revealed that weld strength overmatch OM_{FS} defined on the basis of flow stresses (averages of yield strength and ultimate tensile strength, Eq. (2.18)) is stronger related to strain capacity than more common strength overmatch definitions based on either yield or ultimate tensile strength. The actual relation between OM_{FS} and strain capacity is approximately linear up to the point where collapse in the pipe body governs failure. This observation is in full agreement with the empirical strain capacity equation of Denys et al. [9.2] based on a database of several hundreds of curved wide plate test results.

The linear relation prior to gross section collapse is influenced by the base metal's uniform elongation (or, related to this, stress-strain curve shape), pipe and weld geometry, flaw size and position. Other expected effects (i.e. HAZ softening, misalignment, ...) have not been explicitly investigated in the performed research.

An analytical framework for strain capacity prediction has been deduced from the abovementioned observations (figure 8.8).

9.1.4 Combined numerical-experimental framework for strain based design and flaw assessment

Combining literature with obtained results, a framework has been developed for the strain based design of pipeline girth welds and the strain based assessment of detected flaws. Both aspects are separately covered in the following sections. At every step of the framework, it is attempted to obtain correspondence with earlier proposed frameworks where adequate. It must be emphasized that the framework merely considers tensile loaded (pressurized) pipelines and materials with sufficient toughness to avoid brittle fracture.

9.1.4.1 Strain based design

Figure 9.1 depicts the proposed framework. The following steps are followed.

1. Operational requirements (e.g. throughput of fossil fuel) and the design with respect to internal pressure (Eq. (1.2)) impose unavoidable restrictions to the pipeline design. Under these restrictions, a preliminary design of pipe steel grade, pipe wall thickness, diameter, and internal pressure follows from economical considerations (figure 1.15). Important at this stage is a bidirectional transparency with potential pipe suppliers to avoid the introduction of unrealistic demands with respect to line pipe

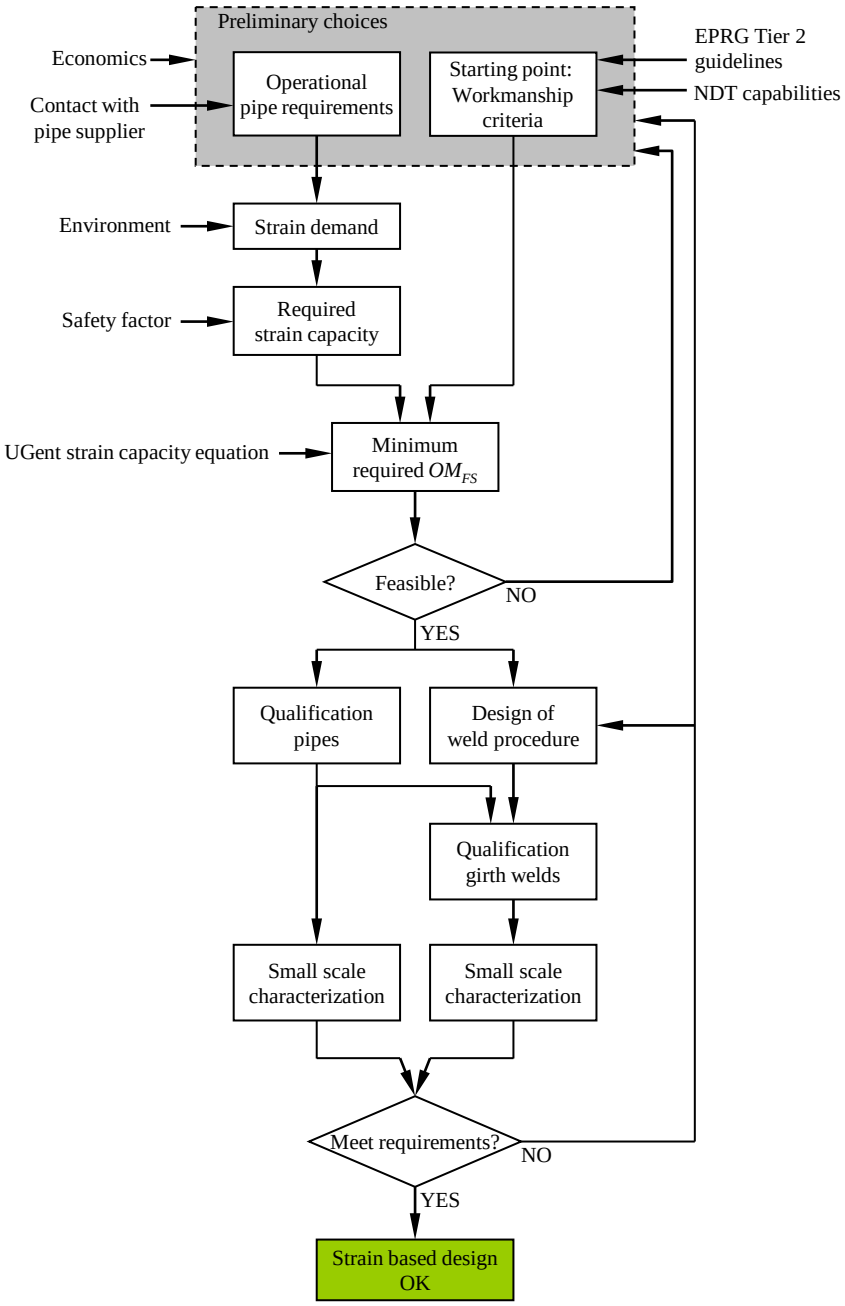

Figure 9.1: Proposed framework for strain based design.

steel characteristics [9.3]. Apart from the line pipe steel grade, particular attention should be given to its strain hardening behaviour, uniform elongation, strain ageing resistance and toughness [9.4].

2. The preliminary pipeline design is used for an estimation of strain demand [1].

3. Applying a safety factor on strain demand leads to a minimum required strain capacity. This factor should be carefully selected using known key ideas of safety assurance:

   - Frequence: *What is the possibility of occurrence of the considered strain demand mechanism(s)?*
   - Severity: *What are possible consequences of a pipeline failure with respect to people and environment?*
   - Detectability: *Can severe strains be monitored and be acted upon in time?* This is possible if strain develops slowly, e.g. in cases of permafrost heave and thaw [9.3]. For instance, the Enbridge Northern pipeline case study (section 1.6.3) illustrates how advanced pigging technology supports the prevention of failure.

4. Workmanship criteria and non destructive testing (NDT) capabilities are adopted for a first estimation of realistic allowable and identifiable flaw sizes. The EPRG Tier 2 guidelines (section 2.6.1) are proposed to the former's respect, given their strong experimental basis and close link with strain based assessment. Charpy impact energy requirements advised by the revised EPRG Tier 2 guidelines (minimum 60 J and above 80 J on average for plastically deformed pipelines) are also adopted at this stage.

5. At the early stage of a strain based design, validated analytical equations are required to make initial choices [9.3]. In this respect, the required strain capacity and selected flaw sizes are used in the UGent strain capacity equation (Eq. (2.23)) to obtain a minimum required weld flow stress overmatch level OM_{FS} [2].

6. The minimum required weld flow stress overmatch level may result in unrealistic weld metal specifications (e.g. combination a very high strength and sufficient toughness). Welding engineers decide on the feasibility of the specifications and – if necessary – suggest the need for design adaptations.

[1] Note that, although mostly imposed by environmental conditions, this strain demand is influenced by the pipeline itself (e.g. due to pipe-soil interaction effects) [9.5, 9.6].

[2] Note that the UGent strain capacity equation represents lower bound strain capacities obtained from experimental results and, thus, has a conservative basis.

7. Qualification pipes are ordered for small scale characterization of line pipe steel (tensile testing, toughness). The tensile test procedure of section 3.3.6 is advised [3].

8. A girth weld procedure is developed and investigated on the basis of qualification girth welds connection qualification pipe pups. Tensile, toughness and hardness tests should characterize weld metal and HAZ properties [9.4].

9. If all specified requirements are met, the strain based design is considered successful. If not, adaptations are made on the level of preliminary choices and/or girth weld procedure.

9.1.4.2 Strain based flaw assessment

Figure 9.2 depicts the proposed framework. Starting from qualification pipes and girth welds (see figure 9.1), the following steps are followed.

1. Starting from the small scale characterization of qualification pipes, theoretical worst case base metal combinations are selected and girth welded using the procedure developed in the framework of figure 9.1. Potential worst case combinations are listed in section 9.1.3.1.

2. Curved wide plates are extracted from the girth welded qualification pipes and tested. Advice with respect to specimen geometry, instrumentation and test protocol is provided in chapter 5.

3. It is attempted to approximate the experimental results by means of finite element analysis using the model explained in chapter 4. This provides an improved analysis of their evolution towards failure using techniques explained in chapter 7 (e.g. unloading compliance mapping, CMOD mapping). Also, the successful numerical replication of experimental results provides a validation of the representativeness of the finite element model under the investigated conditions.

4. The finite element model of chapter 4 is used for a parametric study covering different but representative material combinations, geometry and boundary conditions. With respect to the last aspect, full scale (pressurized) pipes are chosen for in this study. The 'UGent' stress-strain model (chapter 3) allows for the parametric description of line pipe steel properties. Flaw dimensions are varied within ranges of interest. Statistical techniques (e.g. design of experiments, section 5.4.2) may be applied to reduce the number of required finite element simulations.

[3] Note that the evaluation of qualification pipes is advised in [9.3] if 'relevant prior experience is not available' and allows for the production of qualification girth welds in step 8.

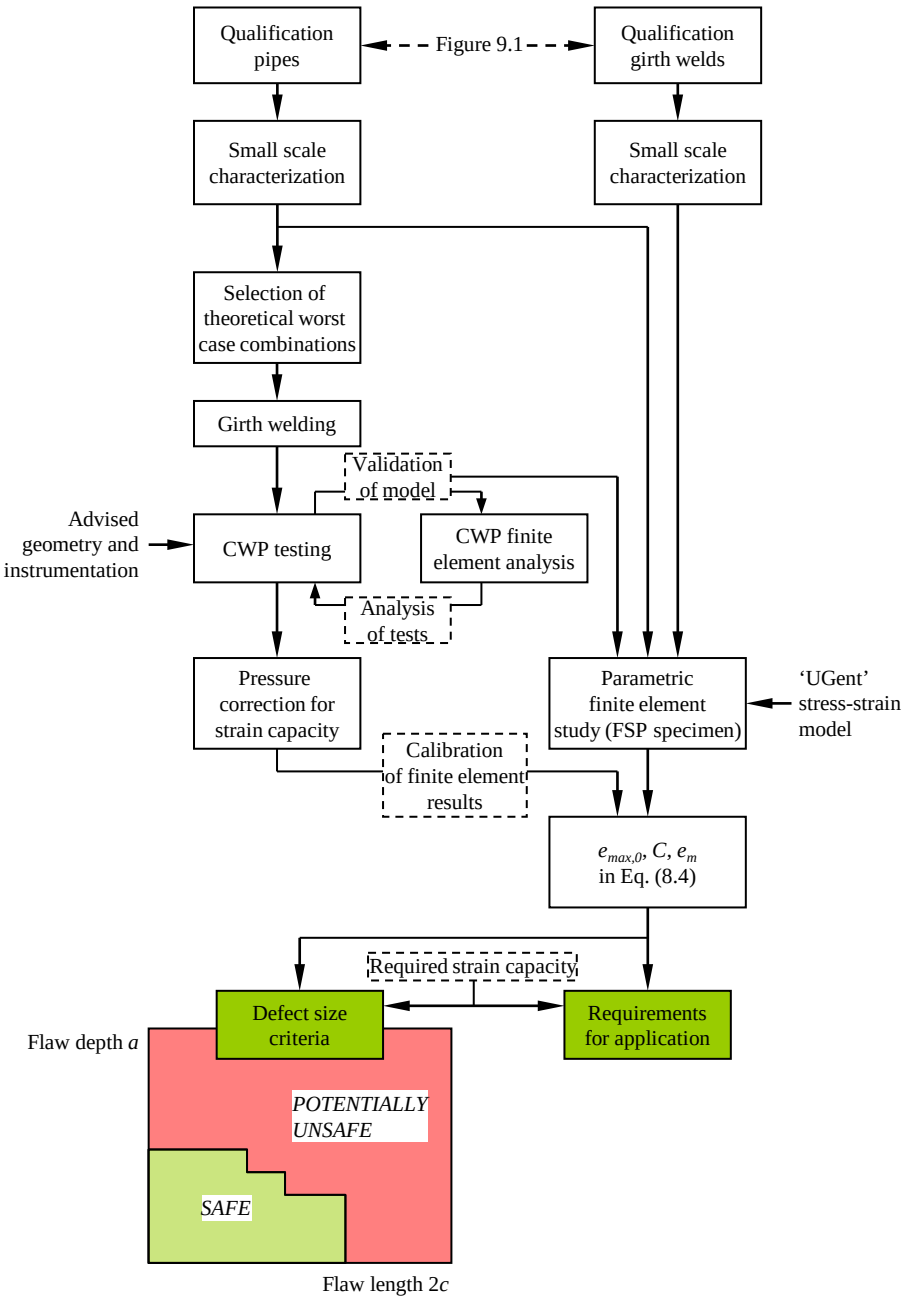

Figure 9.2: Proposed framework for strain based flaw assessment.

5. The parametric study allows to tabulate worst case parameters ($e_{max,0}$, C, e_m) in the proposed strain capacity equation (Eq. (8.4)) as a function of flaw dimensions. These parameters can be 'calibrated' by pressure corrected experimental CWP strain capacities to account for modelling assumptions [4].

6. The obtained results are translated into concrete defect size criteria (allowable flaw length $2c$ versus flaw depth a) to meet the required strain capacity, identified in figure 9.1. These criteria may be involve a set of requirements for application (e.g. a limitation on allowable weld misalignment).

9.2 Recommendations for future research

9.2.1 Characterization of heterogeneity and anisotropy of all involved materials and their influence

First, the experimental results (chapter 6) have indicated that base metal heterogeneity can strongly influence the strain capacity of a flawed girth weldment. The selection of two potential worst case base metal combinations (section 8.4), however, was based on severe assumptions which may not be fully representative to the actual structural problem. For instance, the tendency of decreasing uniform elongation for increasing line pipe yield strength has not been accounted for. An extensive parametric (finite element) study may reveal other potential worst case pipe combinations and will give a better quantification of effects of base metal heterogeneity on strain capacity.

Second, apart from heterogeneity between different pipes there may be a pronounced effect of heterogeneity in the girth weld, which is a continuous transition between different microstructures. It was assumed in this dissertation that welds can be characterized on the basis of their average stress-strain properties. Local microstructures near a flaw tip may, however, play an important role in the development of crack driving force and/or ductile tearing. An investigation of their influence is advised for future work.

Third, anisotropy in pipe (which was found to be pronounced in section 3.3.2) and weld metals has not been covered in the performed finite element analyses. This approximation was adopted from current common practice [9.7]. It is expected that influences of anisotropy may be considerable, given the global biaxial stress state in pressurized pipes under longitudinal plastic deformation. Therefore, anisotropy may be implemented and investigated in a more advanced finite element model.

[4] Similarly, the ExxonMobil strain capacity equations were calibrated by experimental results as some numerical predictions proved to be overly conservative. The identified cause of this conservatism was the absence of crack path deviation in the finite element model [9.1].

Finally, the measurement of girth weld metal properties in the direction of the pipe axis is challenging. To date, it requires either

- tests with a challenging execution (i.e. very small (micro) tensile test specimens [9.8, 9.9]). For instance, reported micro tensile test specimen geometries had a cross section of 0.5 mm $\times$ 2 mm.

or

- tests with a problematic analysis (i.e. notched cross weld tension tests [9.10, 9.11] or instrumented indentation tests [9.12]). The determination of weld metal properties from these tests mostly requires an iterative inverse finite element modelling framework.

Investigations into this matter are strongly advised since longitudinal weld properties are required to properly characterize weld metal anisotropy.

9.2.2 Relation between curved wide plate and full scale pressurized pipe tests

The effect of internal pressure on strain capacity is not covered by CWP tests. The concept of a pressure correction factor P_c which relates CWP test results with full scale pressurized pipe test results has received recent attention [9.2, 9.13]. Knowledge of this factor is important for the application of the proposed strain based design and assessment frameworks (figures 9.1 and 9.2).

Influences of geometry (e.g. weld misalignment), operation (e.g. internal pressure) and material (e.g. weld strength mismatch) properties on P_c are not yet fully quantified. More research in this respect is therefore strongly encouraged.

9.2.3 Further parametric studies

This dissertation has proven the ability of the parametric finite element model to gain insights in specific aspects of strain based flaw assessment. Focus has gone to influences of constitutive properties of base and weld metal. In addition, the finite element model can be readily (i.e. without modification) used for investigation of a variety of other factors, such as

- internal pressure of full scale pressurized pipe specimens,
- weld geometry (weld misalignment, fusion line profile, weld cap reinforcement or undercut),
- pipe geometry (diameter, thickness and variations of these characteristics between different pipes),
- heat-affected zone softening,

- flaw location and shape,
- ductile tearing resistance.

This list is far from exhaustive. For instance, minor modifications could include a deviation of the crack extension path, pipe out-of-roundness, angular misalignment, field cold bended pipes, bending loads, creating pipes with multiple flaws, ... These modifications mostly involve the mere implementation of an additional nodal coordinate transformation or boundary condition.

9.2.4 Analytical strain based flaw assessment

The strain capacity equation based on weld flow stress mismatch (Eq. (8.4)) requires knowledge of three parameters: $e_{max,0}$, C and e_m. Future efforts are advised to quantify these parameters as a function of various parameters related to loading (e.g. biaxiality effects in pressurized pipes), geometry (e.g. flaw size, weld geometry, flaw location), and material (e.g. base metal heterogeneity).

Additional validations of Eq. (8.4) may focus on cases of combined weld strength undermatch-overmatch (e.g. a weld with overmatching yield strength but undermatching tensile strength). These specific cases have not been investigated in the parametric study that led to the development of Eq. (8.4).

9.2.5 Broad perspectives

The presented dissertation is considered as a step forward towards a better understanding of the issue of strain based weld integrity, which is highly challenging due to the many parameters involved.

Despite the advances made, many issues remain unresolved. The increasing economical incentive to find, develop and exploit new fossil fuel resources in harsh regions will unavoidably result in ongoing research efforts in the field of strain based design and flaw assessment. After all, the avoidance of catastrophic events remains essential for the justification of pressurized pipelines as a means to transport fossil fuels.

Bibliography

[9.1] D.P. Fairchild, M.L. Macia, S. Kibey, X. Wang, V.R. Krishnan, F. Bardi, H. Tang, and W. Cheng. A multi-tiered procedure for engineering critical assessment of strain-based pipelines. In *Proceedings of the 21st International Offshore and Polar Engineering Conference (ISOPE)*, pages 698–705, Maui, Hawaii, USA, 2011.

[9.2] R. Denys, S. Hertelé, M. Verstraete, and W. De Waele. Strain capacity prediction for strain-based pipeline designs. In *Proceedings of the Internal Workshop on Welding of High Strength Pipeline Steels*, Araxá, Brazil, 2011. CBMM.

[9.3] M.L. Macia, S. Kibey, H. Arslan, F. Bardi, S.J. Ford, W.C. Kan, M.F. Cook, and B. Newbury. Approaches to qualify strain-based designed pipelines. In *Proceedings of the 8th International Pipeline Conference (IPC)*, Calgary, Alberta, Canada, 2010. IPC2010-31662.

[9.4] M.W. Hukle, D.B. Lillig, B.D. Newbury, J. Dwyer, and A.M. Horn. Development and qualification of pipeline welding procedures for strain based design. In *Proceedings of the 26th International Conference on Offshore Mechanics and Arctic Engineering (OMAE)*, San Diego, California, USA, 2007. OMAE2007-29581.

[9.5] W.C. Kan, M. Weir, M.M. Zhang, D.B. Lillig, S.T. Barbas, M.L. Macia, and N.E. Biery. Strain-based pipelines: design consideration overview. In *Proceedings of the 18th International Offshore and Polar Engineering Conference (ISOPE)*, pages 174–181, Vancouver, Canada, 2008.

[9.6] H. Arslan, J. Hamilton, L. Suvrat, K. Minnaar, B. Albrecht, M.F. Cook, and P. Wong. Strain demand estimation for pipelines in challenging arctic and seismically active regions. In *Proceedings of the 8th International Pipeline Conference (IPC)*, Calgary, Alberta, Canada, 2010. IPC2010-31505.

[9.7] Y. Shinohara, Y. Madi, and J. Besson. A combined phenomenological model for the representation of anisotropic hardening behavior in high strength steel line pipes. *European Journal of Mechanics A/Solids*, 29(6):917–927, 2010.

[9.8] W. Mohr. Strain-based design: strain concentration at girth welds. Technical Report 47447GTH, Edison Welding Institute, 2007. 190 pages.

[9.9] M. Koçak. Structural integrity of welded structures: Process - Property - Performance (3P) relationship. In *Proceedings of the 63rd Annual Assembly & International Conference of the International Institute of Welding*, Istanbul, Turkey, 2010.

[9.10] Z.L. Zhang, M. Hauge, C. Thaulow, and J. Odegard. A notched cross weld tensile testing method for determining true stress-strain curves for weldments. *Engineering Fracture Mechanics*, 69(3):353–366, 2002.

[9.11] A. Fonzo, G. Mannucci, L.F. Di Vito, and G. Richard. Advanced tensile behaviour evaluation of girth welds. In *Proceedings of the 18th International Offshore and Polar Engineering Conference (ISOPE)*, pages 57–63, Vancouver, Canada, 2008.

[9.12] M.-Q. Le. Material characterization by instrumented spherical indentation. *Mechanics of Materials*, 46:42–56, 2012.

[9.13] M. Verstraete, W. De Waele, R. Denys, and S. Hertelé. Pressure correction factor for strain capacity predictions based on curved wide plate testing. In *Proceedings of the 9th International Pipeline Conference (IPC)*, Calgary, Alberta, Canada, 2012. IPC2012-90592; accepted for publication.

Appendix A

Theoretical relations between n, Y/T and e_m for the Ramberg-Osgood model

This appendix provides a mathematical proof of the validity of Eqs. (3.18) and (3.28) for the Ramberg-Osgood model given by Eq. (3.15).

A.1 Background: the R6 relation between Y/T and n

This section mentions the mathematical proof of the R6 relation between Y/T and n [A.1]. This proof is given since it provides intermediary results (e.g. equations for uniform elongation) which have also been used.

Considère's necking criterion for true stress and strain (Eq. (3.3)) can be alternatively expressed as follows:

$$\frac{\mathrm{d}\epsilon}{\mathrm{d}\sigma}(\sigma_m) = \frac{1}{\sigma_m} \tag{A.1}$$

Application of this criterion on Eq. (3.15) yields:

$$\frac{1}{E} + 0.002n\frac{\sigma_m^{n-1}}{\sigma_{0.2}^n} = \frac{1}{\sigma_m} \tag{A.2}$$

$1/E$ is much smaller than $1/\sigma_m$ and can therefore be neglected. This leads to:

$$\frac{\sigma_{0.2}}{\sigma_m} \approx (0.002n)^{1/n} \tag{A.3}$$

From this equation, the true value of ultimate tensile strength σ_m is:

$$\sigma_m \approx \sigma_{0.2} \left(\frac{1}{0.002n} \right)^{1/n} \tag{A.4}$$

The true uniform elongation ϵ_m can be found by substituting σ in Eq. (3.15) by σ_m:

$$\epsilon_m \approx \frac{\sigma_{0.2}}{E} \left(\frac{1}{0.002n} \right)^{1/n} + \frac{1}{n} \tag{A.5}$$

For realistic values of $\sigma_{0.2}$, E and n, the first term in the equation above becomes marginally small, compared to the second term. Hence:

$$\epsilon_m \approx \frac{1}{n} \tag{A.6}$$

Converting this equation to engineering uniform elongation through Eq. (3.1) yields:

$$e_m \approx \exp\left(\frac{1}{n}\right) - 1 \tag{A.7}$$

$Y/T = R_{p0.2}/R_m$ can be obtained by substituting n in Eq. (A.4) using Eq. (A.7), and noting that $\sigma_{0.2} \approx R_{p0.2}$ and $\sigma_m = R_m\,(1 + e_m)$ (Eq. (3.2)):

$$Y/T \approx (0.002n)^{1/n} \exp\left(\frac{1}{n}\right) \tag{A.8}$$

Eq. (A.8) is given in R6 [A.1].

A.2 Inverse relation between n and Y/T

As shown in figure A.1, Eq. (A.8) is properly represented by Eq. (3.28), which provides an inverse relation between n and Y/T.

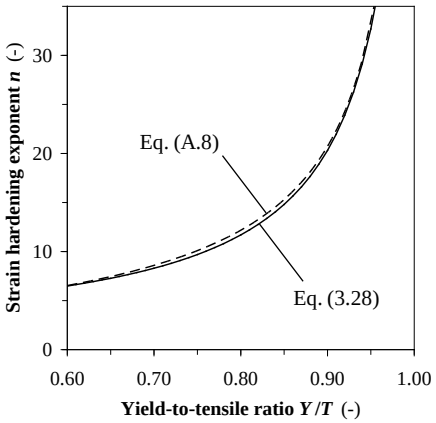

Figure A.1: Eqs. (3.28) and (A.8) roughly agree.

A.3 Relation between Y/T and e_m

Combining Eqs. (A.7) and (A.8) yields Eq. (3.18).

Bibliography

[A.1] *Assessment of the integrity of structures containing defects, R6-Revision 3.* British Energy Generation Ltd, 1999.

Appendix B

Procedures for determining suited 'UGent' model parameters: additional information

The following sections have been adopted from [B.1, B.2] and mostly provide mathematical details. For explanations and motivations, the reader is referred to these two papers.

B.1 Numerical procedure

B.1.1 Minimization algorithm

The Levenberg-Marquardt algorithm [B.3] was used for minimization of ϵ_{RMS} (Eq. (3.25)). This algorithm is robust but may lead to a local function minimum rather than the absolute minimum.

B.1.2 Initial parameter guesses

Aiming to avoid that the Levenberg-Marquardt algorithm would reach a local minimum for ϵ_{RMS} rather than the absolute minimum which characterizes the optimal parameter set, it has been applied with three different initial parameter guesses (table B.1). Apart from some rare exceptions, satisfactory results were readily obtained with this method. For a very limited number of stress-strain curves, further initial guesses were tried case specifically until an accurate representation of the experimental curve was obtained.

Table B.1: Initial parameter guesses for the least-squares curve fitting algorithm.

Initial guess nr.	Parameter				
	$\sigma_{0.2}$	σ_1	σ_2	n_1	n_2
	Initial value				
1	$R_{p0.2}$	$\min(1.08R_{p0.2}, FS)$	$\min(1.16R_{p0.2}, R_m)$	15	10
2				20	15
3				25	20

B.1.3 Selection of stress-strain data points used in the minimization function

The calculation of ϵ_{RMS} through Eq. (3.25) requires a selected set of experimental true stress-strain datapoints (ϵ_i, σ_i), $i = 1 \ldots N$. These points were systematically chosen starting from engineering stress-strain curves. Concretely,

1. the parts after initiation of localized necking (e_m, R_m) were cut off.
2. engineering stress-strain values were converted to true values using Eqs. (3.1) and (3.2). In particular, (e_m, R_m) were converted to (ϵ_m, σ_m).
3. the obtained curves were reduced to a set of 100 $(= N)$ stress-strain points each. Of these, 80 points were taken in the strain interval $[0.00, 0.01]$ which represents early yielding. The other 20 datapoints were uniformly distributed over the remaining part of the curve.

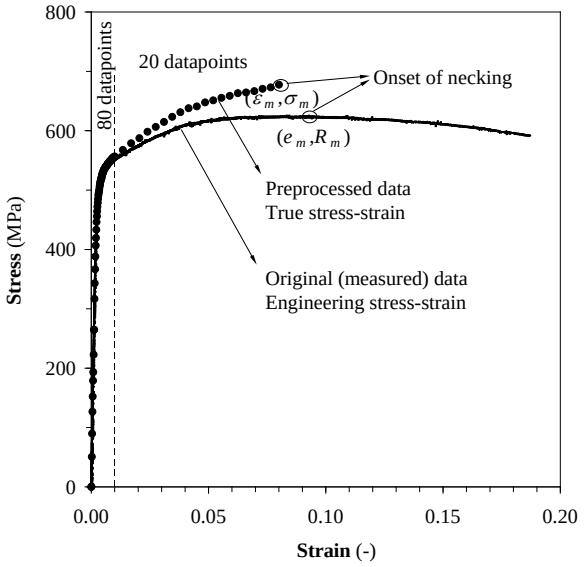

Figure B.1: A graphical overview of the applied procedure for stress-strain data preprocessing.

B.2 Analytical procedure

B.2.1 Step 1: defining and delimiting the linear elastic area

E is readily adopted from the experimental stress-strain curve. Further,

$$\sigma_{0.2} = R_{p0.2}\left(1.002 + \frac{R_{p0.2}}{E}\right) \tag{B.1}$$

B.2.2 Step 2: defining the early yielding area

$$n_1 = \frac{\ln\left(0.010/0.002\right)}{\ln \sigma_{1.0}/\sigma_{0.2}} = \frac{\ln 5}{\ln \sigma_{1.0}/\sigma_{0.2}} \tag{B.2}$$

with

$$\sigma_{1.0} = R_{p1.0}\left(1.010 + \frac{R_{p1.0}}{E}\right) \tag{B.3}$$

B.2.3 Step 3: estimating the extensive yielding area

A first estimation of n_2 (denoted n_{2i}) is obtained as follows:

$$n_{2i} = 3 + 2.5\frac{Y/T}{1.03 - Y/T} \tag{B.4}$$

with $Y/T = R_{p0.2}/R_m$.

B.2.4 Step 4: defining the transition area

σ_1 is estimated as

$$\sigma_1 = \sigma_{0.2} \tag{B.5}$$

σ_2 is estimated as

$$\sigma_2 = \sigma_{0.2}\left(0.99 + \frac{0.7}{0.9 + 0.22\Omega}\right) \tag{B.6}$$

with ($n_{max} = \max(n_1, n_{2i})$ and $n_{min} = \min(n_1, n_{2i})$):

$$\Omega = n_{max} - 0.35n_{min} - 1.5\left|\Delta\epsilon_i\right|^{2-0.1(n_{max}-n_{min})} \tag{B.7}$$

where ($\epsilon_m = \ln(1 + e_m)$)

$$\Delta\epsilon_i = \min\left[\max\left(\frac{1}{n_{2i}} - \epsilon_m, -0.02\right), 0.02\right] \tag{B.8}$$

Note the validity area for application of Eq. (B.5), shown in figure 3.29.

B.2.5 Step 5: modifying the extensive yielding area

$\sigma_{0.2}$, σ_1, σ_2, n_1 and n_2 are used to calculate an updated value for $\Delta\epsilon$ (denoted $\Delta\epsilon_{ii}$) through Eq. (3.24). Then, n_2 is determined as follows:

$$n_2 = \frac{\ln\left(\frac{\epsilon_{m,pl}+\Delta\epsilon_{ii}}{0.002}\right)}{\ln(\sigma_m/\sigma_{0.2})} \tag{B.9}$$

with $\sigma_m = R_m(1 + e_m)$ and $\epsilon_{m,pl} = \epsilon_m - \sigma_m/E$.

Bibliography

[B.1] S. Hertelé, W. De Waele, R. Denys, and M. Verstraete. Full-range stress-strain behaviour of contemporary pipeline steels: Part I. Model description. *International Journal of Pressure Vessels and Piping*, 2012. In Press. doi 10.1016/j.ijpvp.2012.01.006.

[B.2] S. Hertelé, W. De Waele, R. Denys, and M. Verstraete. Full-range stress-strain behaviour of contemporary pipeline steels: Part II. Estimation of

model parameters. *International Journal of Pressure Vessels and Piping*, 2012. In Press. doi 10.1016/j.ijpvp.2012.01.007.

[B.3] K. Levenberg. A method for the solution of certain non-linear problems in least squares. *Quarterly Journal of Applied Mathematics*, 2(2): 164–168, 1945.

Publications

List of scientific publications of Stijn Hertelé (first author or co-author).

A1 - Peer reviewed journal publications included in Science Citation Index

First author: 7 publications
Co-author: 2 publications

1. A. Temmerman, **S. Hertelé**, W. Teughels, C. Dekeyser, R. Jacobs, and M. Quirynen. Are panoramic images reliable in planning sinus augmentation procedures? *Clinical Oral Implants Research*, 22(2):189–194, 2011.

2. **S. Hertelé**, W. De Waele, and R. Denys. A generic stress-strain model for metallic materials with two-stage strain hardening behaviour. *International Journal of Non-linear Mechanics*, 46(3):519–531, 2011.

3. **S. Hertelé**, W. De Waele, and R. Denys. Development of an analytical reference stress equation for inner-diameter defected curved plates in tension. *International Journal of Pressure Vessels and Piping*, 88(5-7):256–261, 2011.

4. **S. Hertelé**, W. De Waele, R. Denys, M. Verstraete, and J. Van Wittenberghe. Parametric finite element model for large scale tension tests on flawed pipeline girth welds. *Advances in Engineering Software*, 47(1):24–34, 2012.

5. J. Van Wittenberghe, P. De Baets, W. De Waele, W. Ost, M. Verstraete, and **S. Hertelé**. Resonant bending fatigue test setup for pipes with optical displacement measuring system. *Journal of Offshore Mechanics and Arctic Engineering - Transactions of the ASME*, 134(3):031702 (6 pages), 2012.

6. **S. Hertelé**, W. De Waele, R. Denys, and M. Verstraete. Full-range stress-strain behaviour of contemporary pipeline steels: Part I. Model description. *International Journal of Pressure Vessels and Piping*, 92:34–40, 2012.

7. **S. Hertelé**, W. De Waele, R. Denys, and M. Verstraete. Full-range stress-strain behaviour of contemporary pipeline steels: Part II. Estimation of model parameters. *International Journal of Pressure Vessels and Piping*, 92:27–33, 2012.

8. **S. Hertelé**, W. De Waele, R. Denys, and M. Verstraete. Investigation of strain measurements in (curved) wide plate specimens using digital image correlation and finite element analysis. *Journal of Strain Analysis for Engineering Design*, Accepted for publication.

9. **S. Hertelé**, W. De Waele, R. Denys, and M. Verstraete. Sensitivity of plastic response of defective pipeline girth welds to the stress-strain behavior of base and weld metal. *Journal of Offshore Mechanics and Arctic Engineering - Transactions of the ASME*, Accepted for publication.

A2 - Peer reviewed journal publications not included in Science Citation Index

First author: 2 publications

1. **S. Hertelé**, W. De Waele, and R. Denys. Full range stress-strain modelling of pipeline steels. *Journal of Pipeline Engineering*, 8(9):213–221, 2009.

2. **S. Hertelé**, W. De Waele, R. Denys, and M. Verstraete. Analytical validation of crack driving force calculations for defects in plates and pipes under tension. *Mechanical Engineering Letters*, 5:81–88, 2011.

C1 - Publications in conference proceedings

First author: 11 publications
Co-author: 18 publications

1. **S. Hertelé**, W. De Waele, and R. Denys. A new stress-strain model for linepipe steels in strain-based design. In *Proceedings of the 8th National Congress on Theoretical and Applied Mechanics (NCTAM)*, 8 pages, Brussels, Belgium, 2009.

2. R. Denys, **S. Hertelé**, W. De Waele, and A. Lefevre. Estimate of Y/T ratio and uniform elongation capacity of pipeline steels from yield strength. In *Proceedings of the 5th International Conference on Pipeline Technology*, 10 pages, Ostend, Belgium, 2009.

3. **S. Hertelé**, W. De Waele, and R. Denys. Full range stress-strain relation modeling of pipeline steels. In *Proceedings of the 5th International Conference on Pipeline Technology*, 11 pages, Ostend, Belgium, 2009.

4. J.B. Wellekens, W. De Waele, R. Denys, **S. Hertelé**, and M. Verstraete. Interpretation of stress-strain curve in pipeline research. *Sustainable Construction and Design*, 1(1):40–45, Ghent, Belgium, 2010. ISSN 2032-7471.

5. **S. Hertelé**, W. De Waele, R. Denys, M. Abdel Wahab, and M. Verstraete. Inherent possibilities and limitations of finite element modelling of defective girth welds. *Sustainable Construction and Design*, 1(1):127–135, Ghent, Belgium, 2010. ISSN 2032-7471.

6. M. Verstraete, W. De Waele, **S. Hertelé**, and R. Denys. Evaluation of pipe bending reference stress equations. *Sustainable Construction and Design*, 1(1):190–205, Ghent, Belgium, 2010. ISSN 2032-7471.

7. **S. Hertelé**, W. De Waele, R. Denys, J. Van Wittenberghe, and M. Verstraete. Limit load and reference stress for curved wide plates. In *Proceedings of the 8th International Pipeline Conference (IPC)*, 8 pages, Calgary, Alberta, Canada, 2010. IPC2010-31290.

8. **S. Hertelé**, W. De Waele, and R. Denys. Determination of full range stress-strain behavior of pipeline steels using tensile characteristics. In *Proceedings of the 8th International Pipeline Conference (IPC)*, 10 pages, Calgary, Alberta, Canada, 2010. IPC2010-31291.

9. **S. Hertelé**, W. De Waele, R. Denys, J. Van Wittenberghe, and M. Verstraete. Investigation of pipe strain measurements in a curved wide plate specimen. In *Proceedings of the 8th International Pipeline Conference (IPC)*, 10 pages, Calgary, Alberta, Canada, 2010. IPC2010-31292.

10. J. Van Wittenberghe, P. De Baets, W. De Waele, W. Ost, M. Verstraete, and **S. Hertelé**, Pipe resonant bending fatigue test setup with optical measuring system, In *Proceedings of the 8th International Pipeline Conference (IPC)*, 8 pages, Calgary, Alberta, Canada, 2010. IPC2010-31115.

11. R. Denys, **S. Hertelé**, and M. Verstraete. Longitudinal strain capacity of GMAW welded high niobium (HTP) grade X80 steel pipes. In *Proceedings of the International seminar on Application of High Strength Line Pipe (HSLP)*, pages 62–74, Xi'an, China, 2010.

12. R. Denys, **S. Hertelé**, and M. Verstraete, Strain capacity of weak and strong girth welds in axially loaded pipelines. In *Proceedings of the International Pipeline Technology Conference (IPTC)*, pages 116–124, Beijing, China, 2010.

13. M. Verstraete, W. De Waele, and **S. Hertelé**. Development and validation of a high constraint modified boundary layer finite element model. In *Sustainable Construction and Design*, 2(2):228–236, Ghent, Belgium, 2011. ISSN 2032-7471.

14. **S. Hertelé**, W. De Waele, R. Denys, and M. Verstraete. Design of a (mini) wide plate specimen for strain-based weld integrity assessment. In *Sustainable Construction and Design*, 2(2):258–268, Ghent, Belgium, 2011. ISSN 2032-7471.

15. K. Van Minnebruggen, D. Van Puyvelde, W. De Waele, M. Verstraete, **S. Hertelé**, and R. Denys, Implementation of an unloading compliance procedure for measurement of crack growth in pipeline steel. In *Sustainable Construction and Design*, 2(3):397–406, Ghent, Belgium, 2011. ISSN 2032-7471.

16. K. De Keyser, F. Van Acker, **S. Hertelé**, M. Verstraete, W. De Waele, and R. Denys. Validation of a wide plate finite element model using digital image correlation. In *Sustainable Construction and Design*, 2(3):416–423, Ghent, Belgium, 2011. ISSN 2032-7471.

17. M. Verstraete, W. De Waele, **S. Hertelé**, R. Denys. Evaluation of strength mismatch by FE Analysis and DIC measurements on cross weld tensile specimens. In *Proceedings of the 21st International Offshore and Polar Engineering Conference (ISOPE)*, pages 698–705, Maui, USA, 2011.

18. **S. Hertelé**, W. De Waele, R. Denys, and M. Verstraete. Sensitivity of plastic response of defective pipeline girth welds to the stress-strain behavior of base and weld metal. In *Proceedings of the 30th International Conference on Ocean, Offshore and Arctic Engineering (OMAE)*, 11 pages, Rotterdam, The Netherlands, 2011. OMAE2011-49239.

19. R. Denys, **S. Hertelé**, M. Verstraete, and W. De Waele, Strain capacity prediction for strain-based pipeline designs. In *Proceedings of the International seminar on Welding of High Strength Pipeline Steels*, 13 pages, Araxá, Brazil, 2011.

20. J. Maelfait, M. Cauwelier, M. Verstraete, **S. Hertelé**, K. Van Minnebruggen, and W. De Waele. Validation of a finite element model for fracture mechanics specimens. In *Proceedings of the 4th Conference on Sustainable Construction and Design (SCAD)*, pages 8–18, Ghent, Belgium, 2012. ISSN 2032-7471.

21. J. Beddeleem, W. De Waele, **S. Hertelé**, M. Verstraete, and K. Van Minnebruggen. Characterization of mechanical properties in weld metal using inverse modelling. In *Proceedings of the 4th Conference on Sustainable Construction and Design (SCAD)*, pages 19–24, Ghent, Belgium, 2012. ISSN 2032-7471.

22. M. Verstraete, **S. Hertelé**, W. De Waele, and R. Denys. Influence and evaluation of constraint on fracture toughness in pipeline research. In *Proceedings of the 4th Conference on Sustainable Construction and Design (SCAD)*, pages 25–35, Ghent, Belgium, 2012. ISSN 2032-7471.

23. **S. Hertelé**, W. De Waele, R. Denys, and M. Verstraete. Justification of the mapping approach for finite element modelling of ductile tearing. In *Proceedings of the 4th Conference on Sustainable Construction and Design (SCAD)*, pages 36–43, Ghent, Belgium, 2012. ISSN 2032-7471.

24. **S. Hertelé**, W. De Waele, R. Denys, M. Verstraete, and K. Van Minnebruggen. Curved wide plate testing with advanced instrumentation and interpretation. Accepted for *9th International Pipeline Conference (IPC)*, Calgary, Canada. IPC2012-90591.

25. M. Verstraete, W. De Waele, R. Denys, and **S. Hertelé**. Pressure correction factor for strain capacity predictions based on curved wide plate testing. Accepted for *9th International Pipeline Conference (IPC)*, Calgary, Canada. IPC2012-90592.

26. M. Verstraete, W. De Waele, **S. Hertelé**, and R. Denys. Comparison of pipeline girth weld defect acceptance at the onset of yielding according to CSA Z662 and EPRG guidelines. Accepted for *9th International Pipeline Conference (IPC)*, Calgary, Canada, 2012. IPC2012-90593.

27. **S. Hertelé**, W. De Waele, R. Denys, M. Verstraete, K. Van Minnebruggen, and A.J. Horn. Effect of pipe post-yield behaviour on crack driving force in a mismatched girth weld. Accepted for *Pressure Vessels and Piping Conference (PVP)*, Toronto, Canada, 2012. PVP2012-78306.

28. M. Verstraete, W. De Waele, R. Denys, **S. Hertelé**, and K. Van Minnebruggen. Measurement of ductile crack extension in single edge notch tensile specimens. Accepted for *International Conference on Experimental Mechanics*, Porto, Portugal, 2012.

29. M. Verstraete, W. De Waele, **S. Hertelé**, R. Denys. Constraint analysis of Curved Wide Plate specimens. Accepted for *19th European Conference on Fracture (ECF)*, Kazan, Russia, 2012.

C3 - Conference abstracts

First author: 3 publications
Co-author: 2 publications

1. **S. Hertelé**, W. De Waele, R. Denys, and J. Van Wittenberghe. Numerical evaluation of the CMOD of defects in pipeline girth welds under remote plastic deformation. Abstract, *International Conference on Advanced Computational Engineering and Experimenting (ACE-X)*, Rome, Italy, 2009.

2. J. Van Wittenberghe, P. De Baets, W. De Waele, and **S. Hertelé**. Parametric model for evaluating the performance of threaded pipe connections. Abstract, *International Conference on Advanced Computational Engineering and Experimenting (ACE-X)*, Rome, Italy, 2009.

3. **S. Hertelé**. Development of a strain-based flaw assessment method for defective pipeline girth welds. Abstract, *11e UGent-FirW Doctoraatssymposium*, Ghent, Belgium, 2010. **Best presentation award, category 'Senior PhD researchers'.**

4. **S. Hertelé**, W. De Waele, R. Denys, and M. Verstraete. Gekoppeld experimenteel-numeriek onderzoek naar de vervormingscapaciteit van pijpsecties met omtrekslasfout. Abstract, *BIL/NIL Lassymposium*, Antwerp, Belgium, 2012. In Dutch.

5. M. Verstraete, W. De Waele, R. Denys, and **S. Hertelé**. Evaluatie van de vervormingscapaciteit van lasverbindingen. Abstract, *BIL/NIL Lassymposium*, Antwerp, Belgium, 2012. In Dutch.